UNIVERSIDAD DE LA RIOJA

TESIS DOCTORAL

Título
Novel Advances in Bioprinting Based on the Mechanical Design and Optimization of Open-source Systems
Autor/es
Enrique Sodupe Ortega
Director/es
Alpha Verónica Pernía Espinoza y Andrés Sanz García
Facultad
Escuela Técnica Superior de Ingeniería Industrial
Titulación
Departamento
Ingeniería Mecánica
Curso Académico

Novel advances in bioprinting based on the mechanical design and optimization of open-source systems

Enrique Sodupe Ortega

A thesis submitted in

fulfillment of the requirements for the

Degree of Doctor of Philosophy

DEPARTMENT OF MECHANICAL ENGINEERING

UNIVERSITY OF LA RIOJA

MARCH 2019

I hereby declare that this thesis entitled "Novel advances in bioprinting based on the mechanical design and optimization of open-source systems" is the result of my own research except as cited in the references. This thesis has not been accepted for any degree and is not concurrently submitted in candidature of any other degree.

Signature :

Student : Enrique Sodupe Ortega

Date : March 2019

Supervisors : Dra. Alpha Verónica Pernía Espinoza

Dr. Andrés Sanz García

To my parents

Acknowledgments

First of all, I want to express my sincere gratitude to my supervisors Dra. Alpha Pernía Espinoza and Dr. Andrés Sanz García for their continuous support, constructive criticism and encouragement throughout this research. Special thanks to Dr. Francisco Javier Martinez de Pisón, who always trusted in me and provided the best possible advice. I also want to express special gratitude to Dr. Eduardo Martinez de Pisón for its support in the first years of this journey. These acknowledgments are also extended to the members of the EDMANS research group, Javier, Fernando, Julio, Manuel and especially to Rubén for their feedback, cooperation and friendship over these years.

I would like to acknowledge the financial support provided by the Government of La Rioja through its doctoral fellowship program FPI-CAR-2014. I also want to express my gratitude to "Instituto de Estudios Riojanos" and ATUR grants (2015, 2016 and 2017) for funding parts of this research. Research funding No. 266486, 273689 and 273689 (FINSKIN) from the Academy of Finland also funded parts of this research. I also want to thank BQ for providing some of the equipment utilized in this thesis.

Special thanks to Prof. Tatsuya Shimizu for letting me collaborate with his research group at TWIns research center. I would like to thank Daisuke, Sakaguchi, Kosuke, Risa, Hiroki, Allie and all members of TWIns institute for making my research stay in Japan so pleasant. I also want to acknowledge Dra. Carmen Escobedo for kindly hosting my research visit at the University of Helsinki, and for giving me the best support and counseling whenever I needed. I am also grateful to Leena and Heikki for their support and assistance during my stay at the University of Helsinki. I would also like to thank Alejandro, Carolina and both Cristinas for our friendship and making the Finish winter so pleasant.

Finally, a special thanks to my family, friends and all those who have supported me over these years in one way or the other. Words cannot express how grateful I am to my parents for their unconditional love and the support they have provided me. It would not be possible to conduct this research without them.

Enrique Sodupe Ortega, Logroño, Spain

Agradecimientos

Primero de todo quiero expresar mi más sincero agradecimiento a mis supervisores Dra. Alpha Pernía Espinoza y Dr. Andrés Sanz García por su continuo apoyo, su crítica constructiva y su estímulo a lo largo de esta investigación. Quiero hacer un agradecimiento especial para el Dr. Francisco Javier Martínez de Pisón, quien siempre confió en mí y me brindó el mejor consejo posible. También quiero expresar un agradecimiento especial al Dr. Eduardo Martínez de Pisón por su apoyo en los primeros años de este viaje. Estos agradecimientos también son extensibles a los miembros del grupo de investigación EDMANS, Javier, Fernando, Julio, Manu y especialmente a Rubén por sus comentarios, cooperación y amistad a lo largo de estos años.

Quiero agradecer el apoyo económico ofrecido por el Gobierno de La Rioja a través del programa doctoral FPI-CAR-2014. También quiero expresar mi agradecimiento al Instituto de Estudios Riojanos y a las becas ATUR (2015, 2016 y 2017) por financiar parte de esta investigación. Los proyectos de investigación No. 266486, 273689 y 273689 (FINSKIN) de la Academia de Finlandia también han financiado parte de esta investigación. También quiero agradecer a BQ por proporcionar algunos de los equipos empleados en esta tesis.

Agradecimientos especiales al Prof. Tatsuya Shimizu por permitirme colaborar con su grupo de investigación en el centro de investigación TWIns. Me gustaría agradecer a Daisuke, Sakaguchi, Kosuke, Risa, Hiroki, Allie y todos los miembros del instituto TWIns haber hecho mi estancia de investigación en Japón tan agradable. También quiero agradecer a la Dra. Carmen Escobedo haberme permitido realizar mi estancia en la Universidad de Helsinki, así como por darme el mejor apoyo y consejo siempre que lo he necesitado. También estoy agradecido a Leena y Heikki por su apoyo y asistencia a lo largo de mi estancia en la Universidad de Helsinki. Me gustaría agradecer a Alejandro, Carolina y las dos

Cristinas por su amistad y haber hecho que el invierno finlandés fuese mucho más agradable en vuestra compañía.

Finalmente, un agradecimiento especial a mi familia, amigos y todos aquellos que me han apoyado a lo largo de estos años de una forma u otra. No se puede expresar con palabras lo agradecido que estoy a mis padres por su amor incondicional y todo el apoyo que me han brindado. No habría sido posible llevar a cabo esta tesis sin ellos.

Enrique Sodupe Ortega, Logroño, España

Abstract

Three-dimensional (3D) bioprinting promises to be a practical solution for solving the increasing demand for organs and tissues. Several 3D bioprinters with different specifications are commercially available, but the impact on the field of tissue engineering (TE) is still limited, mainly due to the high costs and the unfamiliarity of researchers with this technology. As with the current bioprinters, for many years the access to 3D printers was very expensive and its use was restricted to a few companies and research centers. However, the appearance of open-source 3D printing projects such as Fab@Home or RepRap and commercial desktop 3D printers have permitted to democratize the access to this technology. These printing platforms can serve as a springboard to expand the potential of bioprinting technology to all the scientific community. In that sense, this thesis presents a set of bioprinting tools that include the generation of a fully open-source bioprinting platform and several extrusion-based printheads for the deposition of bioinks and scaffold materials. Moreover, using this open-source printing platform, it was possible to address specific problems for the generation of complex multi-material and cell-laden constructs with high cell-viability percentages.

Addressing the complexity of organs and living tissues will require combining multiple building and sacrificial biomaterials and several cells types in a single biofabrication session. This is a significant challenge, and, to tackle that, we must focus on the complex relationships between the printing parameters and the print resolution. We proposed a standard methodology to quantify the print resolution of a bioprinter and establish a comparison framework between bioprinters. The calibration models utilized also permitted to identify which are the most important factors affecting printing accuracy. In this line, an automatic and non-expensive calibration system was also proposed, which can be utilized in bioprinters with multiple printheads. This system permits to obtain faster and more accurate alignment of the printheads, as the whole calibration process is done at once and without manual adjustments. We also performed a compre-

hensive study of all the parameters involved in the printing process (pressure, temperature, speed, nozzle size and morphology) and including different types of biomaterials. These experiments permitted to understand the influence of each parameter on the printing process and select the optimal configurations for each application.

Overall, the contributions presented in this thesis posses the potential to expand bioprinting technology among the TE laboratories. Moreover, it enhances the collective knowledge of the bioprinting community with particular innovative proposals.

Resumen

La bioimpresión tridimensional (3D) promete ser una solución práctica para resolver la creciente demanda de órganos y tejidos. Ya podemos encontrar varias impresoras 3D comerciales con diferentes especificaciones, sin embargo, su impacto en el campo de la ingeniería de tejidos todavía es limitado, debido principalmente a los altos costes y la falta de familiaridad de los investigadores sobre esta tecnología. Al igual que ocurre con las bioimpresoras actuales, durante muchos años el acceso a las impresoras 3D era muy costoso y su uso estaba limitado a unas pocas empresas y centros de investigación. Sin embargo, la aparición de proyectos open-source de impresión 3D como Fab@Home o RepRap, así como las impresoras domésticas comerciales, permitieron democratizar el acceso a esta tecnología. Estas plataformas de impresión pueden servir de trampolín para expandir el potencial de la tecnología de bioimpresión a toda la comunidad científica. En este sentido, esta tesis presenta un conjunto de herramientas de bioimpresión que incluyen la creación de una plataforma de bioimpresión plenamente open-source y varios cabezales de extrusión para la impresión de biotintas y materiales de soporte. Además, mediante el uso de esta plataforma de impresión open-source, ha sido posible abordar problemas específicos para la generación de impresiones multimaterial complejas y cargadas de células con altos porcentajes de viabilidad celular.

Abordar la complejidad de los órganos y tejidos vivos precisa de combinar varios biomateriales de construcción y sacrificiales, así como diferentes tipos celulares en una sola sesión de biofabricación. Todo esto supone un desafío considerable, y para poder solucionarlo debemos centrarnos en las complejas relaciones existentes entre los parámetros de impresión y la resolución de impresión. Nosotros proponemos una metodología estándar para cuantificar la resolución de impresión de una bioimpresora y establecer un marco de comparación común entre impresoras. Los modelos de calibración empleados también permiten identificar cuáles son los factores más importantes que afectan a la precisión en la impre-

sión. En este sentido, también proponemos un sistema de calibración automático y asequible, el cual puede ser empleado en bioimpresoras con múltiples cabezales. Este sistema permite obtener una alineado de los cabezales de impresión más rápido y preciso, ya que todo el proceso de calibración se produce de una sola vez y sin ajustes manuales. También hemos realizado un estudio exhaustivo de todos los parámetros de impresión involucrados en el proceso de impresión (presión, temperatura, velocidad, tamaño y morfología de las boquillas de impresión) e incluyendo diferentes tipos de biomateriales. Estos experimentos permitieron comprender la influencia de cada parámetro en el proceso de impresión y seleccionar la configuración óptima para cada aplicación.

En líneas generales, las contribuciones presentadas en esta tesis tienen el potencial de expandir la tecnología de bioimpresión a todos los laboratorios de ingeniería de tejidos. Además, aumenta el conocimiento colectivo de la comunidad de bioimpresión con innovadoras propuestas.

Contents

List of Figures

List of Tables

Notation

η	Viscosity
η_0	Zero-shear viscosity
η_t	Viscosity at some reference temperature
$\dot{\gamma}$	Shear rate
λ	Relaxation time
ρ	Density
$2D$	Two-dimensional
$3D$	Three-dimensional
ABS	Acrylonitrile butadiene styrene
$AFA-LIFT$	Absorbing film-assisted laser-induced forward transfer
Al	Aluminum
Alg	Alginate
AM	Additive manufacturing
$BioLP$	Biological laser processing
CAD	Computer-aided design

CFD	Computational fluid dynamics
CFM	Cubic feet per minute
CMS	Critical micelle concentration
CMT	Critical micelle temperature
CT	Computed tomography
D	Strand diameter
DOD	Drop-on-demand
E_a	Activation energy
EBB	Extrusion-based bioprinting
ECM	Extracellular matrix
FDM	Fused deposition modeling
FFF	Fused filament fabrication
G	Gauge
G'	Storage modulus
G''	Loss modulus
Gel	Gelatin
$GelMa$	Methacrylated gelatin
h	Hour
HA	Hyaluronic acid
$hASCs$	Human adipose derived mesenchymal stem cells

HDT	Heat deflection temperature
$HMVEC$	Human microvascular endothelial cells
HP	Hewlett Packard
HTC	Heat transfer coefficient
ID	Inner diameter
LAB	Laser-assisted bioprinting
$LG-DW$	Laser-guided direct writing
$LIFT$	Laser-induced forward transfer
LVR	Linear viscoelastic region
$MAPLE-DW$	Matrix-assisted pulsed laser evaporation direct writing
$MEBB$	Microextrusion-based bioprinting
min	Minute
$MOSFET$	Metal-oxide-semiconductor field-effect transistor
MRI	Magnetic resonance imaging
P	Pore size
$P407$	Poloxamer 407
$P\#$	Printhead#
PBS	Phosphate buffered saline
PCL	Polycaprolactone
PEG	Poly(ethylene glycol)

PLA	Polylactic acid
R	Thermodynamic constant
RT	Room temperature
s	Second
SS	Strand spacing
STL	Standard tessellation language
T_0	Lowest absolute temperature
T_{ref}	Reference temperature
TE	Tissue engineering
UV	Ultraviolet

Chapter 1

Introduction

1.1 Background

Transplantation has become one of the most common medical procedures for the treatment of tissue damage or organ failure. Since the first organ transplantation in 1954 of human kidney (JP *et al.*, 1956), thousands of transplants of complex organs as liver, lungs or heart have been performed with successful results. Despite the countless lives saved since the 1950s and having improved substantially the quality of life of the population, organ transplantation is extremely influenced by the current donor shortage. The organ waiting lists are still growing each year as the transplants demand exceeds the current supply of organs. A total of 33.4 thousand organs were transplanted in the EU (505.9 million inhabitants) in 2016. However, 59 thousand patients remained on the waiting list (Europe, 2017). In the U.S (323.4 million inhabitants) a total of 115 thousand patients are currently on the waiting list and an average of 20 people died each day waiting for a transplant in 2016 (UNOS, 2018). Finding a compatible donor and avoid possible rejection responses after transplantation are additional challenges that increase the shortage of available organs. All these limitations require the search for alternative solutions to provide substitutes to the growing need of tissues and organs.

Within this context tissue engineering (TE) emerged in the early 1970s as a possible solution to the aforementioned problems. TE is a multidisciplinary field that utilizes the principles of engineering and life sciences with the ultimate goal of the developing of biological substitutes that can restore, improve or maintain damaged tissues or organs (Langer & Vacanti, 1993). The terms TE and regenerative medicine have become largely interchangeable, including various

disciplines such as medicine, bioengineering, chemistry, biology and materials science. All these disciplines complement each other and allow scientists to search new insights for the development of innovative biofabrication strategies. One of the main advantages of TE is the high customization of engineered organs and tissues, which can be generated with the patient´s cells. This feature permits to overcome the risks of organ rejections and the use of immunosuppressive therapies, which can make a difference for all those patients with failing organs after transplantation. Despite the significant advances in TE over the last decades, the generation of functional organs and tissues still faces several challenges that need to be solved. These include among others, searching for fully compatible biomaterials that mimic the ECM, finding reliable sources of cells or developing new biofabrication technologies capable of generating more complex and accurate constructs (Langer & Vacanti, 1999). In this regard, the generation of thick vascularization tissues remains as one of the most important challenges in the generation of artificial tissues and organs. Most tissues require the fabrication of an embedded vascular network that provides sufficient oxygen and nutrients (Ali Khademhosseini, 2009). The difficulties to provide an appropriate blood supply have limited the size of artificial tissues generated. As a result, tissues with limited vascular networks, like cartilage, were the first to be tried and fabrication of complex engineered organs still remain as a major challenge.

An approach for the formation of engineered tissues is to use living cells, which are expanded in culture and then seeded in a scaffold that guides the development of the tissue. The scaffold provides a three-dimensional (3D) structure were cells can adhere, proliferate and differentiate before this temporary construct degrades. Several scaffold manufacturing technologies have been developed over the last 40 years. Among all of them, the most important are solvent casting, gas foaming, particulate leaching, phase-separation and freeze-drying (Chua & Yeong, 2014). Even though these technologies are able to produce functional scaffolds, they do not permit to control aspects as the internal microarchitecture and interconnectivity of pores, and some organic solvents utilized in their formation might have toxic effects to cells (Seol *et al.*, 2012).

The emergence of new additive manufacturing (AM) technologies such as stereolithography (SLA), selective laser sintering (SLS) or fused deposition modeling (FDM) brought new possibilities to the conventional scaffold fabrication methods. AM technologies allowed the generation of scaffolds with better control of their internal and external architecture, such as pore size and pore connectivity. Parameters of great importance in the transport of oxygen and nutrients within

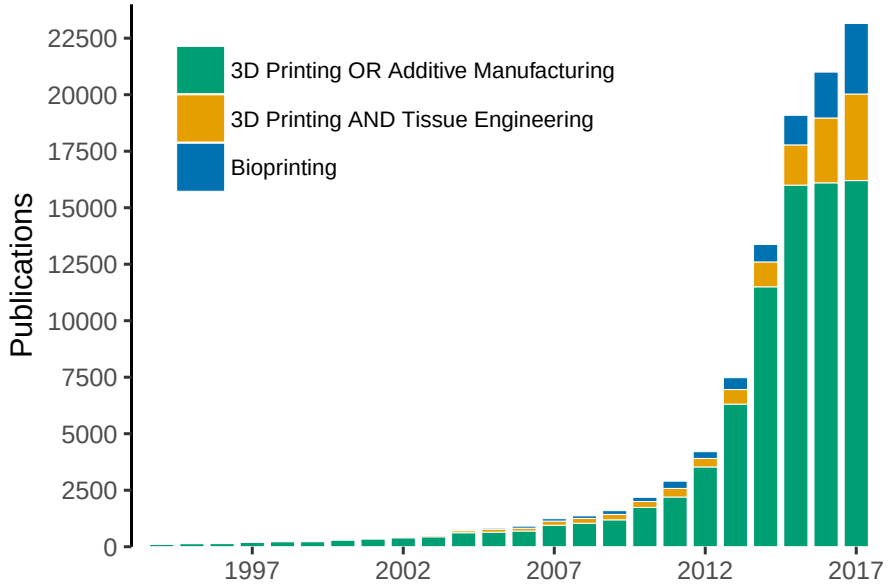

Figure 1.1: *Evolution of bioprinting and 3D printing publications measured by the number of Google Scholar hits. The keywords utilized for the searching included: "3D printing" OR "additive manufacturing", "3D printing" AND "tissue engineering" and "bioprinting".*

the scaffold and ensuring the viability of seeded cells. However, despite the AM scaffold fabrication has played an important role in the generation of engineered tissues over the last years, and its advantages respect to the conventional scaffold fabrication procedures, this technology present some constraints that hinder its expansion. This approach is often limited to a low density, adhesion and distribution of seeded cells. Indeed, another important challenge is to place multiple cell types, biomaterials and bioactive molecules at accurate locations within the scaffold, which hinder the generation of complex tissues (Seol *et al.*, 2014).

The rise of the 3D printing field in the last years have also permitted the arrival of a new TE biofabrication technology called bioprinting. In contrast to the AM scaffold-based approach previously described, 3D bioprinting deposits at the same time cells and biomaterials with precise control over their compositions, spatial distributions and architectural accuracy (Zhang *et al.*, 2017). Guillemont et al. defined bioprinting as "the use of computer-aided transfer processes for patterning and assembling living and non-living materials with a prescribed 2D or 3D organization to produce bioengineered structures serving in regenerative medicine, pharmacokinetic and basic cell biology studies" (Guillemot *et al.*, 2010). Besides, the terms bioprinting and biofabrication have been often utilized as synonyms, since they have similar definitions and sometimes is difficult to distinguish them. A recent definition provided by Groll et al., included bioprinting as a technique within biofabrication, defining the latter as "the automated generation of

biologically functional products with structural organization from living cells, bioactive molecules, biomaterials, cell aggregates such as micro-tissues, or hybrid cell-material constructs, through bioprinting or bioassembly and subsequent tissue maturation processes" (Groll *et al.*, 2016). Since the appearance of the first bioprinting studies in 2003 introduced by Wilson and Boland (Boland *et al.*, 2003), the field has experienced a growing interest in the last decade by the scientific community. This tendency is evidenced by the rapid increase in the number of related publications (figure 1.1). The research in the bioprinting field not only has been related to the development of new bioprinting technologies, but also in the search of innovative biomaterials to be printed often called "bioinks". Bioinks can be defined as a formulation of cells suitable for processing by an automated biofabrication technology that may also contain biologically active components and biomaterials (Groll *et al.*, 2018).

With the emergence of bioprinting technology, scientists try to overcome some of the limitations present in the scaffold-based approach. They have been able to generate multi-material constructs with several cell types and biomaterials. However, there are still great constraints associated with the technology and bioinks utilized. Especially those related with the integration of intricate vascular networks inside of complex shape constructs and achieving relevant cell densities. Many efforts have been made to develop the ideal bioink. However, it results complicate to find a balance between the viability of printed cells and providing accuracy and ease of deposition of printed constructs. Additional features are also required to mimic native tissue functionalities, like those found in sacrificial materials utilized for the generation of support structures and perfusable channels. Besides the search of new bioinks, several bioprinting technologies have been developed over these years, foremost among which are inkjet, laser and extrusion-based systems. Each of these bioprinting technologies has been utilized in several biological applications, offering different features in terms of cell viability, deposition speed, resolution, repeatability, scalability, cost or bioink compatibility. Therefore, it would result appropriate to consider bioprinting technology more as a set of different techniques instead of a single one, each one bringing specific capabilities that could be combined to overcome the existing limitations.

Extrusion-based bioprinting (EBB) has been the most extended technique among the scientific community and bioprinters manufacturers in the last decade. EBB provides significant advantages with respect to other bioprinting technologies as the laser-based and inkjet. It offers excellent flexibility processing a wide range of bioinks at fast deposition speeds, which permits a rapid gener-

ation of large-scale constructs (Ning & Chen, 2017). Another important benefit is the possibility to generate porous constructs with accurate control of their internal architecture, geometries that are more complex to be generated using other technologies such as drop-on-demand (DOD). Besides, the available EBB technologies are relatively easy to implement and can be utilized by users with limited exposure to the technology (Ozbolat & Hospodiuk, 2016).

Several bioprinters have started to be commercialized in the last years. Nevertheless, the high acquisition and maintenance costs of this equipment limit their spread to a larger amount of laboratories. As with the current bioprinters, for many years the access to 3D printers was very expensive and its use was restricted to a few companies and research centers. However, the expiration of 3D printing key patents and the appearance of open-source 3D printing projects such as Fab@Home or RepRap around 2005, permitted to democratize the access to 3D printing reducing the costs and releasing all the knowledge necessary to build a 3D printer. Since that time, thousands of new 3D printers have been built around the world, expanding the access to 3D printing technology each day. These open-source printing platforms can serve as a springboard to expand bioprinting technology to a broader number of laboratories. Indeed, several authors have already utilized desktop 3D printers in bioprinting applications (Hinton *et al.*, 2015; Miller *et al.*, 2012). However, it is necessary to expand all the open-source bioprinting tools available, to make this approach a real alternative to the commercial bioprinters. In this regard, the appearance of open-source bioprinters could help to democratize the 3D bioprinting field in the same way that happened with 3D printing. For a more detailed review on current progress in bioprinting technologies and open-source bioprinting trend the reader is referred to chapter 2.

1.2 Problem statement and motivation of this thesis

Since the invention of 3D printing technology in the 80s, it has been possible to fabricate complex 3D objects using digital computer-aided design (CAD) files and a layer-by-layer approach. Within this framework, 3D bioprinting technology has emerged as a promising candidate to overcome the current limitations of conventional TE techniques. The deposition of various biomaterials and cells types has enhanced the levels of complexity that can be accomplished in the production of tissue engineered constructs. Simple functional living tissues have already been produced using this approach. In this context, several bioprinting

systems have been developed in the last years. Among all of them, we can find bioprinters with variable deposition accuracies and capabilities (Ozbolat *et al.*, 2017).

The evolution of the bioprinting field has also brought the emergence of new companies that have developed commercially available bioprinters. The ideal bioprinter should provide some specific requirements as a high printing resolution, high throughput, ability to dispense various biomaterials, ease of use, high cell viability, affordability, and the ability to control dispensing of multiple bioinks with different viscosities (Dababneh & Ozbolat, 2014). However, not all the bioprinting platforms possess all the features mentioned above. Bioprinters often require high investment costs, which also includes the maintenance and upgrading of their hardware and software. This aspect significantly limits the number of laboratories that can afford this type of technology. An additional drawback of commercial bioprinters is the proprietary nature of their software and hardware, which sometimes restricts the customization of these systems to the specific requirements of each application. Therefore, it seems increasingly necessary to develop more affordable and accessible solutions to the current commercial bioprinters that permits the expansion of this technology to a larger number of laboratories.

Desktop 3D printers have already been utilized by several researchers in bioprinting applications. This approach has permitted the use of bioprinting technologies at much-reduced cost with higher levels of customization and achieving similar printing accuracies. However, among all these modifications, there is a lack of open-source printheads that incorporate an accurate control of bioinks temperature and dispensing pressure. This reduces dramatically the range of biomaterials to be printed and the bioprinting resolutions that can be achieved. The aforementioned limitations and challenges have inspired the search for innovative open-source bioprinting printheads within this thesis.

Nevertheless, it should be noted that the open-source bioprinting approach is not only focused on the development of new bioprinters printheads. These printheads are installed in conventional desktop 3D printers and specific hardware and software modifications are required to transform them into bioprinters. Most of the open-source bioprinting research works found in the literature show some of these modifications. However, sometimes these modifications are difficult to replicate due to an insufficiently detailed description of the hardware utilized, how the G-code is generated or which firmware modifications have been

introduced. Besides, some of these modifications can only be applied to the specific 3D printer utilized, which significantly reduces the adoption of these research works among the scientific community. All these limitations have motivated the use of freely available tools, the use of universal hardware components and to provide a detailed description of all the steps followed to transform most of the desktop 3D printers into 3D bioprinters. Thus, with the development of innovative low-cost open-source bioprinting platforms, it is sought not only to drive down the entering costs of this technology as an alternative to the commercial bioprinters, but also to enhance the collective knowledge about bioprinting among the scientific community.

As stated before, bioprinting accuracy is one of the key points to be considered on each bioprinting process. However, measuring the bioprinting accuracy it is not an easy task as each printing process depends on multiple factors, including the printhead deposition performance, the positioning resolution of the bioprinter and the printability of the biomaterial deposited. Besides, the lack of standard methodologies to measure the bioprinting accuracy, hinder the comparison of the capabilities between bioprinters. Likewise, it is necessary to identify and quantify which are the printing accuracy errors of each bioprinter to obtain the best possible performance. It is therefore necessary to create a standard methodology that would help to determine which are the bioprinting accuracies of a bioprinter and establish a common comparison framework between bioprinters.

Moreover, the generation of complex tissue engineered constructs requires the use of multiple biomaterials and cell-types. In that sense, the use of multi-material bioprinting strategies are mandatory if higher levels of complexity want to be achieved. When multiple printheads are utilized within the same bioprinter, it entails some difficulties regarding the calibration of all printheads utilized. As more printheads are installed, it is more feasible to have misalignments between them and consequently printing errors. A new calibration methodology would reduce drastically the time required to start the printing process and enhance the accuracy of multi-material bioprinting platforms. This motivated the search for a non-expensive and automatic calibration system exportable to any multi-material bioprinting process, where the whole calibration process is performed at once.

Hybrid constructs have gained attention in the last years due to their potential application into the generation of human-scale tissue constructs. Within these hybrid constructs are combined scaffolds of complex architectures, cell-

laden bioinks and microchannels that allows the diffusion of nutrients and oxygen. When building hybrid constructs, each biomaterial is highly influenced by several printing parameters which are highly correlated between them. Some of these parameters include print speed, pressure, temperature, nozzle morphology and inner nozzle diameter among others. Selecting the correct printing configuration is crucial to obtain optimal printing accuracies. Understanding how these parameters influence the printing process is vital not only to control the final shape of the printed construct but also to ensure high cell-viabilities when cell-laden bioinks are utilized. Nevertheless, finding the correct printing parameters it is not an easy task and a trial an error approach is often utilized. Besides, as these parameters are highly correlated, it is necessary to find methodologies that identify those with higher influence in the printing process. Therefore, a comprehensive analysis of the parameters involved in the printing process would be a powerful tool for all the bioprinting community, with the aim to select the best possible printing configuration for each biomaterial.

1.3 Scope of research and objectives

The initial scope of this thesis is the development of an open-source EBB bioprinting platform that democratizes the access to this technology to the scientific community. This democratization would permit to obtain affordable 3D bioprinters and provide all the necessary tools to operate them. Once these objectives are fulfilled, several strategies and methodologies are proposed to maximize the printing accuracy of EBB bioprinters, obtain a comprehensive understanding of most of the printing parameters involved in the bioprinting process and provide useful knowledge for all the bioprinting community.

The following particular objectives are addressed in the course of this thesis:

1. Develop new EBB printheads capable of providing precise control of biomaterials deposition, including temperature and dispensing pressure, as well as permit the utilization of syringe barrels with different sizes.
2. Provide a universal procedure with all the steps required to transform most of the open-source desktop 3D printers into 3D bioprinters.
3. Establish a standard methodology to determine the bioprinting accuracy of any bioprinter and a common comparison framework between bioprinters.

4. Develop a strategy for the automatic calibration of multi-material bioprinters (with multiple printheads) to reduce the time required to align all printheads and increase bioprinting accuracy.
5. Study the influence of different printing parameters regarding accuracy and cell-viability through methodologies that determine which are the optimal printing configurations for several biomaterials and bioinks.

1.4 Thesis outline

This doctoral dissertation is organized in ten chapters. The first chapter briefly introduces the topic of bioprinting and open-source 3D bioprinters, explaining the motivation of this research, along with its scope and objectives. Chapter 2 contains the literature review of the most important 3D bioprinting technologies, with a particular emphasis on EBB technology. This chapter also includes the state-of-art of previous works related to open-source bioprinters and the applications of hydrogels in EBB technology. Chapter 3 contains some of the experimental methods utilized in this research. Chapter 4 focuses on the new EBB printheads designs proposed, a detailed description of its manufacture and assembly, as well as their thermal performance. Chapter 5 describes all the steps required to transform a desktop 3D printers into a bioprinter. Chapter 6 focuses on the development of a methodology to determine which is the accuracy of a bioprinting process and compare different open-source bioprinting platforms. Chapter 7 presents an automatic calibration system for bioprinters with multiple printheads and different strategies to analyze the influence of the main printing parameters in the bioprinting process. Chapter 8 focuses on finding the optimal bioprinting configuration that could help in generating precise scaffolds and hybrid constructs minimizing print times. Chapter 9 includes the rheological tests performed to the hydrogels utilized, as well as the printing accuracy and cell viability results of cell-laden printed constructs. Finally, chapter 10 presents the main conclusions obtained in this dissertation and suggests new research lines for future works.

Chapter 2

Literature review

The literature review presented in this chapter is subdivided in three sections. In the first section, it is included a detailed state-of-the-art of the most common bioprinting technologies. These technologies have been categorized into three different groups, which are also subdivided in several techniques (figure 2.1). Particular emphasis has been placed in the extrusion-based bioprinting (EBB) technology, which has been utilized in the bioprinting experiments conducted in this research. In the second section, it is explained the current state of the open-hardware 3D bioprinters, as well as their current limitations, challenges and potential applications. In the last section, it is detailed the importance of hydrogels and bioinks in the bioprinting process, along with their applications in EBB and the characteristics of the hydrogels utilized in this research.

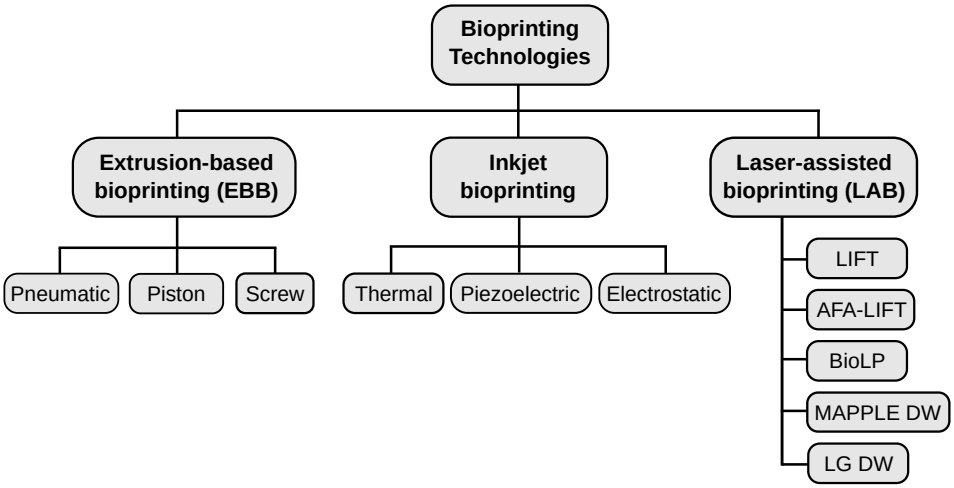

Figure 2.1: *Overall scheme of most utilized bioprinting technologies.*

2.1 3D bioprinting technologies

2.1.1 Extrusion-based bioprinting (EBB)

2.1.1.1 Working principle and technologies

Extrusion-based bioprinting (EBB) refers to the technology where bioinks are dispensed in continuous cylindrical filaments from a movable printhead, controlled by a computer, to construct cell-laden 3D structures using a layer-by-layer approach (Ozbolat & Hospodiuk, 2016). Bioinks are usually introduced inside syringe barrels and extruded through a nozzle by applying a force. With this bioprinting technology, custom 3D models can be designed using a computer-aided design (CAD) software or modified from medical imaging data obtained from computed tomography (CT) and magnetic resonance imaging (MRI) scans (Billiet *et al.*, 2012). The CAD software allows customizing the external design of the 3D model, but also its internal architecture (dimensions of pores, channels, or internal walls), which has a direct effect on the behavior and health of the encapsulated cells (Chua & Yeong, 2014). The primary mechanism utilized in EBB printheads is quite similar for all the different technologies available (pneumatic, piston and screw), but there are some differences in the way that the extrusion force is driven.

Pneumatic-driven configuration represents one of the most utilized EBB systems in literature (Smith *et al.*, 2004; Billiet *et al.*, 2014; Kolesky *et al.*, 2016). With this configuration, pressurized air is utilized to push a piston permitting the extrusion of the bioink. A pressure regulator controls the pressure of the air intake applied and the volume flow rate. The shape fidelity of the bioprinted constructs is highly dependent on multiple variables, affected by the characteristics of both the printhead and the specific bioink utilized. The nozzle diameter, pressure and printing speed on one hand, and the rheological properties of the bioink on the other are the main features to be considered (Smith *et al.*, 2007). Pneumatic printheads are divided into two categories according to the extrusion mechanism utilized in valve-free or valve-based systems (Ozbolat & Hospodiuk, 2016). The valve-free system (figure 2.2a) has been the most utilized configuration in literature, due to the simplicity of its design and ease of manipulation (Kolesky *et al.*, 2014; Shim *et al.*, 2012). In the valve-based configuration, the pneumatic pressure is utilized to lift a piston against a spring that opens the nozzle tip, letting the bioink to be extruded out (Khalil *et al.*, 2005). When the pneumatic pressure ends, the valve is shut and the extrusion is stopped.

Piston-driven EBB technology utilities a lead screw motor that converts a rotary motion into a linear motion and pushes down the piston placed inside a syringe (figure 2.2b) (Geng *et al.*, 2005; Skardal *et al.*, 2010). In screw-driven EBB printheads, the printed material is gradually fed into a container with a turning screw and extruded through a nozzle (figure 2.2c). In this system, the own screw is responsible of pushing the biomaterial through the nozzle without using any piston (Chen *et al.*, 2000). Piston and screw driven configurations usually permit better spatial control over the flow of the bioink than pneumatic printheads, because of the delay of the compressed gas volume in pneumatic configurations (Murphy & Atala, 2014). Pneumatic valve-based and screw-driven systems usually have complex mechanisms with small components, which might hinder the sterilization process of these printheads. On the contrary, pneumatic valve-free and piston-based printheads have fewer components in contact with the bioink (syringe, piston and nozzle) and some of them are disposable, which make it preferable for an easier sterilization. In piston and screw-based configurations, both mechanisms can provide large extrusion forces which permit the deposition of higher viscosity solutions (Ning & Chen, 2017). However, the screw-driven approach can also introduce an additional negative influence on cell-viability, mainly due to the high friction forces produced in the rotational movement of the screw (Dababneh & Ozbolat, 2014). Pneumatic printheads are also able to manage high viscosity solutions, but they are mainly limited by the characteristics of the pressure regulator utilized.

2.1.1.2 EBB systems

Extrusion-based 3D printing has its origins in the late 1980s with the creation of fused deposition modeling (FDM) technology by Scott Crump and the commercialization of the first FDM printers by Stratasys (Matias & Rao, 2015). In FDM technology, a thermoplastic filament is heated above the melting temperature and extruded through a thin nozzle controlled by a computer. When the melted material leaves the printhead and contacts the printer build plate, it hardens immediately (Melchels *et al.*, 2012). However, the high melting temperatures utilized are far away from the human physiological temperature, which prevents the integration of cells and growth factors inside the printed biomaterial (Liu *et al.*, 2007). Besides, the scaffold fabrication process should limit a direct contact with cells during extrusion to avoid harmful overheating. Despite these limitations, FDM technology permits the generation of bioresorbable 3D scaffolds with precise control over their external macrostructure and internal microstructure (Hutmacher *et al.*, 2004, 2001).

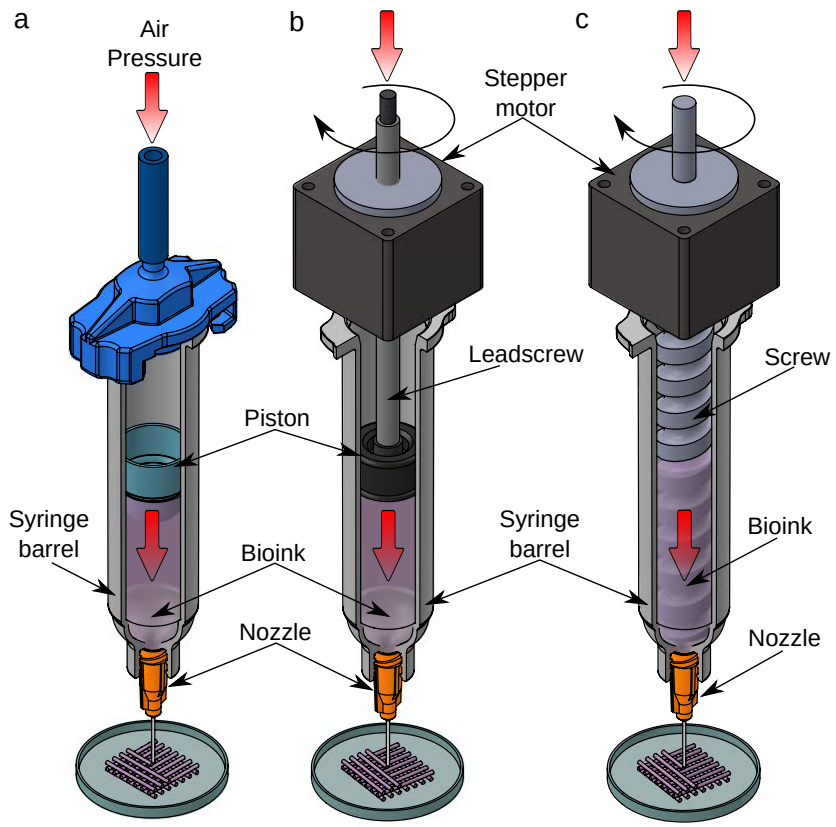

Figure 2.2: *Components of EBB printheads. (a) Pneumatic, (b) piston and (c) screw-based.*

The majority of the EBB applications utilizes hydrogel-based bioinks to fabricate cell-laden constructs. A wide range of hydrogels with different properties has been utilized in EBB in the last years, including natural and synthetic (Chimene *et al.*, 2016). EBB technology requires that hydrogels have specific properties such as fast gelation time triggered by a crosslinking process. The selection of the hydrogel and its crosslinking mechanism will influence the bioprinting process itself and the following steps of the deposition process. Therefore, hydrogel-based EBB can be classified according to the crosslinking mechanism utilized in physical and chemical (Hennink & van Nostrum, 2002). In physically crosslinked hydrogels, their networks have transient internal junctions from physical stimuli like temperature, electric or magnetic fields, light, sound and pressure. While chemically cross-linked hydrogels generate internal networks with permanent junctions due to stimuli that include pH, solvent composition, ionic strength and molecular species (Ahmed, 2015). The crosslinking mechanism of hydrogels has also served as the key factor to develop new EBB fabrication strategies. A brief description of these methodologies is described as follows.

- **Bioplotting**: the first EBB approach consisted of printing living cells using the bioplotting approach. This technology was developed at the Freiburg Ma-

terials Research Center by Muelhaupt group and based on the 3D plotting technology for the dispensing of liquids and pastes in a liquid medium (Landers *et al.*, 2002; Pfister *et al.*, 2004). Muelhaupt et al. were able to print for the first time low viscosity thermoreversible hydrogels with encapsulated cells avoiding the collapse of the printed constructs. To that end, solutions were deposited inside a liquid bath below the gelation temperature of the hydrogels. The printed solutions were quickly crosslinked right after extrusion, generating constructs with enough shape fidelity. The liquid medium serves as a mechanical support and a crosslinking agent. As a result, the printed material can be crosslinked right after extrusion, generating complex constructs without temporary support structures and any time delay (Zehnder *et al.*, 2015). The liquid media should have similar rheological properties than the extruded material, permitting the use of a wide range of biomaterials (Maher *et al.*, 2009). In addition to thermal crosslinking, the plotting medium can also contain chemical crosslinking agents like a calcium chloride (Tabriz *et al.*, 2015). For example, cell-laden alginate/HA porous constructs were printed inside calcium chloride medium with high cell viability (Rajaram *et al.*, 2014). Results showed not only better printing resolutions, but higher cell-viabilities than depositing hydrogels directly in air. Another example of the bioplotting approach is the development of FRESH printing technology, which permits the fabrication of complex geometries (Hinton *et al.*, 2015). This approach consists of extruding a cell-laden hydrogel in a liquid state inside a gelatin support bath. The viscosity of the gelatin bath prevents the diffusion of the printed filaments and the crosslinking agent added to the bath provoke a rapid gelation of the construct.

- **Pre-crosslinking:** EBB of pre-crosslinked hydrogels represents another technique utilized by some researchers. The rheological properties of bioinks are usually tailored through the modulation of the hydrogels concentration and temperature; however, they can also be modified performing a pre-crosslinking process before printing takes place. Once the deposition of bioinks is completed, bioprinted constructs usually need a secondary crosslinking to complete the process and obtain mechanical stable constructs. In the research presented by Chung et al. (Chung *et al.*, 2013), a pre-crosslinking technique was utilized to tailor the rheological properties of gelatin-alginate and alginate bioinks. Bioinks were ionically crosslinked prior to being printed to adequate their rheological properties to the requirements needed in extrusion bioprinting. A photo-crosslinking approach was investigated by Ouyang et al. (Ouyang *et al.*, 2017), where hydrogel viscosities were compared between pre-crosslinking and post-crosslinked printed constructs. In this research, several polymers were

mixed with methacrylated hyaluronic acid (MeHA) and exposure to UV light prior deposition (using a photopermeable capillary nozzle) and right after being deposited. All the printed constructs presented high cell viabilities (>90 %) and hydrogels could be printed without limitations of ink viscosity. Skardal et al. utilized a two-step photocrosslinking strategy to deposit a bioink composed of a methacrylated gelatin (GE-MA) and a methacrylated hyaluronic acid (HA-MA) using a Fab@Home 3D printer (Skardal *et al.*, 2010). In the first step, a partial crosslinking was performed to generate an extrudable gel-like bioink. Then a second irradiation of the printed constructs permitted to form a more rigid and stable structure.

- **Aerosol:** some researchers use an aerosol-based crosslinking process at the same time bioinks are printed (Marquez *et al.*, 2001). The spraying of the crosslinking agent during the bioprinting process may contribute to a more uniform gelling conditions inside the printed constructs and between layers; which helps to avoid the formation of gelled and non-gelled regions (Lee *et al.*, 2015). In the research work presented by Lee et al., a collagen-based hydrogel was printed in several layers to construct a skin tissue and was crosslinked using an aerosolized $NaHCO_3$solution (Lee *et al.*, 2013). Alternatively, calcium chloride solutions have also been utilized to crosslink cell-laden alginate structures, demonstrating a better shape fidelity of final constructs if compared with the process without using the aerosol (Ahn *et al.*, 2012b). As the alginate-based bioinks are deposited, the shear modulus of the hydrogel increased significantly due to gelling of the surface region of the printed constructs, resulting in more stable porous structures (Lee *et al.*, 2015). However, exposure to calcium chloride should be controlled, as an excessive exposure might influence the final cell viability of printed constructs (Lee *et al.*, 2014).
- **Coaxial:** this EBB approach permits the creation of tubular structures directly from the printhead nozzle (Zhang *et al.*, 2013a; Gao *et al.*, 2015b). The coaxial bioprinting operation is based on printing the bioink and the crosslinking solution simultaneously. One of the approaches more utilized consists of that crosslinking solution flows through the inner core of the nozzle, while the polymer is extruded through an external tube (Zhang *et al.*, 2015). Other approaches utilize microfluidic devices to mix crosslinking agent with the bioink flow at the same time they are being deposited (Beyer *et al.*, 2013) or use a PDMS mold to facilitate the mixture of both solutions (Attalla *et al.*, 2016). Coaxial nozzle printheads have been utilized in combination with pre-crosslinking techniques generating perfusable channels (Ouyang *et al.*, 2017) and highly viable and functional in-vitro constructs with simultaneous multi-material deposition (Colosi *et al.*, 2016).

An alternative approach to hydrogel-based EBB is the scaffold-free technique. The scaffold-free approach has been considered a promising technique to generate living tissues that exploits the innate properties of cells to produce their own ECM. It is based on the assumption that cells can undergo biological self-organization and self-assembly, without any external influence that supports or directs its structure through rigid templates or solid scaffolds (Mironov *et al.*, 2009). Cells self-assembly and organization at the microscopic level will tend to generate tissues and organs at the macroscopic level. Instead of depositing cells inside hydrogels, this technique permits the generation of constructs with higher cell-densities, where the own cells are able to generate the ECM in predefined geometries. The technique of printing scaffold-free cell aggregates approach was introduced in 2004 (Karoly Jakab, Adrian Neagu & Forgacs, 2004) and later on the adoption of this technology has proved to be an efficient way to generate tissues such as blood vessels (Norotte *et al.*, 2009) or grafts (Owens *et al.*, 2013). Different scaffold-free biofabrication approaches have been developed, with particular attention to the deposition of cell aggregates through spheroids (Mironov *et al.*, 2009). In this approach, tissue spheroids are deposited in a layer-by-layer fashion and then perform a fusion of the discrete units in a post-printing process. Despite the promising opportunities of the scaffold-free approach, this technology faces several disadvantages that hinder its adoption by the research community. Generation and manipulation of spheroids represent one of the leading challenges, avoiding fusion during the delivering process and depositing spheroids close enough to generate cohesive structures (Mironov *et al.*, 2009). For that reason, most of the bioprinting research groups prefer hydrogel-based techniques due to its higher simplicity, scalability, accessibility, affordability and ease of use (Ozbolat & Hospodiuk, 2016).

One of the main challenges of EBB is the control of the shear stress produced in the printhead during extrusion. During the bioprinting process, cells are constantly subjected to mechanical forces and can be damaged if the printing pressures or manipulation time exceeds certain levels (Li *et al.*, 2009). Even though cells can to resist some of these stresses, it has been demonstrated that shear-stress induced cell membrane damage and a significant drop in the number of living cells when the cell density is high (Kong *et al.*, 2003) and high dispensing pressures are applied (Nair *et al.*, 2009). To improve printing resolution, it is necessary to reduce the inner diameter of the nozzle. However, smaller diameters can induce a greater cell-damage due to higher shear stresses. Therefore, researchers need to to find a compromise between the best printing resolution that can be achieved for the bioink utilized, with acceptable cell-viabilities levels

(Chung *et al.*, 2013). But not only the diameter size has a significant influence, the nozzle shape chosen can enhance or decrease the shear-stresses generated and subsequently the final cell-viability. Several nozzle shapes are available in EBB, being the cylindrical and tapered nozzles the most used. Enhanced viability levels have been obtained when using conically shaped needles instead of cylindrical (Billiet *et al.*, 2014; Li *et al.*, 2011).

Depending on the dispensing technology utilized, EBB is able to process a wide range of bioinks with viscosities ranging from 30 mPa s^{-1} to >6 x 10^7 mPa s^{-1} (Murphy & Atala, 2014). High viscosity and shear thinning bioinks are more suitable for EBB to ensure mechanical stability and shape fidelity of printed constructs. However, the higher the viscosity utilized, the greater the shear stress will be generated in the nozzle walls. Lower viscosity bioinks are more appropriate to ensure cellular viability, but might not have enough gelation requirements after extrusion to maintain the desired shape. Another consequence of using high viscosity materials is the clogging inside the extrusion nozzle caused by bioink solidification in the tip, which represents one of the major problems in EBB and should be corrected reconsidering the diameter of the nozzle or bioink viscosity (Ozbolat & Yu, 2013). Despite the low bioprinting resolutions of EBB technology if compared with other technologies such as inkjet or LAB (Tasoglu & Demirci, 2013), one of the main advantages of EBB is the fast deposition speeds achieved, which facilitate the production of large scalable constructs (Zhang *et al.*, 2013b).

2.1.2 Inkjet

Inkjet bioprinting technology, also known as drop-on-demand (DOD), can be divided into three different technologies according to the printhead utilized: thermal, piezoelectric and electrostatic. All of them share some essential features, with differences in the way that drops are generated and ejected. In general, inkjet bioprinters consist of a single or multiple printheads that contain the bioinks to be printed. Each bioink is held inside the printhead cartridge preventing uncontrolled leaking due to the surface tension generated at the orifice. Biological constructs are generated using a layer-by-layer approach, where each layer is deposited successively above the previous one. Bioink droplets are forced through printhead orifices applying a pressure pulse inside the fluid chamber and overcoming the surface tension, falling under the action of gravity until they con-

tact the printer substrate. The pressure pulse can be generated using thermal, piezoelectric or electrostatic forces.

In thermal inkjet bioprinters, a small electric resistance is located inside the cartridge and in contact with the bioink. The electric resistance heats the bioink locally when a voltage pulse is applied, reaching high temperatures between 200 ºC to 300 ºC (Nakamura *et al.*, 2005). The local heat applied to the bioink rapidly increases its temperature above its boiling point and a vapor bubble is generated (figure 2.3a). The collapse of the vapor bubble generates a pulse that propagates through the cartridge chamber ejecting a droplet through its orifice. Despite the high temperatures produced inside the printhead, well above physiological temperatures, several studies have shown that printed cells are not stressed beyond other normal handling, such as pipetting and centrifuging (Cui *et al.*, 2010). For example, cellular properties and functional fidelity of printed neurons were evaluated in the deposition of fibrin controlled patterns (Xu *et al.*, 2006). Other bioinks as collagen hydrogels have been utilized for the fabrication of multicellular patterns with a resolution of 350 µm, using a modified commercial thermal inkjet printer (Roth *et al.*, 2004). Commercial thermal inkjet desktop printers have also been utilized to print alginate bioinks droplets of 30-60 µm in diameter containing from single to few cells (Xu *et al.*, 2008a) and for the generation of complex and heterogeneous 3D tissue constructs using three cell types simultaneously in a sodium alginate-collagen bioink (Xu *et al.*, 2013). In this work, Xu et al. demonstrated the ability of printed constructs to survive and mature into functional tissues with adequate vascularization in vivo. Other studies regarding vascularization have tried to accomplish microvasculature fabrication using fibrin hydrogel and human microvascular endothelial cells (HMVEC), showing proliferation into tubular structures and functionality of the printed human microvasculature (Cui & Boland, 2009).

Piezoelectric deposition technology utilizes a piezoelectric actuator that rapidly changes its shape when a voltage pulse is applied. This deforms the fluid placed inside the cartridge, generating a pressure wave in the interior of the chamber. Consequently, the pressure generated is enough to overcome the surface tension and a fixed quantity of the bioink is ejected through an orifice in the shape of a droplet (figure 2.3b). Variations in the amplitude and rise time of the electrical pulse applied to the piezoelectric actuator influence the stresses experienced by the cells, with a small decrease in cell survival rate when the voltage is increased (Saunders *et al.*, 2008). Several studies have investigated the potential of piezoelectric printheads for the construction of cell-laden 3D structures. For

example, Christensen et al. utilized a piezoelectric inkjet printhead with a 120 μm orifice diameter to fabricate vascular-like cellular constructs (Christensen *et al.*, 2015). A calcium chloride solution was utilized as both a cross-linking agent and support material, permitting the formation of vascular structures with horizontal and vertical bifurcations. A similar approach was utilized by Xu et al. where fibroblast-based zigzag tubes with complex overhang structures were fabricated (Xu *et al.*, 2012). The bioprinter utilized consisted of a piezo printhead attached to a motorized xy-stage and a z-moving platform placed inside a calcium chloride solution where constructs were printed. Other studies have focused on the control of the number of cells contained on each droplet generated. Yusof et al. developed a single-cell-manipulator (SCM) able to isolate single cells encapsulated in picolitre sized droplets reaching an 87 % efficiency (Yusof *et al.*, 2011).

As with thermal and piezoelectric technologies, electrostatic printheads consist of a DOD technology capable of generating small droplets on demand. Electrostatic printheads consist of a raised meniscus in a nozzle, which is deformed when an external electrostatic field is applied (figure 2.3d). When the electrostatic field achieves a certain threshold, the meniscus forms a cone shape reducing the surface tension forces of the liquid to be printed (Hoath, 2016). This technology offers several advantages such as the ability to produce droplets with a size a much lower than the nozzle diameter (in the range of femtoliters) and the printing resolution is not so affected by the nozzle quality (Kim *et al.*, 2008). However, its use in the bioprinting field had not been so widespread as piezoelectric and thermal actuators. One possible reason is that the fluid density of bioinks is quite limited if compared with the two other DOD technologies. Nakamura et al. utilized a commercial inkjet printhead combined with a dispensing desktop robot to deposit bovine endothelial cells in predefined patterns (Nakamura *et al.*, 2005). Cells deposition and survival were analyzed after printing, showing successful cell viabilities and survival rates. Nishiyama et al. developed a custom-made inkjet electrostatic bioprinter that permitted the creation of sodium alginate biological structures in a calcium chloride liquid substrate (Nishiyama *et al.*, 2009). Electrostatic printheads also have been mainly utilized by Umezu and co-workers for the fabrication of cell-laden 3D structures of highly viscous liquid and media (Umezu *et al.*, 2011), multi-material bioprinting of biodevices using sodium alginate (Umezu *et al.*, 2013) and complex structures with internal caves simulating blood vessels (Umezu & Ohmori, 2014).

Bioprinting technology has its origins in the use of inkjet technology with the research work developed in 1988 by Klebe (Klebe, 1988). This technology

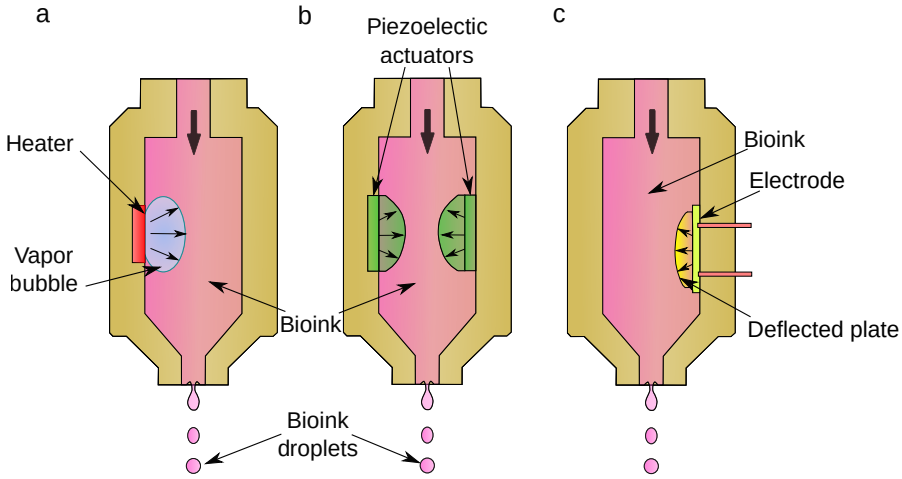

Figure 2.3: *Main components of inkjet printheads: (a) thermal, (b) piezoelectric and (c) electrostatic.*

was termed as "cytoscribe" and utilized a modified Hewlett Packard (HP) inkjet printer to deposit fibronectin on a substrate to promote predefined cell adhesion patterns. Although no cells were printed, it was the first time that a bioink solution was deposited in a controlled manner using a desktop inkjet printer. The first time inkjet technology was utilized to bioprint a cell-laden solution was introduced in 2003 by Wilson and Boland (Wilson & Boland, 2003). In this work, the hardware and software of an HP inkjet printer were modified to dispense cell solutions and proteins instead of ink. Most of the works related to inkjet bioprinting have utilized commercial desktop printers through the appropriate modifications (Pardo *et al.*, 2003; Xu *et al.*, 2004). To that end, desktop printer cartridges were previously emptied of the original ink and rinsed exhaustively with ethanol and sterile water (Xu *et al.*, 2005). The use of commercially available inkjet printers already provides a robust and precise hardware deposition tool, which permits movements in the x-y axes and the possibility of using four different printheads (including black and color cartridges). However, movements in the x-axis are restricted to the tray width and particularly y-axis is limited only to the length of the printhead. Consequently, constructs to be generated are not just limited to the 2D but also are significantly restricted in size (Binder *et al.*, 2011). To stack multiple layers and generate 3D constructs, it is also necessary to integrate a z-axis moving platform in the paper tray (Xu *et al.*, 2012). This platform will lower a specific height each time a new layer is generated (Arai *et al.*, 2011).

Inkjet bioprinting resolution relies on several factors such as the droplet volume, droplet velocity, interactions between droplet-substrate, the crosslinking method utilized and the behavior of ejected droplets after the jetting action

(Gudapati *et al.*, 2016). The resulting droplet properties are subjected to other factors including jetting conditions and ambient properties (Singh *et al.*, 2010). Droplet generation properties and printing principles of inkjet technology have been comprehensively described by Herman Wijshoff (Wijshoff, 2010).

Inkjet bioprinting technology has several advantages if compared with other bioprinting technologies. Highlights among these advantages include the low cost and the ease of use of modified commercial desktop printers. It is possible to completely hack a desktop printer and convert it into a bioprinter with a budget lower than $200 (Binder *et al.*, 2011). To that end, some of the protections and checking systems of the printer must be disabled, as well as cleaning and sterilization of the printing cartridges. However, although these machines provide excellent printing resolution capabilities, their hardware has been designed to deposit inks only in a 2D fashion and using very reduced dimensions. Therefore, if the final objective is to generate scalable objects (as the ones produced using EBB), essential modifications of this equipment are needed and even the construction of entirely new custom bioprinters that utilize commercial inkjet printheads (Nishiyama *et al.*, 2009). As a non-contact depositing technology, there is a lower risk of contaminating substrates and permits the possibility of printing on non-flat surfaces (Campbell & Weiss, 2007). Inkjet bioprinting studies found in literature have reported high cells viabilities in printed constructs with results often close to 80 % and 90 % (Christensen *et al.*, 2015; Xu *et al.*, 2008b). It has been widely studied that during generation of droplets, the application of electric fields or hydrodynamic pressure leads to alterations in cell membrane permeability that permits the introduction of DNA and other macromolecules into cells (Xu *et al.*, 2008b). However, it has been proved that the pores generated in the cell wall during printing have a transient nature, decreasing and virtually disappearing with time (Cui *et al.*, 2010). Resolution of the inkjet deposition systems is also one of the main advantages of this technology. The minimum droplet size that can be generated depends on the type of printhead utilized. Thermal mechanisms tend to create droplets with a size slightly bigger than the nozzle diameter, while electrostatic printheads are capable of generating droplets with a size much lower than their orifice. Nevertheless, most of the inkjet printheads are capable of producing droplets in the range of picoliters, a size that is is quite far from the minimum volumes generated by EBB.

Despite the advantages and abundant applications of inkjet bioprinting described, some disadvantages hinder the expansion of this technology. One of the main limitations of DOD bioprinting is the clogging of the nozzles of the

printheads, which is generated by the deposition of small particles of bioink or cells in the orifices of the printhead. Most of these particles consist of protein adsorption, cellular debris and salts generated when droplets are ejected (Parzel *et al.*, 2009). This phenomenon complicates the ejection of droplets and even blocks the bioink flow completely, causing continuous interruptions that might hinder the production of large structures. Once one or several orifices are clogged, sometimes it is necessary to replace the entire printhead if the material cannot be removed or dissolved. The viscosity of the bioinks utilized can also have a direct effect in the clogging of printhead orifices, generating more frequent clogging problems when high viscosity hydrogels are utilized (Gao *et al.*, 2015a). Therefore, a small number of bioinks can be utilized in inkjet deposition systems and are limited to low-viscosity hydrogels in the range of 3.5 to 12 mPa s^{-1} (Murphy & Atala, 2014). This limitation contrast with the great variety and flexibility of EBB systems, capable to manage bioinks viscosities in the range of 30 to $6x10^7$mPa s^{-1}. This limitation forces to utilize bioinks practically in a liquid form and crosslink droplets afterward ejection, which makes it difficult to stack multiple layers for the generation of 3D constructs.

2.1.3 Laser-assisted bioprinting (LAB)

Laser-assisted bioprinting (LAB) or laser direct writing, consists of a printing technique that was first utilized for the processing of electronic devices and sensors using rapid prototyping techniques (Piqué *et al.*, 1999; Fitz-Gerald *et al.*, 2000). The high resolutions achieved with LAB technology (sub-10 μm) for the production of active and passive prototype circuit elements (Chrisey *et al.*, 2000), drew the attention of the biomedical community to be used as a cell printing technique. Since then, several LAB technologies have been utilized for the deposition of cells and biological materials in predefined patterns. Among all the available LAB techniques, those with a greater impact in the field of bioprinting are laser-induced forward transfer (LIFT), absorbing film-assisted laser-induced forward transfer (AFA-LIFT), biological laser printing (BioLP), matrix-assisted pulsed laser evaporation direct writing (MAPLE DW) and laser-guided direct writing (LG DW).

Despite LIFT, AFA-LIFT, BioLP and MAPLE DW have some characteristic differences, all these technologies share some common similarities in their working principle. A LAB bioprinter consists of five distinct parts: a pulsed laser beam, a mirror, a focusing system, a ribbon and a substrate (figure 2.4). The

ribbons utilized are often made from glass and covered on the top side with a thin metallic layer (i.e. gold, silver, titanium or titanium dioxide) that absorbs the energy transmitted by the laser. The other side of the ribbon is coated with a thin layer of biological material that contains cells suspended in a liquid or gel-like solution and facing the collector substrate. When the pulsed laser hits the ribbon absorbing layer, a rapid volatilization of the biomaterial is produced through local heating and a bubble is generated ejecting the biomaterial toward the receiving substrate. Once biomaterial particles are ejected, the droplets have to cross the small air gap between the ribbon and the substrate and are deposited in a predefined manner. The receiving substrate is generally coated with a cell culture medium or a hydrogel to alleviate the impact of the ejected cells and promote cellular adhesion (Tasoglu & Demirci, 2013). The laser beam direction is guided onto the ribbon using galvanometric mirrors, which permit a higher processing speed if compared with a fixed laser and a motorized stage (Gaebel *et al.*, 2011).

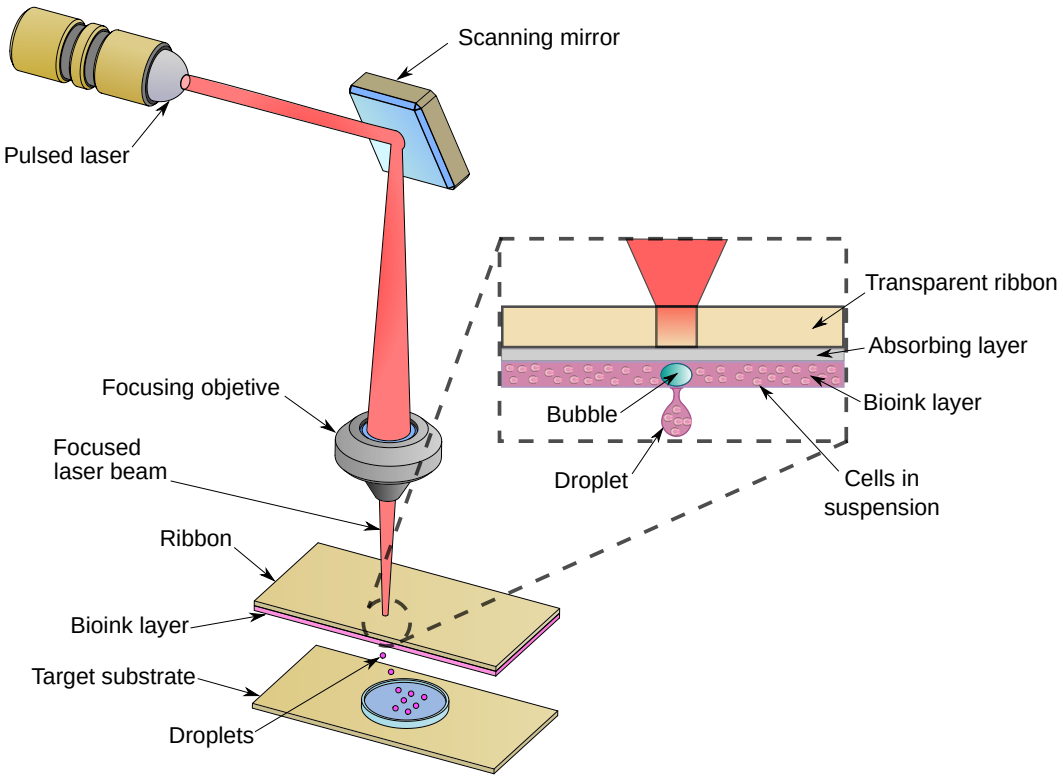

Figure 2.4: *Components of LIFT, AFA-LIFT, BioLP and MAPLE DW LAB technologies and schematic representation of droplet formation.*

Laser-induced forward transfer (LIFT) is a technique in which the laser beam is focused onto a laser-absorbing transparent holder with a thin absorbing film and placed parallel to the substrate at a short distance (Fernández-Pradas *et al.*, 2004). The intermediate absorbing layer is utilized to protect the cells from the damage caused by the high-power laser pulses. LIFT technology has

been utilized initially for non-biological purposes such as the rapid deposition and patterning of superconducting thin films (Fogarassy *et al.*, 1989). However, the great spatial resolutions achieved permitted the experimentation with other materials such as liquid biological materials and biomolecules for the production of microarrays and biosensors (Duocastella *et al.*, 2007, 2008). Resolution and droplet formation using LIFT was analyzed varying bioprinting parameters as film thickness, the gap between film and substrate and laser beam energy. The influence of other bioprinting parameters as the solution viscosity and the receiving substrate wettability have also been studied, showing a direct impact on the final size of patterned droplets (Dinca *et al.*, 2008). LIFT technology has also been utilized in conjunction with two-photon polymerization (2PP) process for the seeding of highly porous 3D constructs with cells, permitting precise control of the density and deposition of cells (Ovsianikov *et al.*, 2010). Bioprinting of skin cells and human mesenchymal stem cells (hMSC) have also been printed using LIFT with survival rates of 90-98 % and demonstrating the ability of this technology to precisely deposit unharmed cells (Koch *et al.*, 2009).

Absorbing film-assisted laser-induced forward transfer (AFA-LIFT) is a variant of LIFT technology that utilizes a high absorption coefficient thin film (∼50-100 nm) placed on a quartz ribbon, permitting a higher energy absorbing of the laser beam. This configuration prevents photonic damage of the biological samples and a minimization of the metal nanoparticles impurities present in the transferred material (Hopp *et al.*, 2005b,a). Smausz et al. studied the influence of the laser fluence and silver film thickness in the transmission of metal particles in the ejected droplets (Smausz *et al.*, 2006). These researchers found silver submicrometer particles (250–700 nm) removed from the ribbon in most of the deposited water droplets and an increasing number of smaller particles with the increase of the laser fluence.

Biological laser printing (BioLP) is a similar technology than AFA-LIFT and MAPLE DW, however, it utilizes a laser absorbing interlayer usually made of titanium or titanium oxide with a thickness of 75–85 nm which prevents the possible damage of biological material from the laser radiation Barron *et al.* 2004a,b, 2005. BioLP technology has demonstrated to be completely compatible with the deposition of cells with high viabilities (95 %), showing the ability to produce droplets of 100 picoliters at repetition rates up to 100 Hz (Barron *et al.*, 2004b). Experiments performed by Barron et al. demonstrated the ability of BioLP of printing human osteosarcoma single cells into a biopolymer matrix, showing a 100 % viability after 6 days of incubation (Barron *et al.*, 2005).

Matrix-assisted pulsed laser evaporation direct writing (MAPLE DW) is a deposition technology that utilizes a ribbon coated with a sacrificial biological material layer (i.e. Matrigel), instead of a metallic interlayer such as LIFT, BioLP or AFA-LIFT. To prevent cell damage of the biological layer, a low-powered beam laser is utilized operating in the UV or near-UV region (Schiele *et al.*, 2010). Movements in x-y-z axes are controlled trough motorized translation stages, changing the gap between the ribbon and substrate with a moving platform using a joystick or computer controlled x-y stage for the generation of patterns (Doraiswamy *et al.*, 2007). Several studies have demonstrated the ability of MAPLE DW technology of precisely deposit patterns of a wide variety of biological materials such as proteins, bacteria and mammalian cells (Barron *et al.*, 2004c; Patz *et al.*, 2006).

Laser-guided direct writing (LG DW) consists of a micro-patterning rapid prototyping technique able to deposit cells in as a steady stream on non-absorbing substrates (Nahmias *et al.*, 2005). Instead of using a ribbon and a pulsed laser beam, two different techniques can be utilized using LG DW (Odde & Renn, 1999). In the first technique, a laser beam that is weakly focused into a liquid suspension and particles are moved through by the light to a receiving substrate (figure 2.5a). In the second technique, the light is utilized combined with a hollow optical fiber, permitting the transmission of both light and cells through the core of fiber at the same time to the target substrate (figure 2.5b) (Odde & Renn, 2000). The second technique offers several advantages over free-space guidance, as a more protective environment from the surroundings, better control of light intensity and proper isolation of the source and deposition regions. Both deposition techniques can be controlled in real time using light microscopy. LG DW technology has been applied in the TE field for the3D micropatterning of endothelial cells on Matrigel with micrometer accuracy (Nahmias & Odde, 2006) and the formation of vascular structures in-vitro (Nahmias *et al.*, 2005).

LAB technology has been developed in parallel with other bioprinting techniques as inkjet and EBB as an alternative approach for the deposition of cells and bioinks. It offers several advantages if compared with other technologies that make this approach especially appealing for specific TE applications. Unlike other bioprinting techniques that utilize orifices (EBB and inkjet), LAB is capable to deposit small volume droplets of biomaterials with an orifice-free methodology, eliminating potential clogging problems (Barron *et al.*, 2004a). Most of the LAB bioprinters utilize a CAD/CAM rapid prototyping procedures to design and build 3D structures with complex geometries (Guillemot *et al.*, 2011) and a single cell or

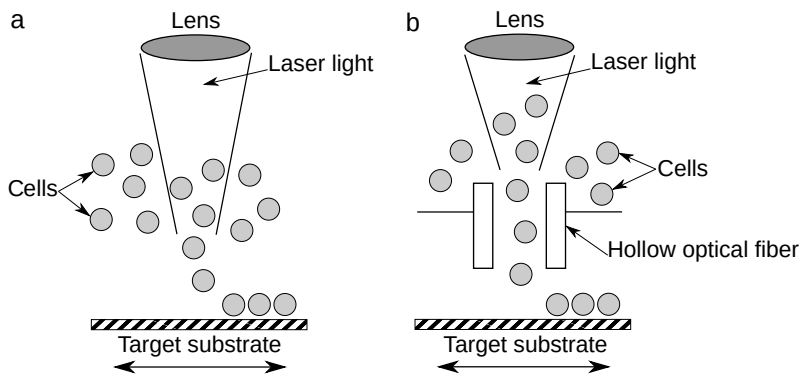

Figure 2.5: *LG DW bioprinting system. (a) Cells in suspension propelled by the laser light. (b) Using a hollow optical fiber (adapted from (Odde & Renn, 1999)).*

picoliter level resolution (Devillard *et al.*, 2014; Schiele *et al.*, 2010). The absence of contact with the receiving substrate also minimizes the risk of contamination during the bioprinting process (Catros *et al.*, 2011).

Despite the advantages mentioned above, LAB also posses its own disadvantages that limit a wider dissemination and adoption of this technology. Except for LG DW, the rest of LAB approaches (LIFT, AFA-LIFT, BioLP and MAPLE DW) require the use of a ribbon that absorbs laser beam energy. Manipulation of the ribbon and preparation of the bioink layer sometimes represents a challenge, due to the proximity to the receiving substrate and the necessity to form thin cell-laden coatings. Despite the use of thin intermediate layers placed in the ribbon that absorbs most of the laser energy, the use of UV radiation might cause cell damage and should be calibrated to not affect cell viability. Other possible potential sources of cell damage during the laser deposition include heat exposure and shear stress generated during droplet ejection and impact on the receiving substrate (Ali *et al.*, 2014). However, if all these variables are properly adjusted cell viabilities close to 100 % can be achieved (Gaebel *et al.*, 2011; Koch *et al.*, 2009). The use of metallic coated ribbons generates an additional drawback with the detach of micrometer and sub-micrometer metallic particles from the ribbon and their deposition within the bioinks. These metallic residues sometimes act as non-desired impurities and should be avoided whenever possible (Smausz *et al.*, 2006). Even though the high resolution of LAB (at a single cell level), this technology is greatly restricted in the deposition of macroscopic amounts of biomaterial, which represents a limitation regarding scalability and the fabrication of large complex tissues (Schiele *et al.*, 2010). As an additional drawback, LAB bioprinters are costly equipment, an aspect that hinders the spread of this technology to a broader number of laboratories.

2.2 Open-hardware 3D bioprinters

Several bioprinting systems have started to be commercialized in last decade (table 2.1). However, their implementation in the laboratories is still discrete, mainly due to the lack of knowledge about the technology and possibilities. Besides, the high acquisition and maintenance costs of this type of equipment also represent one of the most relevant entry barriers to this technology. Commercially available bioprinters are mainly standardized products (Ng *et al.*, 2016; Neufurth *et al.*, 2014; Dubbin *et al.*, 2017), which offer a ready-to-use bioprinting option that should be adapted for each specific application. As a less costly and more customizable alternative to the commercial bioprinters, several research groups have developed their own bioprinting systems. These machines consist of in-house modifications of already existing machines or complete new machine designs. The printheads designs use primary EBB technology with pneumatic (Kolesky *et al.*, 2014; Blaeser *et al.*, 2016; Smith *et al.*, 2004; Kang *et al.*, 2016) and piston-based (Bertassoni *et al.*, 2014b; Blaeser *et al.*, 2013) print-heads.

Another approach, which avoids the proprietary nature of the commercial products and the high cost associated, is to build bioprinters based on low-cost collaborative open-source projects such as Fab@Home (Malone & Lipson, 2007) or RepRap (Jones *et al.*, 2011). These initiatives were created with the aim of spread 3D printing technology to a broader range of communities, which include small laboratories with a lower budget. Open-source 3D printing projects like Fab@Home have played a crucial role in the expansion of bioprinting around the world. The Fab@Home project was founded by Evan Malone and Hod Lipson and developed by students at Cornell University's Department of Mechanical & Aerospace Engineering. Fab@Home printers consist of a three-axis Cartesian moving system with a gantry structure. Positioning is driven by stepper motors which are attached to lead screws that control movement in the x-y-z axes. A modular material deposition system is moved through the x-y axes, with the printing platform moving independently in the z-axis. Its main structure is based on the use of laser cut acrylic sheets that are assembled together using snap-fit joints and threaded inserts. The release of the first Fab@Home 3D printer (Model 1) was in 2006 (figure 2.6a) (Malone & Lipson, 2007), which included a piston-based extrusion printhead that used a linear stepper motor to control the syringe plunger position (Skardal *et al.*, 2010). Some of the first applications of Fab@Home Model 1 included the 3D bioprinting of cell-laden alginate constructs (Cohen *et al.*, 2008) and the fabrication of native cardiac valves replicas (Lixandrão Filho *et al.*, 2009). An improved version of the first printer model was

released in 2009 with the name of Fab@Home Model 2 (Lipton *et al.*, 2009) and a later model (Model 3) was released in 2012 (Lipton *et al.*, 2012). Fab@Home printers have demonstrated a good performance printing mechanically heterogeneous aortic valves (Hockaday *et al.*, 2012) and incorporating a dual deposition system of different cell types (Duan *et al.*, 2013a). Other approaches have been focused on printing alginate scaffolds for application in bone TE (Diogo *et al.*, 2014) and living trileaflet heart valve conduit with decent accuracy and high cell viability (Duan *et al.*, 2014). Fab@home printers permit to control the deposition process of multiple syringes independently with a microliter precision. A key aspect of using a syringe deposition system is the possibility to print a wind range of materials, including anything that can be placed inside a syringe and extruded through a nozzle. Being the first low-cost 3D printing system that allowed the deposition of multiple materials (including viscous fluids), it provided Fab@Home with a clear advantage for bioprinting applications. However, the initial design of its printhead does not include a specific temperature control in the printing process. To overcome this limitation, Wüst et al. (Wust *et al.*, 2014) modified the original Fab@Home printheads with a heating pad and a temperature control unit. However, this enhancement only permitted the heating of bioinks inside the syringes and cooling was not implemented, which is especially appealing for the deposition of thermosensitive bioinks. Fab@Home z-axis has also been modified to enable the deposition of bioinks inside a $CaCl_2$ bath solution during printing (Tabriz *et al.*, 2015).

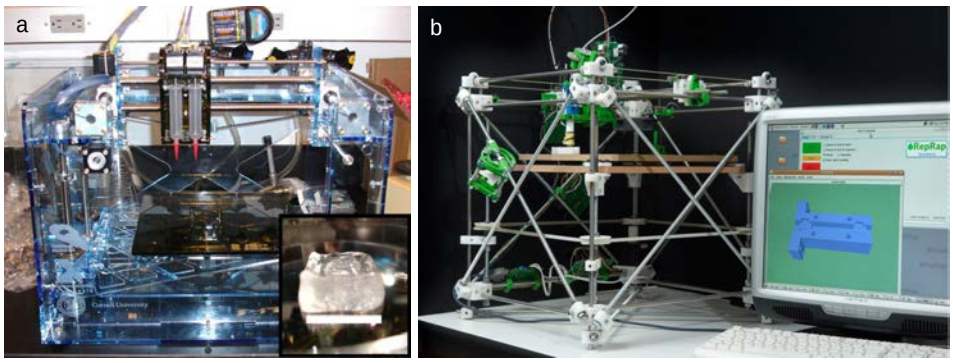

Figure 2.6: *Images of Fab@Home model 1 3D printer (a) (obtained from (Malone & Lipson, 2007)) and first generation of RepRap 3D printer Darwin (b) (obtained from (Jones* et al.*, 2011)).*

The beginning and current development of new open-source 3D printing devices has another key pillar in the RepRap project. Unlike Fab@Home project, whose upgrading of new 3D printers has stagnated in the last years, the RepRap project has an active and large community that regularly releases new 3D printers designs. The RepRap project was started in 2005 by Adrian Bowyer at the University of Bath. Its main objective is to expand 3D printing technol-

Table 2.1: *List of commercial available bioprinters*

Bioprinter	**Provider**	**Bioprinting technology**	**Build volume x-y-z (mm)**	**Resolution (μm)**
3D Bioplotter™ (starter)	Envisiontec	Pneumatic	150x150x140	1
3D Bioplotter™ (developer)	Envisiontec	Pneumatic	150x150x140	1
3DDiscovery	RegenHU	Pneumatic	130x90x10	5
3DDiscovery BioSafety	RegenHU	Pneumatic	130x90x10	5
BioFactory	RegenHU	Pneumatic	60x55x55	5
BioScaffolder 3.1	GeSim	Pneumatic	100x346x40	
Allevi 2	Allevi	Pneumatic	90x90x90	5
Allevi 6	Allevi	Pneumatic	130x90x60	1
BioBot™ Basic	ASLS	Pneumatic	190x190x100	10
BioAssemblyBot™	ASLS	Pneumatic	300x250x150	2-10
3DS Alpha	3Dynamic Systems	Mechanical	150x150x60	75
3DS Omega	3Dynamic Systems	Mechanical	210x100x60	50
Regemat3D	Regemat 3D	Mechanical	150x150x110	150
Bio X Printer	Cellink	Pneumatic-mechanical	130x90x70	1
Inkredible +	Cellink	Pneumatic	130x80x100	10
Inkredible	Cellink	Pneumatic	130x80x50	10
Rokit Invivo	Roki	Pneumatic-mechanical	100x100x80	80

ogy around the world through the development of low-cost, self-replicating and open-source 3D printers. The first generation of RepRap 3D printers was called Darwin (figure 2.6b) (Jones *et al.*, 2011), however, the accomplishment of the complete self-replication of Darwin printer was not achieved until 2008. The first generation of RepRap machines was followed by the release of the second generation in 2009 (called Mendel) and the third generation in 2010 (called Huxley). Over the following years, new 3D printers designs as the Prusa i2 or the Prusa i3 (Prusa, 2018), among many others, have been released and improved the old designs. RepRap printers were thought as a filament-deposition rapid prototyping tool that allowed the manufacture of the majority of the parts needed for its construction (Pearce *et al.*, 2010). This deposition system is called fused filament fabrication (FFF), a process that continuously melts a thermoplastic material in a filament form through a heated print-head (figure 2.7). The printhead moves in a layer-by-layer fashion, that deposits one horizontal layer at a time before moving to the next slice. The term FFF was coined by the RepRap project community to be used without any legal constraint and is equivalent to the term fused deposition modeling (FDM), which is a trademark of Stratasys Inc. Printer components that cannot be 3D printed have been designed to be standard engineering parts, which are widely available worldwide at a low-cost. As the printer designs

are free and open-source, anyone can generate as many copies as he wants to reproduce new RepRap printers or develop improvements to the already existing designs. All the 3D printer designs, software utilized and documentation are publicly available on the official website (RepRap, 2018) and online repositories like GitHub. Since the release of the first generations of RepRap3D printers, thousand of RepRap machines have been designed and assembled around the world (Wittbrodt *et al.*, 2013). For a more detailed description of 3D printers models and build instructions the reader is referred to the website (RepRapOptions, 2018).

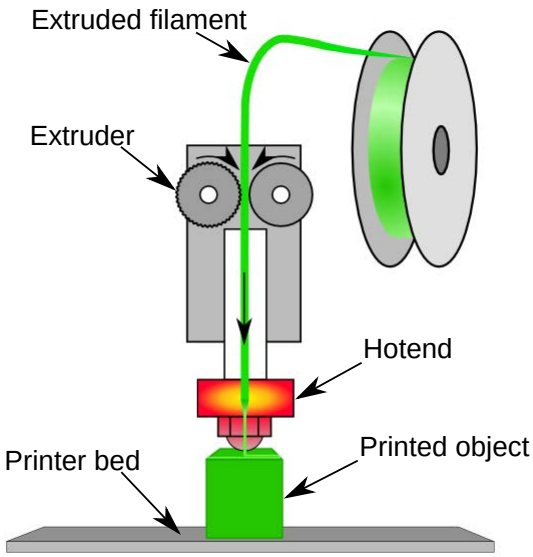

Figure 2.7: *Schematic representation of FFF deposition process (obtained from (RepRap, 2018)).*

In the last years, we can find in the market an increasing amount of commercial desktop 3D printers. This important range of machines also includes several open-source 3D printers with acquisition costs lower than $2.000 USD and accurate printing resolutions in the range of 10-50 μm (i.e. Prusa i3, Ultimaker, Sigma, Witbox, Printrbot, LulzBot) (table 2.2). Open-source 3D printers have been used in various research applications such as engineering (Nilsiam *et al.*, 2018), laboratory equipment (Wijnen *et al.*, 2014; Dhankani & Pearce, 2017; Coakley & Hurt, 2016) or electronic sensors (Shipley *et al.*, 2017) among others. Their programmable Cartesian coordinate position system has demonstrated a high position accuracy, however, only a few of them have been utilized and modified for bioprinting purposes. Unlike Fab@Home 3D printers, most of the desktop 3D printers printheads are only capable of processing thermoplastic materials in a filament form -ABS, PLA, Nylon- with high melting temperatures (200-250 ºC) (Tymrak *et al.*, 2014). This limitation prevents the use of hydrogels with the

original printheads and makes it necessary their replacement them with alternative printheads capable of managing viscous fluids. In the last years, affordable desktop 3D printers such as Printrbot, MakerBot or RepRap-based 3D printers among others, have come into play in the bioprinting field by redesigning their printheads for handling viscous fluids. For example, a MendelMax 2.0 RepRap 3D printer with an open-source syringe-based printhead named "universal paste extruder" (RichRap, 2012) demonstrated good accuracy when extruding a mixture of poloxamer P407 and alginate to build constructs with long-term structural fidelity (Armstrong *et al.*, 2016b). This extruder was also utilized by Bandyopadhyay et al. for the generation of porous constructs with a bioink composed of gelatin, sodium alginate and hydrolyzed Type-I collagen (Bandyopadhyay *et al.*, 2018). Results showed cell viabilities >80% immediately post printing, with an increase of viability percentage for 14 days of incubation. Hinton et al. modified a MakerBot Replicator and Printrbot Jr 3D printers with a custom-built gear drive printhead that utilized the same stepper motors taken from the original printer extruders to push the piston of a 3 mL syringe (Hinton *et al.*, 2015). They were able to deposit hydrogels with low elastic moduli for creating mechanically robust biological constructs. Reid et al. demonstrated the viability of modifying a low-cost desktop 3D printer for bioprinting applications (Reid *et al.*, 2016). The original plastic extruder was replaced with a plunger-driven syringe system that utilized a capillary glass pipette, which permitted the deposition of bioinks within a 50 µm resolution. Goldstein et al. changed only one of the two extruder head units that incorporate the MakerBot Replicator 2x with a syringe-based system to be capable of simultaneously printing cells and scaffolds (Goldstein *et al.*, 2016). Markstedt et al. also utilized a MakerBot Replicator together with a commercial syringe pump and a syringe holder to generate 3D structures using dissolved cellulose (Kajsa *et al.*, 2014). An open-source design of a syringe pump has been presented by Pusch et al, also demonstrating its integration in low-cost 3D printers for the deposition of hydrogels in complex geometries (Pusch *et al.*, 2018). Roehm and Madihally utilized a custom designed piston-based printhead placed on a low-cost 3D printer to dispense chitosan-gelatin hydrogels using 1 mL disposable syringes (Roehm & Madihally, 2018). They were able to print cell-laden structures demonstrating a low-cost alternative to the costly bioprinters available in the market. Attalla et al. modified a RepRapPro Mendel 3D printer, replacing the original thermoplastic extruder with a coaxial microfluidic printhead (Attalla *et al.*, 2016). With this configuration they were able to deposit hollow calcium-crosslinked alginate tubes with accurate control of their diameter between 500 µm - 2 mm by changing the extrusion flow rate and printing speed. Murphy et al. investigated the bioprinting of hASCs together with a polycapro-

lactone (PCL) and borate glass composite using a pneumatic printhead mounted on a RepRap Prusa i3 3D printer (Murphy *et al.*, 2017). The live/dead results of printed constructs showed viabilities of more than 60% of hASCs cells after 1 week of incubation. An alternative design to the open-hardware EBB printheads was presented by Maria et al., whose printhead utilized inkjet technology to deposit cells in a controlled manner (Attalla *et al.*, 2016). Another EBB pneumatic printhead design called Baricuda was presented by Jordan Miller for the deposition of biomaterials at high melting temperatures (Miller, 2012). This printhead was mounted on a RepRap Mendel 3D printer and utilized for the deposition of carbohydrate-glass filaments as a sacrificial material for the generation of perfusable channels (Miller *et al.*, 2012). Miller et al. were able to generate channels of different diameters by changing only the translational velocity of the printhead. This printhead has been utilized also by Trachtenberg et al. for the generation of PCL porous scaffolds, tailoring their geometry through modifications in the pressure and printing speed utilized (Trachtenberg *et al.*, 2014).

Table 2.2: *List of commercial available open-source desktop 3D printers*

3D Printer	**Provider**	**Print volume x-y-z (mm)**	**Price (US$)**	**Resolution x-y-z (µm)**
Witbox 2	BQ	297-210 -200	1791	Up to 20
Hephestos 2	BQ	210-297-220	1059	Up to 50
Fab@Home m1	DIY	200-200-200	~2290	15-15-15
Fab@Home m2	DIY	200-200-200	~1760	6-3.5-3.6
Ultimaker Original+	Ultimaker	210-210-205	1055	12.5-12.5-5
Ultimaker 2+	Ultimaker	223-223-205	2009	12.5-12.5-5
Lulzbot Mini	Aleph Objects	152-152-158	1250	-
Printrbot Simple	Printrbot	200-150-200	509	Up to 50
BCN3D+	BCN3D Technologies	252-200-200	1055	50-50-100
Sigma	BCN3D Technologies	210-297-210	2814.3	12.5-12.5-1
Rostock Max v3	SeeMeCNC	265-265-400	924	100
Prusa i3	Prusa Research	250-200-200	845	10-10-50

2.3 Hydrogels as bioinks

Hydrogels can be defined as a water-swollen and crosslinked polymeric network produced by the simple reaction of one or more monomers (Ahmed, 2015). Another possible definition is that hydrogels are crosslinked hydrophilic polymers capable of absorbing large volumes of water but remain insoluble in water because of their network structure (Kalshetti *et al.*, 2012). Hydrogels have the ability to swell in contact with water and increase up to thousands of times their dry weight. Hydrogels have received considerable attention in the past decades and have been utilized in several applications such as the food industry, drug delivery

systems, wound dressing or pharmaceutics (Ratner & Hoffman, 1976). They have been widely utilized in biomedical applications, including 3D bioprinting. This is because they offer unique properties, such as exceptional biocompatible and mechanical properties, large water content and high degree of flexibility.

2.3.1 Nature of hydrogels

Hydrogels can be classified in different categories according to their origin as either natural, synthetic or a combination of both (table 2.3). Hydrogels derived from natural polymers have been widely used for TE applications due to their biocompatibility and non-toxic properties (Jeong *et al.*, 2012). Some of the first works related to cell encapsulation utilized natural hydrogels (Hospodiuk *et al.*, 2017). Natural hydrogels are made of polymers similar to the biological macromolecules engineered by nature to carry out the particular functions required for each environment (Gasperini *et al.*, 2014). For that reason, when natural hydrogels are utilized in the bioprinting field, the constructs produced have an internal structure that resembles the ECM present in many human tissues.

Natural hydrogels utilized for bioprinting are composed of animal ECM such as collagen (Kim *et al.*, 2015), fibrinogen (Skardal *et al.*, 2012), hyaluronic acid (Duan *et al.*, 2013b) and have the advantage of being inherently bioactive and biocompatible. Other polymers derived from plants, insects or animal components such as chitosan (Zhang *et al.*, 2013b), alginate (Duan *et al.*, 2013a), agarose (Blaeser *et al.*, 2013) or cellulose (Kajsa *et al.*, 2014), also provide a good environment for cell culture. Unlike natural polymers obtained from animals (i.e. gelatin, fibrin, collagen), polymers derived from other organisms as plant sources (i.e. algae, seaweeds) present more difficulties to promote cells adhesion, proliferation and spreading inside printed hydrogels over time. We can find a wide range of commercially available natural polymers with several molecular weights and structure, which offer the possibility to generate hydrogels with different properties, gel strengths and gelation temperatures. Alternatively, the mechanical properties of hydrogels can be tailored through different ways, which include the combination with other polymers and the use of different crosslinking methods.

Although natural hydrogels have demonstrated great success since the beginning in growing tissues, some critical aspects such as the gelation process, degradation and mechanical stability are difficult to tune to the desired values. For this reason, there is a growing need to find polymers with better control of the

hydrogel chemistry, macroscopic properties, gelation process and degradation to enhance cell encapsulation and to promote functional tissue growth (Nicodemus & Bryant, 2008). Limitations of natural hydrogels have motivated a search for alternatives through synthetic polymers or a combination of both (Lee & Mooney, 2001). A wide range of synthetic hydrogels have been engineered during the last years with a higher potential to adapt their properties to the user needs. Synthetic polymers possess strong covalent bonds within their matrix, which improves the mechanical strength, service life and absorbability of the gels (Gyles *et al.*, 2017). Some of the most common synthetic polymers utilized in bioprinting include poloxamer, poly-N-isopropylacrylamide (PNiPAAM), polyethylene glycol (PEG) or polyethylene glycol methacrylate (PEGMA).

Table 2.3: *Commonly used hydrogels for bioprinting*

Origin	Polymer	Cross-linking
Natural	Gelatin	Thermal
	Collagen	Thermal and pH variation
	Chitosan	Thermal/chemical
	Agarose/agar	Thermal
	Fibrin	Enzymatic reaction (thrombin-fibrinogen)
	Hyaluronic acid (HA)	Chemical
	MatrigelTM	Thermal
	Alginate	Chemical ($CaCl_2$)
Synthetic	Methacrylated gelatin (GelMa)	UV-Photopolimerization
	Poly(ethylene glycol) (PEG)	UV-Photopolimerization
	Polycaprolactone (PCL)	Melting ath high temperature
	Pluronic	Thermal

2.3.1.1 Hydrogels utilized in this thesis

Alginate, commonly known also as alginic acid or sodium alginate, is an anionic polysaccharide found in the cell walls of brown seaweed and brown algae (Turksen, 2015). Alginate is a linear copolymer with homopolymeric blocks of α-L-guluronic acid (G) and (1-4)-linked β-D-mannuronic acid (M) monomers (Chua & Yeong, 2014). M and G monomers can appear distributed in consecutive G-blocks, consecutive M-blocks and alternating M and G-blocks (figure 2.8). Alginate properties can differ from batch to batch, varying the quantity and distribution of each monomer depending on the seaweed utilized and its specific conditions (age, origin or species). Alginate has a great capacity to absorb water, capable of absorbing 300 times its weight (Turksen, 2015). It is a well-known material in regenerative medicine applications, utilized due to its structural similarities to natural ECM, good biocompatibility and the ease at which gelation is generated (D Augst *et al.*,

2006). Alginate crosslinking is produced chemically when contacting ionic solutions (Ca^{2+}, Zn^{2+}, Mn^{2+}, Mg^{2+}), forming a gel that remains stable under room and physiological temperatures (Khalil & Sun, 2009). If utilized for bioprinting applications, alginate rheological properties depend on the solution concentration (increasing the viscosity at higher concentrations), temperature (decreasing viscosity at higher temperatures), molecular weight (increasing the viscosity for higher molecular weights) and shear stress (decreasing viscosity at higher shear rates) (Turksen, 2015). One of the most important limitations when using alginate as a bioink is that the low viscosity of bioprinted solutions hinder the creation of constructs with completely interconnected pores and enough thickness, as the material will tend to spread when is deposited due to its own weight (Atala & Yoo, 2015). This situation can be solved increasing the polymer concentration, thus increasing the stiffness of the pre-gelled solution. However, an excessive mechanical strength of the pre-gelled solution is often undesirable, as it increases the damage induced to printed cells by the high shear forces produced during extrusion (Nair *et al.*, 2009). Alternative methodologies to enhance shape fidelity can be utilized in the bioprinting process through cross-linking processes. Alginate bioinks can be printed directly on a $CaCl_2$ bath to improve the structural integrity of the resulting constructs (Rajaram *et al.*, 2014). Another approach consists in printing a pre-crosslinked alginate solution in $CaCl_2$ and then enhance the stability of the printed construct with a printing treatment of $BaCl_2$ (Tabriz *et al.*, 2015). However, an excessive exposure time of cells to the cross-linking agent can have a harmful effect on cell viability and affect the rheological properties of bioinks Cohen *et al.* (2011). An alternative crosslinking approach consists of dispense the crosslinking agent during bioprinting using an aerosol-spraying method, which permits a more homogeneous gelation of printed structures (Ahn *et al.*, 2012a).

Gelatin hydrogels are defined as protein-based polymers derived from collagen through a partial hydrolysis process (Skardal & Atala, 2014). Gelatin hydrogels have been widely utilized for TE applications since they have an almost identical composition to collagen, the main component of natural ECM (Atala & Yoo, 2015). Gelatin polymers are well-known for their thermoresponsive properties and their ability to form gel solutions at RT. Due to its thermoresponsive behavior, gelatin transforms its physical network from coil to helix (or vice-versa) during temperature changes in the solution (figure 2.9). If gelatin is cooled below temperatures of 20 ºC to 25 ºC (depending on the concentration of the solution), the protein coils of its internal network will start to form triple helices and a more stable 3D network will be formed. On the contrary, when gelatin temper-

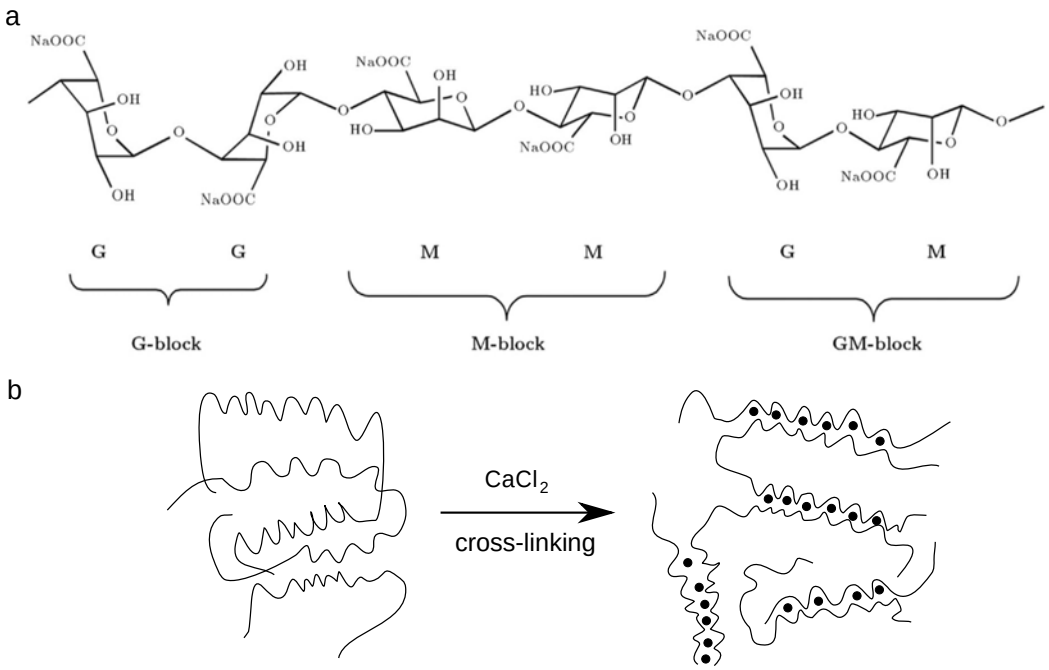

Figure 2.8: *a) Chemical structure of alginate (Chua & Yeong, 2014). b) Cross-linking process of alginate with the binding process of monomers blocks.*

ature is heated above 25 ºC to 30 ºC the opposite transition will occur (helix to coil) and gelatin will transform from a gel to a liquid solution (Joly-Duhamel *et al.*, 2002). However, the liquid state of gelatin at temperatures above RT limits its use in biomedical applications, where better stability and mechanical properties are needed. For that reason, gelatin solutions often require an additional combination with other materials that enhance its stability and prevent dissolution at physiological temperatures (Skardal & Atala, 2014). One of the hydrogels most used to be combined with gelatin is alginate (Chung *et al.*, 2013). Gelatin-alginate blendings combine the thermoresponsive capacity of gelatin and the cross-linking ability of alginate polymers. This combination allows to print at temperatures close to RT with enough stability, and subsequently perform a cross-linking that allows structural integrity at physiological temperatures. The selection of the gelatin-alginate blending ratio will alter the rheological properties of the bioink in the bioprinting process and the following cross-linking stability of printed constructs (Panouille & Larreta-Garde, 2009). If the proportion of alginate in the solution is increased, the bioprinting process tends to generate less accurate and stable constructs due to bioink spreading. If an elevated amount of gelatin is added, the viscosity of the solution is increased, hindering the bioprinting extrusion process (Duan *et al.*, 2013a). The blending ratio will also modify the phase transition temperature of the solution, which will affect the selection of the optimal bioprinting temperature and the final shape fidelity of the printed construct (Zhao *et al.*, 2015).

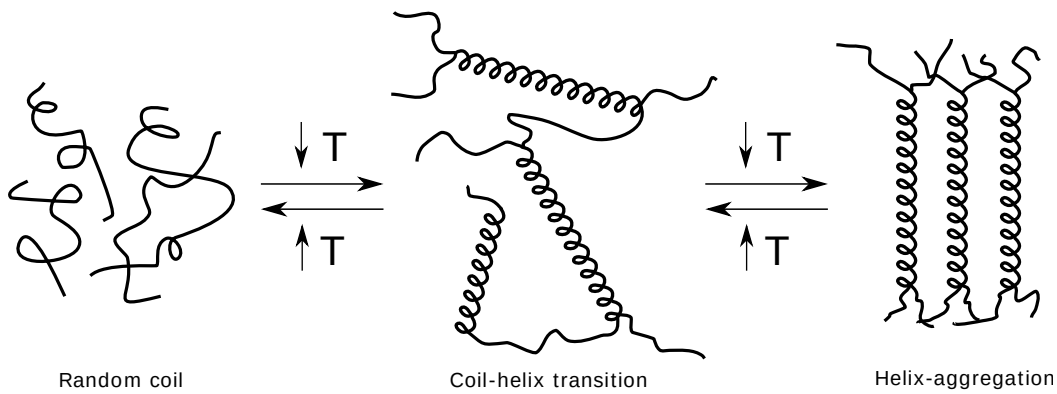

Figure 2.9: *Thermoresponsive behavior of gelatin solutions and its effect on coil-helix transitions (adapted from (Jeong* et al.*, 2012)).*

Poloxamer 407, also known by the BASF trade name Pluronic F127, is a synthetic hydrogel with thermo-sensitive properties in aqueous solutions. Poloxamer is a triblock copolymer with the base molecular structure polyoxyethylene-polyoxypropylene-polyoxyethylene (PEO–PPO–PEO). The gelation of poloxamer solutions is produced due to changes in its micellar properties, which are produced as a function of both temperature and concentration changes. If the temperature is considered, the polymer becomes less-soluble when a threshold temperature is reached, usually known as the critical micelle temperature (CMT). Depending on the concentration utilized, this temperature usually stands somewhere between 22 ºC and 37 ºC (Atala & Yoo, 2015). The ability to have stable bioinks at physiological temperatures just by changing its temperate is one of the main advantages of poloxamer solutions. It represents a clear advantage if compared to other bioinks that utilize more complex and time consuming crosslinking methods (i.e. chemical, UV-light). Besides to the CMT, the critical micelle concentration (CMS) represents the specific polymer concentration which above this value the polymer molecules aggregate and form micelles (figure 2.10). Poloxamer 407 can form a gel at physiological temperatures at concentrations between 15%-20% (Matthew *et al.*, 2002). Therefore, poloxamer concentrations above 15% are mostly utilized in bioprinting applications. However, depending on the polymer concentration utilized, viability and proliferation of encapsulated cells might be significantly reduced due to the disruption of the cell membrane. Khattak et al. determined that when low concentrations of poloxamer are utilized (0.1%–5% w/w), cells can proliferate and maintain high viabilities (Khattak *et al.*, 2005). However, these low concentrations only permit to have solutions in a liquid state at physiological temperatures. If higher concentrations are utilized, results showed a significant decrease in cell viability for 10% and a complete cell death in 5 days for 15%-20% concentrations. Despite the potential toxic effect of poloxamer, one of its main advantages is the ability to create accurate structures with optimal

shape fidelity and reduced swelling. Poloxamer has been utilized mainly in EBB due to its high viscosity and shear-thinning behavior, which permits a fast gelation right after extruded. Poloxamer has been proved as an efficient sacrificial bioink in bioprinted structures. Chang et. all have utilized poloxamer to provide structural integrity and generate temporary molds for lower viscosity materials (Chang *et al.*, 2011). Another interesting approach consists of printing sacrificial microchannels, which are subsequently washed away, generating perfusable microfluidic networks (Kolesky *et al.*, 2014, 2016; Wu *et al.*, 2011).

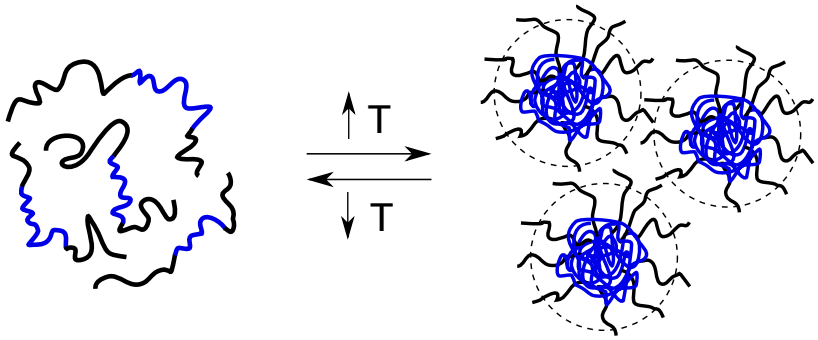

Figure 2.10: *Micellization process of P407 as a function of temperature changes.*

2.3.2 Applications in EBB

Despite the remarkable properties of hydrogels and the large number of research works related with bioprinting over the last years (including the development of new biomaterials and bioprinting technologies), one of the main limitations in the expansion of bioprinting technology is the lack of bioinks that mimics native tissues and permits an easy printability. When hydrogels are utilized in bioprinting processes, cells are encapsulated inside bioink solutions within strict conditions to avoid cell damage. These conditions include the adjustment of bioinks pH, the selection of a non-toxic environment, a limitation on the shear stresses generated or the necessity to maintain processing temperatures below physiological values to ensure optimal cell viabilities (Chung *et al.*, 2013). Another relevant aspect to consider is the maximum time that cells can be encapsulated inside the bioprinter or the printhead recipient, which limits the time between bioinks are cell-loaded and their final deposition.

Bioprinted constructs and bioinks utilized should permit three main objectives: (i) define a space that molds the regenerating tissue produced, (ii) provide a temporary substitution of tissue functions and (iii) permit a guide for tissue ingrowth (Billiet *et al.*, 2012). Ideal bioinks should mimic ECM properties

and allow the secretion of the ECM generated by the bioprinted cells (Tibbitt & Anseth, 2009). Besides, hydrogels utilized in bioprinting must support cellular activity (e.g. cell proliferation, migration, and differentiation) without leading to cell functional damage (Ning & Chen, 2017). Cell-laden printed bioinks tend to degrade with time, especially if they are utilized in long-term transplantations or other maturation processes. The degradation rate of each bioink should be calculated for each application and desired tissue, as well as considering the correct flow out of wastes generated. To that end, high porosity bioprinted constructs are preferred to allow maximum interconnectivity for waste and nutrient flow (Armstrong *et al.*, 2016a). To maintain stable mechanical properties as degradation progresses, it is necessary that ECM secreted from cells inside the construct gradually replace the lost biomaterial. To that end, hydrogels are expected to be biocompatible with cells utilized and have sufficient mechanical stability to not dissolve too quickly in cell culture media. Some hydrogels as poloxamer P407 remains liquid at low temperatures and in a solid-gel state at physiological temperatures. However, other thermoresponsive hydrogels as gelatin or agarose show the opposite behavior, which undergo a fast dissolution when their external conditions are close to physiological temperatures. Single polymer bioinks properties as print fidelity and mechanical stability are usually tailored and enhanced by increasing polymer concentration or through a stronger crosslinking degree. However, these methodologies are detrimental to the spread and migration of encapsulated cells as porosity is reduced, and limit nutrient diffusion (Chimene *et al.*, 2016).

To increase bioink stability respect external conditions without affecting cells viability, researchers try to find more stable and printable bioinks by mixing different hydrogels, which generally offer better performance than using individual polymers (Naahidi *et al.*, 2017). Different formulations and blendings have been investigated in the last years to generate multi-material bioinks that adapt more specifically to each study and expand the range of possible applications. For example, bioinks formed by pure gelatin offers a good printability at RT, however, they are not stable at physiological temperatures due to its reversible sol-gel transition properties, which hinders the control of mechanical properties and shape fidelity. To overcome this limitation, gelatin bioinks can be blended with alginate solutions, which permits to control the bioink strength through an ionic cross-linking (Chung *et al.*, 2013). We can find another example with the use of gelatin methacrylate (GelMa), that is synthesized by adding methacrylate groups to the amine-containing side groups of gelatin (Lin *et al.*, 2013). The presence of a photo-initiator provides researchers with the ability to generate

stable bioprinted structures at body temperature in the presence of UV-light. It also permits a finer tune of the mechanical properties of bioinks by modifying the degree of photo-initiator and polymer concentrations, cross-linking time exposure and UV intensity (Loessner *et al.*, 2016). Other hydrogels, such as chitosan and agarose, present slow gelation rates once printed, which results in spreading of the printed construct as a consequence of standing their own weight. When these bioinks are utilized it is necessary to prepare highly viscous solutions due enhance their low mechanical properties, however, a high viscous polymer can produce excessive shear stress during extrusion, resulting in lower cell viability (Ozbolat & Hospodiuk, 2016). To enhance printability and mechanical stability of chitosan bioinks at lower concentrations, it should be blended with other polymers such as gelatin or alginate to improve gelation and final shape fidelity of printed constructs (Yan *et al.*, 2005; Ng *et al.*, 2016). Agarose has not been so extended in bioprinting as other natural hydrogels and it has been mostly used as a sacrificial structure (Bertassoni *et al.*, 2014a).

Rheological properties of bioinks must be considered in the bioprinting process and will vary greatly depending on the polymers utilized and their concentrations. Hydrogel properties as viscosity play a crucial role in the success of bioink deposition process. In contrast to other bioprinting technologies as inkjet, EBB technology is capable of depositing high-viscous bioinks and produce an accurate shape fidelity. After deposition occurs, printed geometries should maintain their shape and not collapse under its own weight or successive layers. An appropriate gelation process requires the deposition of bioinks in a controlled manner and a subsequent solidification after deposition, which would permit to have enough stability to avoid the collapse of the printed construct (Hölzl *et al.*, 2016). In EBB bioinks require flowing through the nozzle during extrusion and a shear-thinning behavior is needed to prevent excessive shear stresses during extrusion which have a direct effect on cell damage. For example, fibrinogen hydrogels are viscoelastic biomaterials, but unlike most of the polymers utilized in bioprinting, they have a non-shear-thinning nature. This behavior implies a substantial increase in the storage modulus (G´) when the material is deformed, representing a big challenge for being extruded through a nozzle (Hospodiuk *et al.*, 2017). Rheological measurements allow determining the suitability of each bioink to be printed and provide a starting point to optimize the printing variables (Cheng *et al.*, 2008; Wu *et al.*, 2011). However, although the rheological characterization helps to select the appropriate bioink, there is a great number of variables on each bioprinted process which are mutually dependent. These variables include nozzle shape, nozzle diameter, extrusion pressure, printing speed and temperature

among others (Smith *et al.*, 2007). Each of these parameters should be adjusted for each bioink trying to find a compromise between printing resolution and cell viability, and a trial and error approach is usually needed to determine the best printing configurations.

Table 2.4: *List of commercial available bioinks*

Provider	Bioink	Composition	Use
RegenHU	ECM-Bioink™	Peptide nanofiber bioink	Cell-laden bioink
RegenHU	Osteoink™	Calcium phosphate paste	Bone, cartilage or structural scaffolds
RegenHU	Stark™	Not specified	Fugitive support and temporary scaffolds
Cellink	Bioink	Alginate and nano-cellulose	Cell-laden bioink
Cellink	Cellink A	Algiante from brown algae	Cell-laden bioink
Cellink	PCL	Polycaprolactone	Structural and mechanical support
Cellink	GelMa	Gelma methacrylate	Cell-laden bioink
Cellink	Pluronic	Pluronic	Fugitive support and temporary scaffolds
Cellink	Star	Polyethylene oxide blend	Support material
Biobots	PCL	Polycaprolactone	Structural and mechanical support
Biobots	Pluronic	Pluronic F127	Fugitive support and temporary scaffolds
Biobots	LifeInk® 200	Bovine type I collagen	Designed for printing with FRESH method
Biobots	FRESH kit	Gelain, alginate and collagen	Kit for printing with FRESH method
Bioink Solutions, Inc.	Gel4Cell®	Phtosensitive gelatin-based	Cell-laden bioink
Bioink Solutions, Inc.	Gel4Cell®-BMP	Gel4Cell based	Bone
Bioink Solutions, Inc.	Gel4Cell®-VEGF	Gel4Cell based	Vascularization
Bioink Solutions, Inc.	Gel4Cell®-TGF	Gel4Cell based	Cartilage
Envisiontec	LT support RG	Saccharide	Sacrificial and support material
Envisiontec	HT support RG	Sugar derivative	Sacrificial and support material
Envisiontec	PCL 45K RG	Polycaprolactone	Structural and mechanical support
Envisiontec	Silicone TG	Silicone	Soft implants, wound dressing, testing

Bioinks affordability and ease of manufacture also represent key aspects to be considered. The range of prices of hydrogels can significantly vary from one to another. Hydrogels like gelatin or alginate can be considered as affordable biomaterials while using bioinks composed of materials like fibrin or Matrigel entails higher costs. This aspect must be considered when selecting the appropriate bioink for each application, including the degree of scalability and the number of bioprinting tests needed. In spite of the budget limitations, most of the hydrogels found in literature can be easily acquired through the usual commercial providers. In most of the cases found in literature, the researcher is in charge of prepare and process bioinks from the initial polymer form (generally powder). Bioink prepara-

tion is another key point to be considered, as some hydrogels require preparation processes more elaborated than others. Some bioinks as gelatin methacrylate (GelMa) require a preparation much complex than others like Gelatin or Alginate, where a strict and time-consuming protocol must be followed to succeed on this task (Loessner *et al.*, 2016). The commercial expansion of bioprinters has also brought the commercialization of bioinks through bioprinters companies or specialized providers (table 2.4). These companies offer a broad catalog of bioinks that mimics ECM, including both synthetic and natural hydrogels, and others utilized to generate sacrificial or support structures. The commercialization of these products can speed and facilitate the production of bioinks by researchers. However, rheological properties of this type of products usually are not available, which hinder the selection of the bioprinting parameters and restricts the customization of bioinks for each specific application. Another important drawback is related to the final cost of the already prepared commercial bioinks, which generally is much higher than if they are prepared by the researcher.

Chapter 3

Experimental methods

3.1 Materials preparation

3.1.1 Poloxamer P407

Poloxamer 407 (Pluronic® F127; Sigma-Aldrich) was prepared by weighing the quantity of polymer required and mixing in cold Milli-Q water at 4 ºC. Poloxamer 407 powder was added gradually to Milli-Q water to facilitate the dilution and stirred vigorously for 3h using a magnetic stirrer. Once the solution was homogenized, it was centrifuged and stored overnight at 4 ºC to remove air bubbles. If a high concentration of poloxamer is prepared (i.e. 40 % w/v), a more exhaustive centrifuged will be required. Poloxamer 407 prepared solutions were stored at 4 ºC until further use.

3.1.2 Gelatin-Alginate

Gelatin and alginate were prepared both separately and afterward blended together. Gelatin from porcine skin (type A; 300 bloom; G1890, Sigma-Aldrich) was dissolved in phosphate buffered saline PBS (1×Dulbecco's PBS Ca- Mg-; ph=7.4) at different concentrations (10 wt % and 5 wt %). Sodium alginate (low-viscosity from brown algae; A0682, Sigma-Aldrich) was dissolved in phosphate buffered saline (PBS) (1×Dulbecco's PBS Ca- Mg-; ph=7.4) at different concentrations (4 wt %, 2 wt % and 1 wt %). Both gelatin-alginate solutions were blended using a vortex, centrifuged at 1000 rpm for 1 min to remove air bubbles and its pH was adjusted to 7.2-7.4 (table 3.1). Solutions were sterilized by autoclave at 120 ºC for 20 min, stored at 4 ºC, and prior use heated at 37 ºC more than 30 min in a water bath. Gel-Alg printed constructs were crosslinked

in 3 wt% calcium chloride ($CaCl_2$; Wako) for 6 min and then washed three times with phosphate buffer (PBS) and replaced with growth medium.

Table 3.1: *Bioinks solutions and blendings utilized in this research*

Final solution	Blending	Ratio
Gel5%	20% w/v gelatin and PBS	1:2
Gel10%	20% w/v gelatin and PBS	1:1
Gel10%+Alg2%	20% w/v gelatin and 4% w/v alginate	1:1
Gel10%+Alg1%	20% w/v gelatin, 4% w/v alginate and PBS	1:1:1
Gel5%+Alg2%	10% w/v gelatin and 4% w/v alginate	1:1
P407 40%	-	-

3.1.3 Polycaprolactone

Polycaprolactone (PCL, CAPA 6400; Perstorp, Sweden) with a mean molecular weight of 37 kDa was used as received from Perstorp Holding AB as the base polymer biomaterial for the scaffolds. The PCL has a melting point of 59 °C, and a melt flow index of 70.8 - 27 g / 10 min^{-1} according to provider´s reports.

3.2 Hydrogels rheological measurements

3.2.1 Equipment utilized and samples preparation

Rheological properties of Gel and Gel-Alg hydrogels at various concentrations were measured using a rotational controlled stress rheometer (AR-G2; TA Instruments) (figure 3.1). A 20 mm plate-plate configuration and a temperature controlled Peltier plate were utilized in all test performed. When a parallel plate configuration is utilized, one of the two plates remains stationary (lower plate) while the other plate rotates (upper plate).

The sample volume loaded in the rheometer lower plate depends on to the gap utilized, the plate diameter and plate geometry utilized for each experiment. A final gap of 500 μm selected, and the plate diameter and geometry was kept constant for all the experiments. Each hydrogel sample was loaded using a disposable 1 mL syringe (Terumo) and a metallic needle (18G; ID: 838 μm). Prior to loading the hydrogel sample, the hydrogel was kept at 37 ºC on a water bath and the temperature of the Peltier plate was set to 37 ºC to prevent the gelation of the sample and facilitate the preparation of the experiment. Once the hydrogel was loaded into the center of the plate, the 20 mm upper plate was lowered until contacting the hydrogel surface. For a 200 μm sample, the upper

Figure 3.1: *Rheometer AR-G2 utilized in this research.*

plate usually touched the sample within a gap around 1200 µm to 1500 µm. Then the gap was progressively reduced to 1000 µm and finally to 500 µm to facilitate an appropriate spreading across the entire plate surface. When the final gap was achieved, it was necessary to check that the sample entirely filled the perimeter of the plate, removing the excess of material with a thin napkin or a right edged tool. When cone and plate geometries are utilized, it is recommended to load some extra material larger than required (overfilled state) and then trim the excess of material to achieve a correct filling of the gap (figure 3.2). A solvent trap was utilized in all the tests performed to minimize sample dehydration during the experiment.

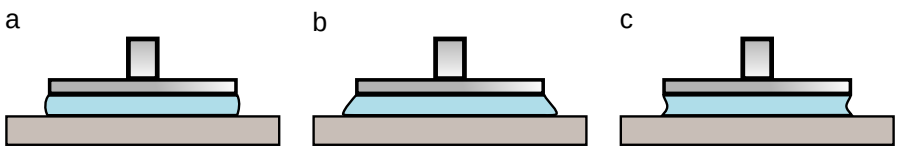

Figure 3.2: *Rheometer gap filling using a parallel plate head. (a) Correct-filling. (b) Over-filling. (c) Under-filling.*

3.2.2 Determination of hydrogels phase transition

Gel and Gel-Alg hydrogels changes from liquid to gel states are performed within the liquid-gel transition process, with the critical transition point as the gelation point. The gelation point can be determined rheologically through the oscillatory temperature sweep test. In this experiment, results were plotted in storage (G´) and loss modulus (G´´) over temperature (ºC) graphs. The critical point or gelation temperature of each material was determined when G´ and G´´ curves

intersect in the graph. The oscillatory temperature sweep test performed began with a temperature equilibrium time of 5 min and a temperature of 5 ºC (which must be equal to the starting temperature utilized in the test). Both parameters were configured in an initial conditioning step, to make sure that the isothermal conditions had been fulfilled when the measurements started to be recorded.

Tests were performed over a range of temperatures that varied from a starting temperature of 5 ºC to an end temperature of 45 ºC (table 3.2). An increment of 1 ºC was utilized for each time step, with an equilibration time of 1 min. Therefore, the total time needed to perform the complete test was 45 minutes, including the initial conditioning step. Temperature changes were performed increasing the temperature (from cold to heat) to prevent faster evaporation of the sample during the experiment, which would result in measurement errors due to an under-filling of the gap. If the end temperatures chosen for the experiment are higher than 45 ºC, a higher temperature change rate should be utilized to prevent evaporation of the sample. Storage modulus (G´) and loss modulus (G´´) were measured using a constant frequency of 1 Hz and an oscillatory strain of 1 %. These conditions were previously checked to stand within the linear viscoelastic region (LVR).

Table 3.2: *Oscillatory temperature sweep test configuration*

Oscillatory Temperature Sweep	
Temperature sweep (ºC)	5-45
Temperature increment (ºC)	1
Equilibration time (hh:mm:ss)	0:01:00
% Strain	1
Frequency (Hz)	1
Conditioning Step	
Initial temperature (ºC)	5
Equilibration time (hh:mm:ss)	0:05:00

3.2.3 Determination of time dependence in hydrogels rheology

The oscillatory time sweep test allows determining how the material properties change over a specific time interval. This type of experiment is important when using materials such as polymers, which undergo an internal structural rearrangement over time that changes their rheological properties. In this experiment, storage (G´) and loss modulus (G´´) were measured and plotted against time.

The determination of the time dependence rheological properties of hydrogels results of vital importance in the bioprinting process. Once bioinks are loaded in a printing syringe and set to the specific bioprinting temperature, the rheological properties of the material loaded will need some time to remain stable. Or put it in another way, a bioink will not be printed in the same way if it is printed right after changing its temperature or if we wait for some time until is internal structure is more stable (i.e. 30 min).

Table 3.3: *Oscillatory time sweep test configuration*

Oscillatory Time Sweep	
Duration (hh:mm:ss)	0:30:00
Delay time (hh:mm:ss)	0:00:05
Temperature (ºC)	10-15-20
Strain (%)	0.1
Frequency (Hz)	1
Conditioning Step	
Initial temperature (ºC)	10-15-20
Equilibration time (hh:mm:ss)	0:00:00

In the oscillatory time sweep tests performed, the temperature was maintained constant during each test. Different experiments were performed at constant temperatures of 10 ºC, 15 ºC and 20 ºC (table 3.3). The oscillation procedure utilized did not require a conditioning step because we were interested in knowing the hydrogel rheological behavior without any previous equilibration time. A constant strain of 0.1 % and a frequency of 1 Hz were selected and kept constant. The duration time for all the experiments was set to 30 min and the delay time chosen to apply the specified amplitude and frequency prior to data collection was 5 seconds.

3.2.4 Determination of hydrogels viscosity

One of the procedures to measure the viscosity of a non-Newtonian sample at a constant temperature is to perform a steady state flow test. When testing these type of materials, both the measuring instrument and the sample utilized need sometime to reach constant conditions. In other words, it is necessary to wait some time before measured values are recorded until the whole system is in equilibrium and has reached a steady state flow (figure 3.3). After that, the stress or shear rate is increased logarithmically and the process is repeated

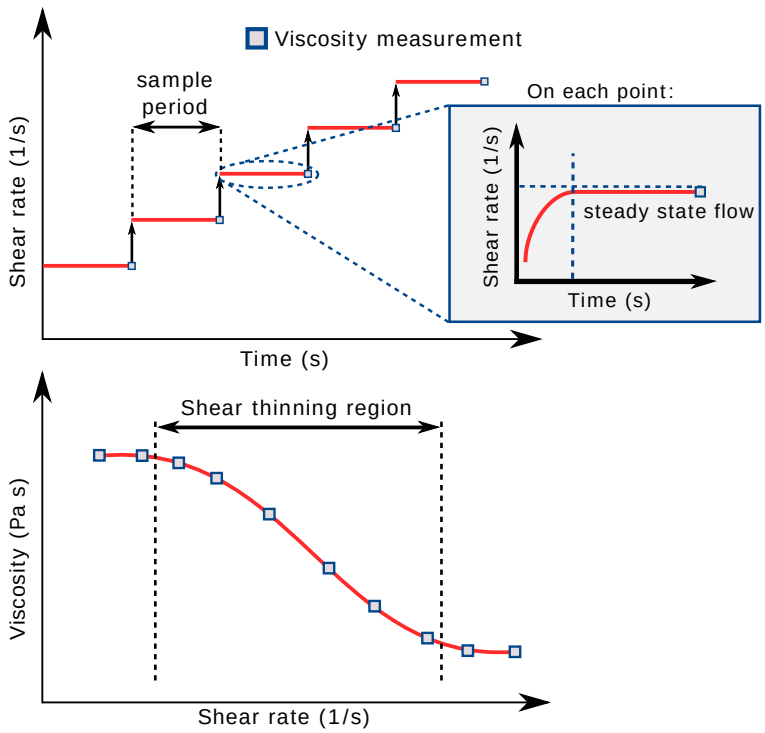

Figure 3.3: *Steady state flow test performed to obtain viscosity measurements of hydrogels. Successive shear rate values are applied, where viscosity measurements are obtained when equilibrium is reached. Each step generates one measurement for the final viscosity vs shear rate graph.*

yielding the viscosity or flow curve. When polymers as hydrogels are analyzed, the viscosity function is usually shown as a function of the shear rate. Viscosity depends on many factors including shear gradient, time, temperature, density and molecular weight; therefore it is advisable to maintain as many constant conditions as possible when it is measured.

In this experiment, a steady-state flow test was performed to analyze the viscosity of hydrogels. Results were plotted in viscosity (Pa s) over shear-rate (s^{-1}) graphs. Viscosity measurements were performed under continuous flow steady state conditions. Shear rate was selected as the control variable, changing logarithmically from 0.01 s^{-1} to 200 s^{-1}(table 3.4). The temperature was kept constant during all the test using values of 10 ºC, 15 ºC and 20 ºC. During the test, the dependent variable (torque if the controlled shear rate mode is used and speed for the controlled stress mode) was monitored over time to decide when the stability had been reached (figure 3.3). An average value was then recorded during the sample period of 10 s and when this value remained within the tolerances imposed the data was considered valid. If those tolerances had not been reached, the software recorded the value at the end of the maximum point time (1 min).

Table 3.4: *Viscosity test configuration*

Viscosity	
Shear Rate (s^{-1})	0.01-200
Mode	log
Points per decade	10
Temperature (ºC)	20
Sample period (hh:mm:ss)	0:00:10
Percentage tolerance	5
Consecutive within tolerance	3
Maximum point time (hh:mm:s)	0:01:00
Conditioning Step	
Initial temperature (ºC)	5-20
Equilibration time (hh:mm:ss)	0:05:00

3.3 3D bioprinter sterilization

The sterilization of the bioprinters (or a modified desktop 3D printers) here utilized consisted in disassembling all the printer components, sterilize each of them separately and then reassemble them inside a sterile environment. However, depending on the 3D printer utilized, not always is possible to disassemble and reassemble all its components in an easy way. In that case, it is important to clean carefully all its components with particular attention to all those parts that are going to be close or in direct contact with the cells utilized. These critical parts include 3D printer components as the printing surface in which bioinks are deposited, the printhead and all the components of the xy axes of the printer. It is important to carefully follow the procedure here described, due to desktop 3D printers utilized were not thought initially to be used as bioprinters and follow a sterilization process.

Prior to introducing the 3D bioprinter in the sterile hood, it is necessary to soak all its components by hand. The soaking bath utilized was a mixture of detergent (7x - Decon), bleach (sodium hypo chlorite 5000 ppm) and tap water. Once all the components were brushed, they were rinsed thoroughly in 5 complete changes of tap water followed by 3 changes of Milli-Q water. The addition of Milli-Q water ensured that there were no left-over salts in the components cleaned. After rinsing thoroughly, all the components were collected in a clean drying basket. When all the components were dried, all the equipment surfaces were wiped down with disinfectant (70 % ethanol). Finally, all the elements were

placed in a laminar flow hood with the blower turned on and irradiated with UV light overnight. It is important to place the critical components of the printer visible to the UV light without creating shadows.

Small components such as syringe barrels or nozzles can be sterilized using an autoclave. However, not all the printers/printheads components can be autoclaved because they would melt. In that case, the sterilization procedure here described should be utilized.

3.4 3D printer slicing setup for FFF materials

Some of the components utilized for the creation of the bioprinters components and the printheads were generated using FFF technology. Materials utilized in this study were acrylonitrile butadiene styrene (ABS) (ABSTech; FFFworld), polylactic acid (PLA) (PLATech; FFFworld) and polycarbonate (PC) (Ultimaker PC; Ultimaker) (table 3.5). These materials are thermoplastics with different glass transition temperatures that will affect their final use. Above the glass transition temperature and below its melting point, 3D printed materials will remain in a solid state, but their mechanical properties will change significantly. Glass transition temperatures are also related with the heat deflection temperature (HDT), which is the temperature at which a material deforms under a specific load. HDTs of ABS, PLA and PC utilized were 88 ºC, 70 ºC and 110 ºC, respectively. Values that restrict the maximum temperature that the 3D printers components can achieve without any deformation. Printing settings and properties of ABS, PLA and PC filaments utilized are detailed in the following table:

Table 3.5: *Properties of ABS, PLA and PC filaments utilized.*

Feature	**ABS**	**PLA**	**PC**
Printing temperature (ºC)	240 -245	190 - 210	265
Build plate temperature (ºC)	80 - 100	20 - 60	110
Density (g/cm^3)	1.05	1.24	-
Heat deflection temperature (HDP) (ºC)	88	70	110
Melting temperature (ºC)	200	160	-
Decomposition temperature (ºC)	>260	>235	-

Prusa i3 (Prusa Research), BCN3D Sigma (BCN3D Technologies) and Ultimaker 3(Ultimaker) desktop 3D printers were utilized to 3D print the com-

ponents needed for this research. Prusa i3 hotend was designed to use filament diameters of 1.75 mm, while Sigma and Ultimaker utilized a 3 mm diameter. These printers are able to print ABS, PLA and PC with similar levels of accuracy using a 0.4 mm diameter nozzle. Open-source Cura software (Ultimaker) was used to slice the STL files, create the G-code and configure the printing settings.

3.5 Cell culture

Human adipose derived mesenchymal stem cells (hASCs) were isolated from lipoaspiration procedures from healthy donors, aged between 18 and 35, following written informed consent and Research Ethical Board approval by Clinica Isabel Moreno and Fundación Hospital General, Valencia, Spain. Donors were previously screened for Human Immunodeficiency Virus (HIV), hepatitis C and other infectious diseases. hASC were expanded following the protocol described by Escobedo-Lucea et al. 2013 (Escobedo-Lucea *et al.*, 2013) and harvested with Tryple® (Invitrogen) at 80 % confluence. Their undifferentiated stem cell profile was assessed by flow cytometry at the starting of the experiments. Cells were positive for CD90, CD73, CD29, CD105, CD146 and CD166 and negative for CD34 and CD45 (data not shown).

3.6 Live/dead assay and cell counting

Cell viability of the printed constructs was analyzed by means of live/dead assay (R37601; Life Technologies) according to manufacturer's instructions. Briefly, the live green vial (A) (Calcium-AM; 0.5 l/mL) was transferred into the dead red vial (B) (ethilium homodimer; 2 l/mL) and mixed to prepare a homogeneous 2x stock. This 2x stock must be used within 2 h after preparation. Once green and red vials were mixed, it was added the same volume of culture media. Once the printed samples were crosslinked and washed in PBS three times, bioprinted samples were stained and incubated for 15 min at RT. Fluorescence images of bioprinted samples were captured 1 h and 24 h after printing under a laser scanning confocal microscope (Olympus FV1200, Japan). Three independent samples were utilized for the assay (n=3), with seven stack images (10 layers) per each sample. Each stack image was obtained at different Z-heights, but maintaining the same x-y plane. Fluorescent images were stacked and adjusted the intensity of both

channels (green and red) using the confocal image acquisition software FV10-ASW 4.2 (Olympus; Japan).

Once the images were edited using the microscope software, the number of live and dead cells was counted using the open-source image processing software ImageJ (Rasband, 2018) (figure 3.4). The first step consisted of performing a spatial calibration of the image loaded, to be able to measure distances and areas on it. To that end, already known values as the distance in pixels, the known distance of the image and the unit of length were introduced in the "Set Scale" dialog box (Analyze –> Set Scale) (figure 3.5). The global checkbox should be checked to apply this configuration to all the opened images. The unit of length utilized was in µm.

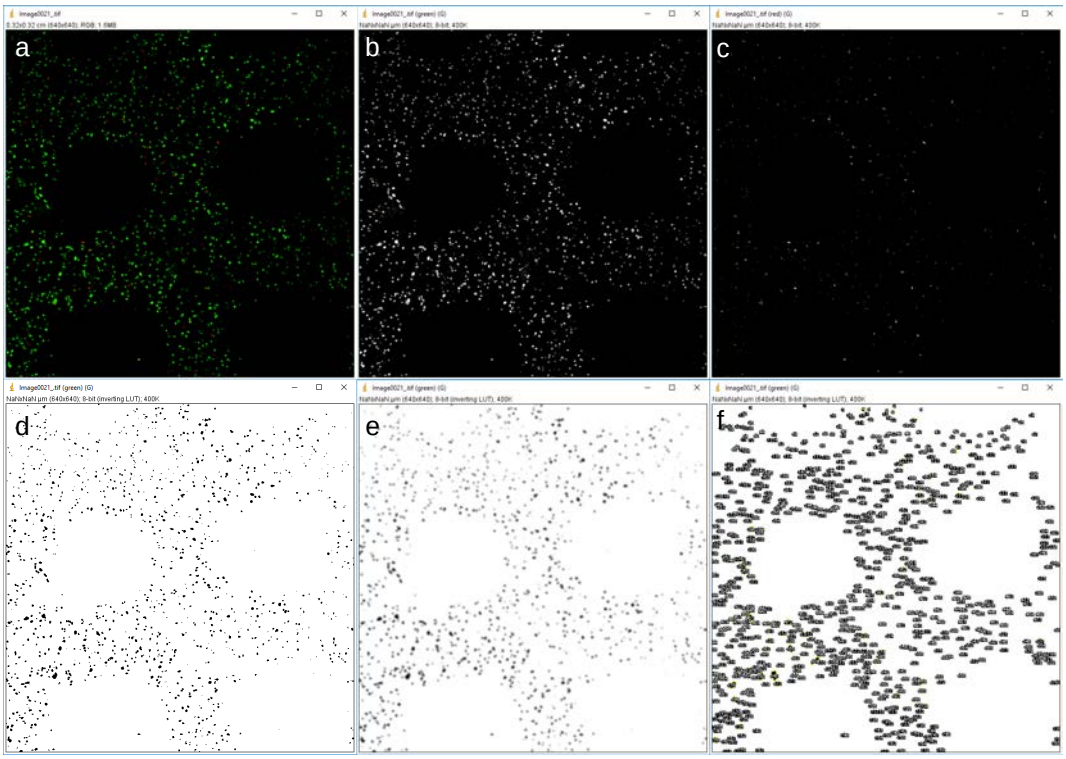

Figure 3.4: *Live and dead fluorescent images imported in ImageJ (a) with the split images in green (b) and red (c). Binary image of the split green channel before (d) and after the smoothing process (e). Image including the numbering of all the living cells when the "Analyze particle" feature is utilized (f).*

As the microscope images were loaded with both red and green colors together, it was necessary to split both channels into two different images (Image –> Color –> Split channel). Both images were then processed as binary images (cells were colored in black and background in white) (Process –> Binary –> Make Binary) and applied a smooth process three or four times (Process –> Smooth). The threshold of the image was modified (Image –> Adjust –> Threshold) to remove the noise and reduce the small particles not considered as cells

and linked cells were split using the "Watershed" option (Process –> Binary –> Watershed).

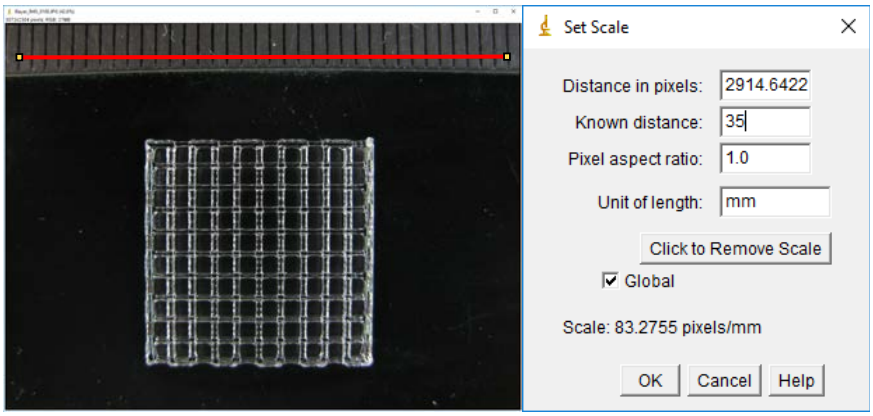

Figure 3.5: *Setting image scale on ImageJ.*

Finally, cells were counted automatically using the "Analyze Particles" feature (Analyze –> Analyze Particles) and data were exported to an Excel file. To get further information from the image beside the area, additional features were checked and exported (Analyze –> Set Measurements), including information as the perimeter, x-y coordinates or image file name among others.

3.7 Measurements of printed models

Printing accuracy was assessed by means of the measurement of characteristic distances in printed calibration models. Measured distances were compared with the theoretical values, obtaining the dimensional errors for each 3D printer and printed geometry. Printed models were photographed right after the printing process to prevent drying of the samples and potential deformations. Pictures of printed samples and videos of the printing process were taken using a DSLR camera (EOS 700D; Canon), placed on a stable tripod and under controlled lighting conditions. Images of printed samples' heights were taken using a USB microscope camera (KKmoon 500; Digital microscope, China).

Images were analyzed and measured using ImageJ open-source software. To that end, it was necessary to set the image scale on ImageJ to convert the measurements from pixels to units like mm or µm. To that end, a scale bar was placed close to the photographed printed sample and once the image was imported into ImageJ drag out a line across the scale bar; after that, the "Set Scale" dialog box was configured (as already described in the previous section). If the sample was slightly rotated and its straight lines were not aligned with the horizontal

and vertical axis, a rotation of the image was performed using the “Rotate” feature (Image –> Transform –> Rotate). To measure the specific distances of each printed samples, different lines were drawn covering those distances and after that selecting the “Measure” option (Analyze –> Measure). The measuring parameters of interest were selected in the “Set Measurements” window (Analyze –> Set Measurements) (figure 3.6).

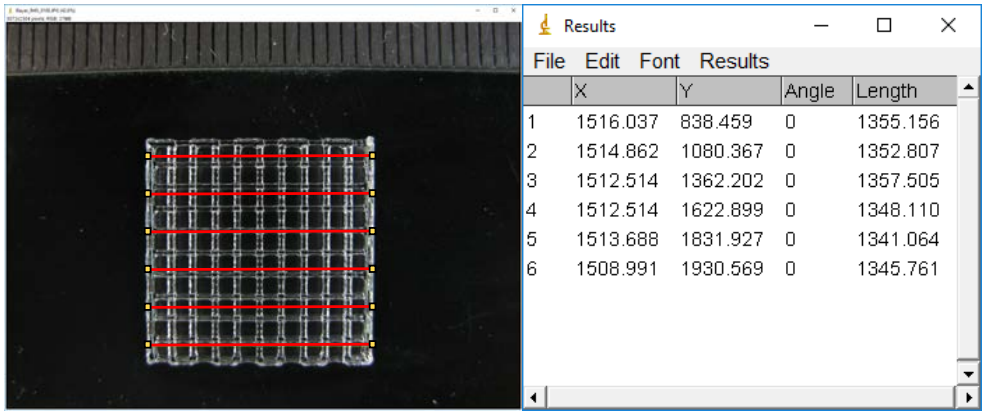

Figure 3.6: *Measuring characteristic distances of calibration models on ImageJ.*

Chapter 4

Development of open-source EBB printheads

Temperature control during bioprinting is essential to adjust the rheological properties of biomaterials and assure an optimal printability and cell viability. In addition to the temperature control, an accurate adjustment of printing pressure is critical to control the deposition rates of bioinks, especially in the case of thermoreversible hydrogels such as gelatin or collagen. Among all the aforementioned bioprinting printheads in chapter 2, there is a lack of open-source printheads incorporating a precise temperature adjustment of bioinks in both heating and cooling modes, which significantly reduces the range of bioinks to be printed. Besides, most of the open-source printheads have traditionally been based on mechanical systems where printing pressure cannot be precisely tailored for each bioink, while pneumatic systems permit a more accurate control of the pressure. It is therefore desirable to develop printheads with an improved control over the main bioprinting parameters and easily exportable to different 3D printers, to provide more versatile bioprinting systems.

In this chapter, three open-source microextrusion-based pneumatic printheads are presented. Two of these printheads (PH and PHR) were designed to deposit biomaterials within a temperature range from 1 ºC to 60 ºC. Both PH and PHR printheads have similar components and assembly steps, however, PHR was conceived as a later version of PH printhead with reduced dimensions. The reduced size of PHR permitted an easier integration of this printhead in multimaterial bioprinting platforms. Both printheads were utilized to print biomaterials such as Gel-Alg and P407. The third printhead was designed to print polymers with higher melting points and is able to heat biomaterials at temperatures up to 140 ºC. This high-temperature printhead was utilized to print PCL scaffolds at different temperatures.

4.1 PH and PHR printheads

4.1.1 Design and fabrication

PH and PHR printheads design allows heating and cooling bioinks, having an operating temperature range from 1 ºC to 60 ºC. Both PH and PHR printheads can be mounted on most of the desktop 3D printers, with an almost negligible cost (70 USD). PH and PHR printheads have a similar design, being the PHR a reduced version of the PH printhead. The design of the PHR printhead was motivated by its use in a multi-material bioprinting approach. When multiple PH were attached to the x-carriage, the large dimensions of these printheads limited the available bioprinting area in the x-y plane. Therefore, a more reduced version of this printhead was designed with overall smaller dimensions, but limiting its use to 3 mL and 5 mL syringe barrels, as the 10 mL syringe had greater dimensions.

The modular design of both printheads permits the use of syringes of different volumes (figure 4.1). PH printhead enables the use of 3 mL, 5 mL and 10 mL syringe sizes, whereas PHR printhead permits the use of 3 mL and 5 mL syringes. Both printheads are broadly adaptable to the x-carriage of most of the open-source desktop 3D printers.

The working principle for both PH and PHR printheads is the same and a schematic representation is depicted in figure 4.2. Briefly, the syringe is surrounded by an aluminum (Al) block, which is customized for each syringe size to fit its particular shape and diameter (figure 4.4). Two Peltier modules (TES1-12704; Hebei I.T.) in contact with the Al block control the heating/cooling operations of the printhead. Technical specifications of Peltier modules utilized are detailed in table 4.1. Each Peltier module has the other side in contact with an Al plate, which is in contact with two heatsinks to exchange heat with the environment. The Al plate placed between the Peltier modules and the heatsinks was utilized for facilitating heatsink placement. Peltier modules were connected in series to the 3D printer electronic board following the wiring diagram detailed in chapter 5. Heatsinks and Peltier are braced to the carcass of the printhead using two 3D printed clamps. The 3D printed clamps are screwed to the M3 brass inserts placed in the front of the carcass using four M3x25 mm screws.

Two EPCOS 100K (B57540G0104J; EPCOS, Spain) thermistors placed inside the Al block and a heatsink were used to measure the printhead temperatures. The printing pressure was controlled pneumatically using a 12 Vdc solenoid

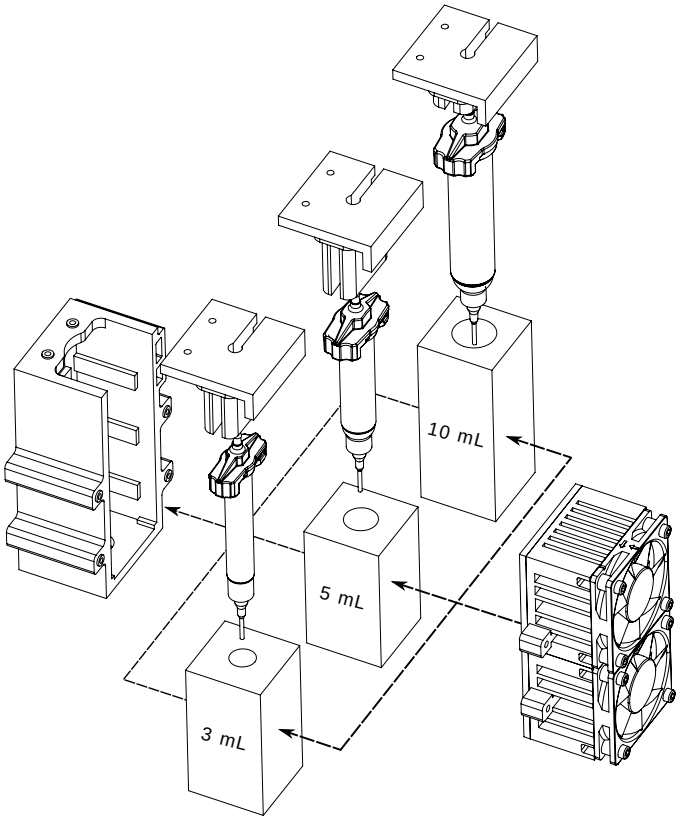

Figure 4.1: *Schematic representation of the modular design of the PH printhead. Syringes of 3 mL, 5 mL and 10 mL can be exchanged using the same printhead.*

valve (VT307-6DZ1-01F-Q; SMC) connected to the 3D printer electronic board and a pressure regulator (ARP20K-N01BG-1Z; SMC). Syringe barrels, pistons and syringe adapters (Nordson EFD) of three different sizes (3 mL, 5 mL, 10 mL) can be used in the PH printhead by changing the Al block. PHR printhead permits the use of 3 mL and 5 mL syringes. Nordson syringes were fixed in the printhead using a 3D printed syringe cover, which was screwed to the M3 inserts placed in the upper part of the printhead carcass. The complete list of materials, providers and approximate cost for both PH and PHR printheads is summarized in tables A.1 and A.2. The 3D printed parts utilized can be printed on any desktop 3D printer and their cost was calculated multiplying their weight by the cost of the ABS filament per kg (~20 USD/kg). The rest of printhead mechanical components are widely available through online providers. Figure 4.3 depicts a general exploded view of all the components utilized in the assembly of PH and PHR printheads. The complete bill of materials of both printheads is detailed in tables A.1 and A.2.

Heatsinks and fans utilized were different for PH and PHR printheads. Both heatsinks and fans utilized in the PH printhead (FANP1003LD; StarTech.com) were purchased jointly and already pre-assembled. Both components had overall

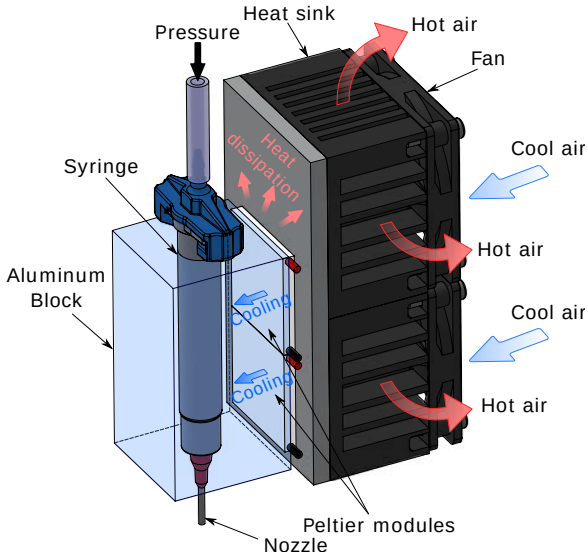

Figure 4.2: *Schematic representation of the operating principle of PH and PHR printheads in cooling mode with a 3 mL syringe loaded in the Al block.*

dimensions of 50x50x41 mm, a thermal resistance of 0.998 ºC/W and an air flow rate of 8.84 CFM (cubic feet per minute). The heatsink (750-0951; RSOnline) and fan (111-8315; RSOnline) utilized in the PHR printhead were purchased separately and later assembled. The heatsink had overall dimensions of 40x40x18 mm and a thermal resistance of 5.1 ºC/W (forced). The axial fan utilized had overall dimensions of 40x40x10 mm and an air flow rate of 9.9 CFM. The axial fans of both printheads required an input power of 12Vdc and were connected to the 3D printer power supply. The heatsinks of both printheads were attached to the Al plate using thermally conductive adhesive foil.

Table 4.1: *Performance specifications of TES1-12704 Peltier modules*

Hot side temperature (ºC)	**25**	**50**
Qmax (W)	34	37
Delta Tmax (ºC)	66	75
Imax (A)	3.3	3.3
Vmax (V)	14	16.1
Module resistance (Ω)	3.1	3.6

Printhead Al syringe blocks and plates were fabricated using an A6061 alloy. Two Al plates were utilized for the PH and PHR printheads, with dimensions of 100x50x3 mm and 80x40x3 mm respectively. Two initial Al blocks (A6061FNM-110-100-35 and A6061FNM-250-250-3; Misumi) were purchased and subsequently divided in smaller pieces for the manufacturing of the syringe blocks and plates. Syringe blocks dimensions were cut according to the dimensions of each syringe size and printhead (table 4.2). The diameter of the hole of the Al

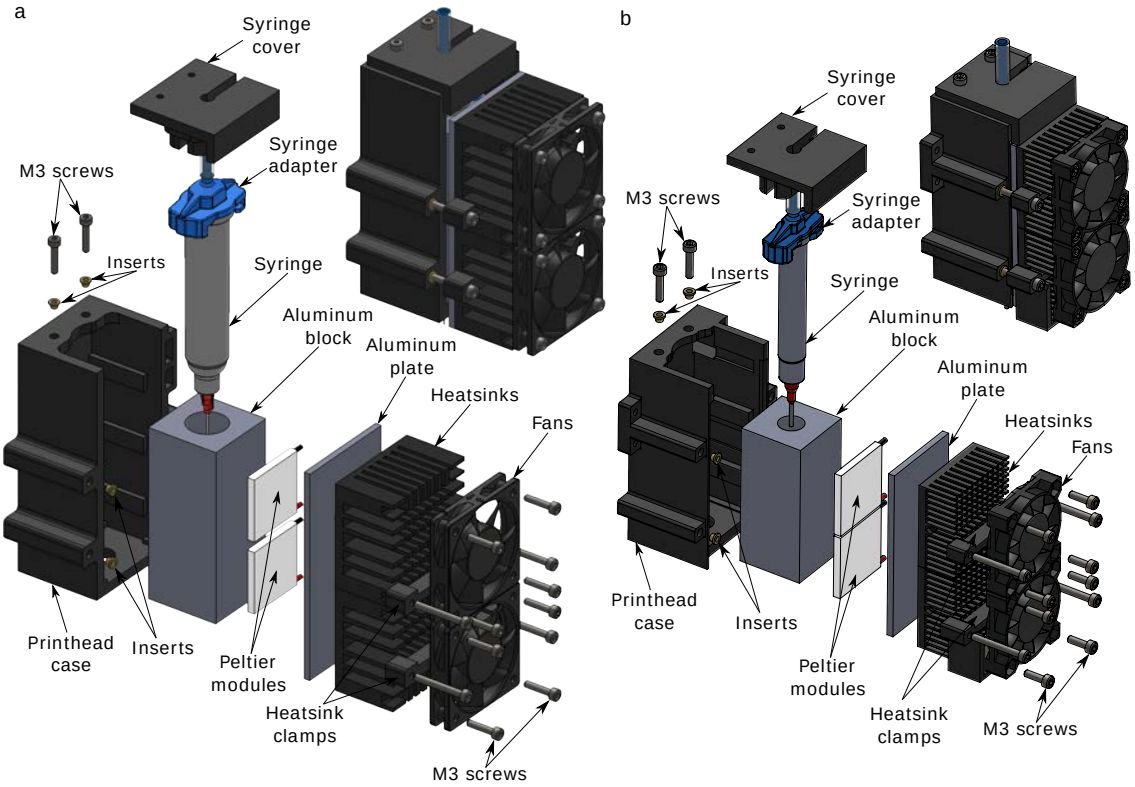

Figure 4.3: *Exploded and assembled views of all the components that composed the (a) PH and (b) PHR printheads.*

blocks was designed to fit the outer diameter of the Nordson syringes (figures A.3 and A.4).

Table 4.2: *Al blocks characteristics utilized in PH and PHR printheads*

	3 ml		**5 ml**		**10 ml**	
	PH	**PHR**	**PH**	**PHR**	**PH**	**PHR**
Side (mm)	35	30	35	30	35	-
Height (mm)	66	66	61	61	83	-
Hole diameter (mm)	11.5	11.5	14.6	14.6	18.7	-
Volume (cm^3)	73.99	52.54	64.51	44.69	78.88	-
Weight (g)	199.78	141.87	174.18	120.65	212.97	-
Contact surface (cm^2)	23.84	23.84	27.97	27.97	48.76	-

Printhead components were designed using a 3D modeling software (SolidWorks; Dassault Systems) and exported as stereolithography (STL) files for 3D printing (figures A.1 and A.2). All the printhead STL files are available at the online NIH repository (TELab, 2018). PH and PHR printhead designs have been distributed under the terms of a Creative Commons Attribution-NonCommercial-ShareAlike (CC BY-NC-SA) license. This type of license permits to share, copy and redistribute the printhead designs in any medium or format providing the appropriate credit to the author. These designs cannot be used for commercial

Figure 4.4: *Al blocks utilized in the PH printhead for the 10 mL, 5 mL, and 3 mL syringe sizes (from left to right).*

purposes and all the modifications performed to the printheads must be distributed under the same license as the original.

The PH printhead was designed to use three different syringes sizes (3 mL, 5 mL and 10 mL) with the same components. Since the height and diameter were different for each syringe size, it was necessary to adjust the Al blocks and syringe covers to fit the dimensions of each syringe. We can observe from figure 4.5 that the same printhead components were utilized for the three syringe sizes (fans, heatsinks, heatsink clamps, Peltier, Al plate and carcass) and only two components varied (Al block and syringe cover). The overall dimensions of the PH carcass and Al block section (35x35 mm) were calculated to fit the 10 mL syringe (syringe with the biggest dimensions of the three proposed). The syringe covers were designed to prevent any vertical and rotational movement of the syringes during printing. To that end, the syringe cover length was designed to ensure the syringe to the upper part of the Al block and lateral walls fitted to the shape of the syringe adapter. The PH printhead is attached to the x-carriage of the 3D printer using three screws placed in the back of the carcass.

The PHR can be considered as a reduced version of the PH printhead. From the original dimensions of the PH printhead (70x115x91.9 mm), we can observe a reduction of 10 mm, 21 mm and 21.2 mm (width, height and depth) in the PHR printhead (figure 4.6). To reduce the overall printhead dimensions, it was necessary to remove the possibility of using the 10 mL syringe (figure 4.5). By removing the 10 mL syringe, it permitted the design of a smaller Al block and carcass. The overall dimensions of the Al plate, heatsinks and fans utilized were also smaller than the PH printhead, permitting a reduction of 13 mm in depth. The PHR printhead can be attached to the x-carriage of the 3D printer using the same system as the PH printhead or using four screws placed on both sides of

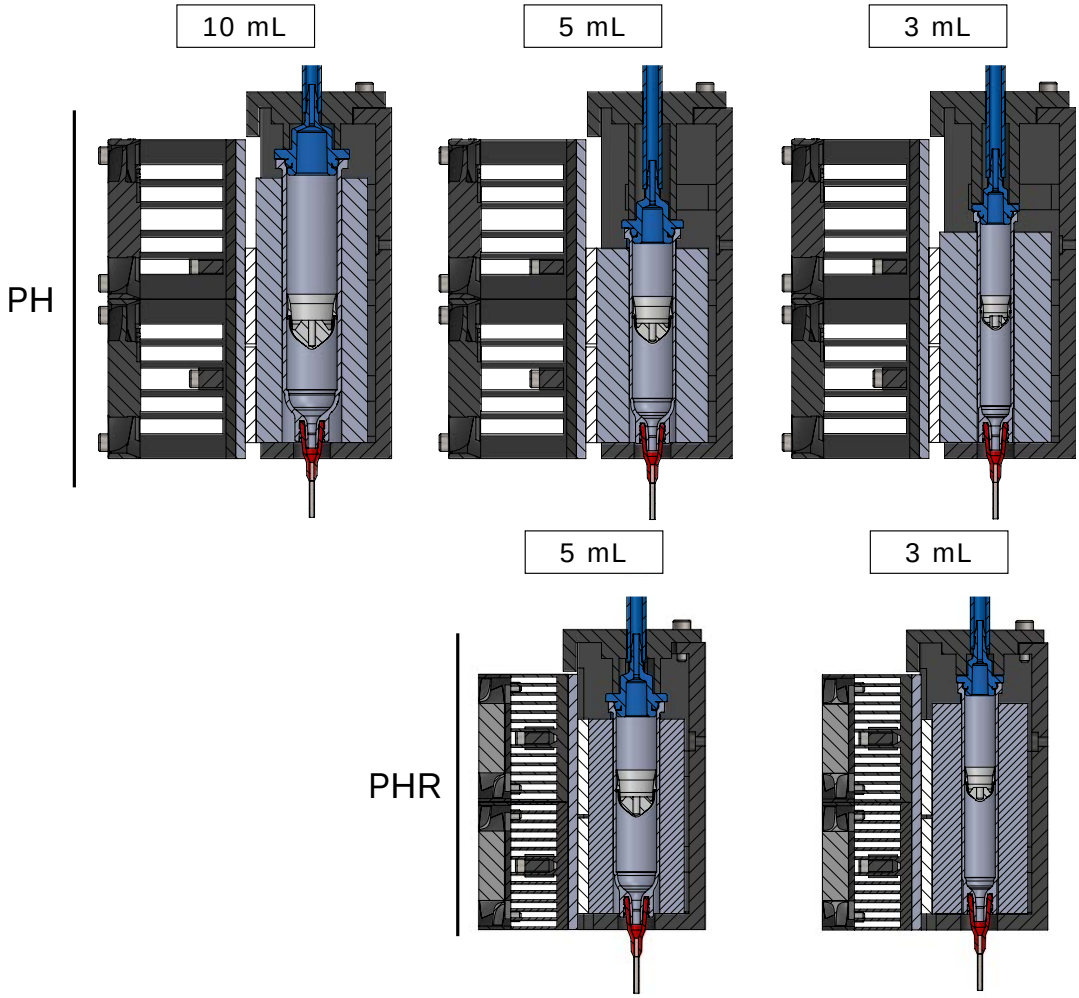

Figure 4.5: *Section view of the PH and PHR printheads with the 10 mL, 5 mL and 3mL syringes loaded.*

the carcass. The use of the outer holes permits an easier and faster attachment system if compared to the one utilized in the PH printhead.

4.1.2 Assembly

Although the components utilized in PH and PHR printheads are not exactly the same, the steps required for the assembly of both printheads are identical and described below. The assembly process does not require any expertise on engineering concepts and can be completed in a few minutes. For a better understanding of components placement, the reader is referred to figures 4.3 and 4.8.

The first part of the assembly requires to stick the Al plate to the heatsinks using thermally conductive adhesive foil. Likewise, the Peltier mod-

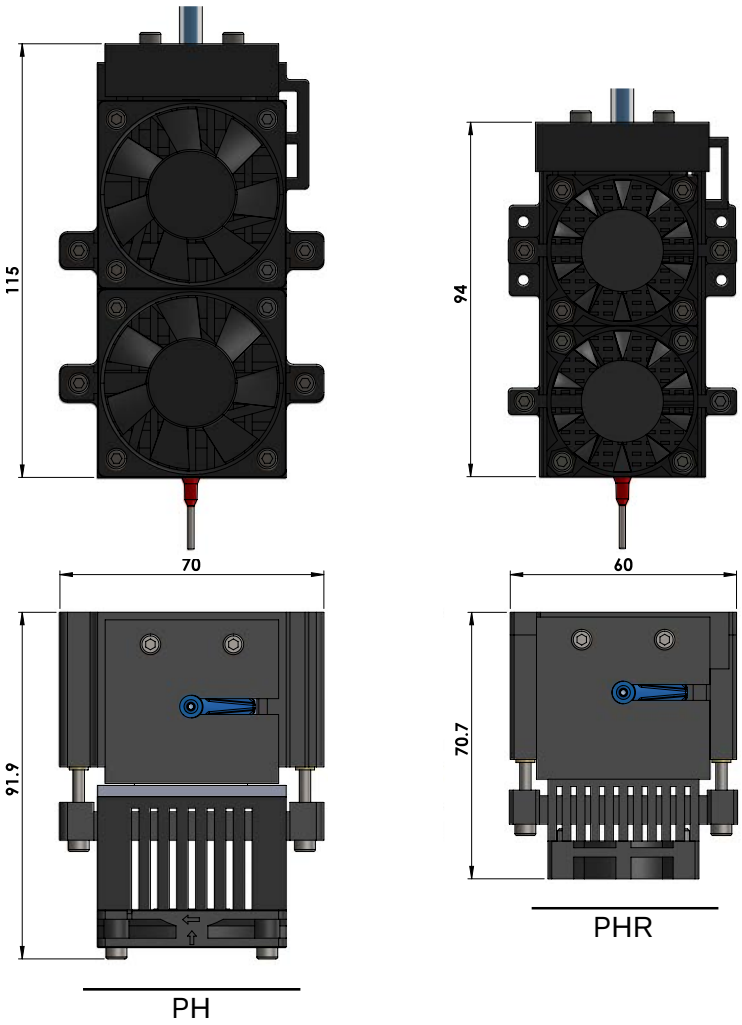

Figure 4.6: *Overall dimensions of PH and PHR printheads.*

ules are stuck to the Al plate using the same adhesive foil. Then, the heatsink clamps are placed inside the heatsinks and the axial fans are attach to the latter using the M3x10 mm screws (figure 4.8a). Six M3 brass inserts are introduced into the printhead carcass (four in the front part and two in the upper part). Inserts can be placed applying hand-pressure or using a soldering iron for a better adjustment. Then, the Al syringe block is placed inside the printhead carcass and fixed using the already assembled Peltier-heatsink module, which is attached to the carcass using the heatsink clamps and four M3x25 mm screws (figure 4.8b). These screws should be fasten until both Peltier modules make full contact with the Al block. Once all printhead components are assembled, the Peltiers and fans wires are introduced through the side holes of the carcass and connected to the 3D printer electronics (figure 4.8c). Prior to load a syringe barrel into the printhead, it will be necessary to attach the syringe adapter and screw the syringe cover to the upper part of the carcass using two M3x10 mm screws (figure 4.8d-f).

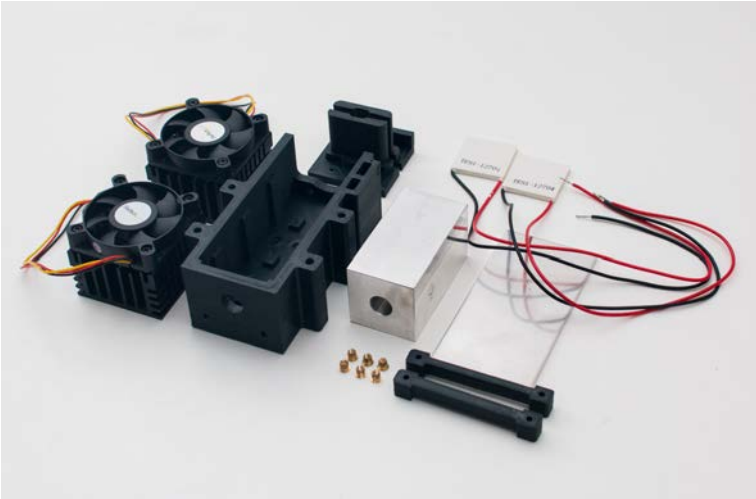

Figure 4.7: *General view of the main parts that compose the PH printhead.*

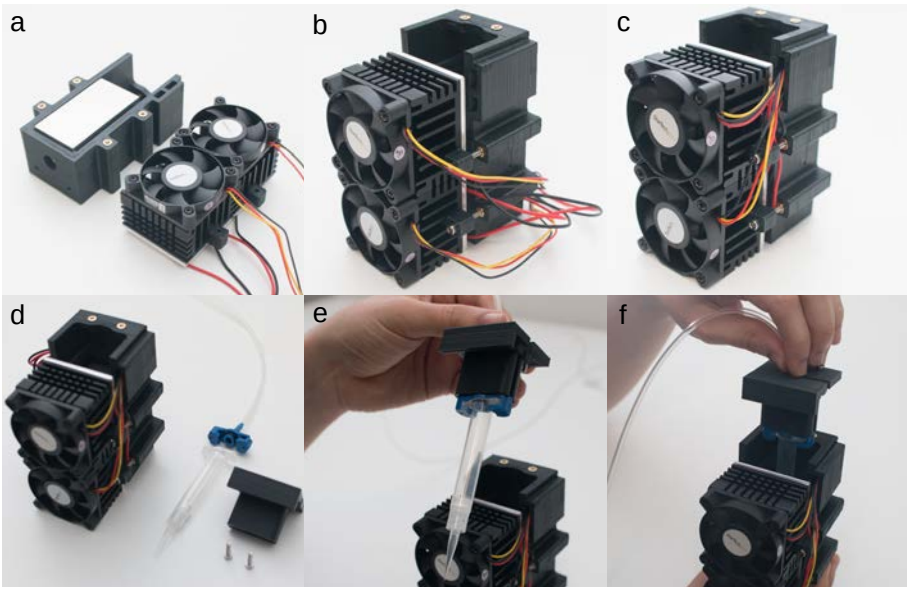

Figure 4.8: *Printheads assembly steps for the PH printhead and a 3 mL syringe.*

4.1.3 Thermal performance

Precise and stable temperature control is essential for maintaining high cell viability when depositing thermoreversible bioinks with resolutions well within a few hundreds of microns range. We evaluated the temperature variation of PH and PHR printheads as a dynamic response to different heating and cooling cycles. Two heating and cooling cycles were performed starting from an initial temperature of 22 ºC to target temperatures of 37 ºC and 5 ºC. Temperature measurements were obtained using two thermistors located inside the Al block (T0) and the heatsinks (T1).

Table 4.3: *Operating temperatures limits of the PH and PHR printheads. The minimum temperature is limited by the cooling capacity of the Peltier units and the maximum temperature established for the safety of the device.*

		3 mL		5 mL		10 mL	
		PH	**PHR**	**PH**	**PHR**	**PH**	**PHR**
Cooling	**Temperature (ºC)**	3.86	1.6	2.86	1.9	4.4	-
	Time (min)	15	8.83	15	13.5	18	-
Heating	**Temperature (ºC)**	60	60	60	60	60	-
	Time (min)	6.05	4.75	4.36	3.5	6.11	-

Operating printhead temperatures, stability and heating/cooling times for the proposed printheads were assessed considering different syringe sizes (3 mL, 5mL and 10 mL for PH; 3 mL and 5mL for PHR). Syringes were filled with water to simulate the presence of a bioink inside the printhead. The maximum and minimum working temperatures of both PH and PHR printheads define their limitations under different heating/cooling conditions (table 4.3). When heating hydrogels, the Al block of both printheads can rapidly reach values up to 80 ºC. However, we limited the temperature to 60 ºC to avoid deformation of either the printhead carcass or the polypropylene syringe barrels.

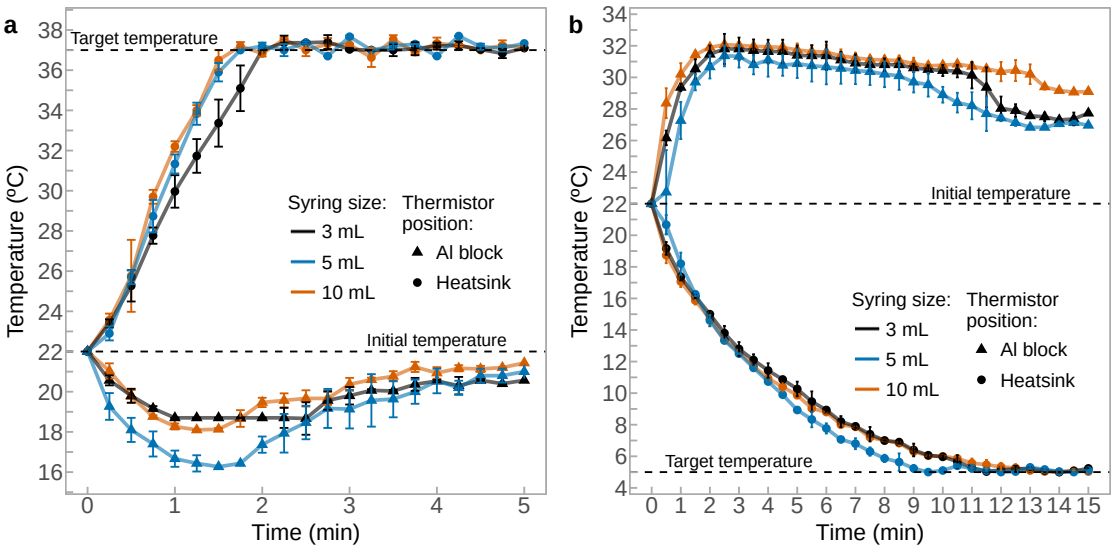

Figure 4.9: *Temperature evolution of PH printhead measured inside the Al block (thermistor T0) and the heatsinks (thermistor T1) when increasing the temperature from 22 ºC to 37 ºC (a) and decreasing the temperature from 22 ºC to 5 ºC (b). The data represent means and standard deviations of three experiments (n=3).*

When using the PH printhead, heating the Al block from 22 ºC to a target temperature of 37 ºC did not last more than 2 min (figure 4.9a) with the heatsink temperature only decreasing 6 ºC. On the other hand, a cooling down from 22 ºC to 5 ºC (figure 4.9b) spent much more time (around 13 min)

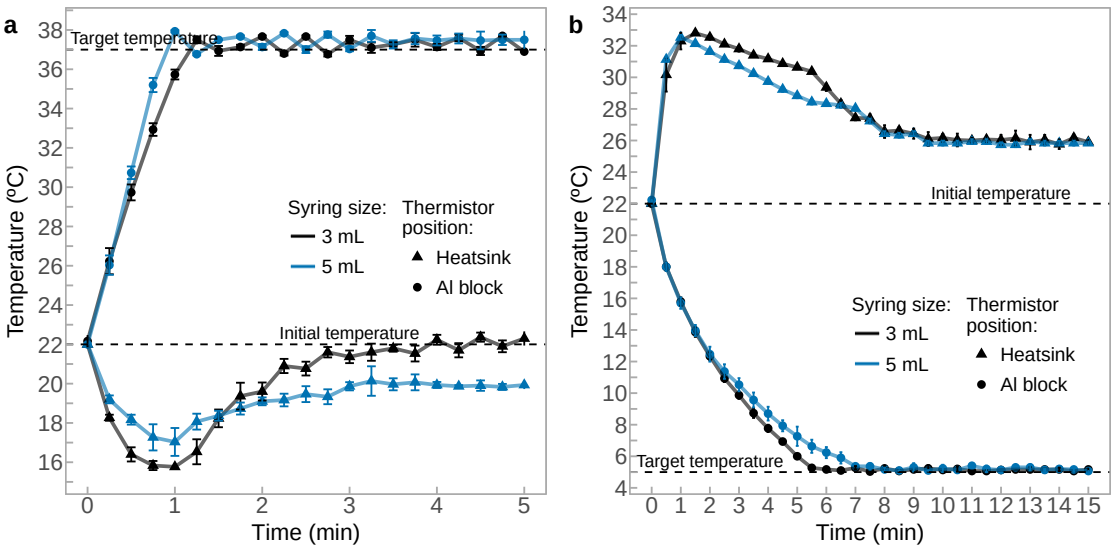

Figure 4.10: *Temperature evolution of PHR printhead measured inside the Al block (thermistor T0) and the heatsinks (thermistor T1) when increasing the temperature from 22 ºC to 37 ºC (a) and decreasing the temperature from 22 ºC to 5 ºC (b). The data represent means and standard deviations of three experiments (n=3).*

with the temperature of the heatsinks never exceeding 32 ºC. Importantly, the steady-state temperatures did not show a maximum variation higher than ±0.3 ºC, which could be considered an acceptable margin of error in bioprinting. The maximum time required for heating any of the Al blocks from 22 ºC to 60 ºC took around 6 min (table 4.3). On the other hand, the minimum temperature measured for all the syringe sizes when cooling down gels was between 2 to 4 ºC. The average time spent in this operation was less than 18 min. Temperature and time variations between the different syringe sizes were almost negligible, which denotes an appropriate design of the Al block, and selection of the Peltier modules.

Response times of PHR printhead were also analyzed for specific target temperatures (figure 4.10). When the 5 mL syringe was installed, it showed a better response times than the 3 mL syringe in the cooling cycles (3 mL: 4.75 min; 5 mL: 3.5 min) (figure 4.10b). On the other hand, the 3 mL module showed better capabilities in heating mode than the 5 mL (3 mL: 4.75 min; 5 mL: 3.5 min) (figure 4.10a). Despite these differences, similar maximum and minimum temperatures were reached for both syringe sizes (table 4.3).

Printhead thermal experiments revealed minor differences between heating/cooling response times among different syringes. However, aspects like bioink volume, the thermal conductivity of syringe walls or the existence of air gaps between the syringe and the Al block may alter significantly the final performance

of the printhead. These aspects could increase the time needed to reach certain bioink temperatures and should be taken into account. We can also observe an overall better thermal performance of PHR printhead in both cooling/heating modes with faster response times and the ability to reach lower minimum temperatures (table 4.3). Therefore, the use of PHR printhead is recommended when syringe volumes of 3 mL and 5 mL are utilized, and the PH printhead should be utilized instead when syringes of 10 mL are required.

A second batch of experiments was performed to measure the time required for bioinks to reach the target temperature once introduced inside the printhead. The mass fraction of water in hydrogels is significantly much higher than the mass fraction of a polymer (Ahmed, 2015). Taking this into consideration, the syringe barrels were filled with water to simulate the presence of a hydrogel and monitored the evolution of water temperature during different heating/cooling cycles. First of all, the printhead temperature without the syringe was set beforehand. Then, the syringe filled with water was introduced and recorded its temperature change. Thermistors were placed in contact with the water that filled the syringes and the heatsink. In the first test, the syringe was previously warmed and stabilized at cell culture temperature (37 ºC). After that, it was introduced inside the printhead at a temperature of 10 ºC preset beforehand and maintained to that temperature. In a second experiment, the syringe temperature was previously set to 22 ºC and then introduced in the printhead at 37 ºC.

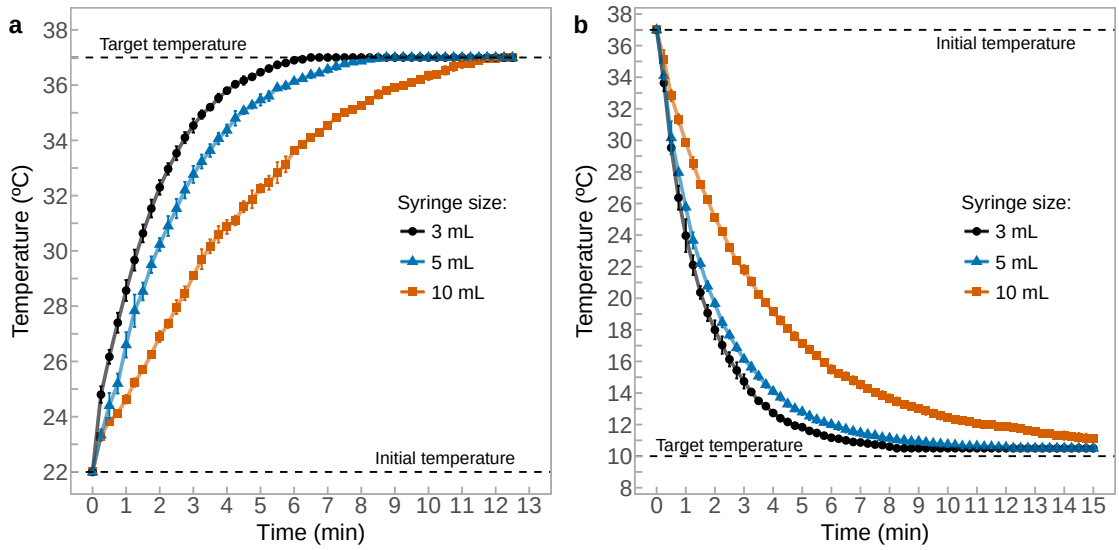

Figure 4.11: *Temperature evolution measured inside the syringe barrel filled with water and loaded in the printhead when increasing water temperature from 22 ºC to 37 ºC (a) and decreasing water temperature from 22 ºC to 10 ºC (b). The data represent means and standard deviations of three experiments (n=3).*

The time required to increase the water temperature from 22 ºC to 37 ºC in the 10 mL syringe was double that in the 3 mL syringe due to the differences in volume (figure 4.11a). Decreasing the temperature of the water from 37 ºC to 10ºC produced similar values with 8 and 15 min for 3 mL and 10 mL syringes, respectively (figure 4.11b). These values should be taken into consideration when establishing the thermal inertia of the system and the time required for the stabilization of the bioinks under significant temperature changes. In this case, results from PH and PHR were the same, as the temperature was recorded inside the water and the temperature of the Al block was already preset beforehand.

4.2 High-temperature printhead

4.2.1 Design and fabrication

A schematic view of the high-temperature microextrusion-based printhead manufactured for this research is shown in figure 4.13a. The printhead utilizes a 220 Vac band heater (25 x 25 mm; LJXH, China) attached to a hollow Al block. A 5 mL stainless steel syringe (SSY-5E; Musashi, Japan) is inserted in an Al block (figure A.6). The syringe receives the pellets of PCL, and it is capable of working under elevated pressure and temperature. A 100K thermistor (B57540G0104J; EPCOS, Spain) is inserted into the Al block to measure its temperature. The thermistor is close to the syringe to obtain more accurate measurements. The Al block insulation from the carcass is made employing cork sheets. Printing pressure is controlled using a 12 Vdc solenoid valve (EVT307-6D-02F-Q; SMC, Japan) and a pressure regulator (AR20-N01BG-RYZ; SMC, Japan). Both the printhead heater and the solenoid valve were controlled from the metal-oxide-semiconductor-field-effect transistor (MOSFET) terminals of the board. The 220v heater used a relay (RLP/5-12D; Nagares, Spain) connected to the 12 Vdc MOSFET controller. PCL extrusion was performed without a piston under compressed air pressure using a special syringe adapter (AT-5E-SUS; Musashi, Japan). The printed parts of the printhead were designed using open-source CAD software (FreeCAD; v0.17) (Riegel J, Mayer W, 2018). Some printhead components were printed with a desktop 3D printer (Ultimaker 3; Ultimaker, Netherlands) in polycarbonate (Ultimaker PC; Ultimaker, Netherlands) (figure A.5). The STL files of the printhead carcass and the fan support can be downloaded from the NIH 3D Print Exchange repository (TELab, 2018). Additional information about the final dimensions of the open-source printhead is available at figure 4.12. The complete bill of materials is detailed in table A.3.

The printhead carcass was made of a PC that exhibits a heat deflection temperature of at least 110 ºC. The measured temperature on the inner face of the carcass was always below 110ºC (figure 4.13b). Besides, the temperature distribution across the external face of the carcass for a target temperature of 120 ºC was obtained using a thermal camera (figure 4.13c and 4.13d). The highest temperatures were found in the middle of the faces with clear hotspots in the lateral faces. These results are consistent with our design because thermal insulation was thinner on the lateral faces than on the front and back ones to reduce the total printhead width. A more compact design is advantageous because this facilitates the installation of multiple printheads on the carriage of the 3D printer.

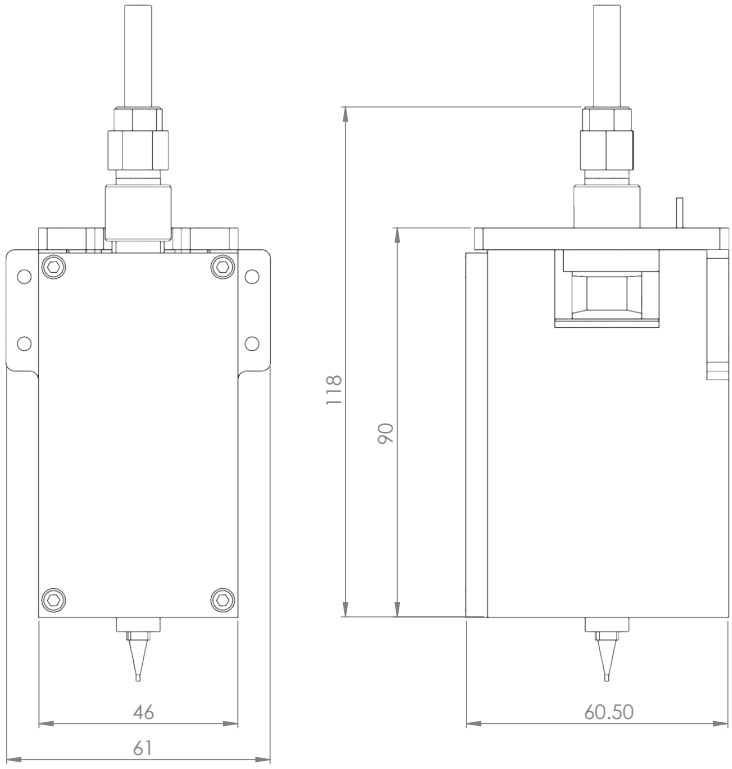

Figure 4.12: *Main dimensions of the open-source high-temperature printhead.*

4.2.2 Assembly

The steps required for the assembly of the high-temperature printhead are quite simple and do not require any expertise in engineering concepts. For a better understanding of components placement, the reader is referred to figure 4.13a. The first part of the assembly is to attach the band heater to the Al block. Then, both are covered with cork sheets and kapton tape to protect the printhead

carcass from the heat. Then, the Al block, band heater and cork sheets are placed inside the printhead carcass. Six M3 brass inserts are introduced into the printhead carcass (four in the front part and two in the upper part). The front cover is then screwed to the carcass with four M3x10mm screws. When the stainless steel syringe and the adapter are introduced in the Al block, the syringe cover is screwed to the upper part of the carcass using two M3x10 mm screws.

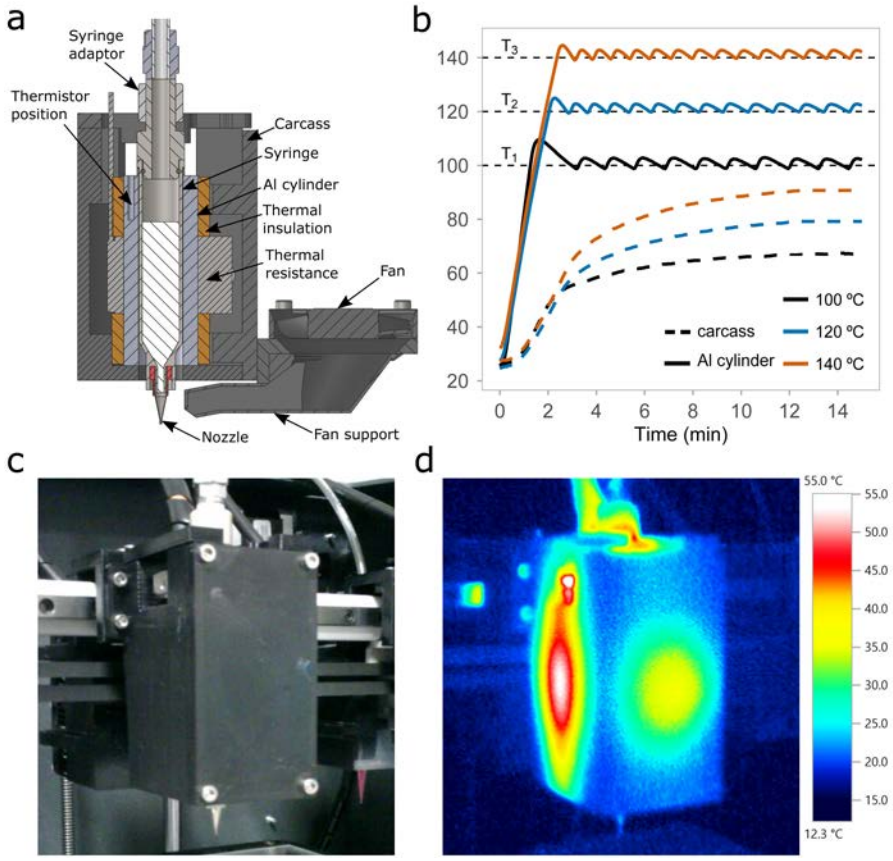

Figure 4.13: *Open-source printhead for 3D printing of polymers of high melting point. (a) Schematic section view of the 3D CAD design of the printhead with all its components. (b) Transient response of the experimentally measured temperatures in the Al block and the interior of the carcass over time at three different target temperatures: 100 ºC, 120 ºC and 140 ºC. (c) Standard and (d) thermal images of the printhead installed in the 3D printer for a target temperature of 120 ºC.*

4.2.3 Thermal performance

The deposition of PCL requires precise control of the print temperature to attain suitable viscosity values and optimal printing performance (Visser *et al.*, 2013). Target operating temperatures of 100, 120 and 140 ºC were established for the extrusion system and several heating cycles were conducted to reach those temperatures. Target temperatures represent the PCL temperatures for the experiments, which were set in the Repetier-Host software. Temperatures inside the

Al block and the interior of the printhead carcass were measured and monitored with two 100K thermistors connected to the Rumba electronics. The temperature outside the carcass was captured by calibrated thermal images obtained with a thermal camera (Testo 871; Testo, Spain). In any case, thermal oscillations were very low over time with temperature fluctuations in the Al block that surrounds the metallic syringe only up to 2.5 ºC (figure 4.13b). Even if we established 140 ºC as the upper limit of the printhead target temperatures, much higher temperatures can be reached with the same band heater. However, it would be necessary to use alternative materials for the carcass, such as high-temperature photocrosslinkable resins or even Bakelite.

4.3 Conclusions

In this chapter we have presented three innovative bioprinting printheads, which permit a precise deposition of most of the biomaterials and bioinks utilized in EBB. These printheads represent an alternative approach to commercially available bioprinting systems, since they are compatible with the majority of the affordable open-source desktop 3D printers (see chapter 5 for more details). A comprehensive description of printheads fabrication, assembly and components utilized was included to facilitate their adoption by the scientific community.

In the first place, PH and PHR printheads were designed to deposit biomaterials within a temperature range from 1 to 60 ºC, which allows deposition of biomaterials with a broad range of viscosities. Despite other open-source bioprinting printheads were found in the literature, all of them are only capable of heating bioinks above RT and were limited to use just one syringe size. Both PH and PHR printheads allow heating and cooling bioinks with the same device. Besides, its modular design allows the use of different syringe sizes, replacing the specific Al block while keeping the rest of the printhead components. The universality, modularity and wide range of printing temperatures make PH and PHR printheads unique tools for bioprinting applications, being the first open-source printheads that provide all these capabilities altogether. The thermal studies performed to both printheads revealed an overall better thermal performance of PHR printhead in both cooling/heating modes with faster response times and the ability to reach lower minimum temperatures than PH printhead. Therefore, the use of PHR printhead is recommended when syringe volumes of 3 mL and 5 mL are utilized, and the PH printhead should be utilized instead when syringes of 10 mL are required.

On the other hand, the high-temperature printhead was designed to print biomaterials with melting points higher than the maximum temperature provided by PH and PHR printheads. This printhead demonstrated its excellent capabilities in terms of temperature response with an upper temperature limit of 140 ºC. As with PH and PHR printheads, the high-temperature printhead can be easily combined with low-cost desktop 3D printers. These three devices can be installed together within the same bioprinter, enabling the deposition of different biomaterials and with great potential for the generation of multi-material complex constructs.

Chapter 5

Conversion of open-source desktop 3D printers into bioprinters

Once bioprinting printheads have been introduced in chapter 4, additional modifications were required to transform standard desktop 3D printers into functional bioprinters. All these modifications are detailed in this chapter and covers from the new hardware components installed (electronics, pneumatic equipment and 3D printed parts), to all the software involved in the bioprinting process (firmware, slicing and host software). All these tools and designs are distributed under a free and open-source format, which implies that anyone can utilize them freely and even contribute to their enhancement. Besides, they are intended to be compatible with most of the desktop 3D printers available to date. To demonstrate the versatility of the bioprinting platform, three different desktop 3D printers were utilized (BCN3D+, Sigma and Witbox 2) and modified to provide them with bioprinting capabilities. With all this, it is sought to provide an overall open-source bioprinting platform that fulfills all the requirements of an EBB bioprinting process, which is intended to be a more accessible alternative to the commercial bioprinters.

5.1 Hardware

Nowadays there are a plethora of open-source desktop 3D printing systems that provide high resolutions and permit an easy customization, all of it at an affordable cost. Among all of them, three open-source 3D printers (BCN3D+ (figure 5.1), Witbox 2 (figure 5.2) and Sigma (figure 5.3) were utilized in this research and modified to be utilized as bioprinters. The use of different 3D printers permitted to demonstrate the versatility of the bioprinting tools presented in this thesis

and compare the capabilities of each platform. Aside from their software, all these 3D printers utilize common components in their x-y-z translational stages, such as stepper motors, endstops, pulleys, belts and bearings. As a result, most of the modifications performed to these machines are easily exportable to other 3D printers. For example, each of the 3D printers utilized is sold with different electronics, however, all of them are compatible with standard RepRap-based electronics and the same open-source board were utilized in all of them (i.e. RAMPS, RUMBA).

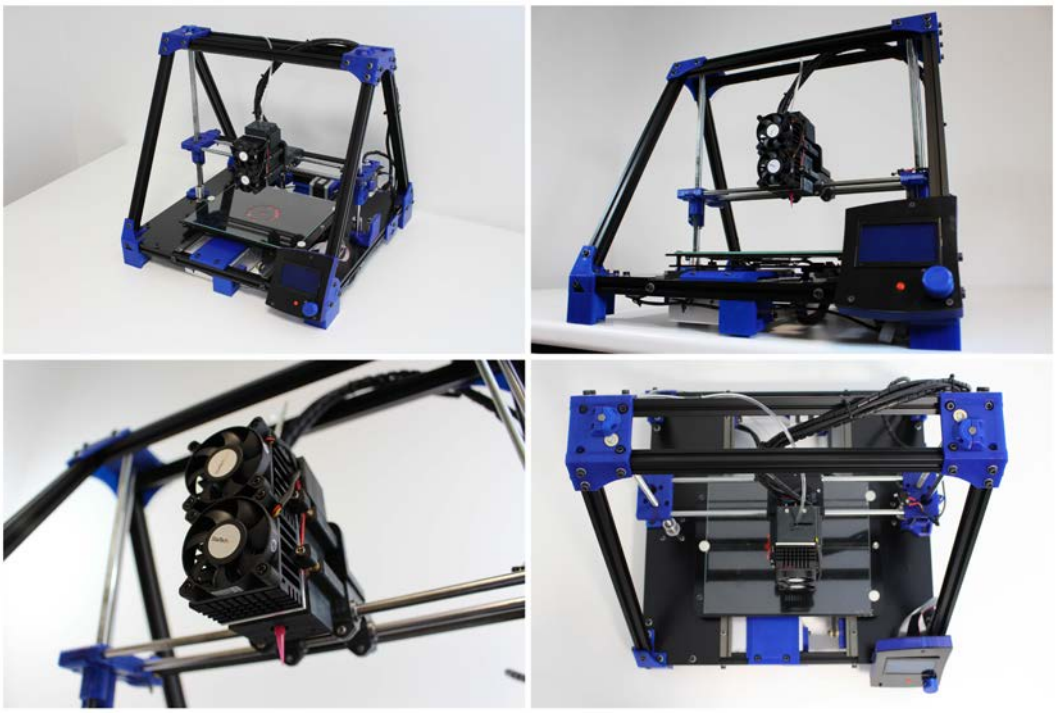

Figure 5.1: *PH printhead installed in BCN3D+ 3D printer.*

As most of the desktop 3D printers, these utilize FDM technology to generate 3D printed models. Thus several components as the hotend or the filament extruder were not required for bioprinting purposes and were removed. These components were replaced with the bioprinting printheads presented in chapter 4, enabling the deposition of biomaterials. As the original printheads were modified, it was necessary to design several components to readjust the way that the new printheads were attached to the x-carriage of the 3D printers. The new printheads also required the use of pneumatic components, such as solenoid valves and pressure regulators, which managed the deposition of bioinks. Finally, the same electronics were utilized in the three bioprinters, with the aim of homogenizing their components.

Regarding bioprinter sterilization, special attention will be given to some specific components such as the electronics, the power supply, solenoid valves or pressure regulators, as those components present difficulties to be sterilized using the procedure detailed in chapter 3 and may become a source of future contamination. Where possible, these components should be placed as far as possible from the printing area, inside a sterile container or even outside the sterile hood. Besides, it is also likely to have 3D printer components which include the use of oils or lubricants (i.e. bearings, shafts, pullets, etc.). Although these substances cannot always be removed, wherever possible it will be necessary to keep all these components as clean as possible. Bioprinters are often placed inside laminar-flow hoods and are exposed to high-intensity UV radiation over long periods to assure sterile conditions. However, these type of machines were not initially conceived to work under these conditions and some of the materials utilized in their construction are not UV-stable. As a result, some of its components might degrade and even crack over time, which might compromise the functionality of the bioprinter. Therefore, special attention should be given to these components in the long-term to prevent any possible malfunctions.

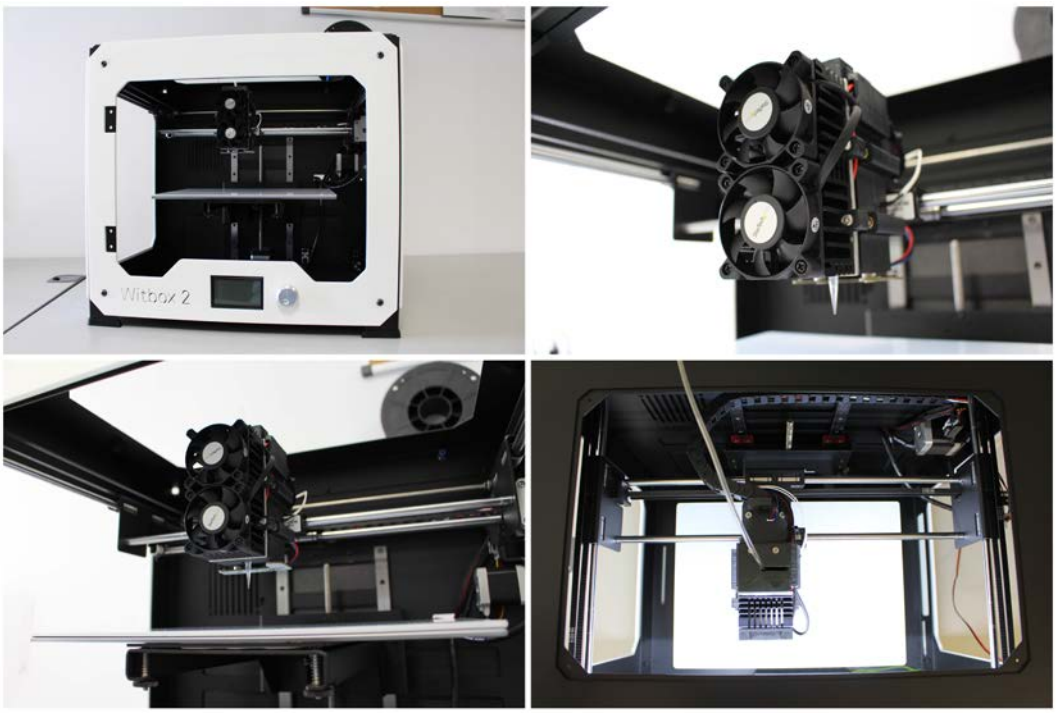

Figure 5.2: *PH printhead installed in Witbox 2 3D printer.*

5.1.1 Modified 3D printed components

The attachment of the bioprinting printheads to the x-carriage of the 3D printers was performed through 3D printed couplings. The x-carriage of all the 3D printers utilized had different dimensions and particularities, therefore a specific coupling had to be created to fit each case. Despite these differences, the way that printheads were attached to the couplings was the same for all of them. To that end, M3 inserts were placed inside the holes of the couplings and once the couplings were installed, the printheads were screwed to them using M3 screws. All the couplings here proposed are compatible with all the printheads presented in this thesis. Figure A.7 shows the couplings utilized for BCN3D+, Witbox 2 and Sigma printers when a single printhead was utilized.

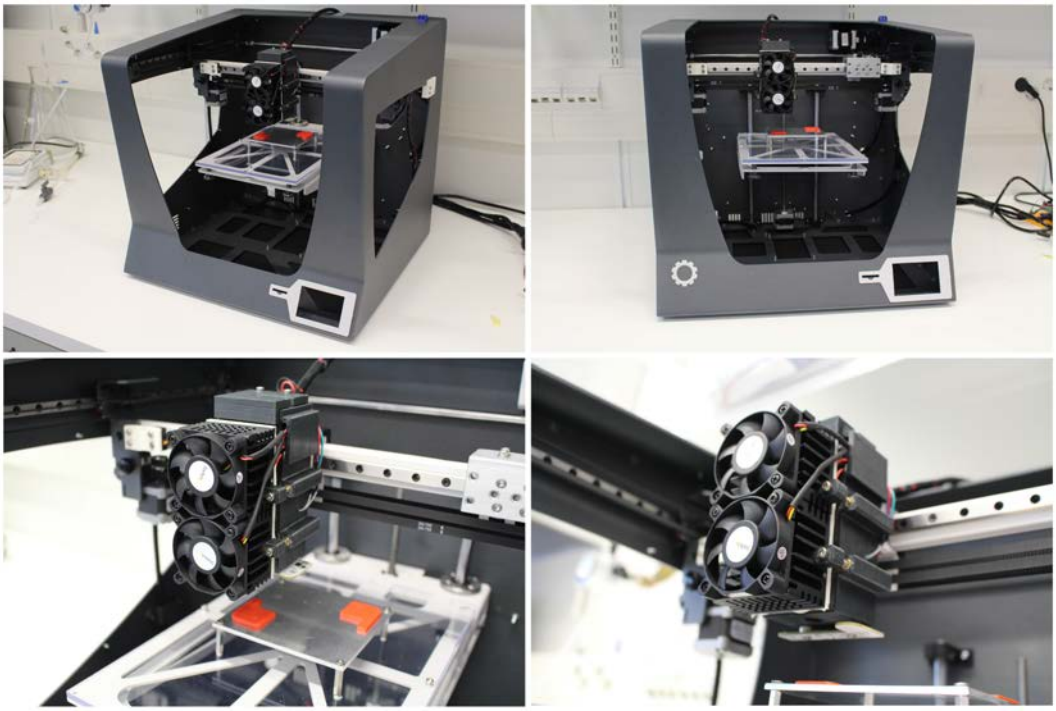

Figure 5.3: *PH printhead installed in Sigma 3D printer.*

Complex bioprinting applications require the deposition of more than one bioink in the same construct. As a result, additional couplings were designed to couple up to four printheads into the 3D printers x-carriage. In this case, only Witbox 2 and Sigma 3D printers were utilized for multi-material bioprinting. The coupling utilized for Witbox 2 printers was installed following the same procedure utilized in the single-printhead version (figure A.8). In the case of Sigma, the same coupling utilized for a single printhead was installed on its two independent x-carriages. Each coupling was able to hold two printheads at the

same time (one on each side), which permitted the use of four printheads in the same experiment.

As the x-carriages of the 3D printers were modified, so they did the location of the components that triggered the x-y endstops. Therefore, it was necessary to design new x-y endstop holders for Witbox 2 (figure A.9) and Sigma (figure A.10) 3D printers. These components were installed by simply screwing them into the 3D printer structure using the existing holes. No modifications of BCN3D+ were required in this case.

5.1.2 Bioprinters electronics

Open-source desktop 3D printers consist of a sort of common electromechanical components (i.e. stepper motors, temperature sensors, endstops, heaters) that can be driven using different electronics. As the RepRap project has been growing, several open-source electronics have been developed over the years. These electronics offer different capabilities and setups options, but always keeping the compatibility with the 3D printer's hardware and software utilized. Some of these electronics have been utilized in commercial desktop 3D printers (BCN3D+ uses a RAMPS 1.4) and other companies have decided to develop their own electronics (Sigma and Witbox 2). However, all of them are fully compatible with the standard RepRap-based electronics.

In this research, two RepRap-based electronics were installed in the three 3D printers utilized (BCN3D+, Sigma and Witbox 2) (table 5.1). The first electronic board utilized consisted of an Arduino microcontroller based on ATmega2560 (Mega 2560 rev3; Arduino) and a RepRap Arduino Mega Pololu Shield v1.4 (RAMPS 1.4; Ultimachine). The second electronic board was a RUMBA (RepRap Universal Mega Board with Allegro driver; RepRapDiscount). RAMPS 1.4 was utilized at the beginning of this research when only a single printhead was utilized in the experiments. As the research progressed, it was necessary to find an alternative board that permitted multi-material bioprinting, since RAMPS 1.4 did not allow to control more than one printhead at the same time. As a result, RAMPS 1.4 was replaced by RUMBA board, which permitted to control up to four printheads. Alternative open-source electronics as RAMBo (RepRap Arduino Mega-compatible mother Board), Megatronics or Smoothieboard are also fully compatible. For a complete list of compatible open-source electronics, the reader is referred to (RepRapElectronics, 2018).

Table 5.1: *Features of open-source electronic boards utilized.*

	License	Stepper motors	MOSFET outputs	Endstops	Thermistors
RAMPS 1.4	GPL	5	3	6	3
RUMBA	GPL	6	6	6	5

A representative scheme of RAMPS 1.4 and RUMBA main components and wiring diagrams utilized are depicted in figures 5.4 and 5.5. The printheads utilized required the use of two Peltier modules and one solenoid valve, both with an input power of 12 Vdc. The Peltiers and solenoid valves were connected to the PWM MOSFET outputs of the electronics, one output MOSFET for the two Peltiers and the other for the solenoid valve. When a single printhead configuration was utilized, MOSFET terminals D9-D10 for RAMPS 1.4 and HE0-FAN0 for RUMBA were used to connect the Peltiers and solenoid valve respectively. Both electronics were connected to a 12 Vdc/30 A power supply (MS-350-12; Hengwei Electric). Thermistors EPCOS 100K were utilized to monitor the temperatures of the printhead in the Al block (T0) and the heatsinks (T1). Three mechanical endstops (one for each x-y-z axis) were connected to the endstop board pins as detailed in the figures.

Table 5.2: *Printheads connections to RUMBA MOSFET outputs*

RUMBA MOSFET	Connected device
HE0	Printhead 1: Peltiers
HE1	Printhead 2: Peltiers
HE2	Printhead 3: Peltiers
FAN0	Printhead 1: solenoid valve
FAN1	Printhead 2: solenoid valve
HB-OUT	Printhead 4: Peltiers
Power expander 1	Printhead 3: solenoid valve
Power expander 2	Printhead 4: solenoid valve

If a multi-material bioprinting approach with four printheads is utilized, a total of eight MOSFET outputs are required for all the printheads. RAMPS 1.4 board only had three MOSFET outputs (D8; D9; D10), therefore it is only possible to connect one printhead. RUMBA electronics comes with six MOSFETs outputs (HE0; HE1; HE2; FAN0; FAN1; HB), three of them with voltage selector for MainPower/12V (HE2; FAN0; FAN1). The absence of the other two MOSFETs was solved adding two power expander boards (RepRap.me), which permitted the use of a fourth printhead. The power expanders were connected to the 3D printer 12 Vdc power supply and their output was controlled using a signal input, which was wired to the RUMBA EXP-3 unused pins (figure 5.6). When the signal input terminal received a voltage, the power expander supplied a

12 Vdc output to the connected device. If the voltage signal was switched off, the power expander 12 Vdc output was disconnected. Both power expanders were connected to solenoid valves and managed using the same G-code instructions detailed in section 5.2.2. The wiring of RUMBA MOSFETs and power expanders to the printheads components was performed according to table 5.2. Five thermistors EPCOS 100K were connected to the T0 (printhead 1), T1 (printhead 2), T2 (printhead 3), T3 (printhead 4) and THB (RT or printing platform) labeled pins. The x-y-z mechanical endstops were connected in the same manner as the single printhead approach.

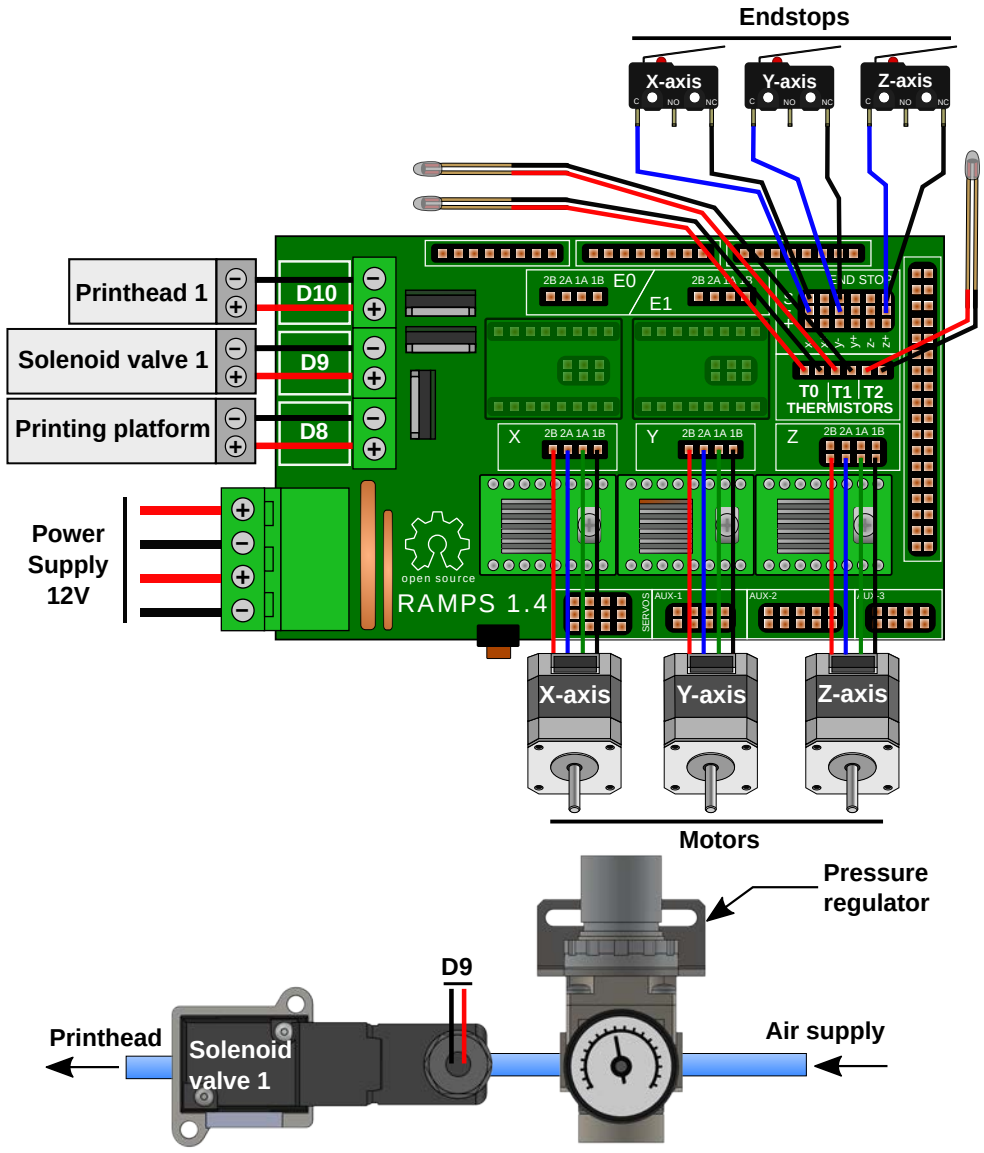

Figure 5.4: *Wiring diagram for a single printhead using RAMPS 1.4 open-source electronics.*

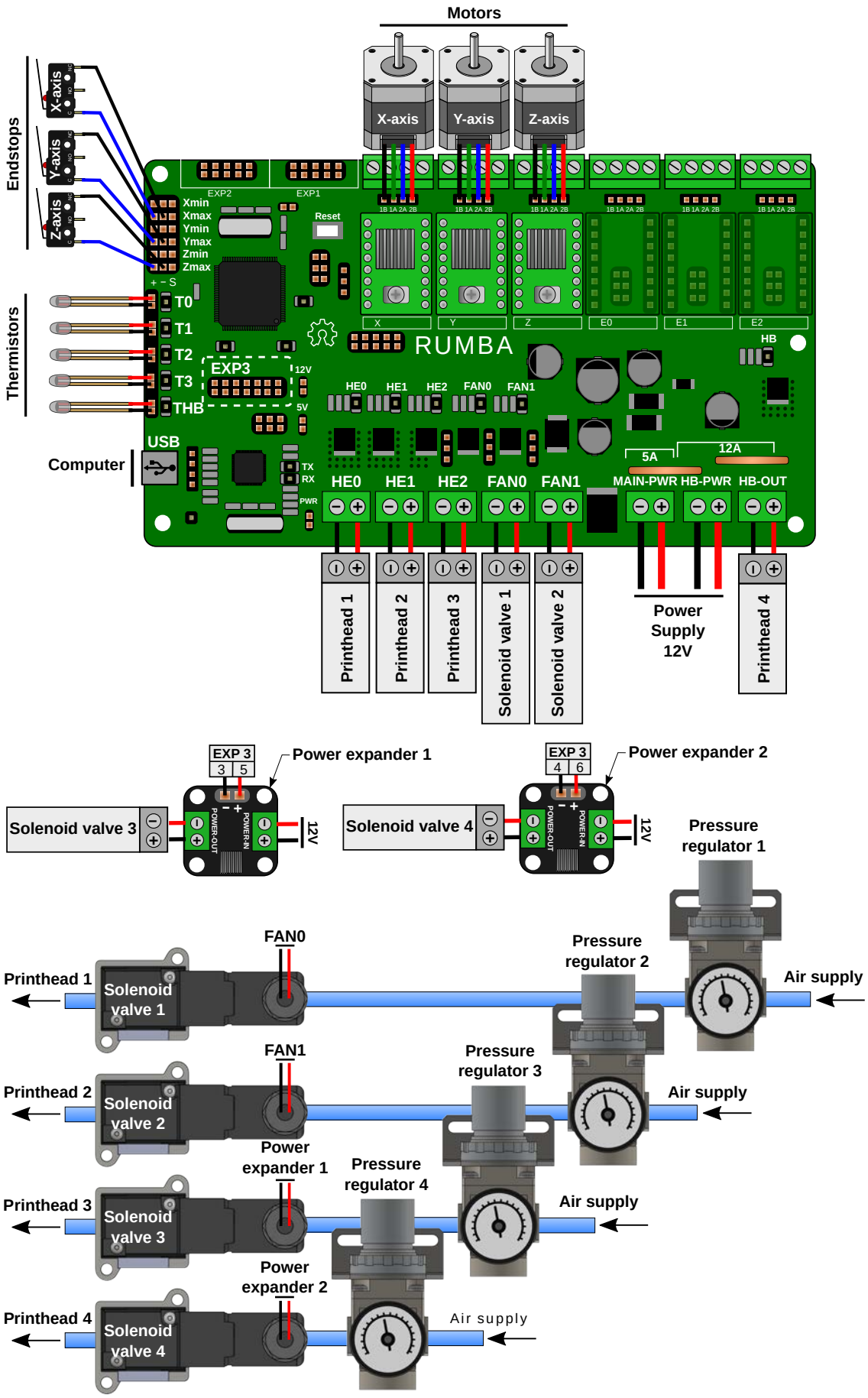

Figure 5.5: Wiring diagram for multi-material printing using RUMBA open-source electronics.

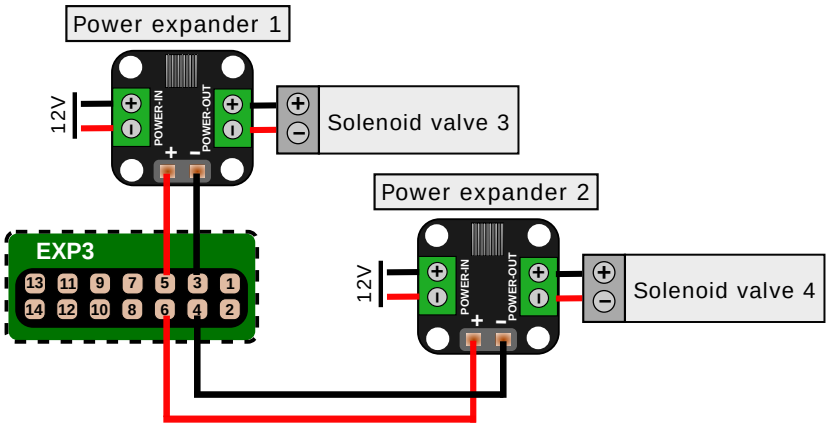

Figure 5.6: *Wiring diagram for the power expander modules utilized in RUMBA board and its connection to EXP3 pins.*

Standard nema 17 stepper motors (1.8º/step) were utilized in all the printers and connected to the x-y-z labeled pins (2B-2A-1A-1B for RAMPS and 1B-1A-2A-2B for RUMBA). A4988 stepper motor drivers were utilized in both electronics. The selection of the step size was performed using the jumpers (RAMPS) or dip switches (RUMBA) located under the driver boards (table 5.3). A 1/16 microstepping size was utilized for all the stepper motors. A4988 stepper drivers permit the adjustment of the current supplied to the stepper motors via a trimpot located in the upper part of the drivers. The current adjustment should be performed to prevent excessive heating of the motors and drivers. A clockwise rotation of the potentiometer increases the current supplied to the motors and a counterclockwise reduces it. A maximum current of 0.5 A was utilized and demonstrated to prevent any possible excessive heating, without affecting the smooth movements of the motors. Small Al heatsinks were glued to the motor drivers to enhance heat dissipation,.

Table 5.3: *Jumper and dip switch position for micro stepping selection in A4988 drivers*

Step size	**1**	**2**	**3**
Full step	0	0	0
1/2 step	1	0	0
1/4 step	0	1	0
1/8 step	1	1	0
1/16 step	1	1	1

5.1.3 Bioprinter pneumatic scheme

As explained in chapter 4, all the pneumatic EBB printheads proposed required a solenoid valve and a pressure regulator. The pneumatic scheme utilized for both single- and multi-material bioprinting is relatively simple and depicted in

figures 5.7 and 5.8. First of all, compressed air was supplied through a central compressor, which was transported through pipes to each laboratory. A first pressure regulator (LFR-D-Midi + LOE-D-Midi; Festo) was utilized to reduce the air pressure to a working value below 200 kPa. This pressure regulator permitted to set a safety margin calculated to avoid damage to the following devices since they work at lower operating pressures. Compressed air was later conducted to a second pressure regulator (ARP20K-N01BG-1Z/AR20-N01BG-RYZ; SMC), that was utilized to set the printing pressure of the printheads. This device permitted to set bioprinting pressures in a range between 5 to 200 kPa and allowed a maximum operating pressure of 700 kPa. Once the printing pressure was set, compressed air was conducted to a 3 port normally closed solenoid valve (VT307-6DZ1-01F-Q/EVT307-6D-02F-Q; SMC).

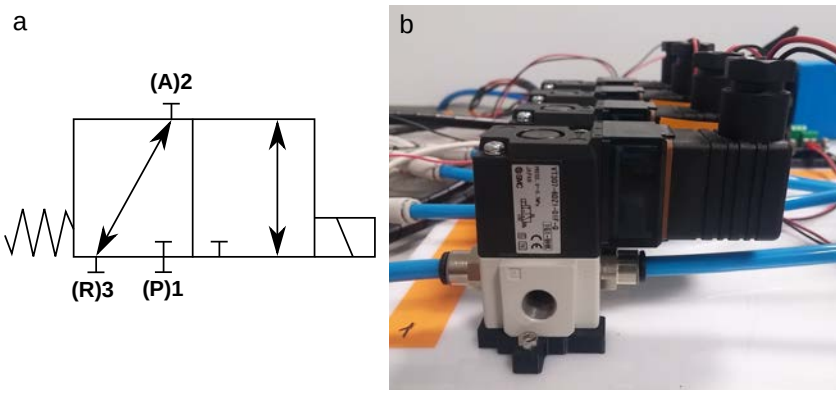

Figure 5.7: *Pneumatic scheme (a) and representative image (b) of the 3 port normally closed solenoid valve utilized.*

Solenoid valves were connected to the MOSFET outputs of the 3D printer electronics, converting the supplied constant air flow into a discontinuous flow via G-code commands. When the valve coil was not energized, the pressure port remained closed, preventing flow through the printhead and permitting the exhaust of the air inside the syringe. However, when the valve coil was energized, the pressure ports were connected and the airflow pushed the syringe piston. The solenoid valves utilized had an operating pressure between 0 to 700 kPa, a response time of 20 ms or less (at 500 kPa) and worked at a rated voltage of 12 Vdc. The last step in the pneumatic scheme was the connection of the syringe adapter tube to the solenoid valve output.

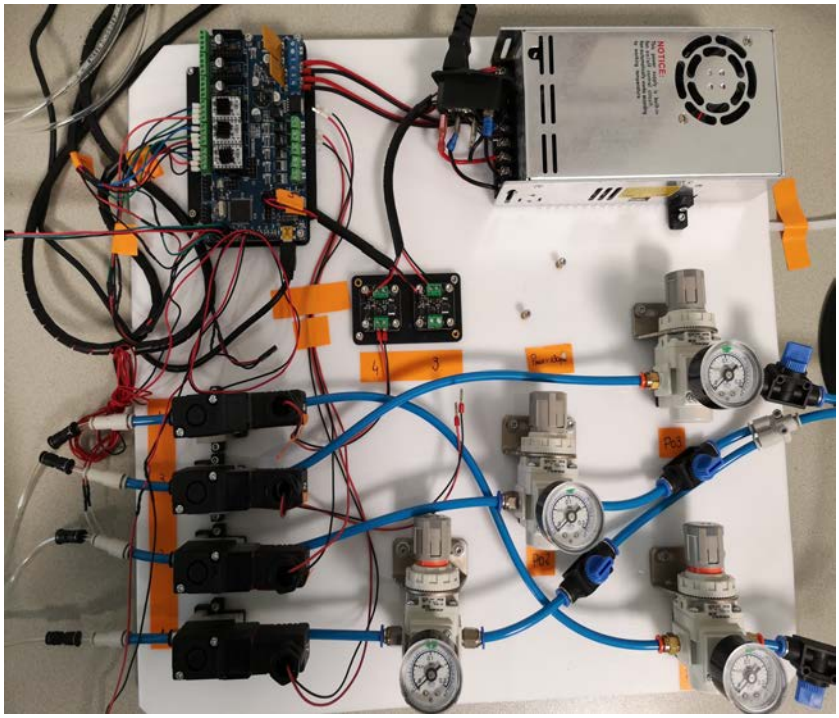

Figure 5.8: *Pneumatic installation utilized when four PH or PHR printheads were installed.*

5.2 Software

The software utilized to control the modified bioprinters and the bioprinting process was comprised of several tools (figure 5.9). First of all, a modification of Marlin firmware was uploaded into the 3D printers main board. The modified firmware permitted to manage and coordinate all the activities of the bioprinters, including, for example, the temperature of bioprinting printheads or 3D printer movements. A CAD software was utilized to create the 3D model to be printed and generate the STL files that will be subsequently sliced. In this research, FreeCAD and SolidWorks CAD tools were utilized to custom design the internal architecture and morphology of the bioprinted constructs. Once the STL files were obtained, they were introduced in the slicing software to generate the G-code file, which provides all the necessary instructions that tell the 3D printer what to do. Slic3r was utilized for G-code generation, however, this software is mainly utilized in FDM processes and is not able to manage pneumatic printheads. For that reason, custom Perl scripts were implemented to adapt the G-code generated to the specific requirements of each bioprinter. Bioprinters printheads moved according to these instructions, depositing biomaterials where it was required. Finally, the G-code was sent to the bioprinter using a host software, such as Repetier-Host, which is also in charge of monitoring the bioprinting process.

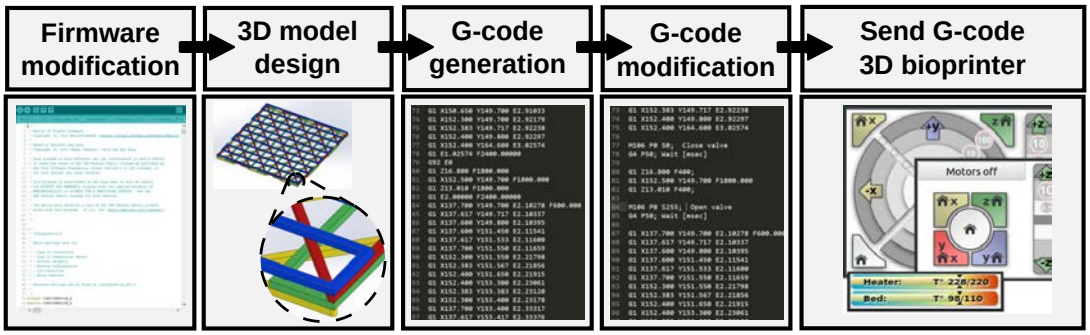

Figure 5.9: *Overall scheme of software utilized during all the bioprinting process.*

5.2.1 Firmware

In this research, a modification of Marlin firmware was utilized to control the modified 3D printers. Marlin is an open-source firmware developed by the RepRap community and distributed under a GPLv3 license. Despite its use is mainly focused on RepRap 3D printers, commercial 3D printers such as Ultimaker, Printrbot or BQ have implemented it in their electronics. Marlin firmware is loaded into the 3D printer main board and is in charge of controlling all the activities involved in the printing process. Some of these activities include the movement of the stepper motors, controlling sensors such as thermistors or endstops or managing printheads temperatures. One of the key aspects of Marlin firmware is that can be utilized in a large number of electronic boards which are based on AVR 8-bit microcontrollers. Those electronic boards are utilized in most of the open-source 3D printing platforms and are compatible with the Arduino environment. As a collaborative project, Marlin has evolved over the years with several modifications and upgrades, which permit to adapt it to a broad range of 3D printers. To date, this is a global project that is constantly changing, adding more features and possible applications into the open-source 3D printing community. Different versions of Marlin are available through its GitHub repository (Marlin, 2018).

As with RepRap 3D printers, Marlin configuration and capabilities are mainly focused on the FDM technology. This allows to control the main functionalities of a bioprinter, however, there are some specific features of the bioprinting printheads utilized that cannot be managed using the original firmware. Within these limitations, we can find the interaction with the pneumatic valves or the possibility to cool down the printheads using the Peltier modules, features that are not utilized in the FDM approach. Therefore, a modification of Marlin firmware (v1.1) was performed to enable the use of the printheads presented in this thesis. The modified firmware can be downloaded from the online repository

placed in GitHub (Sodupe, 2019). Among the main changes in the firmware code, are included the adjustments performed in the "Configuration.h" and "Configuration_adv.h" files, to adapt the firmware to the general specifications of each 3D printer (printer dimensions, steps/mm, simple heating/cooling settings, etc.). More complex changes were needed to enable the use of both cooling and heating modes in the printheads using Peltier modules. To facilitate the understanding of all Marlin changes performed, a brief description of these modifications and their functionality is detailed below:

- **Configuration.h:** the general adjustments of the 3D printer and electronic board utilized are modified within this file. The most important parameters to be adjusted are described below:
  - Select the electronic board connected to the 3D printer (i.e. #define MOTHERBOARD BOARD_RUMBA)
  - Define the number of printheads that are going to be utilized (i.e. #define EXTRUDERS 4)
  - Define the number and type of thermistors utilized (i.e. #define TEMP_SENSOR_#)
  - Change the minimum and maximum temperature of the printheads (i.e. #define HEATER_#_MINTEMP and #define HEATER_#_MAXTEMP)
  - Define the way that current is sent to the Peltier modules and heaters. In this case, Peltiers were controlled using bang-bang mode at full current (i.e. #define BANG_MAX 255). Therefore PID control was disabled commenting the line (i.e. //#define PIDTEMP)
  - Define the endstop settings utilized and how are connected to the electronic board (i.e. homing direction, travel limits after homing, etc.)
  - Adjust the motor steps per mm according to the 3D printer utilized (i.e. Witbox 2 (X, Y, Z, E): {80, 80 , 400, 105})
- **Configuration_adv.h:** this modification was only required for Sigma 3D printer to adjust the duplication mode.
- **pins_RUMBA.h:** this file was modified when four printheads were utilized at the same. As the original firmware only permitted to control the heaters of three printheads simultaneously, it was necessary to include and additional heater for the fourth printhead.
- **pins.h:** this modification was only required for Sigma 3D printer. In our bioprinting application, the stepper motors of extruders 0, 1, 2 and 3 are not utilized, as the bioinks are deposited using pneumatic pressure instead of a stepper motor. As Sigma utilizes two stepper motors in the x-carriage and Rumba electronics do not have a pins output for this configuration, the second x-carriage stepper was connected to the E02 stepper pins. The pins of the

steppers extruder not utilized were reassigned to a value not utilized (i.e. 40 (display LCD)).

- **Temperature.cpp:** traditional FDM 3D printers only require the heating of their printheads at high temperatures to melt the plastics deposited. Therefore, the original temperature control implemented in the firmware only includes a heating mode, as printing this kind of materials below RT is not possible. However, to manage printheads temperatures below and above RT, it was necessary to perform modifications in the code to permit both cooling and heating modes.
- **marlin_main.h, Conditionals_post.h and planner.cpp:** these files were modified to enable the control of a third and fourth fan, which were utilized for the control of the respective solenoid valves.

5.2.2 G-code generation

Marlin firmware utilizes a derivative of G-code programming language. Through G-code commands, it is possible to tell the 3D printers to make simple operations such as motors movement, set printhead temperatures or change the printing speed, among others. The conversion of a digital 3D model (through an STL file) into G-code instructions is performed using a slicing software. In this research, the slicer utilized was the open-source software Slic3r (v1.2.9) (Slic3r, 2018). As with Marlin firmware, Slic3r software has been designed to generate G-code files adapted to the FDM technology. This enables the use of all G-codes involved in the bioprinter movements and toolpaths generation, however, the operation of the printheads solenoid valves is not possible. Additional post-processing of the original G-code generated was performed via custom-made Perl scripts to adapt it to the particular characteristics of the printheads utilized. A complete list of all available G-code commands supported by Marlin firmware is available in (GCode, 2019).

Slic3r permits to load the 3D model and position it in the printing plater, assign the 3D model part to be printed by each printhead, and generate the printheads toolpaths. The customization of the multiple parameters involved in the bioprinting process requires the use of Slic3r "expert" operation mode (File -> Preferences -> Mode: Expert). Within this configuration, the software displays four general tabs (Plater, Print Settings, Filament Settings and Printer Settings) with several printing adjustments for each one. A more extensive documentation of Slic3r printing parameters can be found on its website (Slic3r, 2019). All Slic3r

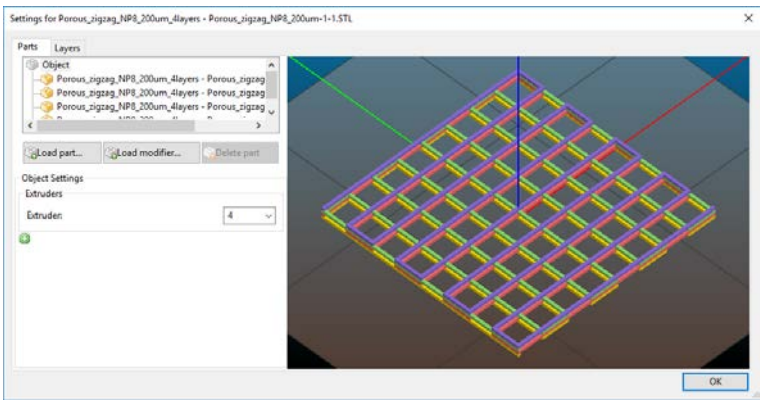

Figure 5.10: *Slic3r software: Plater tab. Porous structure with four layers stacked, each one assigned to a different printhead.*

configurations can be exported (File -> Export Config...) and loaded afterward (File –> Load Config...). The Slic3r configuration utilized in this research and the implications of each section on the G-code generated are outlined below:

1. **Plater**: permits to load the STL file to be printed, modify its position in the printing platform, increase the copies of the 3D model and scale it. If a single printhead approach is utilized, it will be necessary to load just one STL file. However, when multiple printheads are utilized, several STL files need to be loaded and assigned to a specific printhead. The assigning operation is performed using the "Settings..." button. Each STL file will be displayed in a list on the left-hand side of the window and assigned to the number of the extruder (printhead) to be used. When several extruders are assigned, the 3D model visualization will appear with a different color for each printhead (figure 5.10).
2. **Print Settings**: this tab is subdivided into nine additional sections.
   a) **Layers and perimeters**
      i. **Layer height:** as all the AM technologies are based on a layer-by-layer approach, the layer height represents the printing resolution along the z-axis. A lower layer height will result in more accurate prints, but longer printing times. To obtain an optimal deposition rate, the layers heights utilized were mainly equal to the ID of the nozzle.
      ii. **First layer height:** the distance from the nozzle tip to the printing platform in the first layer results of vital importance in the whole printing process to avoid deposition problems. If the nozzle is too far from the platform, the bioprinted construct will not properly adhere and the subsequent layers will not be deposited properly (figure 5.11a). On the other hand, if the tip is too close to the platform,

it might lead to a clogging of the nozzle (figure 5.11c). Despite this adjustment can be performed using the "First layer height" option, the first layer height was calibrated using the "Z-offset" and this value was set to the same layer height utilized in the previous option.

iii. **Perimeters:** all the printed constructs have utilized just one perimeter.

b) **Infill:** density for the internal infill.

c) **Skirt and brim:** skirt and brim options were disabled.

d) **Support material:** support material can be printed when 3D models have overhanging parts, however support structures were not needed for the constructs printed in this research.

e) **Speed:** it is possible to specify the speed for printing movements (depending on the material utilized) and the speed for travel moves.

f) **Multiple extruders:** these parameters were left as default.

g) **Advanced:** all parameters were set to 0 mm, except the number of threads that was set to 2.

h) **Output options:** in this section it is located the path to the post-processing script utilized to customize the G-code (see appendix B). Each time a new G-code is generated using Slic3r, the post-processing script is executed and the original G-code file is modified. Two G-code files will be generated with the following extensions:

i. *.gcode: post-processed G-code that is going to be utilized.

ii. *.gcode.before_postproc: original G-code without post-processing (not utilized).

i) **Notes:** not utilized.

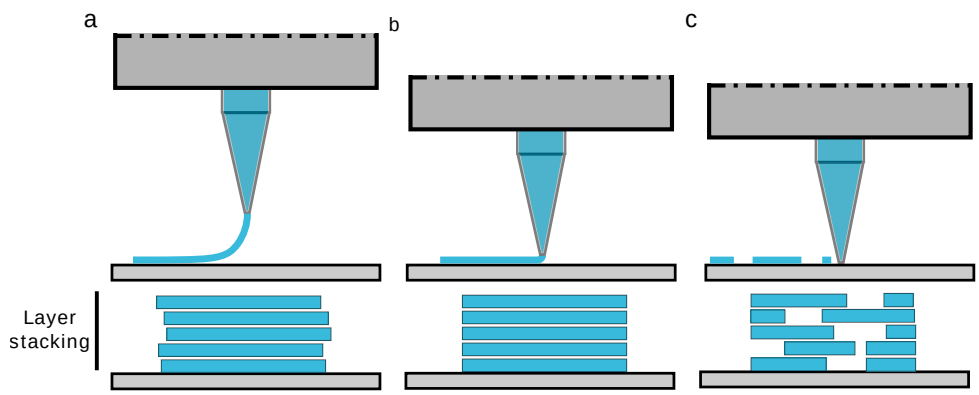

Figure 5.11: *Differences in first layer calibration. (a) Nozzle too far from printing platform. (b) Correct first layer. (c) Nozzle too close to printing platform.*

3. **Filament Settings**: this tab is subdivided in "Filament" and "Cooling" sections. Usually, those options are used when a FDM printing approach is utilized. In this case, neither a filament printing material or cooling fans were

utilized. Therefore, the filament section was left as default and cooling options were disabled.

4. **Printer Settings**: this tab is subdivided in three sections. If more than one extruder is utilized, an additional section will be displayed for each new extruder.
   a) **General**
      i. **Bed shape:** the bed size and origin are crucial parameters that need to be adjusted for each printer dimensions and printing platform. This configuration results especially important if small components, such as glass slides or Petri dishes are going to be utilized as a printing base and the printed construct must be adjusted to their dimensions. Slic3r place the STL files in the center of the printing platform by default. Therefore, it will be necessary to calculate the center of the printing platform and then introduce these values in the x-y coordinates.
      ii. **Z-offset:** this option is utilized to compensate the distance from the nozzle tip to the printing platform once the Z-homing has been performed. The value here introduced will be added or subtracted from all the G-code Z-coordinates in all G-code file generated. For example, if the first layer is printed with the nozzle tip placed too far from the printing platform, the material will not adhere properly. In this case, a negative value will be introduced in the Z-offset to compensate this distance. Alternatively, if the nozzle is placed to close to the printing bed, a positive Z-offset will be set. If multiple printheads are utilized, Slic3r only offers the possibility to manage different x-y offsets between printheads. Therefore, it is not possible to compensate the misalignments in z-axis when multiple printheads are utilized. This situation might occur if nozzles with varying lengths are utilized, for example, tapered and straight nozzles do not always have the same lengths (figure 5.12). This limitation was solved with the push-button proposed in chapter 7, which permitted to compensate the height differences of all the printheads respect to the first printhead (P0) automatically.
      iii. **Extruders:** this parameter permits to select the number of extruders (printheads) that are going to be utilized.
5. **Custom G-code:** this section permits the user to write additional G-code commands at the beginning/end of the original G-code instructions, and before/after a layer change . Additional G-code commands were added in the "Start G-code" section to select the units lengths to mm (G21), use absolute coordinates (G90) and set the default acceleration (M204 S250).

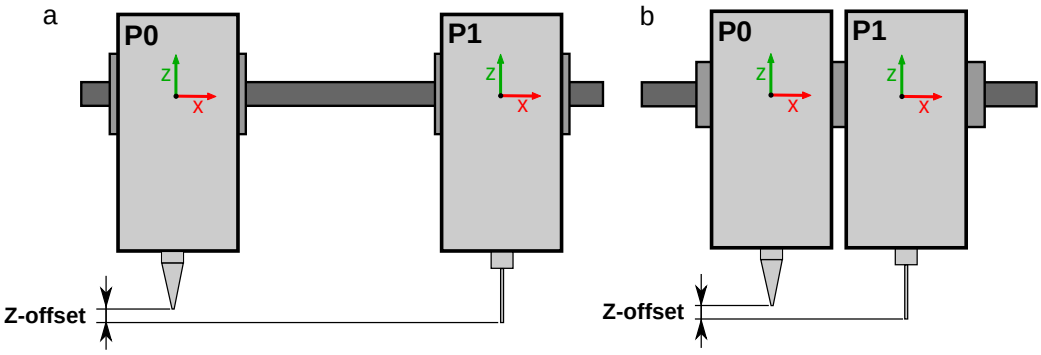

Figure 5.12: *Schematic representation of Z-offsets offsets in Sigma (a) and Witbox 2 (b) printheads.*

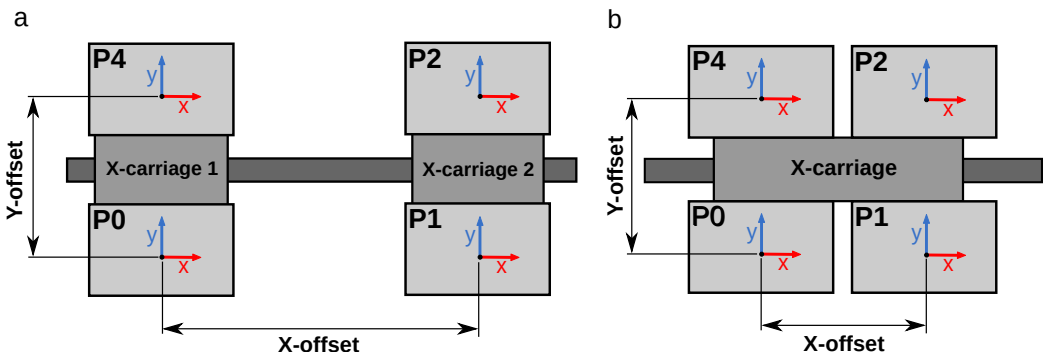

Figure 5.13: *Schematic representation of x-y offsets in Sigma (a) and Witbox 2 (b) printheads.*

a) **Extruder #:** these parameters can be independently modified for each printhead.

   i. **Nozzle diameter:** value of the ID of the nozzle utilized.

   ii. **Extruder offset:** when multiple printheads are utilized, this option permits to introduce the x-y offset coordinates of each printhead respect to the first one. The offset coordinates of the first extruder (printhead 1) are set to x=0 and y=0. Depending on the printer and printheads utilized, the offset coordinates will be different. For example, Witbox 2 3D printer had their four printheads installed in the same x-carriage, therefore the x-y offsets were configured according to figure 5.13b. Sigma 3D printer had two independent x-carriages, therefore the x-offset should be calculated as the distance between both carriages (figure 5.13a).

   iii. **Retraction:** retraction length and speed should be fixed to 2mm and 40 mm s^{-1} respectively, as these values are utilized in the post-processing G-code script. The "Lift Z" value should be between 1-4 mm to prevent the nozzles from touching the already deposited material.

The post-processing of the G-code generated is performed automatically by Slic3r when the G-code is exported. The post-processing script utilized was written in Perl and is detailed in appendix B. One of the main objectives of the script is to determine when the printheads should deposit bioinks. This operation was performed opening and closing the solenoid valve connected to each printhead. The G-code M106 was utilized to control the opening and closing of the valves. Solenoid valve selection was performed using the P_ command parameter (P0: solenoid valve 1; P1: solenoid valve 2; P2: solenoid valve 3; P4: solenoid valve 4). The S_ command parameter is responsible for sending the voltage to the solenoid valve, being S255 the maximum voltage (open valve) and S0 the minimum (close valve). Once the solenoid valve is opened and the pressurized air starts to push the syringe piston, there is not an instant extrusion of bioink through the nozzle because of the delay of the compressed gas volume. Therefore, it is necessary to wait a certain time until the bioink reaches the tip of the nozzle and then start moving the printhead. This waiting time was configured using the G4 command line and the P_ command parameter with the time in milliseconds. The waiting time was predefined as a constant in the Perl script (time_open). A different waiting time constant (time_closed) was utilized when the solenoid valve was closed. An example of the opening and closing G-code utilized would be as follows:

Listing 5.1: *G-code example of opening and closing of solenoid valve*

```
...
M106 P0 S255; Open solenoid valve of printhead 1
G4 P200; Wait 200 milliseconds
...
Move printhead
...
M106 P0 S0; Close solenoid valve of printhead 1
G4 P50; Wait 50 milliseconds
...
```

Additional code has been added to clean some of the G-code commands that are not utilized. For example, commands M104 (set extruder temperature) and M109 (set bed temperature and wait) were deleted in the code as printheads temperatures were set manually using Repetier-Host.

5.2.3 3D printer host software and bioprinting process

All the parameters involved during the bioprinting process were controlled using freely available software Repetier-Host (v1.6.2) (Repetier-Host, 2018). Among the main features of this software, it permits to set and monitor the printheads

temperatures, perform a manual control of the 3D printer movements and send the G-code commands to the printer. The sequence of all steps involved in the bioprinting process, from the generation of the G-code to the deposition of bioinks, is depicted in figure 5.14 and described as follows:

1. Open Repetier-Host.
2. Connect the 3D printer to the computer (via USB port).
3. Perform homing in x-y-z axes. The homing process can be performed using G28 command or using homing buttons placed in Repetier-Host control panel. Once the homing procedure is finished, it will not be necessary to perform any additional homing unless the 3D printer is disconnected.
4. Set printhead temperatures to the printing temperatures using Repetier-Host control panel.
5. Open Slic3r and load the bioprinting configuration for the specific bioprinter that is going to be utilized (File –>Load Config. . .).
6. Open the "Print settings" tab and within the "Output options" section, select the path of the Perl script that performs the post-processing.
7. Select the "Plater" tab and "Add..." the .STL file that is going to be printed.
8. Make the printing adjustments required for the generation of the G-code. Each STL file, printing material and printhead configuration is different, therefore it is not possible to make general adjustment valid for all cases. Some of the most common adjustments to be performed in Slic3r are described below:
   a) Layer height (Print settings –> Layers and perimeters)
   b) Speed (Print settings –> Speed)
   c) Z-offset (Printer settings –> General)
   d) # Extruders (Printer settings –> General)
   e) Nozzle diameter (Printer settings –> Extruder #)
   f) Lift Z (Printer settings –> Extruder #)
9. Export the G-code and save it in a folder. Two G-code files will be generated with the name of the STL file and different extension: *.gcode and *.gcode.before_postproc.
10. Open the *.gcode file using a text editor (i.e. SublimeText), select all the code and copy it.
11. Paste the G-code in Repetier-Host (G-code -> Edit G-code).
12. Load the material to be printed into the printheads.
13. Adjust the printing pressure using the pressure regulators.
14. Send the G-code to the printer.

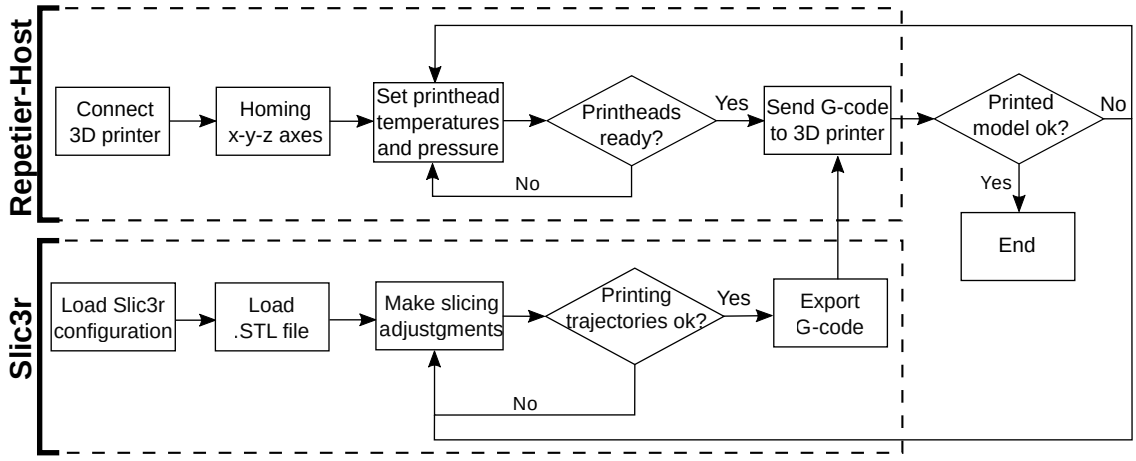

Figure 5.14: *Flowchart for the generation of G-code and the interaction with the 3D printer.*

5.3 Conclusions

This chapter presents a detailed description of all the steps required to transform a conventional desktop 3D printer into a 3D bioprinter. Specific hardware and software modifications were performed to cover all the stages of a bioprinting process. Hardware components of three open-source 3D printers (BCN3D+, Witbox 2 and Sigma) were modified to allow the use of EBB printheads. The original 3D printers electronics were replaced by standard open-source RepRap electronics such as RAMPS and RUMBA, enhancing the replicability of these experiments. Besides, the detailed descriptions of the electronic wiring diagrams and the pneumatic scheme provided facilitate the adoption of this research even by novel users.

Regarding 3D printers software, a modification of Marlin firmware was required to adapt it to the particular functionalities of EBB printheads. In the same line, a custom post-processing Perl script was developed and utilized in conjunction with Slic3r to generate the bioprinting G-codes from STL files automatically. Slic3r permitted to tune all the parameters involved in the bioprinting process and the post-processing script performed all the adjustments required to use the pneumatic-driven EBB printheads. All the software here utilized and the specific modifications performed for this research are freely available to all users through online repositories. This approach allows to enhance the collective knowledge about bioprinting and expand its use through the scientific community.

Chapter 6

Methodology to determine the accuracy and performance of bioprinting platforms

During EBB, 3D printed constructs are subjected to errors during the deposition process which might compromise their final resolution and structural integrity. The reasons that explain these errors can be many and varied, for example, an uneven layer stacking, an incorrect control of bioink extrusion conditions or even a bad calibration of the 3D printer axes. When a new bioprinter or printhead is developed, it is necessary to determine the degree of deposition accuracy that can be achieved to know the limitations and capabilities of each bioprinting system. Besides, these methodologies also permit to carry out useful comparisons between different bioprinting platforms. Several efforts have been made in the 3D printing field to evaluate the dimensional accuracy and reproducibility of each printing system. These studies are often based on the use of comparative models or benchmarking studies (Mahesh *et al.*, 2006; Roberson *et al.*, 2013). Characterization of printer performance is obtained measuring the dimensional accuracy and reproducibility in the x-y plane and z-axis, as well as evaluating the ability to produce geometries such as thin walls or circular shapes (Sanchez *et al.*, 2014). Most of the benchmark studies measure the dimensional printing accuracy of calibration models consisting of simple geometries as squares or circles (Scaravetti *et al.*, 2008).

In this chapter, it is presented a methodology that can be utilized to measure the dimensional accuracy of any bioprinter. Bioprinting resolutions and capabilities of the three open-source 3D printers were obtained using the PH printhead presented in chapter 4, but can be extrapolated to PHR as the working principle is the same. Results obtained permitted to compare the accuracy of each

bioprinting platform in the generation of 3D models with different characteristic features. Besides, by using three different 3D printers, it was demonstrated the versatility of the printhead proposed and its capacity to be utilized as a universal bioprinting tool.

6.1 Standard calibration models design and printing

To determine the accuracy and versatility of the printheads presented, they were installed in three open-source 3D printers (Witbox 2, BCN3D+ and Sigma). Poloxamer 407 (P407) was selected as the material to perform this evaluation. P407, which rheological properties can be found elsewhere (Kolesky *et al.*, 2014), is a synthetic polymer with stable viscosity values above 15 ºC and very low post-printing swelling (Müller *et al.*, 2015). These properties make P407 being particularly appropriate when trying to determine the dimensional errors of printed constructs.

Six calibration models were designed to identify and quantify the accuracy during the bioprinting process with the printhead proposed. 3D models were designed using the modeling software SolidWorks (Dassault Systems) and exported as stereolithography (STL) files. Open-source ImageJ software was used to obtain geometrical measurements of printed parts (chapter 3). A detailed description and justification of the calibration models is provided as follows:

1. **Concentric squares** (based on (Sanchez *et al.*, 2014)): four concentric empty squares of sides 5, 8, 11 and 14 mm were printed varying the number of layers stacked (1, 2, 4, 8, 16 layers). Squares were aligned with the xy-axes (figure 6.1a). Square sides in x-y directions were measured separately and compared with the computational model to detect possible misalignments and instabilities on the printer.
2. **Concentric circles** (based on (Polzin *et al.*, 2013)): concentric empty circles of diameters 5, 8, 11 and 14 mm were printed varying the number of layers stacked (1, 2, 4, 8, 16 layers). Circles involved xy-axes movements at the same time (figure 6.1b). The diameter of all circles was measured and compared to the model diameter.
3. **Multilayer lattice structures** (based on (Chung *et al.*, 2013)): pore size (P), strand diameter (D) and strand spacing (SS) were measured varying the number of layers stacked (2, 4, 8, 16 layers) (figure 6.6). Predefined values of P=1.3mm, D=0.2mm and SS=1.5mm were used (figure 6.1c).

4. **Straight filaments** (based on (Kang *et al.*, 2013)): 30 mm long straight filaments with different strand widths were printed aligned with the y-axis using the same tapered nozzle, but varying the deposition speed from 5 to 16.6 m s^{-1} (figure 6.1e).
5. **Vertical pillars** (based on (Hansen *et al.*, 2009)): vertical pillars allow a better interconnection of vascular networks beyond the horizontal plane. Pillars were printed without stacking layers, maintaining the x-y coordinates, while moving in the z-axis until the desired pillar height was reached. Printing parameters, such as pressure and deposition speed (0.83 to 4.16 mm s^{-1}), were adjusted to withstand their vertical shape and avoid the collapse. Stability was evaluated varying pillar height from 2 to 10 mm (figure 6.1d).
6. **Hierarchical networks of filaments with varying diameter** (based on (Kolesky *et al.*, 2014)): the printed model simulates a hierarchical vascular network. The connected network of curved filaments was printed in four different sections with the same nozzle size at different speeds (figure 6.1f) to change the printed diameter.

The six calibration models proposed were printed using 40 wt% poloxamer P407 on a 25.4x76.2x1 mm glass slide. P407 was loaded into the syringe barrels at 4 ºC and printed using a temperature and pressure of 22 ºC and 124 kPa respectively. Calibration models 1 and 2 were designed to be printed using thin walls. To obtain a homogeneous layer stacking, parameters as printing speed and layer height need to be properly adjusted (Müller *et al.*, 2013). To obtain optimal printing results, the deposition speed for the calibration models 1, 2 and 3 was initially adjusted to 15 mm $s^{-1}$and a layer height of 200 μm. The straight filaments were printed in a range of deposition speeds from 5 to 16.6 mm s^{-1}. The vertical pillars have heights ranging from 2 to 10 mm and were generated varying the vertical speed from 4.16 to 0.83 mm s^{-1}. Finally, the hierarchical network was printed varying the printing speed on each section: S1: 2.5 mm s^{-1}; S2: 5 mm s^{-1}; S3: 8.3 mm s^{-1}; S4: 15 mm s^{-1}. The same tapered nozzle (27G; ID: 200 μm; Nordson EFD) was utilized in all cases.

The printing resolution was evaluated with the six calibration models. In the case of concentric squares, circles and multilayer lattice structures, the printed resolution was computed as the difference between the geometrical dimensions of the printed model and the theoretical values of the virtual model for 1, 2, 4, 8, and 16 layers (equation 6.1):

$$Deviation\ error = dimension_{MEASURED} - dimension_{STL} \tag{6.1}$$

The dimensional error in concentric squares models enables the evaluation of the linear accuracy in the x-axis and y-axis independently. The printing resolution in circular calibration models was evaluated for the x-y axes by measuring the combined axes accuracy. Pore size, strand diameter, and strand spacing were the main quantitative parameters to define the printing quality of the lattice models. Straightness of printed pillars at different heights was categorized as stable when no bending was observed, unstable if the pillar bent to one side and collapsed if the pillar bent completely touching the glass slide. Six samples were printed per calibration model (n=6), and each feature was measured six times per sample using open-source ImageJ software (Rasband, 2018).

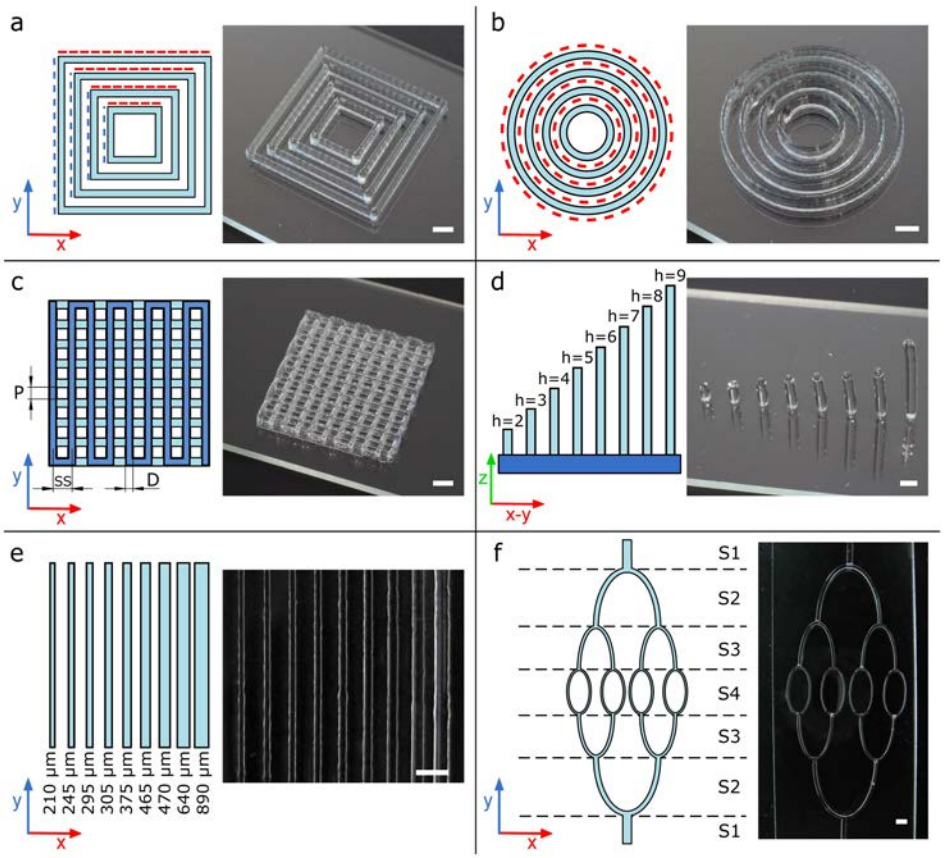

Figure 6.1: *Schematic illustrations and optical images of the 3D calibration models printed to evaluate the printing resolution. (a) Concentric squares with varying sides of 14, 11, 8 and 5 mm aligned with x-y printer axes. (b) Concentric circles with varying diameters of 14, 11, 8 and 5 mm. (c) Porous structure, parameters measured pore size (P), strand diameter (D) and strand spacing (SS). (d) Vertical pillars printed at different heights. (e) Straight filaments of different diameter by varying the deposition speeds. (f) Vascular network with channels of different diameters. Scale bars: 2 mm.*

6.2 Determination of print resolution through calibration models

6.2.1 Concentric squares

Dimensional errors obtained from the squares calibration model were compared between x and y printing axes of each printer. Other parameters, such as the number of layers stacked, the square size and the type of 3D printer utilized were also considered (figure 6.2). It was observed a decrease in the x-y axes accuracy when the number of layers stacked was increased. This behavior was noticed in all the 3D printers used, as well as in all square sizes printed. However, it was more evident for the BCN3D+. Results revealed that Witbox 2 had better accuracy in both axes than BCN3D+ and Sigma, regardless of the number of layers stacked and the square size.

Printing square calibration models of 16 layers was a challenging task. Witbox 2 was the only system capable of creating constructs with sufficient quality. In general, regardless of the number of layers stacked and the square size, Witbox 2 was the only bioprinter with errors between 41 to 204 μm. Nonetheless, there were no statistically significant differences with Sigma printer, which obtained values between 98 to 263 μm in all the conditions. Sigma and BCN3D+ were unable to print any of the squares programmed with 16 layers (figure 6.2e). In BCN3D+, squares with a 14 mm side were impossible to measure in y-axis for 8 layers stacked due to great deformations of the printed samples (figure 6.2d).

The differences between x-axis and y-axis in BCN3D+ were clear, with statistical differences for all the squares sides between both axes and always greater than 100 μm (figure 6.2). These differences increased with the square side and the number of layers stacked, reaching a maximum value of 328 μm for 8 layers and 8 mm square side. On the contrary, Witbox 2 and Sigma printers did not present any significant difference between the x-axis and the y-axis, resulting in a balanced printing accuracy between both directions. The differences between x-y axes can be explained by the working principle and structure of both printers. While Witbox 2 and Sigma printhead moves in the x-y plane and the printed construct only moves a layer height (figure 6.4b), BCN3D+ printed constructs are continuously moving in the y-direction along with the printing platform (figure 6.4a).

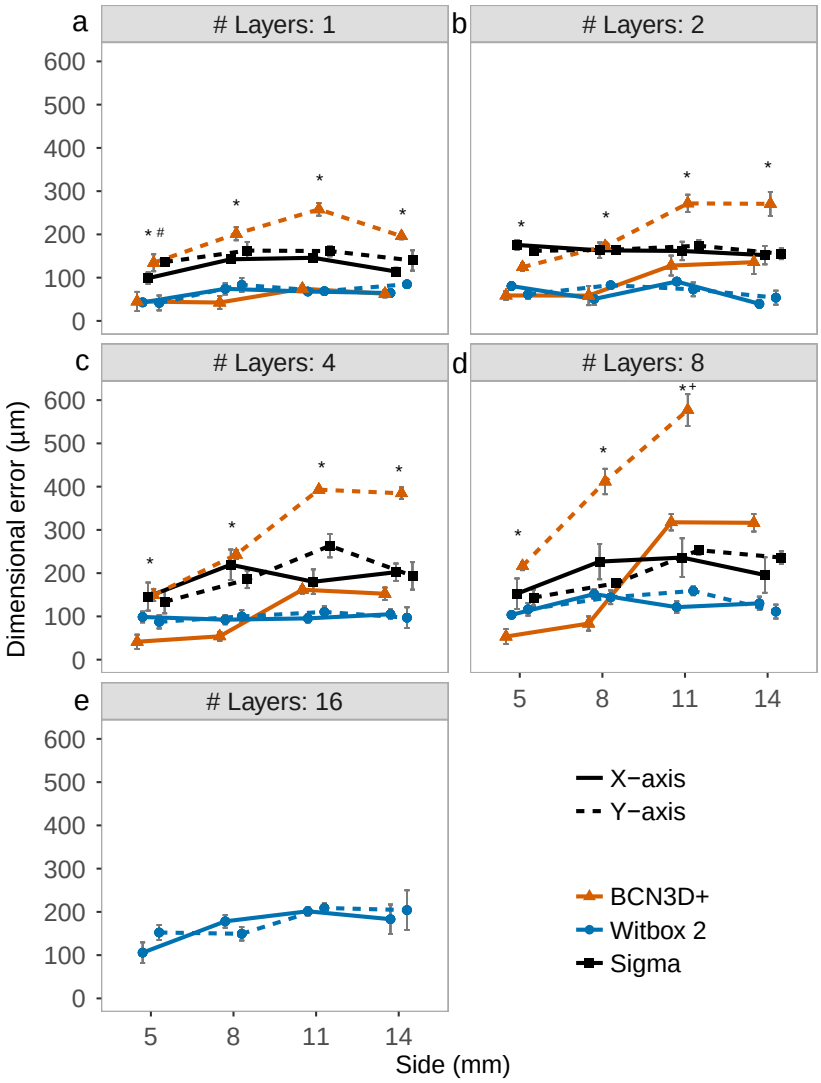

Figure 6.2: *Dimensional errors obtained from squares calibration model printed in P407 at 40 wt% with 1 (a), 2 (b), 4 (c), 8 (d) and 16 (e) layers stacked using three different 3D printers. Asterisk symbol (*) indicate statistical significance between x-y axes of BCN3D+ (p <0.01), cross symbol (+) indicate statistical significance between x-y axes of Witbox 2 (p <0.01) and hash symbol (#) indicate statistical significance between x-y axes of Sigma (p <0.01). The data represent mean and s.e.m. of six different samples (n=6).*

It can be concluded that differences in how 3D printer axes move strongly affect the final accuracy of the printed constructs. Printers with a moving platform in the z-axis are preferred because instabilities during the printing process are reduced. Besides, the better performance of Sigma and Witbox 2 printers respect to BCN3D+ can be due to the fact that the former are sold already assembled and the latter is sold as a kit and has to be assembled by the user. Small imperfections during the assembling process might lead to an increase in the printing tolerances and a thorough review of printer mechanics should be done to ensure a good performance (Kelly, 2013). As a result, some minimum

requirements, such as z-axis moving platform and structural stability, are needed to modify an open-source printer for bioprinting purposes and assure an adequate bioprinting accuracy.

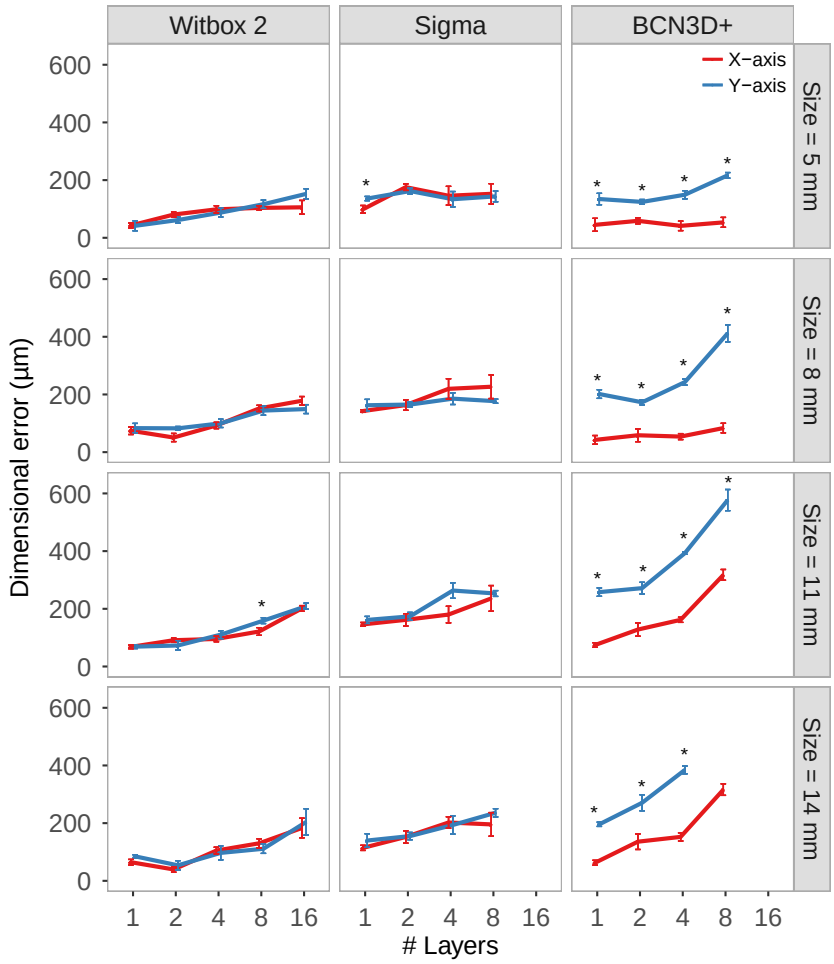

Figure 6.3: *Dimensional errors obtained from squares calibration model printed in P407 at 40 wt%. Differences between x-y axes for each of the 3D printers utilized. Asterisk symbol (*) indicate statistical significance between x-y axes of each 3D printer (p <0.01). The data represent mean and s.e.m. of six different samples (n=6).*

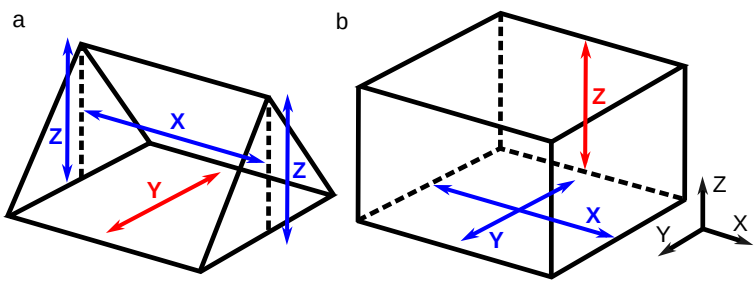

Figure 6.4: *Graphical representation of 3D printers movements in (a) BCN3D+ and (b) Witbox 2 and Sigma. The printing movements of the printhead are colored in blue and the printing platform is colored in red.*

6.2.2 Concentric circles

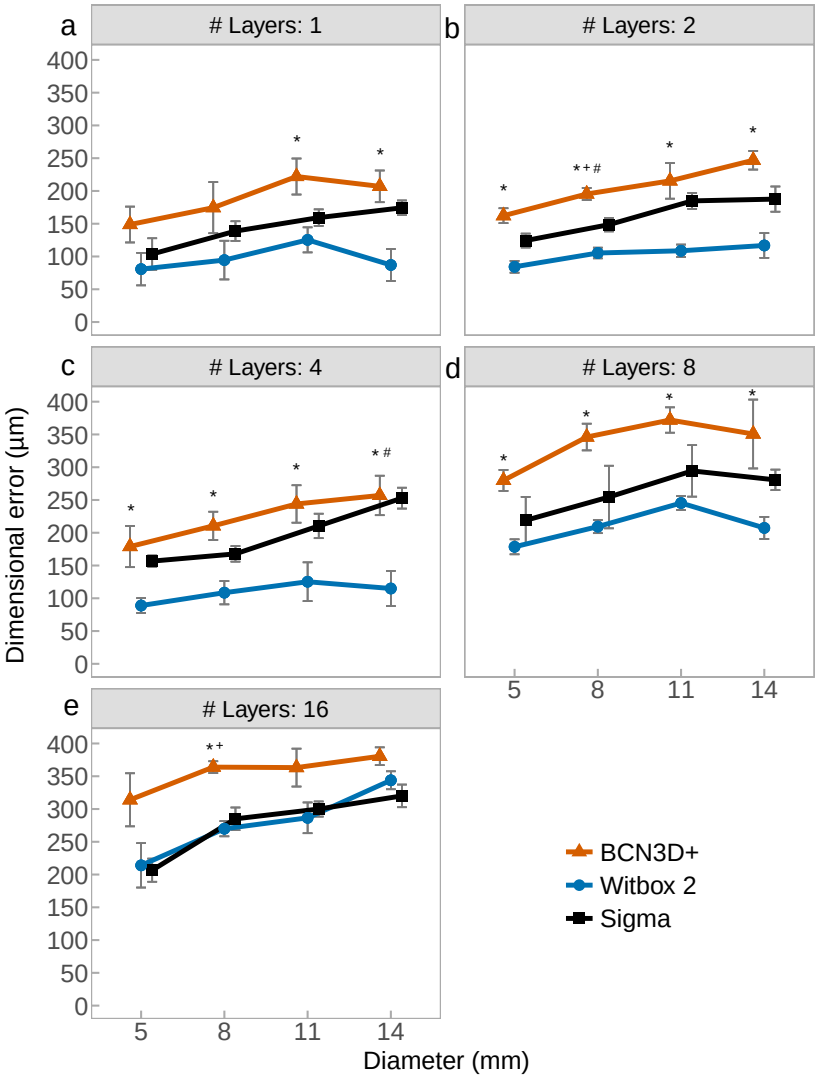

Figure 6.5: *Dimensional errors obtained from circles calibration model printed in P407 at 40 wt% with 1 (a), 2 (b), 4 (c), 8 (d) and 16 (e) layers stacked using three different 3D printers. Asterisk symbol (*) indicate statistical significance between BCN3D+ and Witbox 2 (p <0.01). Cross symbol (+) indicate statistical significance between BCN3D+ and Sigma. Hash symbol (#) indicate statistical significance between Sigma and BCN3D+ (p <0.01). The data represent the mean and s.e.m. of six different samples (n=6).*

Circular, cylindrical, and semi-spherical models can be used to evaluate the print resolution of the installed printhead during the simultaneous movement in both xy-axes. The second calibration model (figure 6.1b) consisted of four concentric circles with a varying number of layers. Once again, the errors obtained with the BCN3D+ were always larger than that of other bioprinters (figure 6.5). Witbox 2 was again the most accurate bioprinter with errors ranging from 80 to 343 µm, but differences with Sigma were not statistically significant. In contrast to the

previous model of concentric squares, the bioprinters were capable of creating cylindrical models with 16 layers.

6.2.3 Multilayer lattice structure

Multilayer lattice structures are the most common 3D models bioprinted for TE applications (figure 6.1c). Pore size and strand diameter are the primary control variables to assure proper structural stability and high porosity, which is essential for long-term cell cultures and excellent cell viability (figure 6.6). Concerning both variables, Witbox 2 and Sigma bioprinters showed a similar performance (figure 6.7) and in both cases significantly better than that of BCN3D+. The maximum error in pore size with the Witbox 2 (39±8 μm) was almost three times lower than that of BCN3D+ (111±8 μm). The weak performance of our printhead installed in the BCN3D+ is particularly significant when printing more than two layers, showing a clear limitation of the BCN3D+ to the creation of 3D patterns. The errors in the strand spacing did not differ so much between the three MEBB systems. The performance of the BCN3D+ showed a significant decrease when printing lattice structures of 16 layers (figure 6.7).

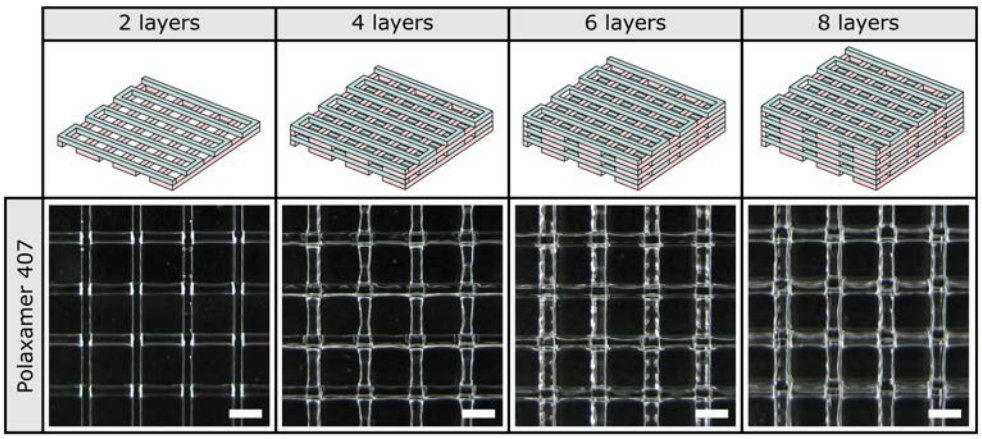

Figure 6.6: *Printed lattice structures with multiple layers using Witbox 2. Schematic representation of the 3D models (top row) and images of printed lattice structures using 40% P407. Scale bars: 1 mm.*

6.2.4 Straight filaments

A set of parallel straight filaments with different widths was another calibration model printed at constant pressure and varying y-axis deposition speeds from 5 to 16.6 mm s^{-1} (figure 6.1e). 3D printed models showing discontinuous filaments were initially discarded. The similar values obtained (figure 6.8b) for the three

3D printers indicates that these results were not dictated by the mechanics of the printer. The printhead worked well in all the bioprinters at low deposition speeds generating threads of widths around 600 µm. The smallest values obtained at the maximum deposition rate were slightly above 210 µm, independently of the printer selected (figure 6.8b).

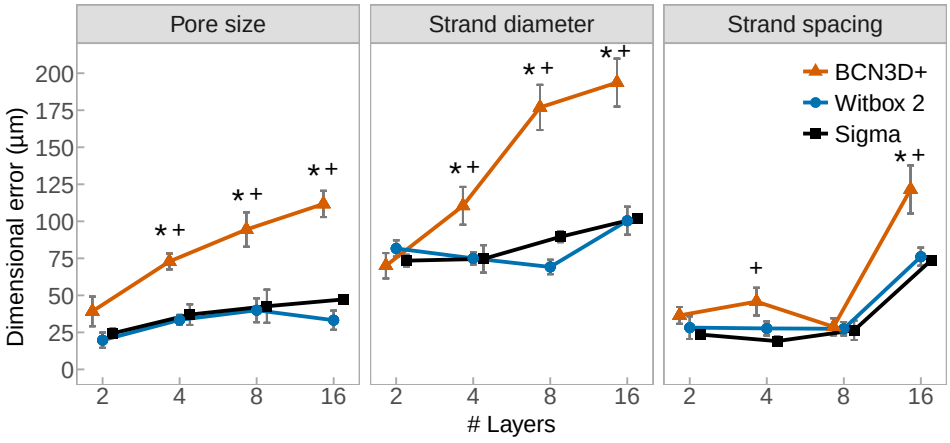

Figure 6.7: *Dimensional errors of printed lattice structures using three different open-source 3D printers. Asterisk symbol (*) indicate statistical significance between BCN3D+ and Witbox 2 (p <0.01). Cross symbol (+) indicate statistical significance between BCN3D+ and Sigma (p <0.01). No statistical differences were found between Witbox 2 and Sigma printers. The data represent the mean and s.e.m. of six different samples (n=6).*

6.2.5 Vertical pillars

Fabrication of microvascular networks requires the creation of complex 2D structures in a layer-by-layer fashion and the ability to interconnect them to build a 3D network. That interconnection can be performed using several approaches by means of horizontal and vertical printed structures (Kolesky *et al.*, 2016). Another calibration model consisted of slender pillars (figure 6.1d) printed at deposition speeds lower than 4.16 mm s^{-1}. The stability of the printed posts was inversely proportional to their height and z-axis printing speed (figure 6.8a). Some pillars behaved more unstable before fall, but in general, they tended to collapse when removing the printed constructs from the bioprinter bed surfaces. The highest stable posts were obtained at minimum deposition speeds of 0.83 mm s^{-1} with a total height of 7.5 mm.

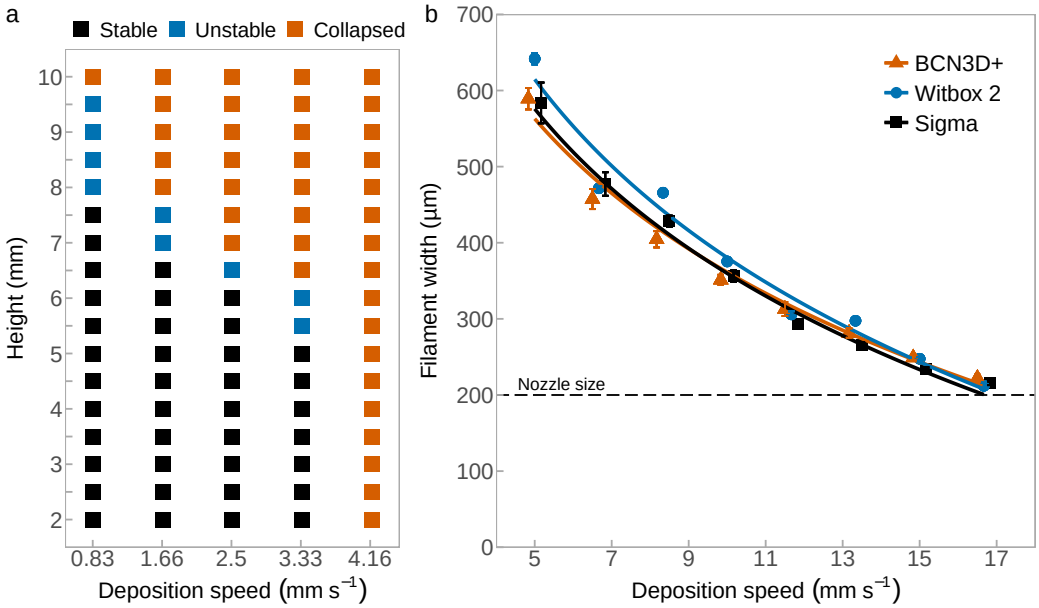

Figure 6.8: *(a) Evaluation of the mechanical stability of printed vertical pillars with heights varying from 2 mm to 10 mm at different deposition speed. (b) Straight channels widths as a function of deposition speed variation. Both calibration models were printed using a tapered nozzle (27G; ID: 200 µm; Nordson EFD).*

6.2.6 Hierarchical network

Although EBB allows the production of large scale structures, bioprinting of highly vascularized tissues already remains as a big challenge. Whatever the dispensing system adopted, the capacity to create filaments makes this approach especially suitable to create geometries that mimic vascular networks. Several techniques have been developed to generate cell-laden vascular constructs. Some of these examples can be found in the bioprinting of sacrificial biomaterials forming a predefined tubular network. After the cell-laden hydrogels have been deposited and gelled, these fugitive inks are removed by a thermal de-crosslinking process, forming an internal vascular network (Wu *et al.*, 2011). Some of these embedded vascular networks are composed of P407, a synthetic hydrogel that becomes liquid when its temperature is decreased (Kolesky *et al.*, 2016, 2014). Other approaches use water-soluble carbohydrate-glass lattices (Miller *et al.*, 2012), gelatin printed channels as sacrificial element (Lee *et al.*, 2010) or agarose fibers to fabricate microchannel networks (Bertassoni *et al.*, 2014b).

If the bioprinting nozzle and speed are the same in all the printing process, constant diameters are generated. This configuration would require one specific nozzle to produce each of the channel's network and that is not always a feasible option. However, it is possible to produce different diameters with the

same nozzle adjusting parameters like printing speed, nozzle size and pressure (Wu *et al.*, 2010).

The last calibration model permitted the generation of a 4-order vascular network with a 200 μm nozzle and different strand diameters. A constant printing pressure was utilized for all filaments, but varying the deposition speed. All three printers utilized showed enough capabilities to print within a wide range of speeds (3.3-13.3 mm s^{-1}) in a hierarchical fashion (figure 6.1f).

6.3 Conclusions

The methodology here proposed have permitted to obtain the overall printing accuracy of three different open-source bioprinting platforms. Each of the calibration models proposed covers specific features to identify and quantify the accuracy during the bioprinting process. Besides, we have demonstrated the versatility of the printheads previously present by its installation in three different 3D printers. Although the mechanical resolution of the open-source 3D printers here utilized (10-50 μm) are lower than other more sophisticated and higher priced bioprinters (up to 1 μm), the final print accuracy achieved creating using P407 could be enough for biological applications. The calibration models proposed permitted to quantify the capabilities and limitations of each modified bioprinter utilized. The results obtained enabled us to discover significant differences in the dimensional errors between x and y-axes in the BCN3D+ printer. It can be concluded that differences in how 3D printer axes move strongly affect the final accuracy of the printed constructs. This behavior could be explained because when using Witbox 2 and Sigma the printed construct only moves a layer height, while in BCN3D+ the printed construct is continuously moving in the y-axis along with the platform. Besides, the better performance of Sigma and Witbox 2 3D printers respect to BCN3D+ could be explained because the former are sold already assembled and the latter had to be assembled by the user. Overall it can be said that the calibration models proposed represents a useful tool to determine the accuracy of a bioprinting platform and establish a common comparison framework between bioprinters.

Chapter 7

Accurate and efficient multi-material bioprinting

Most of the studies in 3D bioprinting have traditionally been limited to the use of a single bioink, which is perhaps an oversimplification that limits the potential of this technology. Employing multiple building and sacrificial biomaterials and cells types in a single biofabrication session seem to be the right way of addressing the complexity of organ engineering and produce outstanding advances in the field of TE (Visser *et al.*, 2013). Multi-material bioprinters have recently been developed by several research groups (Kang *et al.*, 2016; Ozbolat & Hospodiuk, 2016; Liu *et al.*, 2017; Shim *et al.*, 2012; Rocca *et al.*, 2018; Kolesky *et al.*, 2016). These bioprinting systems usually incorporate up to three or four printheads to perform multi-material extrusion like the open-source solution presented in this research.

To the best of our knowledge, advances in multi-material bioprinting will enable researchers to integrate intricate perfusable channels inside of complex shape constructs, and create constructs with several different cell densities, among other advantages. All of this cannot be accomplished without answering fundamental questions such as the ideal properties of the bioinks and the relationships between the bioprinting process parameters and the print resolution and fidelity (He *et al.*, 2016). In the case of hydrogels and MEBB, few research studies have been conducted on correlating the bioprinting parameters, and the printed outcomes to a great extent (Kyle *et al.*, 2017). Suntornnond et al. used poloxamer to develop a mathematical model to correlate print resolution with process parameters (Suntornnond *et al.*, 2016). Similarly, a prediction model was obtained by Trachtenberg et al to determine the suitability of poly-propylene fumarate for MEBB (Trachtenberg *et al.*, 2016) while Ting et al. examined the effect of poly(lactic-co-glycolic acid) (PLGA) composition and printing parame-

ter on print resolution (Wang *et al.*, 2013). However, today, there is no a definite method to calibrate multi-material 3D bioprinters as well as to determine their final print resolution. Understanding how parameters such as printing speed and nozzle height affect the print resolution is vital not only for the shape of the printed constructs but also for their mechanical properties. When encapsulating cells, selecting the optimal printing parameters will reduce the adverse effect of the viscoelastic stresses on the cell viability (Gao *et al.*, 2018; Wang *et al.*, 2013).

In this chapter, it is proposed a method to analyze the influence of the main printing parameters in multi-material 3D bioprinting and accurately control the print resolution. Poloxamer hydrogels with different fluorescent inks were printed into different complex constructs for finding the optimal printing parameters. This allowed to emulate the bioprinting of four materials, but at the same time, also remove other secondary factors such as excessive swelling or temperature dependence. Moreover, we explored alternative 3D bioprinting techniques such as IDEX and simultaneous printing of several constructs from a time-efficient perspective. All the experiments included in this chapter were carried out using Witbox 2 3D printer (figure 7.1) except section 7.6, in which IDEX printing technology was analyzed using Sigma 3D printer (figure 7.14). Four PHR printheads were installed on each 3D printer. The results obtained demonstrate that our proposal has huge potential to help in creating large complex 3D constructs and potential vascular networks for organ engineering.

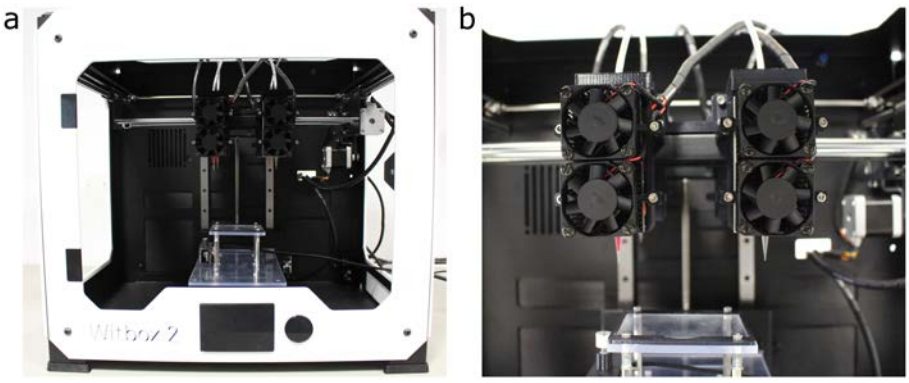

Figure 7.1: *General (a) and detailed view (b) of the modified Witbox 2 3D printer with four bioprinting printheads.*

7.1 Optimal calibration of multi-material bioprinting systems

Two main calibration models were proposed to adjust the four printheads' xy positions with respect to each other and define the optimal printing pressure. These models aim to determine the printability and final print resolution in multi-material bioprinting systems. The proposed calibration 3D models were designed using the CAD modeling software SolidWorks (Dassault Systems, v2016), and exported as STL files. A detailed description and justification of the calibration models are given in the following paragraphs:

- **xy-offset pattern (calibration model 1)**: straight lines were printed in the x and y directions using two different printheads (figure 7.2a). xy-offsets of the four printheads were calculated with regard to the first printhead (P1). For that reason, half of the straight lines were printed using P1 and the other half were printed using a different printhead (P2, P3 or P4).
- **Zigzag path (calibration model 2)**: a continuous zigzag was printed using each printhead in other to determine the correct printing pressure and speed (figure 7.2b). An increasing distance of 20 µm was separated between all of the lines (Δd) with separation between lines ranging from 200 µm to 500 µm. The optimal printing pressure was determined when all the printed lines did not overlap and were printed forming continuous strands.

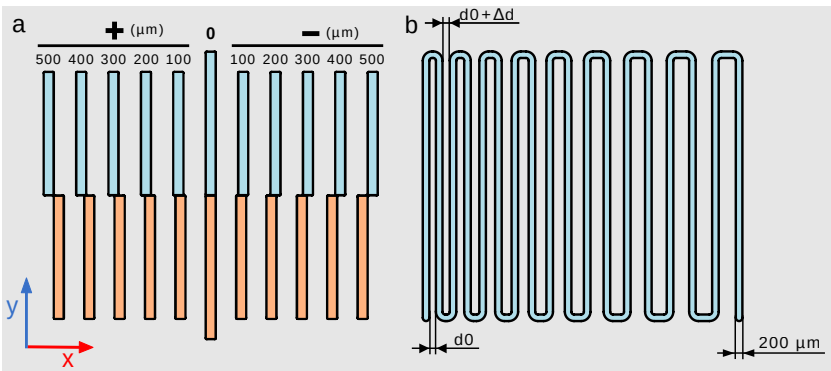

Figure 7.2: *Schematic illustration of the calibration models xy-offset pattern (a) and printing pressure dependent zigzag path (b) where the distance d0 = 200 µm, and the variation Δd = 20 µm.*

Both calibration models were printed using 40 wt % P407 on 50x75x1 mm glass slides (Corning Inc., New York, NY, USA). Bioink P407 was used in the 3D bioprinter calibration, and the evaluation of the printing process. This bioink was selected because of its stable nature, exceptional printability, adequate viscosity, and low swelling (Kolesky *et al.*, 2016; Chang *et al.*, 2011). Note that the P407

allows for evaluating the capabilities of any bioprinter minimizing the influence of material properties and other secondary factors involved. All of the properties mentioned facilitated the creation of complex architectures and their subsequent evaluation. The P407 was loaded into 3 mL and 5 mL syringe barrels (Nordson EFD) at 4 ºC and extruded at 24 ºC. The xy-offset calibration model was printed using tapered nozzles with three different IDs: 200 µm (27G; Nordson EFD), 250 µm (25G; Nordson EFD) and 330 µm (23G; Nordson EFD). The calibration model 2 was printed in a range of pressures from 82 kPa to 138 kPa and speed from 5 mm s^{-1} to 25 mm s^{-1} using a 27G tapered nozzle.

Four different fluorescent dyes were utilized to improve the visualization of P407 and Gel-Alg (except in the case of using cells to avoid cytotoxicity) bioinks: orange (1:100; IFWB-33; Risk Reactor, Santa Ana, USA), clear blue (1:500; IFWB-C0; Risk Reactor), yellow-green (1:1000; IFWB-C8; Risk Reactor) and red (1:1000; IFWB-C7; Risk Reactor).

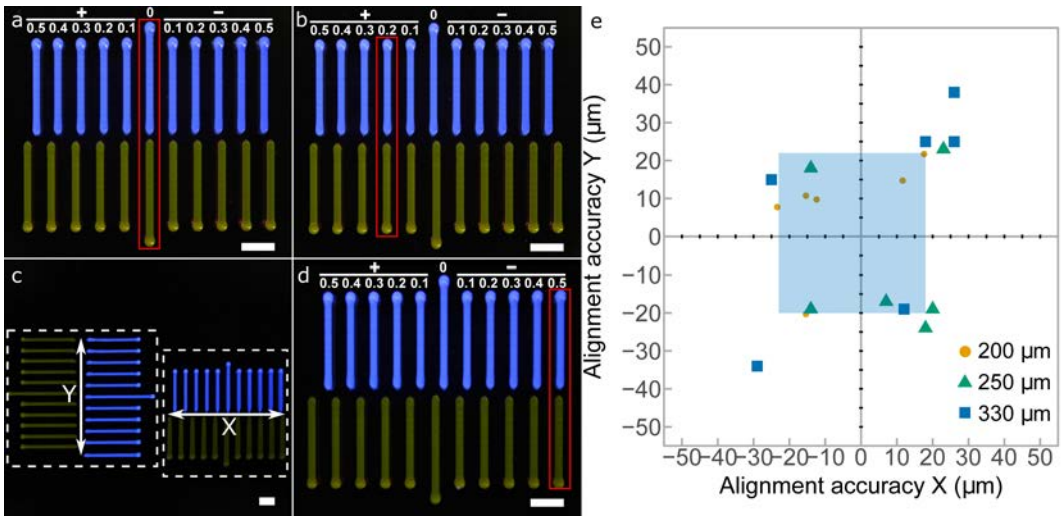

Figure 7.3: *Images of the printed xy-offset pattern calibration model between P1 and P2. (a) perfect alignment between P1 and P2; (b) +200 µm x-offset of P2 respect P1; (c) overall picture of x and y calibration models printed at the same time; (d) −500 µm x-offset of P2 respect P1; (e) alignment accuracy in x and y axes measured for three different nozzle sizes (200 µm, 250 µm, and 330 µm); scale bars: 2 mm.*

First, calibration model 1 was printed to perform a quick visual calibration of the xy-offsets in the four printheads utilized (figure 7.3a–d). Calibration errors or deviations in both x and y axes were measured simultaneously using the printed strand patterns of both axes (figure 7.3c). After printing, the patterns allowed the alignment of the printheads P2, P3, and P4 with respect to P1. We considered either positive or negative misalignments in a range between 100 µm

and 500 μm. For instance, figure 7.3b,d show clear x-axis misalignments of +200 μm and -500 μm, respectively. Once the deviations are visually identified, the correction values can be introduced in the slicing software, and the new G-code will correct the position of the printhead nozzles.

The results of the xy alignment for three different nozzles are shown in figure 7.3e. The increase of the nozzle diameter produced a decrease in the alignment accuracies of both directions. These results can be explained by the much thicker printed lines produced when using bigger nozzles. The same observations, the smaller the nozzle diameter, the higher the line with resolution, were reported by Suntornnond et al. evaluating pluronic F127 (Suntornnond *et al.*, 2016). Therefore, it is preferable to perform the 3D printer calibration with the smaller nozzle available. The light blue area indicates the limits for the 200 μm nozzle in the x and y directions, which obtained the best results of the three nozzles. The maximum alignment errors obtained for this nozzle were in a range from -23 μm to 18 μm in the x-direction and from -20 μm to 22 μm in the y-direction. These values are sufficiently low and guarantee that the alignment accuracy is at least of a similar order of magnitude to the mechanical resolution of the 3D printer (20 μm).

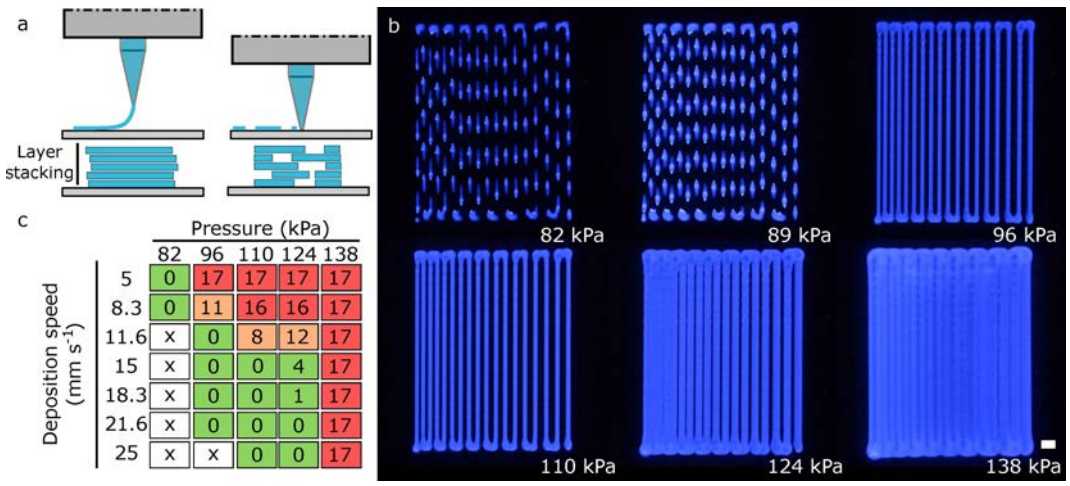

Figure 7.4: *(a) Scheme of the possible defects in the first layer calibration: nozzle too far from printing platform and nozzle too close to printing platform; (b) images of the zigzag path calibration models printed at a deposition speed of 15 mm s^{-1} for various printing pressures; scale bar: 1 mm; (c) quantification of the number of filled spaces between strands in the calibration model 2 varying printing pressure and deposition speed (green: good; orange: normal; red: bad; x: discontinuous printing).*

The layer-by-layer approach characteristic of additive manufacturing (AM) makes the thickness of the printed layers became the primary factor defining the

print resolution along the z-axis. When the nozzle is too far from the platform, the printed layers will not adhere to the surface, creating discontinuous strands, and the next layer will not be deposited adequately (figure 7.4a). On the other hand, if the tip is too close to the platform, it might lead to a clogging of the nozzle or a discontinuous printing. In some research works, the 3D models are sliced into layers with a slicing height equal to 70% or 80% of the inner nozzle diameter (Guo *et al.*, 2017; Paxton *et al.*, 2017). A lower layer height will result in fewer errors between the layers, but longer printing times. Herein, we found that using a slicing height equal to the nozzle diameter was beneficial when determining the effective deposition rate. Therefore, establishing the right distance between the nozzle and the printing bed for the first layer is of vital importance for avoiding further deposition problems.

The second calibration model or zigzag-path model was useful for determining the printing pressure needed to produce strands of the desired diameter. The variation of the printing pressure in figure 7.4b for a fixed deposition speed of 15 mm s^{-1} produced strand widths of different dimensions. As expected, an excessive printing pressure and a low deposition speed produced dramatically wider strands that can eventually overlap (figure 7.4c).

7.2 Z-axis calibration

When multiple printheads are installed within the same 3D printing system, the z-axis calibration of each nozzle results crucial to ensure an accurate and reliable z-positioning of each printhead respect to the others. This feature is especially relevant in the calibration of the first layer height, as it can lead to detaching constructs or nozzle clogging if it is placed too close to the printing surface. Besides, if nozzles tips are not perfectly aligned in the same horizontal plane. Slight differences in z-height of a few microns introduce inadmissible printing errors when multiples layers are stacked. To solve this problematic situation, a z-homing system is proposed which permits an automatic calibration of printheads nozzles heights. To that end, we designed a push button using a mechanical endstop (Makerbot mechanical endstop v1.0) as shown in figure 7.5a. Each time a new printhead is utilized, the printhead moves to the push button xy-coordinates and the nozzle tip touches it using the z-homing G-code command (G28 Z). As the height (h) between the printing surface and the push button do not change, the z-offset for each printhead is always the same once the push button is activated.

This allows using printheads and nozzle types with different dimensions, as the automated z-homing system compensate the unbalanced nozzles heights.

Accuracy and repeatability of the push button were assessed through the probe accuracy test provided by Marlin firmware (G-Code: M48). In this test, the mechanical endstop was pushed 40 times consecutively and variations in the z-height were recorded. Different z-homing speeds were utilized for each test (figure 7.5b). Results revealed that pushing the endstop at speeds lower than 6 mm s^{-1} obtained z-axis errors lower than 5 µm. If higher z-homing speeds were utilized, z-axis errors increased reaching a maximum of 15 µm.

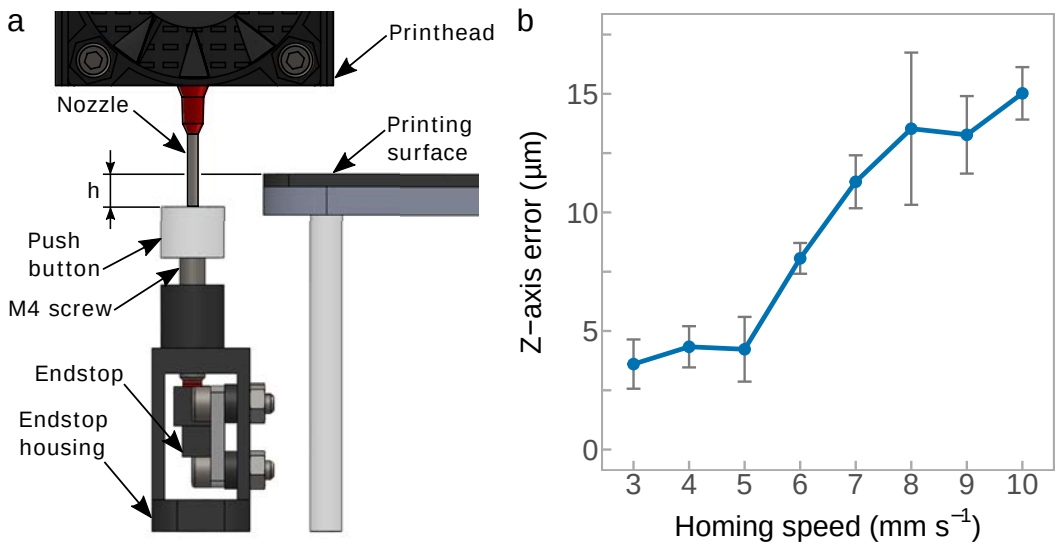

Figure 7.5: *(a) Schematic view of the 3D CAD design of the push button with all its components utilized for automatic Z-homing calibration. (b) Homing accuracy in the z-axis when the push button was utilized. Each point represents z-axis errors for different homing speeds using the probe accuracy test (M48). The data represent the mean and s.d of forty samples (n=40).*

7.3 Print resolution in multi-material bioprinting

Extruded hydrogels usually result in spreading or diffusion from the initial shape as a consequence of standing their weight and their slow gelation rates (He *et al.*, 2016). Besides, the printed strands are never cylindrical, even if we use hollow cylinder-shaped nozzles. For these reasons, we decided to evaluate the print resolution of printed P407 filaments by two dimensions: width and height. We measured these two variables (figure 7.6a and 7.6b) for different values of printing pressure and deposition speed to identify the optimal printing setup.

We observed that pressure and speed are strongly correlated while working at intermediate pressures (96–138 kPa). However, pressure is probably a more critical factor than deposition speed, especially for the height of the filaments printed (figure 7.6a). This is consistent with previous studies on shear thinning hydrogels as the one performed by Trachtenberg et al. printing poly(propylene fumarate) (PPF) (Trachtenberg *et al.*, 2016). They determined that fiber height and width decreased with increasing deposition speed and decreasing pressure. In addition, they also showed the higher effect of pressure with respect to speed and the interaction of both factors (pressure and speed) is of great importance.

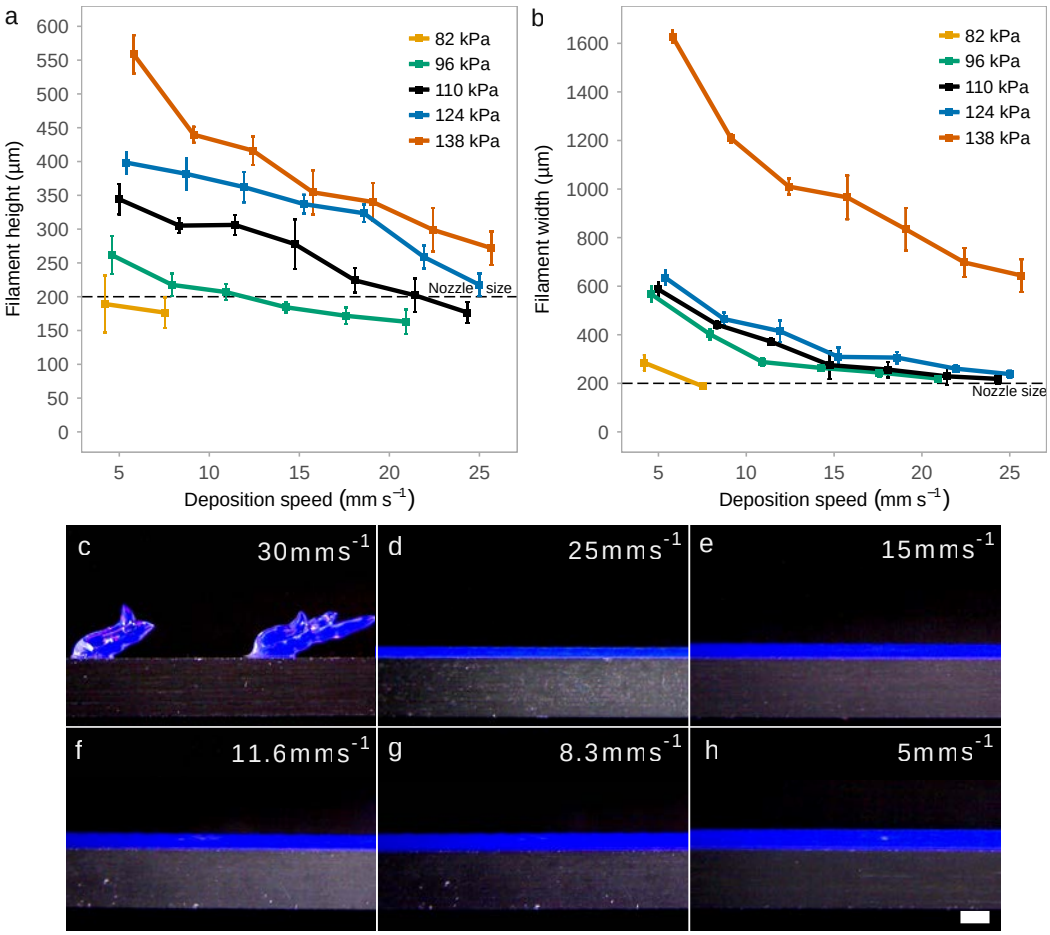

Figure 7.6: *Impact of the printing pressure and deposition speed when creating rectilinear filaments. Quantification of the height (a) and width (b) of the printed filaments using 40 wt % P407 and a 27G tapered nozzle. Data represent the mean and standard deviation of six different samples (n = 6); (c–h) Representative photographs of different filaments printed at a constant pressure of 110 kPa on a cover glass while reducing the deposition speed from 30 mm s^{-1} to 5 mm s^{-1}); scale bar: 500 µm.*

When printing at very low pressures (82 kPa), there was a limitation in the deposition speed (around 8 mm s^{-1}) for creating continuous filaments, much lower value than the 25 mm s^{-1} achieved at the pressure of 110 kPa. Discon-

tinuous strands were usually generated when printing at higher deposition speed (figure 7.6c).

In general, strand width should be almost always greater than height when keeping constant the value of the thickness layer (200 μm) because the nozzle tends to crush the printed samples. We hypothesized that optimal printing configuration would be that that the filaments show similar height and width values with a low swelling ratio. Figure 7.6a and 7.6b demonstrated that these conditions were achieved for printing pressure of 110 and 124 kPa, and deposition speed of around 21 and 25 mm s^{-1}, respectively. Using these parameters and 27G nozzles, the height and width of the strands were very similar: (i) for 110 kPa was around 202 μm and 230 μm; and (ii) for 124 kPa, the height-width values were 219 μm and 238 μm, respectively. Finally, we would like to highlight that using a very high printing pressure (138 kPa) was a synonym of nonlinear response for different deposition speeds, with too much bioink deposition and diffusion.

7.4 Multi-material bioprinting of complex scaffolds and 3D constructs

After the four printheads were calibrated in x, y, and z axes and the appropriate setup was found, representative complex structures were printed to demonstrate the goodness of our proposed method. Different bioinks were printed per each layer to study the accumulated misalignments that produce heterogeneous patterns in the lattice scaffolds, and consequently the further reduction of the porosity.

Firstly, porous lattice structures composed of one bioink per layer were printed using two printheads (two fluorescent bioinks). The lattice structures were printed using infill percentages ranging from 10% to 35%. Low and medium infill percentages produced homogeneous patterns across the xy plane (figure 7.7a–d) because of the successful calibration method. Nevertheless, the higher the infill percentage, the less homogeneous the pattern is. In that case (figure 7.7e,f), there was a difference between the theoretical pore area designed and the total pore area printed. The printed pore area was smaller than the theoretical one, similar to what He et al. reported (He *et al.*, 2016).

After printing the first layer, the second layer became a weight load to the first layer at the intersection. In addition, and as explained by (He *et al.*,

2016), the radial diffusion of the upper hydrogel layer on the lower one at the intersections produced a radial narrowing of the pore. As a result, we obtained more rectangular-shaped pores than squared ones. These observations were more evident when the infill density was between 25% and 35% (figure 7.7d–f). The limiting higher infill percentage seems to be 30%, with only a few overlapping areas observed. Therefore, we demonstrated that conducting an accurate calibration process is a guarantee of the integrity of the structures created layer-by-layer.

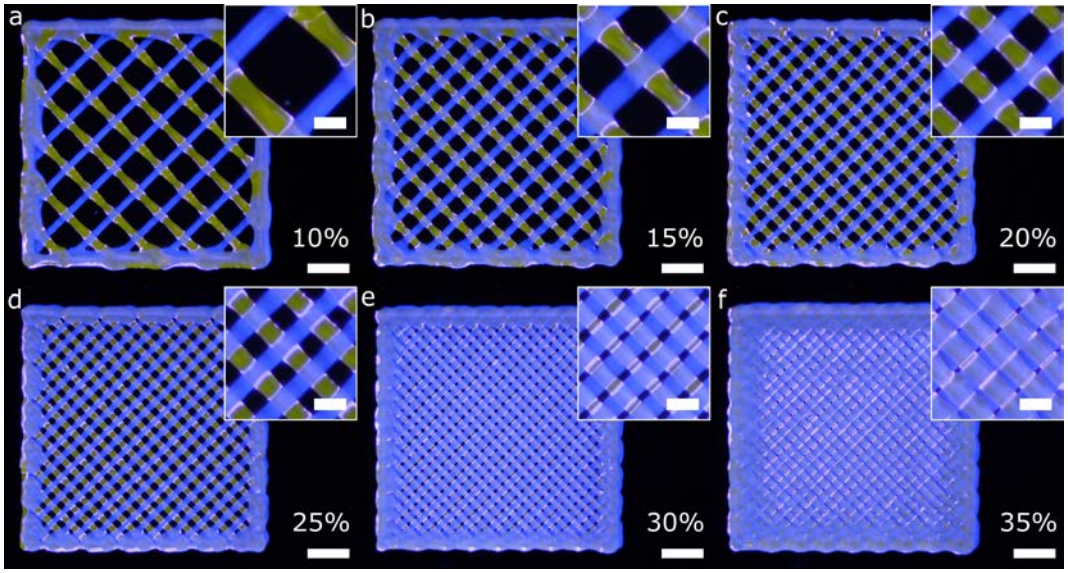

Figure 7.7: *General and detailed views of porous lattice structures printed with two bioinks and two printheads. Each bioink was used in a different layer. The G-code was generated using the slicing software with the infill percentages: 10% (a), 15% (b), 20% (c), 25% (d), 30% (e) and 35% (f). The printing pressure and speed utilized in all the cases were 110 kPa and 15 mm s^{-1}, respectively; scale bars: 2 mm (general views) and 500 µm (detailed views).*

More complex lattice structures with fluorescent bioinks were printed using the four printheads mounted in the bioprinter. Diagonal and rectilinear patterns (figure 7.8a–d) were stacked successfully into two different multi-material scaffolds (figure 7.8g,k). The step by step stacking of the layers is depicted in figure 7.8e–g,i–k. As in the previous scaffolds, the fidelity at the central part of the structures was better than that at the edges. The lack of accuracy near the edges was due to the accumulation of material in the region where the lines change their angles, similar to the mistakes reported by He et al. for single material extrusion (He *et al.*, 2016). Looking at the intersection point of the diagonal diagonal structure (figure 7.8h), we observed that the printheads in charge of dispensing blue and red hydrogels were slightly deviated in the +x coordinate (according to figure 7.3b). This effect was probably the leading cause of the small dissimilarities in shape observed at the empty triangular areas. These

differences were consistent with the geometry tolerances of the structures due to the alignment errors in the x-direction reported in the previous sections. In summary, both multi-material structures were printed successfully due to the automatic calibration system used.

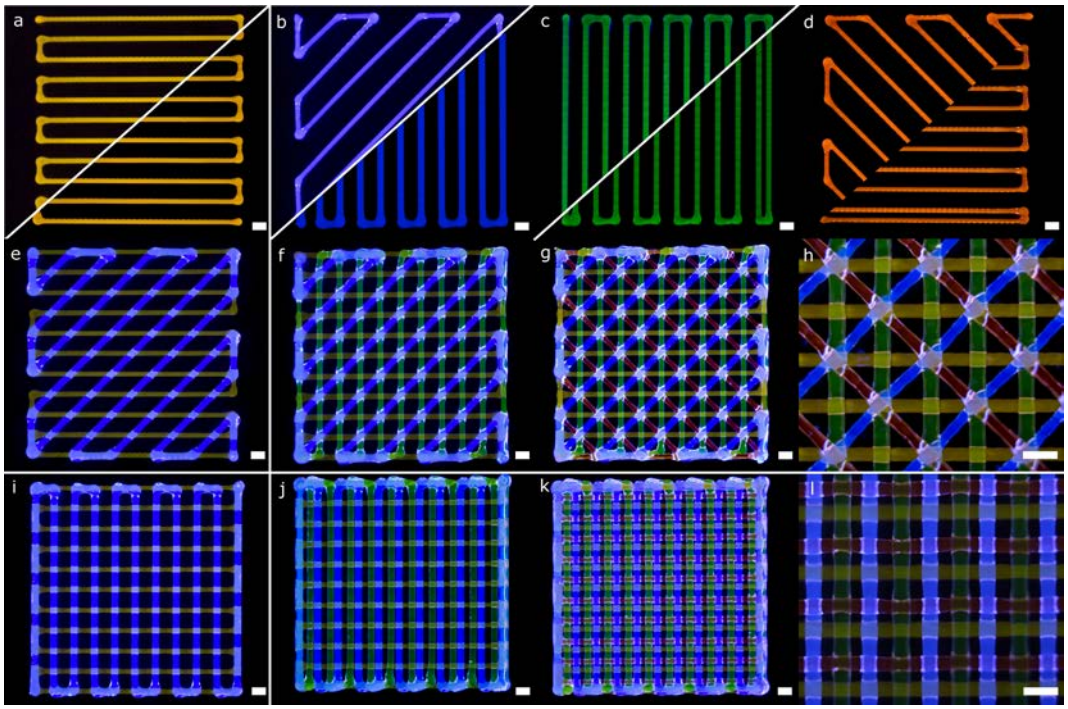

Figure 7.8: *Pictures of a complex porous structures printed using four printheads with parallel and diagonal rectilinear patterns. Each fluorescent bioink was deposited in a different layer (a–d) with a total of four layers stacked (e–g,i–k). Detailed view of the diagonal (h) and perpendicular lattice structures (l); scale bars: 1 mm.*

Regarding the rectilinear scaffold, the structure was created without overlapping areas (figure 7.8i). The diffusion of the upper layer toward the lower one was due to the gravity being more evident than in the previous structure (figure 7.8l). This effect is mainly related to the higher infill density (or smaller pore area). Through the successful printing of these two complex scaffolds, the proposed calibration methodology for multi-material bioprinting was verified. We believe that this approach will allow precise control of the deposition of various hydrogels and cell types for the fabrication of more biomimetic tissue structures.

Another CAD computer model (figure 7.9), which entails greater complexity compared to the previous structures (figures 7.7 and 7.8), and thereby more calibration requirements, was printed using four fluorescent bioinks (figure 7.9b). The model is a lattice structure formed by parallel rectilinear strands, each one with its particular bioink color (figure 7.9c). We checked the existence of overlaps or empty spaces between the strands as a sign of an erroneous cal-

ibration across the xy axes. The overlaps with excessive material accumulated tended to break the continuity of the strands of the next layer (figure 7.9e), whereas the errors in the calibration process produced distinct gaps between the parallel strands (see the blue filament in figure 7.9d). On the other hand, if the xy-offsets of the four printheads were correctly determined, the strands were printed without being merged as shown in figure 7.9f. Note that the slicing of the 3D models took into account the swelling ratio of the hydrogel P407 (figure 7.9a). This ratio was estimated at a 100 μm per strand. Therefore, the initial diameter in the computing model needed to be 200 μm to obtain printed strands of 300 μm without overlapping. We conclude that the structures printed are an excellent example of correct calibration cases.

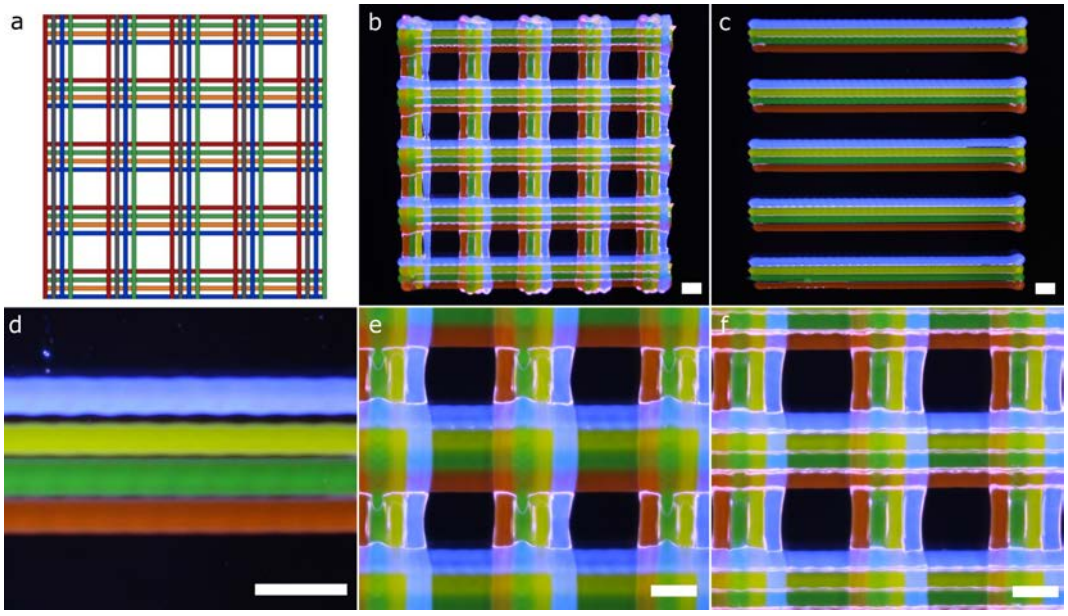

Figure 7.9: *Pictures of a complex porous structure printed using four printheads and rectilinear patterns. The four printheads deposited dyed P407 in the same layer with a total of two layers stacked. General view of the CAD design (a) and printed porous structure (b); (c) general view of the first layer; (d) detailed view of printheads misalignments on the y-axis; (e) detailed view of strands diffusion in the second layer; (f) detailed view of the porous structure printed correctly. Scale bars: 1mm.*

Kang et al. (Kang *et al.*, 2016) proved the immense potential of these kinds of lattice constructs (figure 7.9b) to produce mandible bone and ear-shaped cartilage using cell-laden bioinks side-by-side with PCL to ensure the mechanical strength of the printed constructs. In this research, we followed a similar approach regarding the MEBB system with four printheads but avoiding the proprietary nature of their multi-material bioprinter. Similar geometries with several bioinks printed right next to the other using parallel rectilinear strands (figure 7.9c) but not in a lattice construct were fabricated by Lui et al. (Liu *et al.*, 2017). How-

ever, their approach incorporates an array of bioink reservoirs routed to a single printhead instead of our multiple and separate printheads. An advantage of the Lui et al. system is that it can eject the bioinks in individually or simultaneously, but it is limited to the use of a single nozzle, which restricts the ability to print hydrogels with very different viscosities. Other multi-material bioprinters such as the 3D-Bioplotter (EnvisionTEC, Gladbeck, Germany) incorporates a mechanism designed to exchange the printheads, which gives flexibility but increases the cost and complexity. Multiple bioinks can be printed in the same 3D model, but increasing the total printing time significantly. Although commercially available 3D bioprinters from EnvisionTEC and RegenHU can assure mechanical resolutions up to 1 µm and 5 µm, respectively, we demonstrated that our system with limited mechanical precision also produced complex structures with enough accuracy for TE applications (Wang *et al.*, 2017; Trachtenberg *et al.*, 2016; Guo *et al.*, 2017; Paxton *et al.*, 2017; Ribeiro *et al.*, 2017).

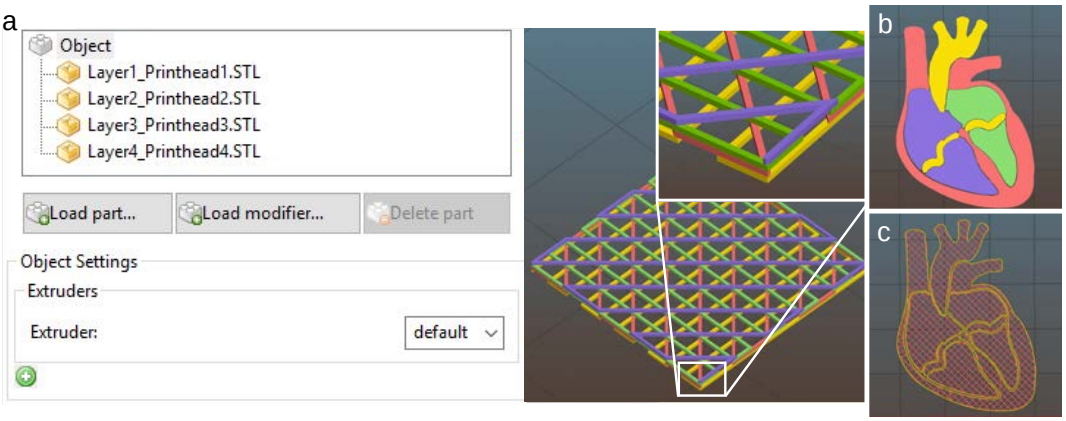

Figure 7.10: *Multi-material printheads assignment using Slic3r software. (a) Porous structure with four layers stacked, each one assigned to a different printhead; (b) 3D model of a heart section composed of four parts; (c) printhead trajectories calculated by the slicing software using a porous infill.*

Another CAD model to show the potential of a well-calibrated multi-material 3D bioprinter for generating complex structures is depicted in figure 7.11. The model represents a human heart section where each of the parts consisted of a single perimeter and a porous infill at 15% printed in two layers. All of the printing trajectories, either for the perimeter or the porous infill (figure 7.10a-c), were generated automatically by the slicing software, which greatly facilitated the printing process. We proceed with the following printing sequence: orange (P1), blue (P2), green (P3) and red (P4), but this ordering can be easily changed.

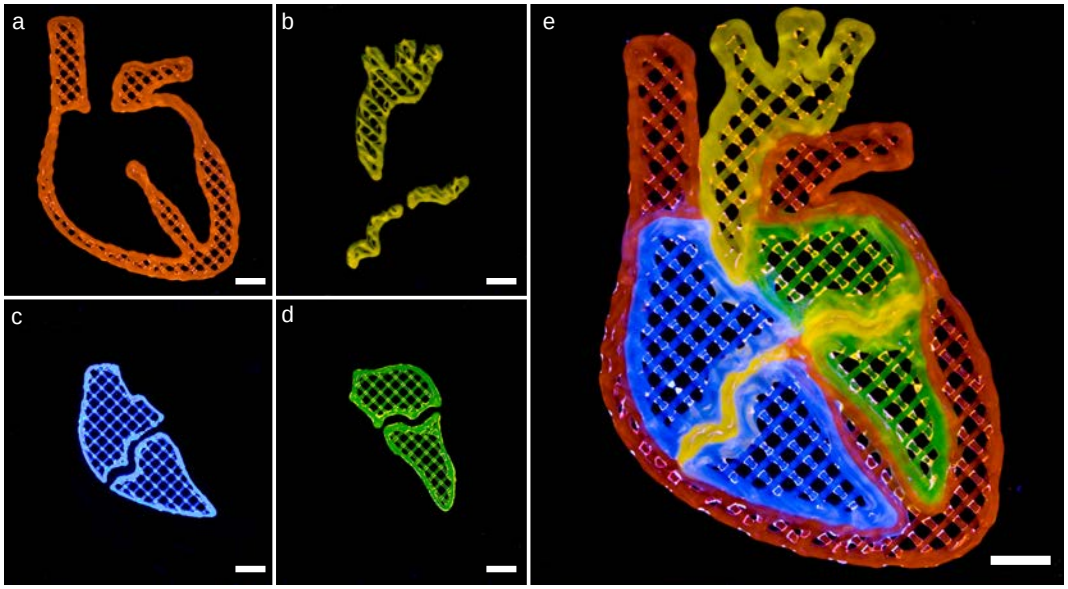

Figure 7.11: *Complex multi-material printing of model that represents a human heart section. The model is composed of heterogeneous bioinks to demonstrate the multi-material capabilities of our system. (a–d) printing of the main parts of the heart section separately; (e) combination of the multiple parts using the four bioinks in a complex structure; scale bars: 5 mm.*

The CAD model of the heart section has curvilinear geometries that create complex trajectories than previous models (figure 7.9) based on straight lines. These geometries increased the number of print errors detected. For instance, blue (figure 7.11c) and green (figure 7.11d) bioinks overlaid the thin middle sections of the heart printed of orange bioink (figure 7.11b). Better calibration procedures might avoid these defects by incorporating the effect of the bioink swelling during CAD models generation. Liu et al. printed a very similar geometry of the human heart section using their multi-material platform described before (Liu *et al.*, 2017). We obtained similar results with our constructs showing good demarcation among adjacent materials.

Gel-Alg and P407 bioinks were printed in a single session creating multi-material constructs (figure 7.12). Gel-Alg represents a more challenging material regarding printability when compared to P407. Consequently, the printed strands were not straight and the openings were irregular, reducing the pore area (figure 7.12a). Other authors also reported complications when printing Gel-Alg mixes. Paxton et al. attributed the weak printability to the lower yield stress point of Gel-Alg blends (Paxton *et al.*, 2017). Despite this, we were capable of calibrating the bioprinter and obtaining the proper printing parameters to create complex constructs from the CAD models in a single multi-material session (figure 7.12b–d).

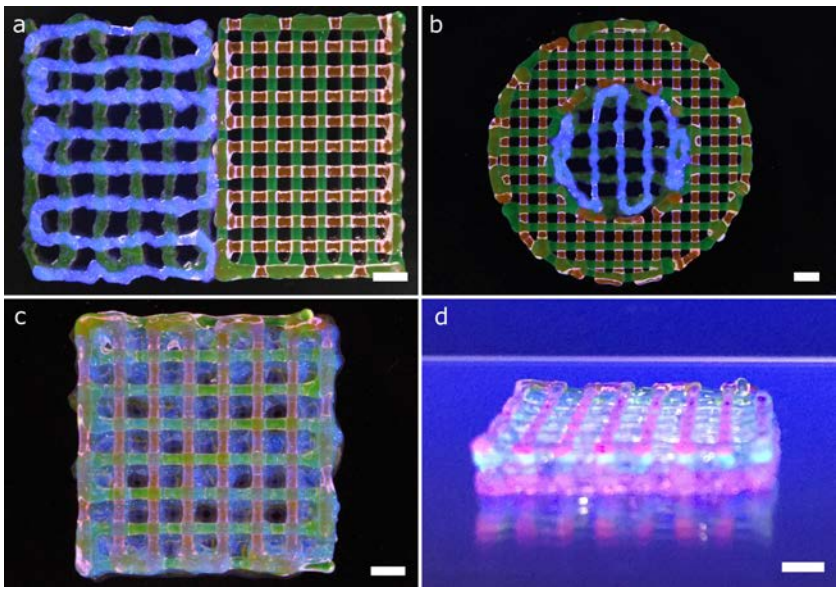

Figure 7.12: *Complex multi-material structures printed. Gel-Alg and P407 bioinks were printed using 25G and 27G tapered nozzles, respectively. (a) general view of a 2-layer porous lattice structures printed with Gel-Alg (left, green for printhead 1 and blue for printhead 2) and P407 (right, green for printhead 3 and red for printhead 4) bioinks; (b) general view of circular lattice structure with the inner circle printed in Gel-Alg (green for printhead 1 and blue for printhead 2), and the outer circle printed in P407 (green for printhead 3 and red for printhead 4); general (c) and side view (d) of an 8- layer porous lattice with alternating layers of Gel-Alg and P407. Sequence of colors: Gel-Alg (orange), Gel-Alg (blue), P407 (green) and P407 (red); scale bars: 2 mm.*

7.5 Multi-material printing of complex 3D vascular networks

Several tests were performed to produce pillars (vertical strands) and hanging bridges between them using P407, similar to the fugitive structures printed by Kolesky et al. that mimic vascular networks (Kolesky *et al.*, 2016). Pillars were printed moving the printhead on the z-axis and keeping constant the xy-coordinates. When printing one pillar, and prior to the printhead movement in the z-direction, the tip of the nozzle was placed at 200 μm from the glass slide and the solenoid valve was opened a waiting time of 500 ms. Within this time, the P407 started to flow and permitted to deposit an excess of material in the base of the pillar to give it more stability (figure 7.13d). If no waiting time was utilized, a weaker pillar base was produced, decreasing the structure stability. Once the nozzle extruded the pillar moving to the desired height, an additional waiting time of 1 s was considered to allow the column to stabilize. After that, the nozzle was raised at a fast speed (25 mm s^{-1}) a distance 2 mm higher than the pillar height to improve its verticality. There was a limit in the column heights that could be achieved without losing verticality.

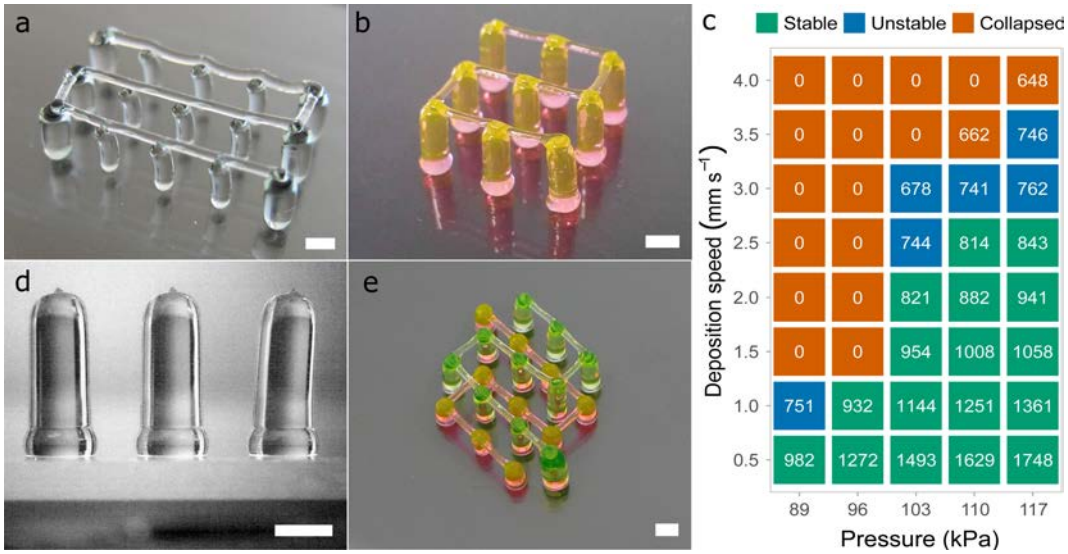

Figure 7.13: *(a,b) Complex vascular 3D networks printed in P407; (c) evaluation of the stability of 3D printed vertical pillars for a fixed height of 8 mm. Printing pressure ranging from 89 kPa to 117 kPa and deposition speeds ranging from 0.5 mm s^{-1} to 4 mm s^{-1}. The data inside the figure represents the mean of pillars diameter (in µm) of six different samples (n = 6); (d) side view of 3D printed 4 mm height pillars; (e) vascular structure printed at two different heights (2 mm and 5 mm) with interconnected bridges; scale bars: 1 mm.*

Different printing pressure (89 kPa to 117 kPa) and deposition speeds (0.5 mm s^{-1} to 4 mm s^{-1}) were tested, producing pillars with different diameters and stability (figure 7.13c). A constant pillar height of 8mm was set for all the vertical pillars printed with a 27G nozzle. As expected, the lower the speed and the higher the pressure, the larger the diameter of the pillars extruded. Regardless of the pressure and the speed utilized, pillars with diameters above 814 µm always remained stable while pillars with diameters between 678 µm and 762 µm tended to bend slightly to losing their verticality. Above these diameters, pillars collapsed utterly touching the glass slide.

Regarding the hanging bridges between pillars, the deposition speed in the xy-plane and the distance between pillars have a direct influence on the straightness of the bridge (figure 7.13a). To generate continuous straight strands (figure 7.13b,e), pillars were spaced up to 4 mm while the deposition speed was set at 7.5 mm s^{-1}. When faster deposition speeds were utilized for the bridges, the pillars tended to collapse by the impact of the deposited strands. In general, the samples printed demonstrated excellent results for maximum heights of 8 mm to 10 mm.

If different materials or even the same material but in different concentrations are used to print this type of vascular 3D networks, it would be first necessary to evaluate the stability of the vertical pillars for different process parameters, as shown in this section (figure 7.13c). Then, the next step would be to find the optimal deposition speed for the hanging bridges. These types of constructs were tested by Ribeiro et al. (Ribeiro *et al.*, 2017) printing poloxamer-poly(ethylene glycol) (PEG) blends at different concentrations (poloxamer/PEG: 30%, 29/1%, 28/2%, 27/3%, 26/4% and 20%). They found that higher concentrations of P407 led to a decrease in bridge sagging, which coincides with our observations at higher concentrations of poloxamer.

We agree with He et al. (He *et al.*, 2016) that the ideal multi-material 3D bioprinter for tissue engineering applications should be high throughput, ease of use, with excellent print resolution, and capability of dispensing multiple bioinks with different viscosities. Even if some of the commercially available bioprinters incorporate all these specifications, we would like to stand up for the open-source bioprinters. This equipment can provide all discussed advantages plus avoiding the proprietary nature of the commercial ones. Indeed, our open-source 3D printing platform was capable of achieving high accuracy and cell viability in multi-material bioprinting with a relatively lower cost than other commercial units.

7.6 Time-efficient 3D printing through IDEX technology

Current multi-material MEBB systems have enough printing resolution to deposit biomaterials and cells in a precise spatial arrangement, however, most of them can only print one material at a time. This increases the print times required to fabricate constructs with clinically relevant sizes, hindering the expansion of this technology to large-scale applications. Besides, the duration of the printing process is a determining factor for cell-viability of printed constructs (Skardal & Atala, 2014). Excessive long bioprinting processes might decrease cell-viabilities, as cells nutrients and oxygen requirements are not fulfilled. In most of the extrusion-based multi-material bioprinting strategies, each biomaterial is loaded on single printhead (Kolesky *et al.*, 2014; Rutz *et al.*, 2015; Sears *et al.*, 2017). In this way, as more biomaterials are utilized, more printheads should be installed in the bioprinter. However, only one material can be deposited at a time and inactive printheads must wait for their printing turn until the active printhead has finished.

Desktop multi-material 3D printers can be divided into two categories according to how their printheads move in standard and independent dual extruders (IDEX) 3D printing systems (table 7.1). Standard multi-material systems integrate two or more printheads within the same x-carriage. This layout requires that all the printheads move at the same time, including those that are not utilized, and only one printhead can be printing at a time. In addition, since inactive printheads are placed close to the 3D printed construct, inactive nozzles could contaminate it with unwanted material or collide with the already printed model. However, in the last years has emerged a new 3D printing technique called IDEX. As its name suggests, IDEX 3D printers are built with independent x-carriages, which allows independent printhead movements from each other in the x-axis. This configuration permits to print multi-material constructs without interferences between printheads, as one x-carriage can be printing while the other is parked outside the printing area. Besides, the use of independent carriages allows the generation of multiple constructs at the same time, as several printheads can be utilized simultaneously. This approach arises as a promising bioprinting strategy to reduce significantly the print times of multi-material constructs, minimizing the idle times caused by inactive printheads.

Table 7.1: *List of commercially available multi-material desktop 3D printers with and without IDEX technology.*

Multi-material 3D printer	**Number of extruders**	**IDEX**	**Price (US$)**	**Positioning resolution x-y-z (μm)**	**Print volume x-y-z (mm)**
BCN3D Sigma R17	2	Yes	2.695	12.5-12.5-1	210-297-210
BCN3D Sigmax	2	Yes	4.295	12.5-12.5-1	420-297-210
Ultimaker 3	2	No	3.495	12.5-12.5-2.5	215-215-200
Ultimaker 3 extended	2	No	4.295	12.5-12.5-2.5	215-215-300
Ultimaker S5	2	No	5.995	6.9-6.9-2.5	330-240-300
FlashForge Creator Pro	2	No	929	11-11-2.5	227-148-150
MakerGear M3-ID	2	Yes	3.299	-	180-228-203
Zortrax Inventure	2	No	3.490	-	135-135-130
Cel RoboxPRO	2	No	5.158	-	210-300-400
Markforged Mark Two	2	No	13.499	-	320-132-154
Raise3D Pro 3D Printer	2	No	3.999	78	280-305-300

In this section, both printing techniques were evaluated from a time-efficient perspective using two open-source desktop 3D printers: Witbox 2 (standard) and Sigma (IDEX). Print times using both 3D printers were measured for the generation of multiple constructs. Four PHR printheads were installed in

both 3D printers, as this printhead permits an easy integration on most of the desktop 3D printers (figures 7.1 and 7.14). Printheads integration in Sigma and Witbox 3D printers was performed by merely changing the x-carriages couplings and screwing to them with four M3 bolts per printhead (see chapter 4 and 5). As shown in figure 7.14, Sigma 3D printer integrates two printheads on each x-carriage, while in Witbox 2 the four printheads were installed in the same x-carriage (figure 7.1). Each printhead contained the same biomaterial (P407) but dyed with a different color for a better error visualization.

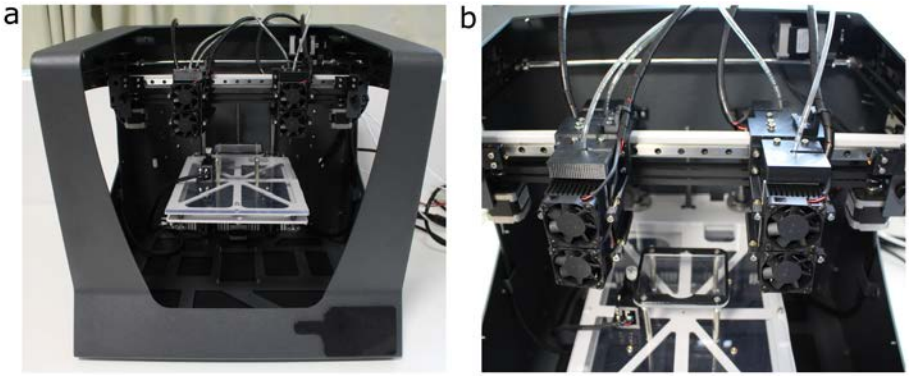

Figure 7.14: *General (a) and detailed view (b) of the modified Sigma 3D printer with four bioprinting printheads.*

The fabrication of multi-material 3D bioprinted constructs requires the use of multiple printheads within the same bioprinter. However, the integration of multiple printheads it is not an easy task, as it depends either on printheads dimensions and the space available in the bioprinter to install them. As a consequence, as more printheads are installed, the final usable print area decreases. We can observe this reduction in the 3D printers utilized for this study. The original print areas of Witbox 2 and Sigma are 297x210 mm and 210x297 mm, respectively. Figure 7.15 shows the print volume of both printers once the four printheads were installed. In standard 3D printing systems (Witbox 2), multiple printheads must be installed within the same x-carriage. This causes a significant reduction of the print area if compared with the use of a single printhead (100x25 mm) (figure 7.15a). However, if IDEX 3D printers are utilized instead (Sigma), the printheads are installed in two different x-carriages, which permits to have a bigger print area (130x140 mm) (figure 7.15b).

One of the key features of IDEX 3D printing systems is the possibility to fabricate multiple multi-material constructs at the same time using both x-carriages independently, either in duplication or mirror modes. This feature is especially useful to reduce print times, as multiple constructs can be generated

simultaneously. Standard 3D printing systems can also be utilized to print multiple constructs jointly, however, they present several disadvantages respect IDEX technology. First of all, while IDEX 3D printers allow controlling the distance between x-carriages, in standard systems the distance between nozzles is fixed. This feature is especially relevant, as the xy distances between printheads nozzles must be the same than the xy distances between the printing surfaces centers. Secondly, in standard systems the print area is considerably reduced, consequently, IDEX systems allow the use of more printing platforms at the same time. As shown in figure 7.15, Witbox 2 permitted the use of only two printing platforms, while in Sigma 3D printer the print area allowed the use of four printing platforms.

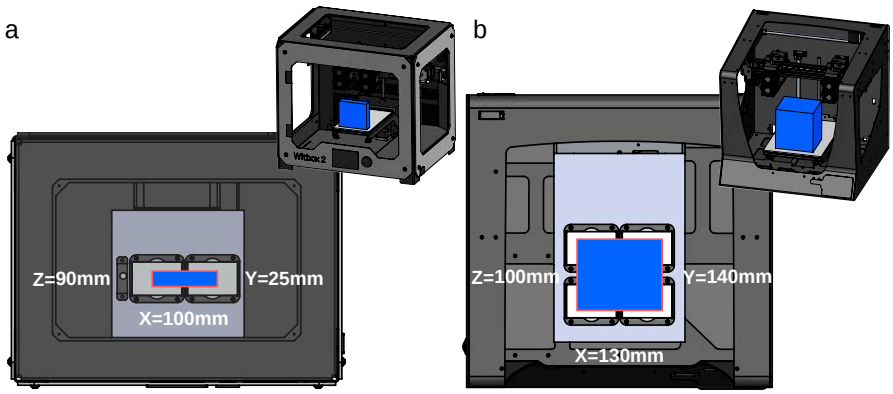

Figure 7.15: *Print volumes of Witbox 2 (a) and Sigma (b) 3D printers for multi-material bioprinting with four printheads installed (measures expressed in mm).*

The first step in the creation of a time-efficient bioprinting strategy was to determine which is the infill pattern that permitted the generation of constructs in the shortest possible time. We evaluated the print times required to print solid 12 mm cubes considering different infill patterns and densities. Four different infill patterns (honeycomb, Hilbert curve, octagram spiral and rectilinear) and infill densities (10%-12.5%-15%-17.5%) were evaluated (figure 7.16). G-codes were generated using Slic3r software, as described in chapter 5. Rectilinear infill revealed as the fastest 3D printing pattern from all tested, followed by octagram spiral (figure 7.17a). Hilbert curve and honeycomb patterns required similar print times, however, they needed twice the time than the rectilinear pattern for the 17.5% infill density. Print times increased rapidly with infill density following similar tendencies for all patterns except the rectilinear, in which a more moderate increase was observed.

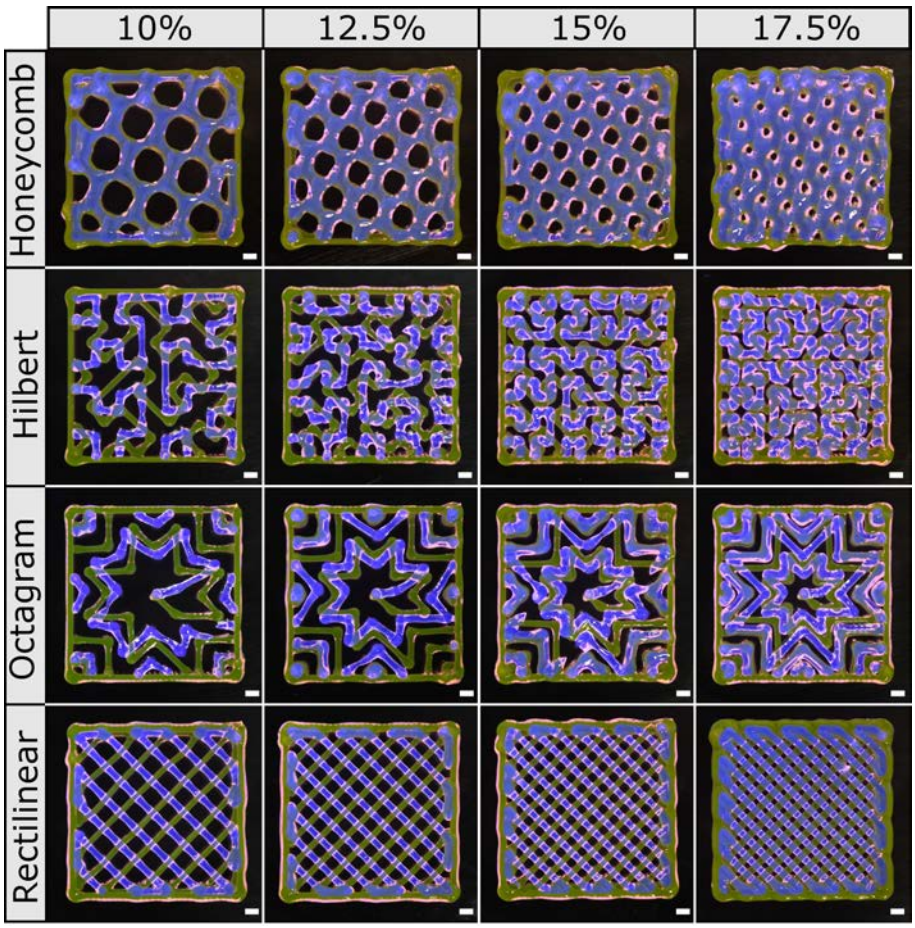

Figure 7.16: *Bi-material constructs printed in 40 wt% P407. P407 was deposited printed at 25 ºC, using a 200 um ID nozzle, a deposition speed of 15 mm s-1 and 2 layers stacked. G-code generated using Slic3r from solid cubes with a 12 mm side, different fill patterns, and densities. Scale bars: 1 mm.*

Once the rectilinear pattern showed as the best infill option in terms of print speed, various multi-material constructs were generated using this pattern. In the conventional 3D printing approach, each construct is printed sequentially in a single printing platform using one printhead at a time. However, the approach here proposed permits to generate several multi-material constructs, printed in different glass slides and using various printheads simultaneously. Both printing strategies (sequential and simultaneous) were analyzed, measuring the print times required to generate the same constructs. Each experiment was named according to the number of printheads (P), printing platforms or bases (B) and materials (M) utilized. For example, a 4P-2B-2M configuration means that 4 printheads have been utilized to print in 2 different printing platforms a bi-material construct. Poloxamer P407 with a deposition speed of 15 mm s^{-1} was utilized in all samples. Printheads travel speed when P407 was not deposited was 60 mm s^{-1}.

The first experiment consisted of printing two bi-material constructs using standard and simultaneous 3D printing strategies. Using the standard approach, the constructs were printed sequentially using two printheads, each with a different material (2P-1B-2M). In the IDEX approach, both constructs were printed using four printheads, two of them being utilized simultaneously, each one on a different printing platform (4P-2B-2M). Results showed that simultaneous deposition is able to reduce print times up to 1.6 times than sequential 3D bioprinting (figure 7.17b). In this case, it was possible to implement the simultaneous 3D printing strategy in Witbox 2 and Sigma 3D printers, as their usable printing area is big enough to place two independent platforms (figure 7.15). No significant differences between both 3D printers were found in this case.

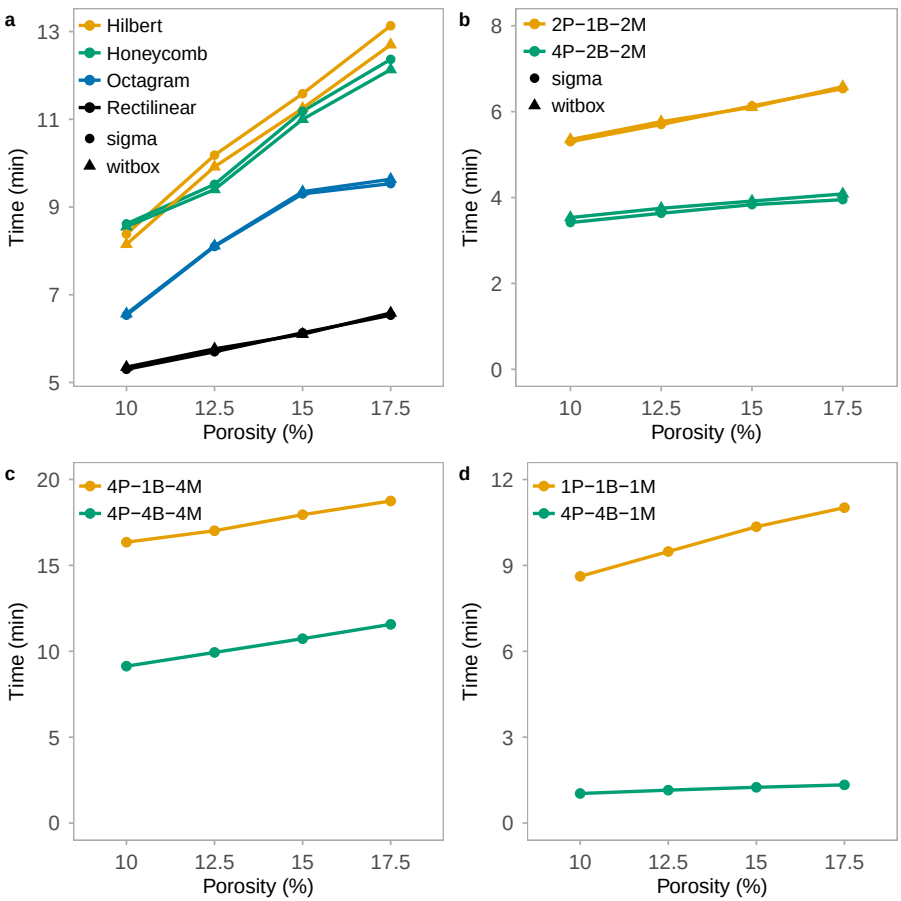

Figure 7.17: *(a) Sigma and Witbox 2 print times for different infill patterns and degree of porosity. (b) Sigma and Witbox 2 print times for a bi-material construct printed simultaneously (4P-2B-2M) and sequentially (2P-1B-2M). (c) Sigma print times for a for-material construct printed simultaneously (4P-4B-4M) and sequentially (4P-1B-4M). (d) Sigma print times for a single-material construct printed simultaneously (4P-4B-1M) and sequentially (1P-1B-1M).*

The second experiment consisted of printing four multi-material constructs using four different materials (figure 7.18a-b). As Witbox 2 print area

was not big enough to hold four independent bases (figure 7.15a), only Sigma 3D printer was utilized in this case. On one hand, four printheads loaded with different materials were utilized to print four-material constructs in four different platforms (4P-4B-4M). On the other hand, each four-material construct was printed in a single platform sequentially (4P-1B-4M). Results revealed that printing the four-material constructs using the simultaneous approach permitted to reduce print times almost by half (figure 7.17c).

Finally, we evaluated the print times required to print four single-material constructs using four printheads simultaneously (4P-4B-1M) and just one printhead sequentially (1P-1B-1M). As explained before, only Sigma 3D printer could be utilized. Results showed that printing with four printheads simultaneously, it was possible to produce the same construct 8 times faster than using the traditional sequential 3D printing (figure 7.17d).

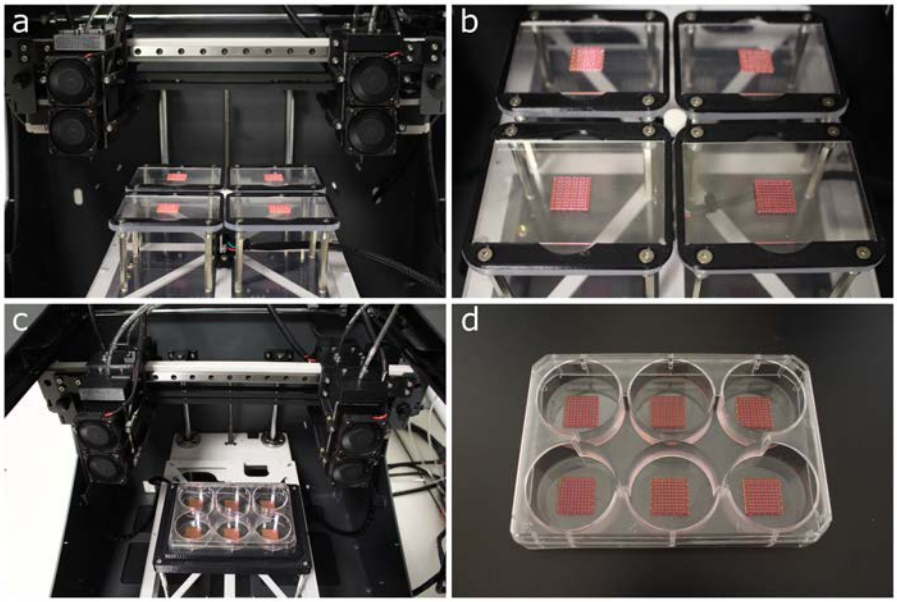

Figure 7.18: *General and detail images of multi-material porous constructs printed in Sigma 3D printer and IDEX strategy using four printing platforms simultaneously (a-b) and a cell culture plate of 6 wells (c-d).*

Besides the glass slides utilized, simultaneous 3D printing can be applied to other printing as printing surfaces such as culture plates with several wells (figure 7.18c-d). In addition, this 3D printing approach can be utilized not only in 3D bioprinting but to any AM process in which a time reduction is required.

7.7 Conclusions

The use of multiple cell types and biomaterials is essential to recapitulate the architecture, mechanical strength, and complexity of human tissues. Moreover, in 3D bioprinting, maintaining the print resolution along the layer-by-layer manufacturing process offers greater stability when creating thick self-supporting tissue constructs. In this chapter, we have presented a non-expensive and useful calibration method applicable to 3D bioprinters with multiple printheads. The particular multi-material 3D bioprinters herein used were desktop 3D printers modified to incorporate four independent MEBB printheads.

P407 hydrogel mixed with four fluorescent dyes was utilized as the base bioink for the calibration due to its remarkable stability. Our calibration procedure is exportable to any bioprinting system, but it is strongly recommended to use the automatic push-button system to reduce the print errors in the z-axis and calibration times drastically. Besides, parameters such as the printing pressure, deposition speed, nozzle height, and nozzle diameter were evaluated from the experimental results to obtain the optimal printing conditions. To prove the method using different biomaterials, multi-material constructs were printed in different combinations of P407 and Gel-Alg bioinks. Besides, complex multi-material 3D models and intricate vascular networks were created assessing the final accuracy and printing precision of the bioprinting platform. Other technologies such as drop-on-demand bioprinting could also benefit from the method proposed, due to the universality of the proposed multi-material calibration method.

Moreover, a novel 3D printing strategy was presented, which implies the use of IDEX technology and the production of multiple constructs using several printheads simultaneously. Two open-source 3D printers (Witbox 2 and Sigma) were utilized to compared both standard and IDEX 3D printing approaches. Simultaneous and conventional 3D printing strategies were evaluated from a time-efficiency perspective. Results showed a substantial print time reduction when multiple printheads were utilized simultaneously, compared with the conventional sequential 3D printing strategy. The results obtained represent an interesting approach in the bioprinting field to generate various constructs simultaneously, which implies a reduction of cell death due to excessive print times. In this way, using several printheads at the same time allowed to minimize idle times caused by inactive printheads, and thus reduce the overall printing times.

Chapter 8

Efficient scaffolds fabrication for printing hybrid constructs

In TE, the use of 3D printing for the fabrication of scaffolds has steadily increased over the past years (Lam *et al.*, 2009; Li *et al.*, 2017; Mitsak *et al.*, 2011). Many biocompatible materials have been successfully printed, but one of the most outstanding synthetic resorbable polymers is polycaprolactone (PCL) due to its mechanical strength, stiffness (enough to influence cell behavior (Hendrikson *et al.*, 2015)) and tailorable degradation kinetics (Lam *et al.*, 2007, 2008). PCL cannot directly be formulated with cells (Groll *et al.*, 2018), but many in-vitro studies have shown clear cell spreading, attachment and extracellular matrix formation over the scaffolds (Li *et al.*, 2003, 2017; Park *et al.*, 2018). It is also easy to manufacture due to its superior viscoelastic and rheological properties over many of its resorbable counterparts (Woodruff & Hutmacher, 2010). These features enable the generation of complex functionally graded scaffolds with precise control of the internal porosity and strands diameter at low cost.

Several AM technologies such as fused deposition modeling (FDM) (Guerra *et al.*, 2018; Ramanath *et al.*, 2008) and microextrusion-based systems (Gupta *et al.*, 2018) are suitable to extrude PCL and produce scaffolds with controlled porosity through a layer by layer approach. FDM is a technology particularly useful for filament-type polymers of very low viscosity at high temperatures such as PLA or ABS. Even if FDM has also been used to produce 3D scaffolds of PCL (Zein *et al.*, 2002), extrusion-based systems can deposit molten PCL at low temperature but at much higher pressure than FDM. Two types of extrusion-based system are currently employed: pneumatic and mechanical. As viscosity and strength of PCL depend on its molecular weight (Grosvenor & Staniforth, 1996),

mechanical-based systems that generate higher extrusion pressures are preferred for PCL of high molecular weight (Kim & Son, 2009; Seyednejad *et al.*, 2011). On the other hand, PCL with low and intermediate molecular weight can be extruded with pneumatic systems due to lower pressure requirements (Trachtenberg *et al.*, 2014; Kundu *et al.*, 2015). Herein, we use a pneumatic printhead for PCL extrusion similar to the ones used for bioprinting, but with the capacity to work at significantly higher pressure, and print temperature above 80 ºC.

Novel AM systems that integrate biomaterials and cell-laden hydrogels deposition have gained much attention for their potential application into the generation of human-scale tissue constructs of any shape such as calvarial bone, cartilage, and skeletal muscle, among others(Kang *et al.*, 2016; Visser *et al.*, 2013; Olubamiji *et al.*, 2016b; Shim *et al.*, 2012). These so-called "printed hybrid TE constructs" combine 3D scaffolds of complex architectures, cell-laden bioinks extruded in integrated patterns, and microchannels that allow the diffusion of nutrients and oxygen across the construct. Their aim is to assure cell survival and enough structural integrity for surgical implantation. While the bioinks support cell survival and proliferation, the scaffold provides enough structural integrity and mechanical resistance needed for surgical implantation (Khademhosseini & Langer, 2016). Building hybrid constructs requires the use of multiple printheads with precise calibration and accurate temperature control (Pati *et al.*, 2013). The use of high print speeds for the generation of hybrid constructs results critical for reducing the total print time. Long print times dramatically decrease cell viability (Skardal & Atala, 2014). Shorter ones are preferred, but the printing accuracy cannot dismiss because a precise material deposition is also essential for cell viability. Also, printing the scaffold at high temperatures decreases cell viability of the already printed bioinks (Shim *et al.*, 2012). Therefore, selecting the most appropriate print parameters for each specific application is needed to balance print temperature, accuracy and carriage speed.

In this chapter, it is explored the possible values of certain print parameters that could help in generating precise scaffolds of PCL while minimizing print times. The main candidates, which have a direct influence on the PCL flow rate, were print temperature, nozzle shape and diameter, carriage speed, and inlet pressure. For the first time, it was investigated the differences in flow using three types of nozzles with different diameters under the same 3D printing platform: conical, cylindrical and cylindrical shortened. Experiments were performed using an open-source 3D printer with a custom-designed high-temperature printhead for extruding PCL (see chapter 4). This makes the results easily replicable by

other laboratories. Computational fluid dynamics (CFD) simulations of the extrusion process were carried out to gain a more comprehensive understanding of the flow of PCL inside the different nozzles. The results obtained are useful when selecting the best configurations to produce the supporting structures of a hybrid construct in the shortest print time without dismissing print accuracy.

8.1 CFD model and constitutive equations

A CFD simulation of PCL flowing through different nozzle geometries was conducted in ANSYS® Academic Research Fluent, Release 19.2 (ANSYS Inc, Canonsburg, PA, USA). The extrusion of PCL was simulated as a non-isothermal steady state process (discarding the melting process, the start-up and the shutdown phases), coupling fluid flow and heat transfer problems. A 2D-axisymmetric model was chosen for the simulations, considering the characteristic volume-of-revolution of both the syringe and the nozzle. Different rectangular cell sizes were tested and the final mesh was chosen for mesh independence of the solution, accuracy and computational effort.

Conical, cylindrical and shortened cylindrical nozzles with the same ID (437 μm) were simulated to evaluate the dynamics of PCL extrusion. The nozzles were modeled as stainless-steel parts that receive the PLC flow heated in the syringe. The heat transfer between the nozzle and the surrounding air was evaluated with an additional simulation using an extended domain. This simulation gave a mean heat transfer coefficient (HTC) between nozzle and air of 4 W/m^2K for an air-free stream temperature of 21 ºC.

A pressure inlet boundary condition of 700 kPa was imposed at the upper part of the syringe. The nozzle output was set as a pressure outlet at atmospheric pressure. The non-slip condition was imposed for all the walls. The stainless-steel syringe, at a constant temperature of 120 ºC, was considered as a thermally insulated part that transferred heat to the incoming PCL fluid.

The pseudoplastic PCL CAPA 6400 was modeled as a generalized Newtonian fluid using the Bird-Carreau viscosity law (Carreau, 1972; Bird & Carreau, 1968):

$$\eta_t(\dot{\gamma}) = \eta_0[1 + (\lambda\dot{\gamma})^2]^{\frac{n-1}{2}} \tag{8.1}$$

where η_t represents the viscosity law at some reference temperature T_{ref}, η_0 the zero-shear viscosity, $\dot{\gamma}$ the shear rate, λ the relaxation time and n the degree of shear-thinning, a material-dependent factor. The parameters of the Bird-Carreau equation (table 8.1) were extracted from the experimental data provided by the manufacturer, showing that this model fitted well the experimental data in those conditions figure 8.1).

Table 8.1: *Bird-Carreau parameters and activation energy value used in the viscosity model of PCL for a T_{ref} of 100 ºC.*

Bird-Carreau parameters			
Zero-shear viscosity (η_0) (Pa s)	n	λ	Activation energy (E_a) (kJ/mol)
291.3	0.8	0.0083	30.7

The temperature dependence of the viscosity was modeled as:

$$\eta = H(T)\eta_t(\dot{\gamma}) \tag{8.2}$$

where η_t ($\dot{\gamma}$) is the viscosity law at some reference temperature T_{ref}, and H(T) is the Arrhenius law (Arrhenius, 1967):

$$H(T) = e^{[\frac{E_a}{R}(\frac{1}{T-T_0} - \frac{1}{T_{ref}-T_0})]} \tag{8.3}$$

where E_a is the activation energy, R is the thermodynamic constant, T_0 corresponds to the lowest absolute temperature that is thermodynamically acceptable and T_{ref} is the reference temperature. E_a was obtained from equations 8.2 and 8.3 using a T_{ref} of 100 ºC and the zero-shear viscosity values provided by the manufacturer at 125 ºC and 150 ºC (152 Pa s and 95 Pa s, respectively).

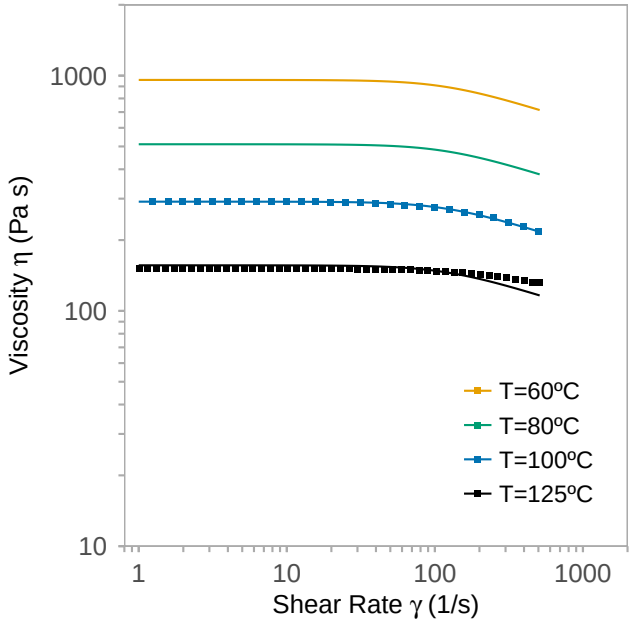

Figure 8.1: *Viscosity versus shear rate relationship of CAPA 6400. Points represent the experimental data provided by the manufacturer for temperatures 100 ºC and 125 ºC. Solid lines are the Bird-Carreau model fittings calculated according to equation 8.2.*

8.2 Influence of temperature, shape and diameter of nozzles on PCL flow rate

Nozzle limitations regarding flow rate were investigated when extruding PCL at 700 kPa with two nozzle geometries: cylindrical (Trachtenberg *et al.*, 2014; Olubamiji *et al.*, 2016a) and conical (Kang *et al.*, 2016). Conical nozzles (Micron-S dispensing tips; Fisnar, United Kingdom) and cylindrical nozzles (Stainless steel dispensing tips; Fisnar, United Kingdom) with different IDs were utilized to print the PCL (table 8.2). Shortened cylindrical nozzles with the same IDs than standard cylindrical nozzles were generated by cutting the needle from 13 to 2 mm (figure 8.2a).

Table 8.2: *Conical and cylindrical nozzles utilized in the experiments with their corresponding gauge and inner diameter (ID).*

	Inner diameter (ID) (μm)									
Conical	233	-	335	437	-	-	-	-	-	-
Cylindrical	-	300	-	-	510	600	690	840	1070	1200
Gauge	*G30*	*G24*	*G27*	*G25*	*G21*	*G20*	*G19*	*G18*	*G17*	*G16*

The volumetric flux, which is the rate of volume flow across a unit area, was calculated to eliminate the influence of the different nozzle diameters and

shapes on the results. To this end, we weighted the quantity of PCL extruded in one minute P and we calculated the volumetric flux as follows:

$$Q = P/(60\rho A) \tag{8.4}$$

where A is the outlet area and ρ is the density of PCL CAPA™ 6400 provided by the manufacturer (1100 kg/m^3).

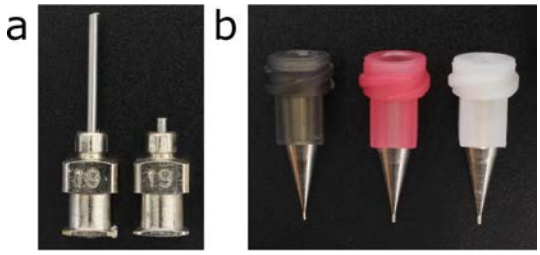

Figure 8.2: *Nozzles selected for the experiments. (a) Stainless steel cylindrical standard (left) and shortened (right) nozzles of gauge G19. (b) Conical nozzles of gauge G30, G27 and G25 respectively, from left to right.*

Cylindrical nozzles are known to produce lower flow rates than conical ones (Olubamiji *et al.*, 2016b; Billiet *et al.*, 2014), but their use is widely extended. However, we first explored the potential benefits of using a so-called cylindrical shortened nozzle, which has a needle of reduced length (figure 8.2a). Shortened cylindrical nozzles exhibited significantly higher volumetric flux than the standard ones (figure 8.3a) because the temperature drop through the needle decreased (figure 8.3b). Interestingly, the differences in flow were even more significant when printing with the largest diameters. For instance, shortened cylindrical nozzles with diameters 690 μm and 840 μm generated volumetric fluxes 7 and 12 times higher than the standard ones, respectively (figure 8.3a). On the other hand, no flow was detected when using standard cylindrical nozzles with diameters less than 600 μm (figure 8.3c). Therefore, a heating cover should be installed till the tip of the dispensing syringe to avoid the dramatic temperature drop that increases the PCL viscosity. However, when building hybrid constructs, these high temperatures near the tip outlet might also affect the evaporation rate of the already printed bioinks.

When printing PCL with nozzles of small diameter (less than 510 μm), conical nozzles always generated greater volumetric fluxes than shortened ones (figure 8.3c). Even if different gauges were used, this trend held over the range

of conical nozzle diameters used in this study. We also confirmed the important variation in the flow depending of the diameter of the conical nozzle chosen (figure 8.3d). Volumetric flux increased more rapidly when printing with nozzles of large diameter at high print temperatures (figure 8.3d). For example, the volumetric flux of the conical G25 nozzle at 140 ºC was around 5 times higher than that at 80 ºC. However, these differences were only around 4 times for nozzles of 335 μm and 233 μm. These observations are meaningful because the higher the flow, the faster the carriage can move. Therefore, even if the user raises the temperature when printing with nozzles of small diameter, the increase in volumetric flux will not be as significant as when using the largest ones. Thus, these results demonstrated that both shape and diameter were essential to facilitate the extrusion flow. Note that the values of volumetric flux displayed before cannot be directly utilized as print speeds for the 3D printing setup because these experiments were generated under constant pressure in free air, and not over a printing surface.

The PCL flow strongly depends on the evolution of the print temperature along the nozzle and on its geometry (Sheshadri & Shirwaiker, 2015). Overall, the results of the CFD simulations allowed foreseeing limitations in the extrusion process and gave a more comprehensive understanding of the PCL flow inside the nozzles studied. The constitutive model incorporated the dependency of the PCL viscosity from the shear rate and the temperature using the Bird-Carreau viscosity law (Bird & Carreau, 1968) along with the Arrhenius law (Arrhenius, 1967). A reasonable agreement was achieved between the experimental data and the simulations with mean relative errors of 6% and 12% in the case of variables temperature and volumetric flux, respectively. The velocity profiles obtained at the tip of the three nozzles (figure 8.3e) confirmed that the conical nozzles showed the highest volumetric flux for both large (figure 8.3a), and small diameters (figure 8.3d).

We determined the influence of the needle length on the extrusion rate by simulating a cylindrical nozzle with needle lengths ranging from 2 to 13 mm (figure 8.3f). The standard cylindrical nozzles (13 mm length needle) are mostly exposed to the air, transferring their heat to the surroundings and producing a dramatic increase in the viscosity of the PCL. The velocity profiles showed the importance of these features in the extrusion of PCL, with greater extrusion flow as the nozzle was progressively shortened. We would also like to point out that the registered velocity profiles (figure 8.3e and 8.3f) follow the parabolic shape representative of Newtonian fluids, perhaps indicating a reduced influence of the shear rates on the PCL viscosity. This could be because the shear rate values

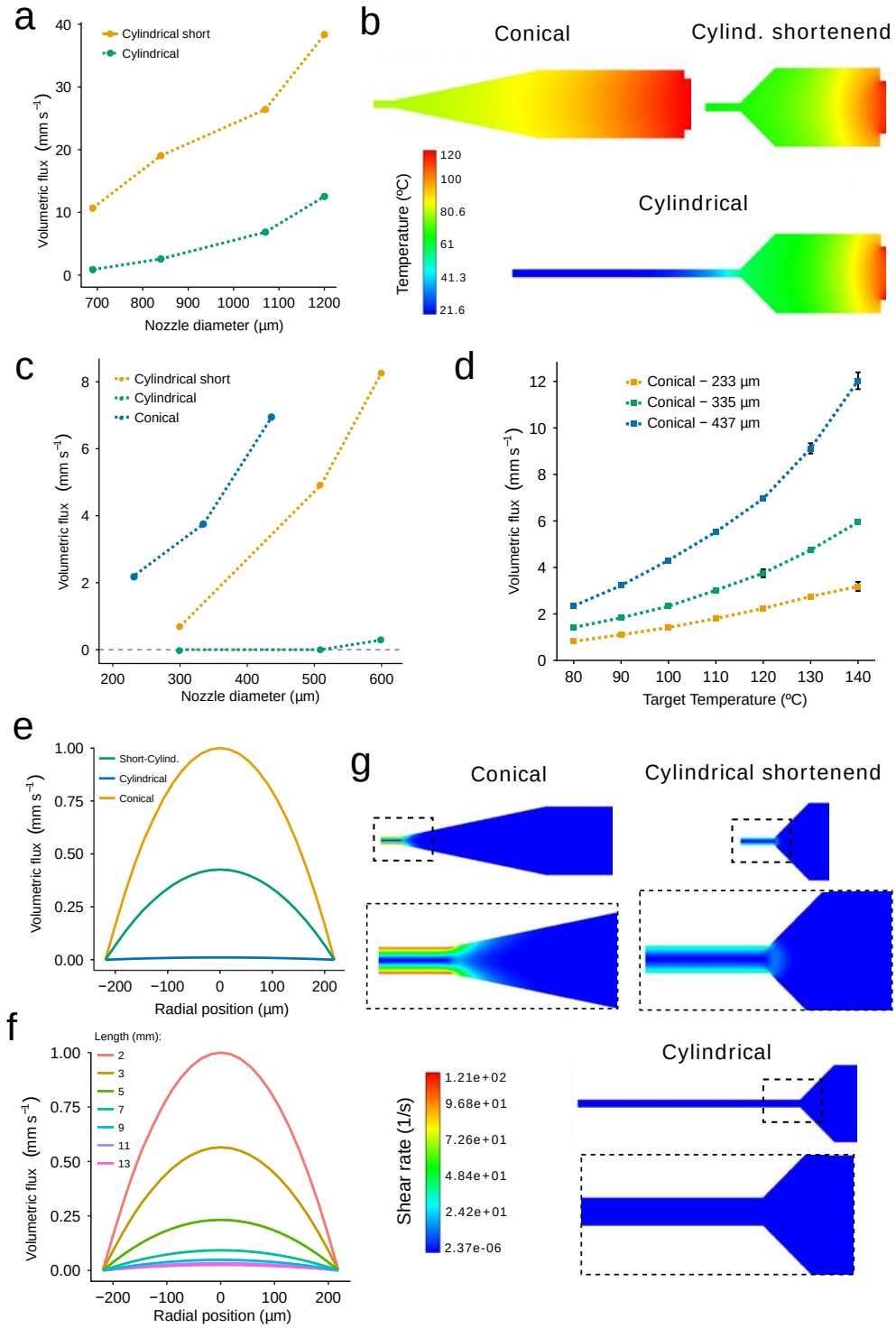

Figure 8.3: *Experimental volumetric fluxes and results from the CFD simulations using different nozzle geometries. Extrusion was simulated at target temperature 120 ºC, inlet pressure 100 kPa, and using a conical G25 nozzle. (a) Relationship between volumetric flux, nozzle shape and ID ranging from 690 µm to 1200 µm for a fixed print temperature of 120 ºC. (b) Temperature contour plots from the CFD simulation using conical, cylindrical and shortened cylindrical (2mm length) nozzles. (c) Relationship between volumetric flux, nozzle shape and ID ranging from 233 µm to 600 µm for a fixed printing temperature of 120 ºC. (d) Influence of print temperature in the extrusion flow rate for different conical nozzles with different IDs. (e) Velocity output profiles from the CFD model when using the three G25 nozzle types. (f) Velocity output profiles from the CFD model when using the cylindrical G25 nozzles with variable lengths, from 13 mm to 2 mm. (g) Shear rate contour plots from the CFD simulation using conical, cylindrical and shortened cylindrical (2mm length) nozzles. The data represent the mean and standard deviation of six experiments (n=6).*

during the extrusion were small in all cases (figure 8.3g), so the PCL viscosity is always near the upper plateau causing the Newtonian behavior. Similar to (Billiet *et al.*, 2014), the nozzle geometry with the highest shear rates was the conical one. In this case, all shear rate values were smaller than 121 s^{-1} and located in a region at 80 ºC. In further investigation, we plan to check possible inconsistencies in the model at low print temperatures (80 - 60 ºC) where the plateau will be reduced because the departure point from the constant-viscosity regime will move towards left.

We can conclude that the PCL volumetric flux at constant target temperature and pressure is strongly dependent on the nozzle morphology that conditions shear rate and print temperature at the nozzle tip. Consequently, the conical nozzles revealed as the best choice concerning extrusion flow, while the shortened nozzles are preferred to the standard cylindrical ones unless the temperature along the nozzle is entirely controlled.

8.3 Determination of the carriage speeds of PCL extrusion

It is well-known that not only pore size and porosity have an impact on cell attachment and proliferation, but also scaffold architecture has a significant influence on tissue growth kinetics (St-Pierre *et al.*, 2005; Bidan *et al.*, 2012). As the degradation of the scaffolds progress, the size of their strands or filaments decreases while their pore size increases (Lam *et al.*, 2008). So, we need above all a precise control of the diameter of the scaffold strands just after printing. Therefore, we first examined the printed strands of PCL regarding section shape (roundness), dimensions, and discontinuities using conical nozzles, which exhibited the best performance in the previous section (figure 8.3c).

Straight PCL filaments were printed onto a glass slide using different values of print temperature, nozzle diameter, and carriage speed. The same printing pressure (700 kPa) was utilized for all samples. In line with the experiments performed in chapter 7 and the scheme of figure 8.4, the layer height in the slicing software was set to the same value as the nozzle diameter. The strand roundness was calculated as the ratio between the measured height and width of the printed filaments. A roundness of 1 represents a perfect circle, and values lower than 0.3 represent flattened strands.

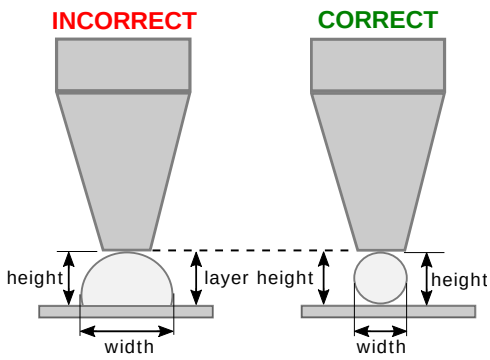

Figure 8.4: *Scheme of the layer height adjustment to evaluate the influence of the carriage speed on the PCL deposition. Slow speed produces wider and flatten filaments of PCL (left) while the correct carriage speed should generate homogeneous filaments of widths similar to nozzle diameter (right).*

The higher the print temperature, the greater carriage speed could be used. The maximum carriage speed at 140 ºC was 14, 9, and 4 mm s^{-1} for the G25, G27, and G30 conical nozzles, respectively. As the print temperature was lowered to 120 ºC, carriage speeds have to be reduced in 21, 33, and 50% for G25, G27, and G30 conical nozzles, respectively. The same trend was observed for 80 ºC, and 100 ºC. Slow carriage speeds generated filaments of low roundness (figure 8.5a), with the worst values (between 0.3 and 0.5) obtained at the lowest carriage speeds (1 - 2 mm s^{-1}). This effect was even more pronounced when the target temperature was higher than 120 ºC due to the low viscosity of the PCL. Visual examination of the printed filaments revealed excessive PCL deposition with the material flattening against the print surface (figure 8.5b and 8.5c). Similar results with a notable increase in the width of the PCL strands as print temperature rises were reported by Sheshadri et al. (Sheshadri & Shirwaiker, 2015).

The increase in roundness was directly proportional to the carriage speed, reaching values close to one in some cases. In addition, we observed that low target temperatures reduced drastically the range of potential values for the carriage speed. This could be mainly due to an increase in viscosity with a decrease in nozzle temperature, which was also evidenced by the constitutive equation (see equation 8.2 and figure 8.1).

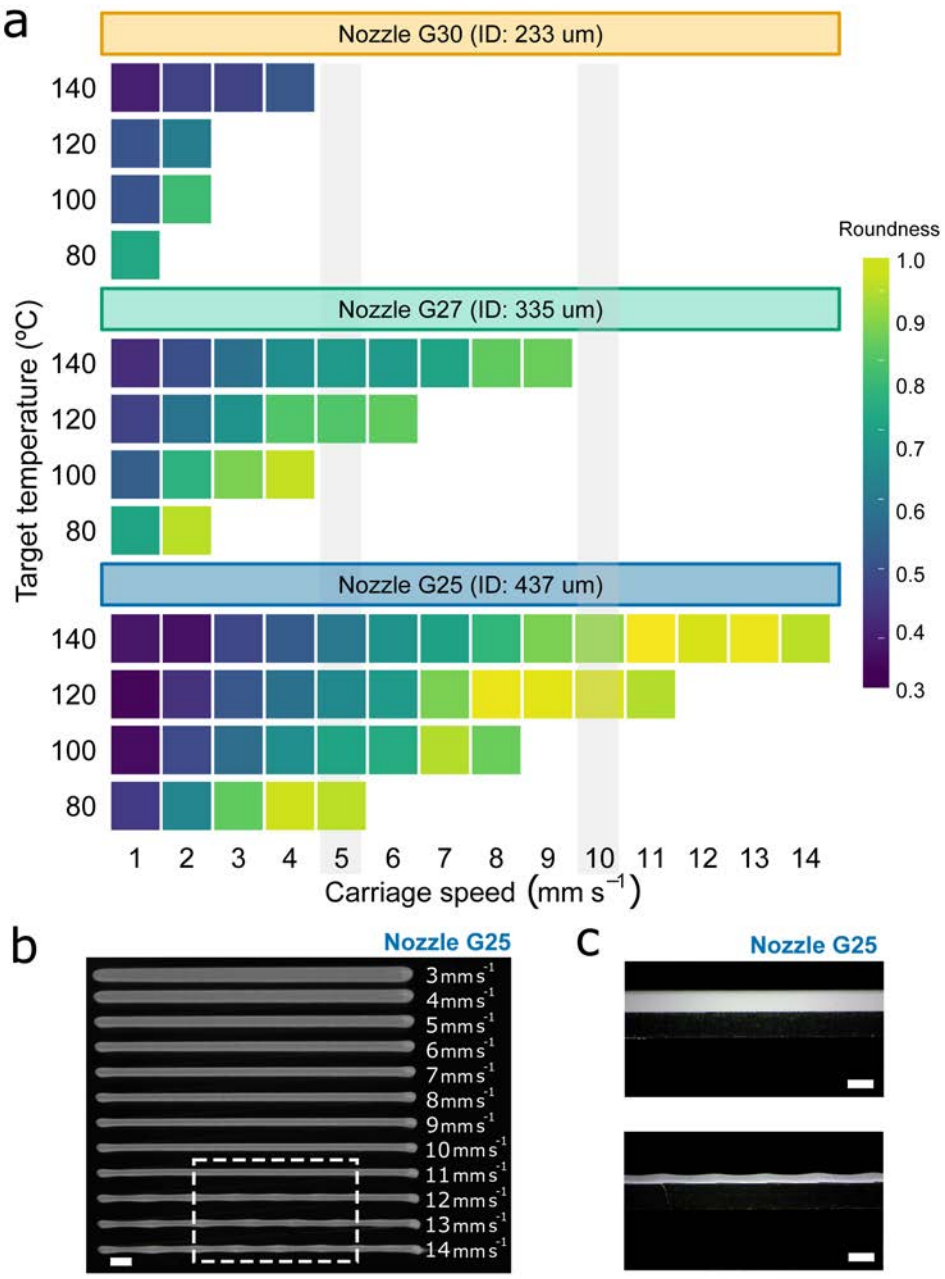

Figure 8.5: *Evaluation of properties of the printed PCL strands. (a) Evolution of the roundness of the printed PCL strands versus the carriage speed for three conical nozzles at different target temperatures. White areas are those in which strands of heterogeneous section are produced due to an excessive carriage speed. (b) Representative image of twelve filaments of PCL printed using a G25 conical nozzle at 120 ºC and carriage speeds ranging from 3 to 14 mm s^{-1}. The white dash box indicates the heterogeneous sections due to the excessive carriage speed. (c) Representative photographs of the height of PCL filaments printed using a G25 conical nozzle at 120 ºC and carriage speeds of 15 mm s^{-1} (upper) and 1 mm s^{-1} (lower). Scale bars: 1 mm.*

When carriage speeds are higher than a particular threshold, small fluctuations on this speed may easily lead to inconsistencies in the extruded material (see the waves at the bottom of figure 8.5b). In these cases, the PCL was de-

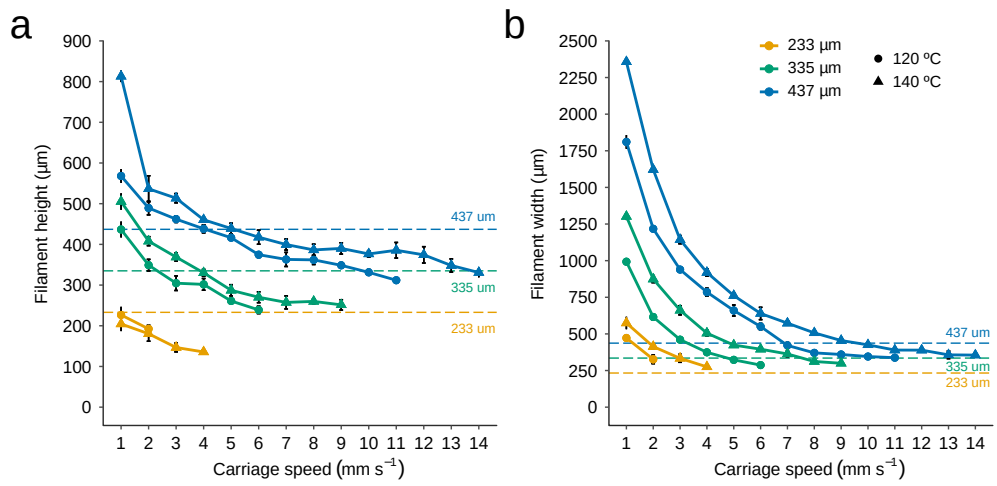

Figure 8.6: *Evolution of the dimensions of the strands of PCL printed versus carriage speed. (a) Height and (b) width of the strands for the three conical nozzles studied were measured at pressure 700 kPa and target temperatures 120 ºC and 140 ºC. Data represent the mean and standard deviation of six different samples (n = 6).*

posited either discontinuously or in strands of heterogeneous section (figure 8.5c). Note that the threshold for the smallest conical nozzle working at low temperatures was so low (around 2 mm s^{-1}) that there was very little room for maneuver. On the other hand, PCL filaments were not only more rounded at high carriage speeds, but also almost always smaller than the nozzle ID (figure 8.6a and 8.6b). This effect was more visible when lowering the target temperature from 140 to 120 ºC. These results agreed with the observations presented by Shim et al. (Shim *et al.*, 2012), where strand widths ranging from 275 µm to 90 µm were generated using a nozzle of ID 200 µm. We conclude that homogeneous strands of small diameter can be printed with nozzles of large gauge (> G20) at a much faster speed (figure 8.6a). This situation is beneficial for our aim of creating hybrid constructs because the higher the speed, the lower the print time results.

8.4 Evaluation of PCL print times

Time is one the most critical problems in biofabrication because it affects productivity, cell viability, and limits the construction of large-scaled tissues, which will ultimately be mandatory if real tissue replacements want to be generated Murphy & Atala (2014). When bioprinting hybrid constructs, there is a notable increase on the time required due to their inherent complexity. Long print times, including the preparation of the bioinks, will severely decrease cell viability burdening the future of the tissue construct because the cell nutrients and oxygen requirements might not be reached on time (Skardal & Atala, 2014).

To study these matters, scaffolds of different porosity were generated using conical nozzles of three distinct diameters (figure 8.7). The target temperature was kept constant (120 ºC) and we adjusted the carriage speeds to each nozzle. The carriage speeds were selected according to the results displayed in figures 8.5a and 8.6 with the widths of the strands matching nozzle IDs. These values were 2, 5, and 7 mm s^{-1} for the 233, 335, and 437 μm nozzles, respectively. Note that smaller nozzles require more trajectories per layer than the large ones to generate scaffolds of similar porosity, as the latter creates thicker strands than the former. A higher number of trajectories also implies longer print times, which is particularly important when creating hybrid scaffolds. For instance, creating the scaffold of porosity 20% with the nozzle of ID 437 μm required 2.6 min, while 335 μm and 233 μm nozzles required 5.9 min and 19.6 min, respectively. Our results confirmed the linear relationship between porosity and print time (figure 8.7b). The implications of these factors should be analyzed carefully when looking for significant reductions in the print time of PCL scaffolds.

As shown in the previous section, it is possible to generate scaffolds with the same strand diameter using different nozzle sizes. For instance, printing the scaffolds in the middle row of figure 8.7 (ID: 335 μm) can be done in three different ways. In figure 8.7, the most obvious solution for creating strands of diameter 335 μm is to employ a combination 335 μm / 5 mm s^{-1} (ID / carriage speed). It would be also feasible to produce these strands with 233 μm / 2 mm s^{-1} or even with 437 μm / 11 mm s^{-1}. The three options would provide the same diameter, but the largest nozzle (437 μm) will demand the shortest print times.

During PCL 3D printing, it is necessary that each layer solidifies (or at least gains enough consistency) before the next layer is stacked. Otherwise, as more layers are stacked, the whole scaffold will deform as a consequence of standing their own weight in a non-consistent state. This aspect will depend on some features such as PCL properties, layer dimensions, processing temperature, print speed or strand diameter. Within these experiments, PCL solidification times varied depending on the printing temperature utilized, with 120 ºC and 140 ºC requiring longer times. When using these printing temperatures with slow print speeds (from 1 to 4 mm s^{-1}), no additional cooling was required for an accurate layer stacking. However, when print speeds were higher than 4 mm s^{-1}, a layer fan was utilized to enhance the cooling of deposited PCL strands (figure 8.8). The layer fan was attached to the printhead using a 3D printed fan support that directed the air flow to the printed construct. The enhanced cooling enabled

using faster print speeds without scaffold deformations when multiple layers were stacked.

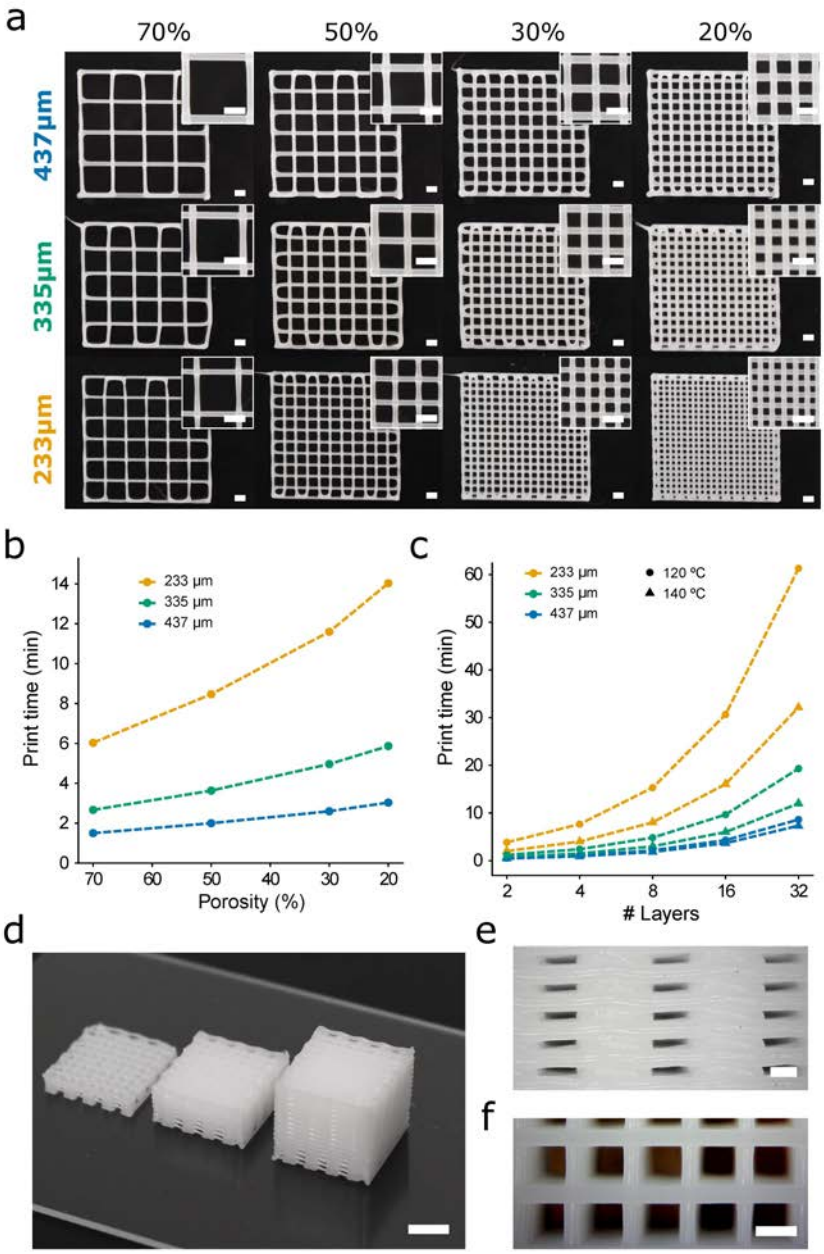

Figure 8.7: *Influence of porosity percentage, and layers stacked on the print time. (a) Two-layered PCL porous scaffolds of porosity ranging from 70 to 20% were printed using conical nozzles of three diameter at target temperature 120 ºC, and pressure 700 kPa. The travel speed of the printhead was adjusted to make the width of the strands match the nozzle ID (233 µm: 2 mm s^{-1}; 335 µm: 5 mm s^{-1}; 437µm: 7 mm s^{-1}). Scale bars: 1 mm. (b) Print times to produce a 12 x 12 mm scaffold of 8 layers and different degrees of porosity at 120 ºC. The carriage speeds selected to produce strands of 335 µm diameter were 2, 5, and 11 mm s^{-1} for nozzles 233, 335, and 437 µm, respectively. (c) Print times for a 12 mm square side scaffold, with a 30 % porosity and several layers stacked. Maximum print speeds were utilized for each nozzle-temperature configuration. (d) PCL porous structures created by stacking 8 (left), 16 (center), and 32 (right) layers. Scale bar: 5 mm. Side (e) and top (f) views of 3D scaffold of 32 layers printed with a 437 µm nozzle at 140 ºC and speed 14 mm s^{-1}. Scale bars: 500 µm.*

Production of scaffolds with clinically relevant size requires a compromise between print speed and resolution. We studied the scalability by printing the same porous scaffold, i.e. the same number of trajectories, but increasing the number of layers stacked. Figure 8.7c illustrates the influence of the carriage speed over the total print time per scaffold. The carriage speed selected for each nozzle was the highest possible at 120 ºC (233 µm: 2 mm s^{-1}; 335 µm: 6 mm s^{-1}; 437 µm: 11 mm s^{-1}) and 140 ºC (233 µm: 4 mm s^{-1}; 335 µm: 9 mm s^{-1}; 437 µm: 14 mm s^{-1}). We observed that the highest speeds, which are associated to large nozzles, permitted faster scaffolds generation. For example, the production of a porous scaffold with 32 layers stacked printed at 120 ºC would require 10 additional minutes if using 335 µm instead of a 437 µm (figure 8.7c). However, if the 233 µm nozzle is utilized instead, the print time increases to 52 min. The great time differences obtained revealed that using non-optimized printing parameters would introduce inadmissible idle times in the bioprinting process, which would ultimately result in low productivity and a great decrease in cell viability when hybrid scaffolds are produced. It is important to note that when using nozzles of small diameter and at a medium-low temperature (120 ºC), print times increased more than 100% (figure 8.7c). On the opposite, the time differences using nozzles of large diameter at low or high temperatures can be neglected. Consequently, nozzles of large diameter and low print temperatures are preferred to get short print times and assure high cell viability in hybrid constructs.

Figure 8.8: *Images of the fan support installed on the printhead to increase the cooling rate of the PCL.*

8.5 Proof of concept of hybrid construct using the selected print parameters

One of the main advantages of using hybrid constructs that integrate soft hydrogels and rigid scaffolds is to provide better mechanical properties and a biological microenvironment suitable for cell survival and growth (Shanjani *et al.*, 2015). A

3D hybrid construct employing PCL and P407 was proposed as a proof of concept (figure 8.9a). This construct was generated using the multi-material bioprinting system presented in chapter 7 with the high-temperature printhead installed. The calibration method proposed in chapter 7 was critical for the alignment of both biomaterials (PCL and P407). We adjusted the print parameters according to the previous results and we were able to print both materials at the same carriage speed. Note that if a cell-laden bioink would be employed, temperatures lower than 140 ºC could be used with the conical G25 without substantially increasing the print time (figure 8.7c).

Hybrid constructs were generated depositing P407 and PCL strands together within the same construct layers. PCL strands were deposited continuously in a zigzag pattern, while P407 strands were deposited independently next to PCL strands. Conical nozzles with different IDs were utilized for both biomaterials: 437 µm (Micron-S dispensing tips; Fisnar, United Kingdom) for PCL and 200 µm (Nordson EFD; Spain) for P407. The carriage (or printhead travel) speed was 14 mm s^{-1} for printing both PCL and P407, which required print temperatures of 140 ºC and 25 ºC, respectively.

In figure 8.9b, we observe that the first layer of the hybrid construct showed a successful alignment of both materials with homogeneous strands one beside the other, while figure 8.9c presents the high shape fidelity of the hybrid construct. The use of PCL provided a stiffer framework to incorporate the P407 than if only a soft hydrogel is used, demonstrating its potential to generate constructs with complex geometries and enhanced mechanical properties.

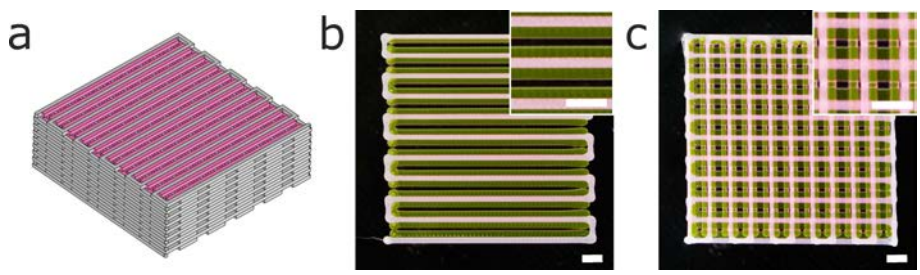

Figure 8.9: *(a) CAD model of a 3D hybrid constructs of dimensions 20 x 20 mm. (b) First layer and (c) stack of two layers printed of the hybrid construct. It is composed of PCL (ID: 437 µm; 14 mm s^{-1}; 140 ºC; 700 kPa) and intercalated filaments of poloxamer P407 (ID: 200 µm; 14 mm s^{-1}; RT; 100 kPa). Scale bars: 2 mm.*

8.6 Conclusions

Herein, we presented a series of experiments that provide useful information to find the best setup for PCL deposition in terms of time efficiency and print accuracy. Nozzle shapes were first analyzed through flow experiments and CFD simulations. Results demonstrated that the internal nozzle morphology represents one of the key points to be considered in the extrusion of PCL. Conical nozzles revealed as the best shape to achieve high print speeds, with significant flow differences respect cylindrical shapes.

Assuming that the carriage speed must always be maximized without reducing the quality of the printed constructs, we explored the optimal values for other printing parameters such as nozzle size and print temperature. Print temperature is a limiting factor as too high temperatures increase drastically cell dead when depositing the next layer of the scaffold over the already printed layer of cells and bioink. On the other hand, too low temperatures resulted in difficulties to get a proper PCL flow.

The scalability was studied by printing PCL scaffolds of different porosity and number of layers. This allowed us detecting the print parameters that have a direct influence on the print time. Results revealed that varying nozzle diameter and target temperature led to time reductions up to 50 min. These results are valuable in the TE field because reducing the print times of hybrid constructs results crucial for building scaffolds of clinically relevant size at high cell viability.

Chapter 9

3D bioprinting of cell-laden hydrogels

3D bioprinting makes it possible to generate cell-laden constructs with complex geometries and customized control over the internal pore architecture, which is not possible using the conventional TE techniques. The development of an open-source 3D bioprinting platform, with all the challenges and improvements encountered, have been detailed in previous chapters. However, any bioprinting tool must be checked to meet its main purpose, the deposition of cell-laden bioinks with high cell-viabilities of printed constructs. In this chapter are described all the steps followed to perform a successful bioprinting of cell-laden constructs, from the choice of bioink to the measurement of cell-viability (figure 9.1). The properties and behavior of bioinks utilized were assessed through rheological measurements. Thermoresponsive bioinks, such as the ones utilized, required finding the appropriate printing conditions to obtain accurate deposition results. Different printing parameters like printhead temperature, pressure, deposition rate, or printing speed were optimized for each bioink based on its rheology and several printing tests. Once all these parameters were set, hASC cells were introduced inside Gel-Alg bioinks and 3D bioprinted inside a sterile hood. Cell-laden porous constructs were generated and subsequently crosslinked with a $CaCl_2$ bath to preserve their shape once deposited. Finally, cell-viability measurements of printed constructs were performed right after extrusion and 24h later, demonstrating the viability of the open-source bioprinting approach presented in this thesis.

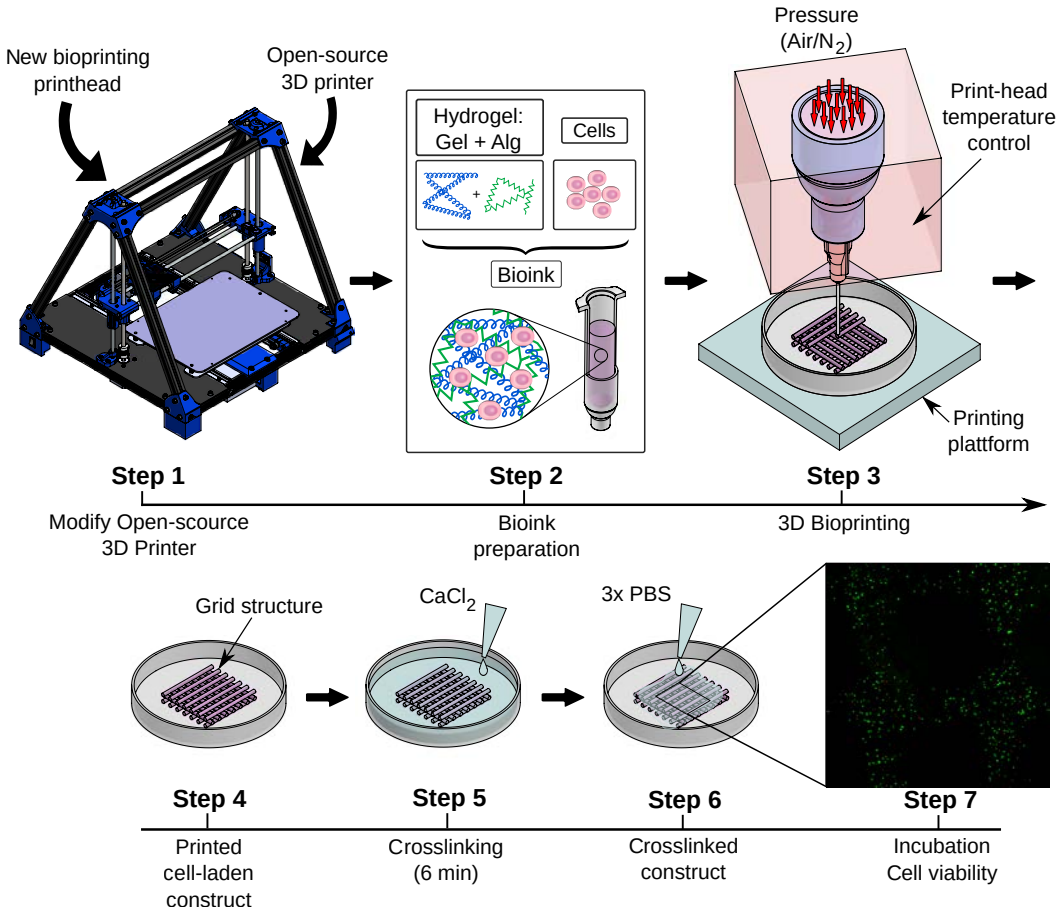

Figure 9.1: *Overall scheme of the bioprinting process utilized.*

9.1 Rheological properties of hydrogels utilized

Rheology can be defined as the study of deformation and flow of matter. If an ideal solid is deformed elastically, the energy required for its deformation will be fully recovered when the stresses are removed. If an ideal fluid (liquid or gas) is subjected to any force, it will deform irreversibly and it will flow. Therefore, the energy generated will be dissipated within the fluid in the form of heat and will not be recovered when the stresses are removed. Nevertheless, the real materials that we find can display either elasticity and viscosity properties or the combination of both. There are only a few liquids that can be considered as ideal and a great majority show rheological properties that remain in a region between the solids and the liquids. Depending on the material of study, they can have both elastic and viscous properties and are often named as visco-elastic materials.

Bioinks are classified under Non-Newtonian fluids and a shear thinning behavior is preferred to facilitate their deposition. Bioinks with high viscosities

are often preferred as they are able to obtain better shape fidelities. However, an increase in the viscosity is also related to an increase in the shear stress produced in the extrusion process, resulting in higher damage of bioprinted cells. Bioinks viscosities are tailored through their molecular weight and polymer concentration. Therefore, when a new bioink is developed it results essential to measure the rheological properties of bioinks produced.

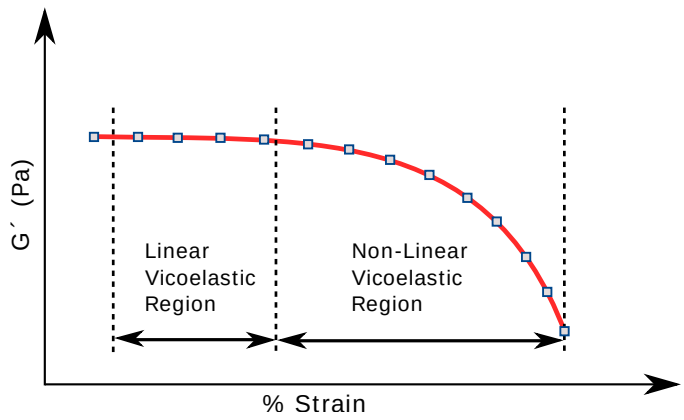

Figure 9.2: *Linear and non-linear viscoelastic regions obtained from a oscillation strain sweep test.*

In order to accurately evaluate rheological properties of Non-Newtonian materials such as bioinks, measurements should be conducted in regions where the viscoelastic properties are independent of the imposed strains or stresses. When a material is rheologically evaluated for the first time, it is important to determine its linear visco-elastic region (LVR) (figure 9.2). This region establishes the limits between the linear and the non-linear behavior when the sample is subjected to several stresses. If a controlled stress rheometer is utilized, it is possible to obtain the LVR through two different tests: creep and dynamic oscillation. In the creep test, a constant stress is applied to the samples and the obtained strain is measured with time. To obtain the LVR, a series of creep curves are plotted increasing the stress applied independently, with the overlapped curves indicating the LVR. The dynamic oscillation test was utilized in this study. Here, a strain sweep was utilized varying the amplitude of oscillation a constant frequency of 1 Hz. Results were plotted as storage (G´) and loss modulus (G´´) versus % strain. When the storage modulus (G´) obtained is constant the sample remains within the LVR. If the G´varied with the strain applied, the sample will stand out of the LVR.

To evaluate the printability of Gel-Alg blends, different concentrations of this mixture were prepared according to rheological measurements, printing resolution and cell viability. Temperature sweep tests performed to Gel and Gel-Alg

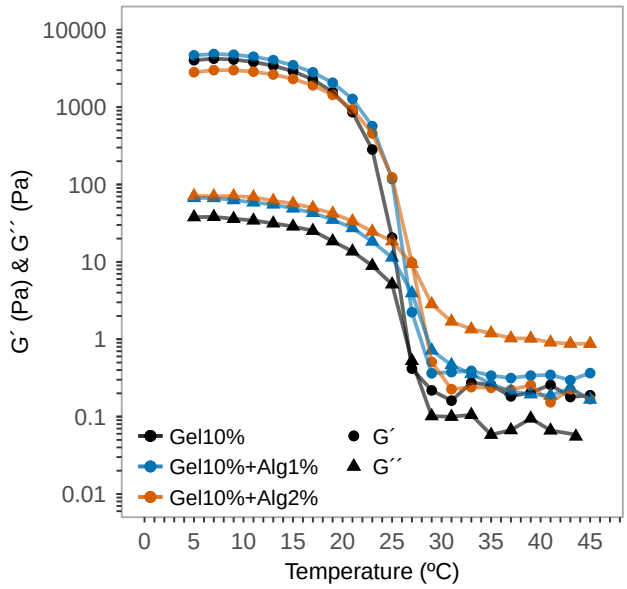

Figure 9.3: *Determination of the gelation temperature by temperature sweep test.*

blendings showed the phase transition temperature, corresponding to the crossing point between the storage modulus (G´) and the loss modulus (G´´) (figure 9.3). Below this critical temperature, solutions undergo a thermally reversible gelation. The gelation temperature for Gel solution with a 10% concentration was 26.1 ºC. The Gel phase transition temperature increased from 26.1 ºC to 26.7 ºC and 27.3 ºC after mixing it with 1% and 2% Alg, respectively.

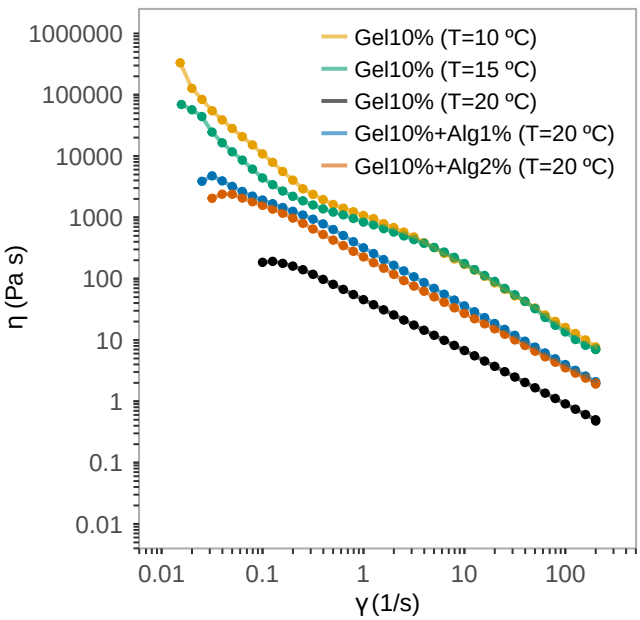

Figure 9.4: *Log-log plot of the viscosity vs. shear rate.*

The rheological behavior of Gel-Alg bioinks under continuous steady shear was analyzed (figure 9.4). All bioinks tested exhibited shear thinning behav-

ior, a property that improves the printability of bioinks (Ozbolat & Hospodiuk, 2016). To achieve the desired viscosity, parameters like temperature and concentration can be tailored. Several tests were performed to Gel solutions at different temperatures (10 ºC, 15 ºC and 20 ºC), with apparent viscosities ranging from $2 \cdot 10^2$ to $3 \cdot 10^4$ Pa s at a shear rate of 0.1 s^{-1}. Limited viscosity changes were detected in Gel solutions at 10 ºC and 15 ºC, however, a significant viscosity reduction of two orders of magnitude can be observed for Gel at 20 ºC. Gel-Alg bioinks exhibit similar shear thinning behavior, with apparent viscosities of $1 \cdot 10^3$ Pa s at a shear rate of 0.1 s^{-1}, a value that lies within the gelatin viscosities defined above. If we consider the same temperature to compare Gel and Gel-Alg bioinks (20 ºC), we observed an order of magnitude increase in the viscosity when Alg is added.

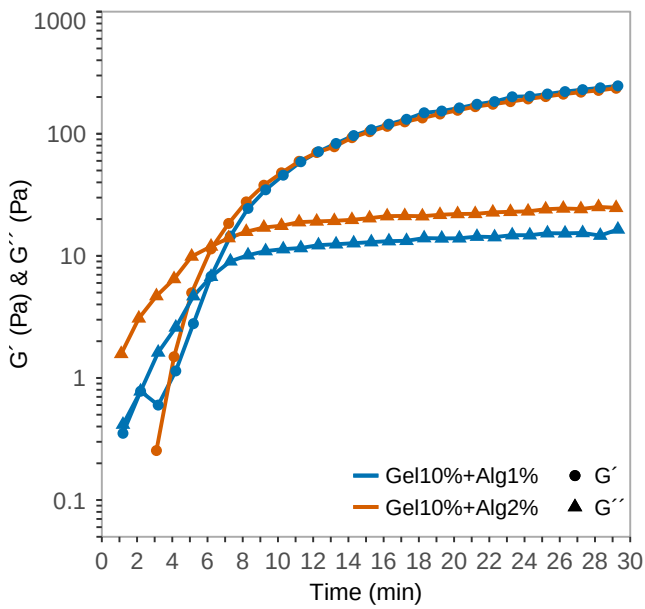

Figure 9.5: *Time sweep test with the time dependence of G' and G" measured at 20 ºC.*

Bioprinting is a time-consuming process that has negative influence on cell viability. Depending on the bioink used, a preliminary holding time is needed to facilitate the stabilization of the bioink at the printing temperature by means of thermal gelation (Zhao *et al.*, 2015). This stabilization time varies from one bioink to another and will also depend on the mixing and bioprinting temperatures. At the beginning of the experiment both Gel-Alg bioinks had an unstable behavior due to samples were loaded at 37 ºC and the experiment was performed at 20 ºC (figure 9.5). From minute 6 in advance, the elastic modulus (G´) curve remains higher than the viscous modulus (G´´), suggesting a gel state in the bioinks. Taking into account these results, a holding time of 30 min was utilized for the bioprinting experiments performed with the cells embedded in Gel-Alg blends.

9.2 3D bioprinting of thermoresponsive hydrogels

Cell viability is greatly influenced by bioprinting parameters like bioink viscosity, pressure, time and nozzle diameter. Each of the parameters involved in the bioprinting process is highly correlated between them. For example, tailoring bioink printing temperatures will lead to important changes in its rheological properties like viscosity. Viscosity changes also imply using different nozzle diameters and pressures. If all these parameters are properly adjusted, bioprinted results most likely will result in higher cell viability constructs, due to the lower shear stress generated in the bioprinting process. For that reason, it is essential to develop versatile bioprinting tools that allow us to customize as far as possible bioprinters to our own needs. This also includes having a precise control over a wider range of temperatures that allow us to tailor bioinks rheological properties and achieve a better printability.

Cell-laden constructs require optimal interconnectivity for an efficient nutrient and waste flow, as well as tissue ingrowth (Billiet *et al.*, 2012). This objective can be achieved by means of porous architectures, that can be tailored using different printing configurations (Trachtenberg *et al.*, 2014). Macroporosity studies using Gel-Alg bioinks have been previously performed by several authors (Zehnder *et al.*, 2015; Chung *et al.*, 2013; Ouyang *et al.*, 2015), measuring parameters like pore size (P), strand diameter (D) and strand spacing (SS).

Gel-Alg bioinks were utilized with a two-fold objective: ensure good cell biocompatibility and precisely control its temperature during bioprinting. Rheological results demonstrated the temperature and time-dependence of Gel-Alg bioinks (Ouyang *et al.*, 2016) and bioprinting experiments revealed that small variations in the printing temperatures produced a significant loss of accuracy in the printed geometries (Zhao *et al.*, 2015). We can observe this effect in the phase transition temperatures obtained in the temperature sweep tests (figure 9.3) and the printing measurements of Gel-Alg lattices at diverse temperatures (figure 9.6 and table 9.1).

Table 9.1: *Measurements of Gel-Alg lattice structures printed at different temperatures. Data represent mean and s.e.m. of six different samples (n=6)*

	Temperature (ºC)		
	20	**22**	**24**
Pore size (mm)	1.5 ± 0.02	1.05 ± 0.02	0.99 ± 0.02
Strand diameter (mm)	0.4 ± 0.01	0.82 ± 0.01	1 ± 0.01
Strand spacing (mm)	1.99 ± 0.02	1.99 ± 0.01	1.99 ± 0.01

Gel-Alg lattices structures were printed at different temperatures using Witbox 2 to determine the optimal printing temperature according to the bioinks rheological properties (figure 9.6). Intended lattice dimensions of P=1.75 mm, D=0.25 mm and SS=2mm were utilized with 2 layers stacked. The optimal printability for 10%Gel-2%Alg was obtained with a printing temperature of 20 ºC (table 9.2). We can observe from figure 9.6 that when the printing temperature is close to the intersection point between G´ and G´´ curves, the Gel-Alg bioink undergoes a gel-to-liquid transition and lattices produced were less accurate. Printing temperatures above 22 ºC generated lattices with pores partially or completely closed, especially for those printing temperatures of 26 ºC and above. On the contrary, printing temperatures below 20 ºC resulted in discontinuous strands due to stronger gelation of the thermoreversible bioink. These results showed the importance of a precise temperature control of bioinks in the printhead during the printing process. A printing temperature difference of only 2 ºC resulted in an increase of the strand diameters of 420 μm and consequently an equivalent reduction in the pore size. Strand spacing measurements remained constant for all the printing temperatures, as it seems that this parameter is more related to the 3D printer resolution than to the bioink rheological properties.

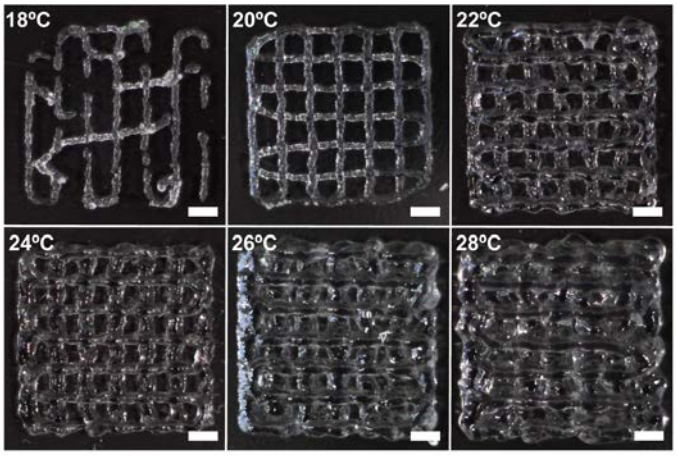

Figure 9.6: *Images of printed lattice structures using 10%Gel-2%Alg Alg and a 25G tapered nozzle at temperatures ranging from 18 ºC to 28 ºC. Scale bars: 2 mm.*

Once an optimal printing temperature of 20 ºC was determined, Gel-Alg lattices were printed with multiple layers stacked (figure 9.7). The viscosity and consistency of 10%Gel-2%Alg bioink was good enough to create lattice models up to 16 layers at 20 ºC. The strand width of the printed models slightly increased proportionally to the number of layers, reducing the pore size (table 9.7). Differences of 200 μm in the pore size and strand diameter were observed between the 2 and 16 layers stacked. However, the constructs showed excellent printed

resolution (figure 9.7) and enough stability to proceed to their crosslinking and incubation.

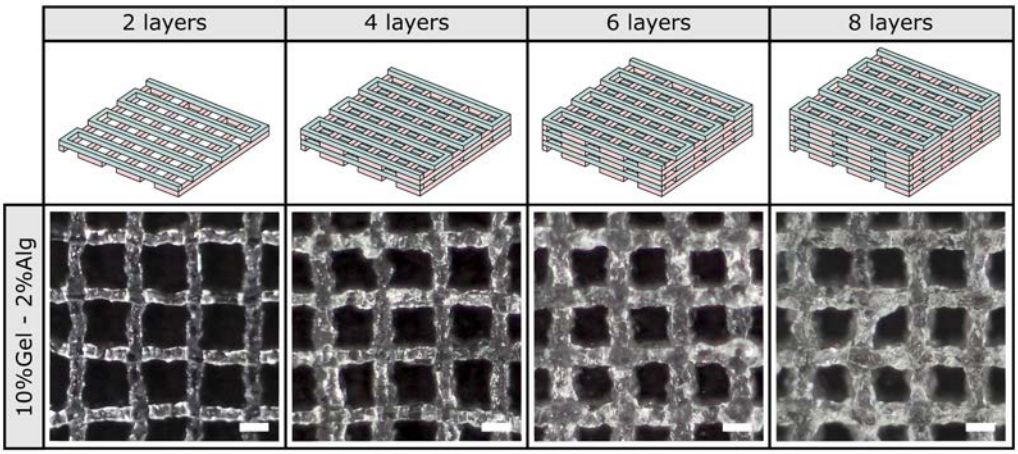

Figure 9.7: *Printed lattice structures with multiple layers using Witbox 2. Schematic representation of the 3D models (top row) and images of printed lattice structures using 10%Gel-2%Alg. Scale bars: 1 mm.*

Table 9.2: *Measurements of Gel-Alg lattice structures printed using an optimal temperature of 20 ºC and stacking layers. Data represent mean and s.e.m. of six different samples (n=6)*

	# Layers			
	2	**4**	**8**	**16**
Pore size (mm)	1.5 ± 0.01	1.41 ± 0.02	1.32 ± 0.02	1.31 ± 0.02
Strand diameter (mm)	0.41 ± 0.01	0.5 ± 0.02	0.58 ± 0.01	0.61 ± 0.02
Strand spacing (mm)	1.95 ± 0.01	1.97 ± 0.03	1.92 ± 0.01	1.89 ± 0.01

9.3 3D bioprinting of cell-laden constructs

Bioprinting experiments performed have shown that small changes in bioprinting temperatures lead to important variations in the printability and resolution. As demonstrated in the rheological tests, temperature changes also cause important changes in the storage and loss moduli of Gel-Alg bioinks, being critical parameters in achieving high cell viabilities in printed constructs. In addition, other parameters such as the extrusion pressure, the deposition speed or the nozzle diameter were also critical. The adjustment of all these parameters will result in greater cell viabilities, due to the lower shear stress generated during the bioprinting process (Blaeser *et al.*, 2016).

3D bioprinting experiments utilize a great number of cells that are quite expensive to produce. For that reason, it was essential not only to ensure a proper processing of cells during the deposition process, but also prevent any possible

contamination that could affect the final viability results. Any bioprinting process requires sterile conditions in all its phases, which include not only the environment where the bioprinter is located, but also the bioprinter itself and all the equipment introduced inside the sterile hood. Witbox 2 3D printer was sterilized according to the procedure detailed in chapter 3 and introduced in a laminar flow hood to ensure sterile conditions.

hASCs were mixed with Gel-Alg bioinks (cell density of 10^6cells/mL) by gentle pipetting to create a homogeneous suspension that was transferred into 3 mL Luer-lock syringes (Nordson EFD) and closed with a piston (SmoothFlow; Nordson EFD). The syringes were introduced inside the bioprinted printhead and connected to a software-controlled solenoid valve and an air pressure regulator for a precise control of the pressure between 96 and 110 kPa. Extrusion was performed under nitrogen pressure, previously filtered using a 40 μm sterile filter. The syringe with the mixture was loaded into a preheated/precooled printhead for the stabilization of the hydrogel for 30 min. Bioinks were extruded into 3D cell-laden structures (size 12 x 12 mm x 4 layers) on 35 mm Petri dishes through a 25G tapered nozzle (Nordson EFD) at a printing speed of 14 mm s^{-1}. The printed constructs were cross-linked in 3 wt% calcium chloride ($CaCl_2$; Wako) for 6 min and then washed three times with phosphate buffer (PBS) and replaced with growth medium, Dulbecco's modified Eagle's medium (DMEM) (Invitrogen) supplemented with 6% human serum.

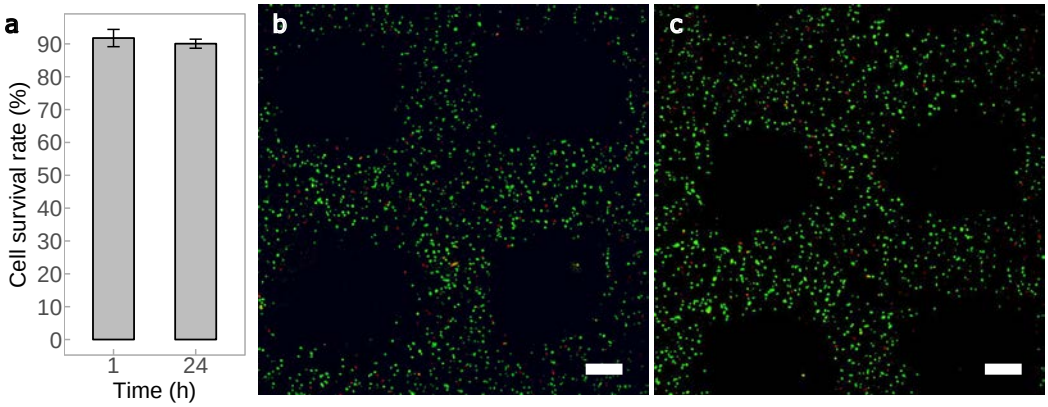

Figure 9.8: *Cell viability after printing hASCs at 20 ºC using 10%Gel-2%Alg and a 25G tapered nozzle. (a) Percentage of cell viability in the printed constructs. Error bars represent s.e.m. (b-c) Representative laser confocal images of cell viability assay 1h (b) and 24 h (c) after printing. Scale bars: 200 μm.*

Cell viability of the hASCs was measured in the 10%Gel-2%Alg cell-laden lattice printed constructs. Using a live/dead assay, cell viability post-printing was evaluated at 1h and 24h resulting in a 91.78±2.63% and 90.06±1.38% of living cells, respectively. Figure 9.8a shows non-statistical differences in cell survival

rate at 24 hours. Figure 9.8b and 9.8c shows fluorescence microscope images of live/dead assays of hASC embedded in the bioinks, where living cells appear in green and dead cells are shown in red. The cell-viability results of Gel-Alg printed lattices (greater than 90%) confirms that the printing process utilized did not appear to damage the vast majority of dispensed cells. In addition, the printability results at different temperatures obtained in the previous experiments confirm the proper adjustment of bioprinting parameters. Demonstrating that the open-source bioprinting platform presented in this thesis is a promising alternative to the proprietary commercial bioprinters.

9.4 Conclusions

In this chapter, we have demonstrated the potential of the open-source bioprinting platform proposed to generate cell-laden constructs. Rheological properties and printability of Gel-Alg bioinks were tailored by altering the ratio and concentration of the hydrogels utilized. Rheological measurements permitted to obtain relevant bioink properties as the phase transition temperature, viscosity and holding time. This information allowed to have a comprehensive understanding of bioinks conditions before and during the printing process, and tailor some printing parameters such as temperature and processing time. Moreover, Gel-Alg printed lattices at different temperatures demonstrated that the printhead utilized had enough capacity to precisely control the printing conditions based on bioinks rheology. The cell-viability percentages (higher than 90%) measured in the Gel-Alg lattice structures demonstrated the excellent biocompatibility of the bioprinting platform proposed. Besides, it permitted to achieve equivalent print accuracies to the ones obtained through commercial bioprinters in the market, which implies a significant leap in bringing 3D bioprinting technology to TE laboratories worldwide.

Chapter 10

Conclusions and future work

10.1 Conclusions

In the framework of 3D bioprinting, this thesis presents a detailed description of a novel open-source 3D bioprinting platform exportable to most of the open-source desktop 3D printers. Within this platform were included all the tools involved in an EBB bioprinting process, from the printheads utilized for bioinks deposition to the software used for G-code generation. Beyond the technological development of this proposal, several innovative methodologies and bioprinting strategies were presented, which would permit to reduce the print times, measure the print resolution and increase the accuracy of bioprinters. Besides, several comprehensive studies of printing parameters were conducted using various biomaterials to obtain the optimal printing configuration for each application. In that sense, all the bioprinting tools here presented can be considered as an easy and affordable way to enter in the bioprinting field and also enhance the collective knowledge of this technology with innovative proposals.

The main findings associated with this thesis work are summarized below:

1. Two novel open-source MEBB printhead designs (PH and PHR) were developed, permitting a precise control of bioprinting parameters such as pressure or temperature. These printheads allow heating and cooling bioinks with the same device. Besides, they allow a fast and easy syringe exchange by merely removing the upper cap of the printhead. Its modular design allows the use of different syringe sizes, replacing the specific Al block for each syringe while keeping the rest of the printhead components. These printheads can be easily

combined with low-cost desktop 3D printers to achieve print accuracies equivalent to the commercial equipment in the market. The universality, modularity and wide range of printing temperatures make these devices a unique tool for bioprinting applications, being the first open-source printheads that provide all these capabilities altogether.

2. Open-source desktop 3D printers were modified to turn them into bioprinters. To that end, hardware and software modifications were required to adapt them to the specific particularities of the bioprinting system proposed. All the modifications here performed are exportable to most of the open-source desktop 3D printers in the market. A detailed description of all these modifications was included to facilitate their adoption among the scientific community. All the software utilized and the specific modifications performed for this research are freely available to all users through online repositories. This approach allows to enhance the collective knowledge about bioprinting and expand its use through the scientific community.
3. A standard methodology was presented to determine the bioprinters accuracy and establish a common comparison framework between bioprinters. The calibration models proposed permitted to quantify the capabilities and limitations of three different open-source bioprinting platforms, as well as compare their print resolutions. Results revealed that differences in how 3D printer axes move strongly affect the final bioprinting accuracy. 3D printers with their printing platform moving in the z-axis are preferred because instabilities during the printing process are reduced.
4. A non-expensive and automatic calibration method was proposed, which is exportable to most of the 3D bioprinting systems with multiple printheads. Complex multi-material 3D models and intricate vascular networks were generated assessing the final accuracy and printing precision of the multi-material bioprinting platform.
5. A novel 3D printing strategy was presented, which implies the use of IDEX technology and the production of multiple constructs using several printheads simultaneously. Two open-source 3D printers were utilized to compare both standard and IDEX 3D printing approaches. Simultaneous and conventional 3D printing strategies were evaluated from a time efficiency perspective, showing a substantial print time reduction when multiple printheads were utilized simultaneously. In this way, using several printheads at the same time allowed to minimize idle times caused by inactive printheads, and thus reduce the overall printing times. The results obtained represent an interesting approach in the bioprinting field, which implies a reduction of cell death due to excessive print times.

6. A novel open-source pneumatic printhead for the fabrication of scaffolds at high temperatures was developed in this research. This printhead demonstrated its excellent capabilities in terms of temperature response and printing accuracy. A series of PCL experiments were presented which provide useful information to find the best setup for PCL deposition regarding time efficiency and print accuracy. Nozzle shapes and inner diameters were also analyzed through flow experiments and CFD simulations, demonstrating that the internal nozzle morphology represents one of the key points to be considered in PCL printing. The scalability was studied by printing PCL scaffolds of different porosity and number of layers. Results revealed that varying nozzle diameter and target temperature led to time reductions up to 50 min. These results are valuable in the TE field because reducing the print times of hybrid constructs results crucial for building scaffolds of clinically relevant size at high cell viability.
7. Rheological properties and printability of Gel-Alg bioinks were tailored by altering the ratio and concentration of the hydrogels utilized. Rheological measurements permitted to obtain relevant bioink properties as the phase transition temperature, viscosity and holding time. This information allowed to have a comprehensive understanding of bioinks conditions before and during the printing process, and tailor some printing parameters such as temperature and processing time.
8. The high cell-viabilities obtained in Gel-Alg printed lattices demonstrated the excellent biocompatibility of the bioprinting platform proposed. Besides, it permitted to achieve print accuracies equivalent to the commercial bioprinters in the market, which implies a significant leap in bringing 3D bioprinting technology to TE laboratories worldwide.

10.2 Future work

Overall it can be said that the results presented in this thesis can contribute to extend the potential of 3D bioprinting technology in the TE field. The open-source bioprinting platform proposed permits to expand EBB technology to a broader number of laboratories. This novel open-source bioprinting platform represents a low-cost and more accessible alternative to the commercial bioprinters, with limitless applications in TE and the ultimate goal of generating engineered living tissues. However, due to the complexity of this final task, there are several topics that could not be covered in this thesis and could inspire new research lines. With

the regard of continuing with the research line here proposed, the following topics are suggested to be investigated in more detail in the future:

1. In the framework of multi-material bioprinting, it would be interesting to explore the creation of complex in-vitro models with different biomaterials and cell types.
2. Other technologies such as drop-on-demand bioprinting could be explored in conjunction with the open-source EBB systems here proposed.
3. The generation of the bioprinting G-code could be enhanced using a dedicated and open-source bioprinting software. This software would permit to increase the user-friendliness by novel users and include specific configurations for bioprinting.
4. Lastly, the potential of IDEX 3D printing technology and the use of several printheads simultaneously could also be further explored to reduce the print times required to fabricate in-vitro models and increase the repeatability of this type of experiments.

10.3 Contributions

The main results of the thesis have been published in the following international journals:

1. **Sodupe-Ortega, E.**, Sanz-Garcia, A., Pernia-Espinoza, A., Escobedo-Lucea, C. et al. (2018). Accurate calibration in multi-material 3D bioprinting for tissue engineering. Materials, 11(8), p. 1402. DOI: 10.3390/ma11081402
2. **Sodupe-Ortega, E.**, Sanz-Garcia, A., Pernia-Espinoza, A., Escobedo-Lucea, C. et al. (2019). Efficient fabrication of polycaprolactone scaffolds for printing hybrid tissue-engineered constructs. Materials. (Accepted).
3. **Sodupe-Ortega, E.**, Sanz-Garcia, A., Pernia-Espinoza, A., Shimizu T., Escobedo-Lucea, C. et al. (2019). A versatile open-source printhead for low-cost 3D microextrusion-based bioprinting. Biofabrication (Submitted).

Bibliography

Ahmed, E.M. (2015). Hydrogel: Preparation, characterization, and applications: A review. *Journal of advanced research*, 6(2), pp. 105–121.

Ahn, S., Lee, H., Bonassar, L.J. & Kim, G. (2012a). Cells (mc3t3-e1)-laden alginate scaffolds fabricated by a modified solid-freeform fabrication process supplemented with an aerosol spraying. *Biomacromolecules*, 13(9), pp. 2997–3003, pMID: 22913233.

Ahn, S., Lee, H., Puetzer, J., Bonassar, L.J. & Kim, G. (2012b). Fabrication of cell-laden three-dimensional alginate-scaffolds with an aerosol cross-linking process. *J. Mater. Chem.*, 22, pp. 18735–18740.

Ali, M., Pages, E., Ducom, A., Fontaine, A. & Guillemot, F. (2014). Controlling laser-induced jet formation for bioprinting mesenchymal stem cells with high viability and high resolution. *Biofabrication*, 6(4), p. 045001.

Ali Khademhosseini, J.P.V..R.L. (2009). Progress in tissue engineering. *Scientific American*, 300.

Arai, K., Iwanaga, S., Toda, H., Genci, C., Nishiyama, Y. & Nakamura, M. (2011). Three-dimensional inkjet biofabrication based on designed images. *Biofabrication*, 3(3), p. 034113.

Armstrong, J.P.K., Burke, M., Carter, B.M., Davis, S.A. & Perriman, A.W. (2016a). 3d bioprinting using a templated porous bioink. *Advanced Healthcare Materials*, 5(14), pp. 1724–1730.

Armstrong, J.P., Burke, M., Carter, B.M., Davis, S.A. & Perriman, A.W. (2016b). 3d bioprinting using a templated porous bioink. *Advanced healthcare materials*, 5(14), pp. 1724–1730.

Arrhenius, S. (1967). On the reaction velocity of the inversion of cane sugar by acids. In: *Selected readings in chemical kinetics*, Elsevier, pp. 31–35.

Atala, A. & Yoo, J.J. (2015). *Essentials of 3D biofabrication and translation*. Academic Press.

Attalla, R., Ling, C. & Selvaganapathy, P. (2016). Fabrication and characterization of gels with integrated channels using 3d printing with microfluidic nozzle for tissue engineering applications. *Biomedical microdevices*, 18(1), p. 17.

Bandyopadhyay, A., Dewangan, V.K., Vajanthri, K.Y., Poddar, S. & Mahto, S.K. (2018). Easy and affordable method for rapid prototyping of tissue models in vitro using three-dimensional bioprinting. *Biocybernetics and Biomedical Engineering*, 38(1),

pp. 158 – 169.

Barron, J., Rosen, R., Jones-Meehan, J., Spargo, B., Belkin, S. & Ringeisen, B. (2004a). Biological laser printing of genetically modified escherichia coli for biosensor applications. *Biosensors and Bioelectronics*, 20(2), pp. 246–252.

Barron, J., Spargo, B. & Ringeisen, B. (2004b). Biological laser printing of three dimensional cellular structures. *Applied Physics A*, 79(4-6), pp. 1027–1030.

Barron, J., Young, H., Dlott, D., Darfler, M., Krizman, D. & Ringeisen, B. (2005). Printing of protein microarrays via a capillary-free fluid jetting mechanism. *Proteomics*, 5(16), pp. 4138–4144.

Barron, J.A., Ringeisen, B.R., Kim, H., Spargo, B.J. & Chrisey, D.B. (2004c). Application of laser printing to mammalian cells. *Thin Solid Films*, 453, pp. 383–387.

Bertassoni, L.E., Cardoso, J.C., Manoharan, V., Cristino, A.L., Bhise, N.S., Araujo, W.A., Zorlutuna, P., Vrana, N.E., Ghaemmaghami, A.M., Dokmeci, M.R. & Khademhosseini, A. (2014a). Direct-write bioprinting of cell-laden methacrylated gelatin hydrogels. *Biofabrication*, 6(2), p. 024105.

Bertassoni, L.E., Cecconi, M., Manoharan, V., Nikkhah, M., Hjortnaes, J., Cristino, A.L., Barabaschi, G., Demarchi, D., Dokmeci, M.R., Yang, Y. *et al.* (2014b). Hydrogel bioprinted microchannel networks for vascularization of tissue engineering constructs. *Lab on a Chip*, 14(13), pp. 2202–2211.

Beyer, S., Bsoul, A., Ahmadi, A. & Walus, K. (2013). 3d alginate constructs for tissue engineering printed using a coaxial flow focusing microfluidic device. In: *Solid-State Sensors, Actuators and Microsystems (TRANSDUCERS & EUROSENSORS XXVII), 2013 Transducers & Eurosensors XXVII: The 17th International Conference on*, IEEE, pp. 1206–1209.

Bidan, C.M., Kommareddy, K.P., Rumpler, M., Kollmannsberger, P., Bréchet, Y.J., Fratzl, P. & Dunlop, J.W. (2012). How linear tension converts to curvature: geometric control of bone tissue growth. *PloS one*, 7(5), p. e36336.

Billiet, T., Gevaert, E., De Schryver, T., Cornelissen, M. & Dubruel, P. (2014). The 3d printing of gelatin methacrylamide cell-laden tissue-engineered constructs with high cell viability. *Biomaterials*, 35(1), pp. 49–62.

Billiet, T., Vandenhaute, M., Schelfhout, J., Van Vlierberghe, S. & Dubruel, P. (2012). A review of trends and limitations in hydrogel-rapid prototyping for tissue engineering. *Biomaterials*, 33(26), pp. 6020–6041.

Binder, K.W., Allen, A.J., Yoo, J.J. & Atala, A. (2011). Drop-on-demand inkjet bioprinting: a primer. *Gene Therapy and Regulation*, 6(01), pp. 33–49.

Bird, R.B. & Carreau, P.J. (1968). A nonlinear viscoelastic model for polymer solutions and melts-i. *Chemical Engineering Science*, 23(5), pp. 427–434.

Blaeser, A., Duarte Campos, D.F., Weber, M., Neuss, S., Theek, B., Fischer, H. & Jahnen-Dechent, W. (2013). Biofabrication under fluorocarbon: a novel freeform fabrication technique to generate high aspect ratio tissue-engineered constructs. *BioResearch open access*, 2(5), pp. 374–384.

Blaeser, A., Duarte Campos, D.F., Puster, U., Richtering, W., Stevens, M.M. & Fischer, H. (2016). Controlling shear stress in 3d bioprinting is a key factor to balance printing resolution and stem cell integrity. *Advanced healthcare materials*, 5(3), pp. 326–333.

Boland, T., Mironov, V., Gutowska, A., Roth, E.A. & Markwald, R.R. (2003). Cell and organ printing 2: Fusion of cell aggregates in three-dimensional gels. *The Anatomical Record Part A: Discoveries in Molecular, Cellular, and Evolutionary Biology*, 272A(2), pp. 497–502.

Campbell, P.G. & Weiss, L.E. (2007). Tissue engineering with the aid of inkjet printers. *Expert opinion on biological therapy*, 7(8), pp. 1123–1127.

Carreau, P.J. (1972). Rheological equations from molecular network theories. *Transactions of the Society of Rheology*, 16(1), pp. 99–127.

Catros, S., Guillotin, B., Bačáková, M., Fricain, J.C. & Guillemot, F. (2011). Effect of laser energy, substrate film thickness and bioink viscosity on viability of endothelial cells printed by laser-assisted bioprinting. *Applied Surface Science*, 257(12), pp. 5142–5147.

Chang, C.C., Boland, E.D., Williams, S.K. & Hoying, J.B. (2011). Direct-write bioprinting three-dimensional biohybrid systems for future regenerative therapies. *Journal of Biomedical Materials Research Part B: Applied Biomaterials*, 98(1), pp. 160–170.

Chen, X., Shoenau, G. & Zhang, W. (2000). Modeling of time-pressure fluid dispensing processes. *IEEE Transactions on Electronics Packaging Manufacturing*, 23, pp. 300 – 305.

Cheng, J., Lin, F., Liu, H., Yan, Y., Wang, X., Zhang, R. & Xiong, Z. (2008). Rheological properties of cell-hydrogel composites extruding through small-diameter tips. *Journal of Manufacturing Science and Engineering*, 130(2), p. 021014.

Chimene, D., Lennox, K.K., Kaunas, R.R. & Gaharwar, A.K. (2016). Advanced bioinks for 3d printing: A materials science perspective. *Annals of Biomedical Engineering*, 44(6), pp. 2090–2102.

Chrisey, D., Pique, A., Fitz-Gerald, J., Auyeung, R., McGill, R., Wu, H. & Duignan, M. (2000). New approach to laser direct writing active and passive mesoscopic circuit elements. *Applied surface science*, 154, pp. 593–600.

Christensen, K., Xu, C., Chai, W., Zhang, Z., Fu, J. & Huang, Y. (2015). Freeform inkjet printing of cellular structures with bifurcations. *Biotechnology and bioengineering*, 112(5), pp. 1047–1055.

Chua, C.K. & Yeong, W.Y. (2014). *Bioprinting: principles and applications*, volume 1. World Scientific Publishing Co Inc.

Chung, J.H., Naficy, S., Yue, Z., Kapsa, R., Quigley, A., Moulton, S.E. & Wallace, G.G. (2013). Bio-ink properties and printability for extrusion printing living cells. *Biomaterials Science*, 1(7), pp. 763–773.

Coakley, M. & Hurt, D.E. (2016). 3d printing in the laboratory: Maximize time and funds with customized and open-source labware. *Journal of Laboratory Automation*,

21(4), pp. 489–495, pMID: 27197798.

Cohen, D.L., Tsavaris, A.M., Lo, W.M., Bonassar, L.J. & Lipson, H. (2008). Improved quality of 3d-printed tissue constructs through enhanced mixing of alginate hydrogels. In: *Proceedings of the Nineteenth Solid Freeform Fabrication Symposium*, volume 676685.

Cohen, J., Zaleski, K.L., Nourissat, G., Julien, T.P., Randolph, M.A. & Yaremchuk, M.J. (2011). Survival of porcine mesenchymal stem cells over the alginate recovered cellular method. *Journal of Biomedical Materials Research Part A*, 96(1), pp. 93–99.

Colosi, C., Shin, S.R., Manoharan, V., Massa, S., Costantini, M., Barbetta, A., Dokmeci, M.R., Dentini, M. & Khademhosseini, A. (2016). Microfluidic bioprinting of heterogeneous 3d tissue constructs using low-viscosity bioink. *Advanced Materials*, 28(4), pp. 677–684.

Cui, X. & Boland, T. (2009). Human microvasculature fabrication using thermal inkjet printing technology. *Biomaterials*, 30(31), pp. 6221–6227.

Cui, X., Dean, D., Ruggeri, Z.M. & Boland, T. (2010). Cell damage evaluation of thermal inkjet printed chinese hamster ovary cells. *Biotechnology and bioengineering*, 106(6), pp. 963–969.

D Augst, A., Joon Kong, H. & J Mooney, D. (2006). Alginate hydrogels as biomaterials. *Macromolecular Bioscience*, 6, pp. 623–33.

Dababneh, A.B. & Ozbolat, I.T. (2014). Bioprinting technology: a current state-of-the-art review. *Journal of Manufacturing Science and Engineering*, 136(6), p. 061016.

Devillard, R., Correa, M., Kériquel, V., Rémy, M., Kalisky, J., Ali, M., Guillotin, B., Guillemot, F. *et al.* (2014). Cell patterning by laser-assisted bioprinting. *Methods in cell biology*, 119, pp. 159–174.

Dhankani, K.C. & Pearce, J.M. (2017). Open source laboratory sample rotator mixer and shaker. *HardwareX*, 1, pp. 1 – 12.

Dinca, V., Farsari, M., Kafetzopoulos, D., Popescu, A., Dinescu, M. & Fotakis, C. (2008). Patterning parameters for biomolecules microarrays constructed with nanosecond and femtosecond uv lasers. *Thin Solid Films*, 516(18), pp. 6504–6511.

Diogo, G., Gaspar, V., Serra, I., Fradique, R. & Correia, I. (2014). Manufacture of β-tcp/alginate scaffolds through a fab@ home model for application in bone tissue engineering. *Biofabrication*, 6(2), p. 025001.

Doraiswamy, A., Narayan, R., Harris, M., Qadri, S., Modi, R. & Chrisey, D. (2007). Laser microfabrication of hydroxyapatite-osteoblast-like cell composites. *Journal of Biomedical Materials Research Part A*, 80(3), pp. 635–643.

Duan, B., Hockaday, L.A., Kang, K.H. & Butcher, J.T. (2013a). 3d bioprinting of heterogeneous aortic valve conduits with alginate/gelatin hydrogels. *Journal of biomedical materials research Part A*, 101(5), pp. 1255–1264.

Duan, B., Hockaday, L.A., Kapetanovic, E., Kang, K.H. & Butcher, J.T. (2013b). Stiffness and adhesivity control aortic valve interstitial cell behavior within hyaluronic acid based hydrogels. *Acta biomaterialia*, 9(8), pp. 7640–7650.

Duan, B., Kapetanovic, E., Hockaday, L.A. & Butcher, J.T. (2014). Three-dimensional printed trileaflet valve conduits using biological hydrogels and human valve interstitial cells. *Acta biomaterialia*, 10(5), pp. 1836–1846.

Dubbin, K., Tabet, A. & Heilshorn, S.C. (2017). Quantitative criteria to benchmark new and existing bio-inks for cell compatibility. *Biofabrication*, 9(4), p. 044102.

Duocastella, M., Colina, M., Fernández-Pradas, J., Serra, P. & Morenza, J. (2007). Study of the laser-induced forward transfer of liquids for laser bioprinting. *Applied Surface Science*, 253(19), pp. 7855–7859.

Duocastella, M., Fernández-Pradas, J.M., Serra, P. & Morenza, J.L. (2008). Laser-induced forward transfer of liquids for miniaturized biosensors preparation. *J. Laser Micro Nanoeng*, 3(1).

Escobedo-Lucea, C., Bellver, C., Gandia, C., Sanz-Garcia, A., Esteban, F.J., Mirabet, V., Forte, G., Moreno, I., Lezameta, M., Ayuso-Sacido, A. & Garcia-Verdugo, J.M. (2013). A xenogeneic-free protocol for isolation and expansion of human adipose stem cells for clinical uses. *PLOS ONE*, 8(7), pp. 1–12.

Europe (2017). Council of europe eueropean committee on organ transplantation. newsletter transplant. international figures on donation and transplantation 2016. Volume 22.

Fernández-Pradas, J., Colina, M., Serra, P., Dominguez, J. & Morenza, J. (2004). Laser-induced forward transfer of biomolecules. *Thin Solid Films*, 453, pp. 27–30.

Fitz-Gerald, J., Chrisey, D., Piqu, A., Auyeung, R., Mohdi, R., Young, H., Wu, H., Lakeou, S. & Chung, R. (2000). Matrix assisted pulsed laser evaporation direct write (maple dw): a new method to rapidly prototype active and passive electronic circuit elements. *MRS Online Proceedings Library Archive*, 625.

Fogarassy, E., Fuchs, C., Kerherve, F., Hauchecorne, G. & Perriere, J. (1989). Laser-induced forward transfer: A new approach for the deposition of high t c superconducting thin films. *Journal of Materials Research*, 4(5), pp. 1082–1086.

Gaebel, R., Ma, N., Liu, J., Guan, J., Koch, L., Klopsch, C., Gruene, M., Toelk, A., Wang, W., Mark, P. *et al.* (2011). Patterning human stem cells and endothelial cells with laser printing for cardiac regeneration. *Biomaterials*, 32(35), pp. 9218–9230.

Gao, G., Yonezawa, T., Hubbell, K., Dai, G. & Cui, X. (2015a). Inkjet-bioprinted acrylated peptides and peg hydrogel with human mesenchymal stem cells promote robust bone and cartilage formation with minimal printhead clogging. *Biotechnology journal*, 10(10), pp. 1568–1577.

Gao, Q., He, Y., Fu, J.z., Liu, A. & Ma, L. (2015b). Coaxial nozzle-assisted 3d bioprinting with built-in microchannels for nutrients delivery. *Biomaterials*, 61, pp. 203–215.

Gao, T., Gillispie, G.J., Copus, J.S., Seol, Y.J., Atala, A., Yoo, J.J. & Lee, S.J. (2018). Optimization of gelatin–alginate composite bioink printability using rheological parameters: A systematic approach. *Biofabrication*, 10(3), p. 034106.

Gasperini, L., Mano, J.F. & Reis, R.L. (2014). Natural polymers for the microencapsulation of cells. *Journal of The Royal Society Interface*, 11(100).

GCode (2019). List of g-codes supported by marlin firmware. `http://marlinfw.org/meta/gcode/`.

Geng, L., Feng, W., Hutmacher, D.W., Wong, Y.S., Loh, H.T. & Fuh, J.Y. (2005). Direct writing of chitosan scaffolds using a robotic system. *Rapid Prototyping Journal*, 11(2), pp. 90–97.

Goldstein, T.A., Epstein, C.J., Schwartz, J., Krush, A., Lagalante, D.J., Mercadante, K.P., Zeltsman, D., Smith, L.P. & Grande, D.A. (2016). Feasibility of bioprinting with a modified desktop 3d printer. *Tissue Engineering Part C: Methods*, 22(12), pp. 1071–1076.

Groll, J., Burdick, J., Cho, D., Derby, B., Gelinsky, M., Heilshorn, S., Jüngst, T., Malda, J., Mironov, V., Nakayama, K. *et al.* (2018). A definition of bioinks and their distinction from biomaterial inks. *Biofabrication*, 11(1), p. 013001.

Groll, J., Boland, T., Blunk, T., Burdick, J.A., Cho, D.W., Dalton, P.D., Derby, B., Forgacs, G., Li, Q., Mironov, V.A., Moroni, L., Nakamura, M., Shu, W., Takeuchi, S., Vozzi, G., Woodfield, T.B.F., Xu, T., Yoo, J.J. & Malda, J. (2016). Biofabrication: reappraising the definition of an evolving field. *Biofabrication*, 8(1), p. 013001.

Grosvenor, M. & Staniforth, J. (1996). The effect of molecular weight on the rheological and tensile properties of poly (e-caprolactone). *International journal of pharmaceutics*, 135(1-2), pp. 103–109.

Gudapati, H., Dey, M. & Ozbolat, I. (2016). A comprehensive review on droplet-based bioprinting: past, present and future. *Biomaterials*, 102, pp. 20–42.

Guerra, A., Cano, P., Rabionet, M., Puig, T. & Ciurana, J. (2018). 3d-printed pcl/pla composite stents: Towards a new solution to cardiovascular problems. *Materials*, 11(9), p. 1679.

Guillemot, F., Guillotin, B., Fontaine, A., Ali, M., Catros, S., Kériquel, V., Fricain, J.C., Rémy, M., Bareille, R. & Amédée-Vilamitjana, J. (2011). Laser-assisted bioprinting to deal with tissue complexity in regenerative medicine. *Mrs Bulletin*, 36(12), pp. 1015–1019.

Guillemot, F., Mironov, V. & Nakamura, M. (2010). Bioprinting is coming of age: Report from the international conference on bioprinting and biofabrication in bordeaux (3b'09). *Biofabrication 2*, 2, p. 010201.

Guo, T., Holzberg, T.R., Lim, C.G., Gao, F., Gargava, A., Trachtenberg, J.E., Mikos, A.G. & Fisher, J.P. (2017). 3d printing plga: a quantitative examination of the effects of polymer composition and printing parameters on print resolution. *Biofabrication*, 9(2), p. 024101.

Gupta, S., Bissoyi, A. & Bit, A. (2018). A review on 3d printable techniques for tissue engineering. *BioNanoScience*, pp. 1–16.

Gyles, D.A., Castro, L.D., Júnior, J.O.C.S. & Ribeiro-Costa, R.M. (2017). A review of the designs and prominent biomedical advances of natural and synthetic hydrogel formulations. *European Polymer Journal*.

Hansen, C.J., Wu, W., Toohey, K.S., Sottos, N.R., White, S.R. & Lewis, J.A. (2009). Self-healing materials with interpenetrating microvascular networks. *Advanced Materials*, 21(41), pp. 4143–4147.

He, Y., Yang, F., Zhao, H., Gao, Q., Xia, B. & Fu, J. (2016). Research on the printability of hydrogels in 3d bioprinting. *Scientific reports*, 6, p. 29977.

Hendrikson, W., Rouwkema, J., Van Blitterswijk, C. & Moroni, L. (2015). Influence of pcl molecular weight on mesenchymal stromal cell differentiation. *RSC advances*, 5(67), pp. 54510–54516.

Hennink, W. & van Nostrum, C. (2002). Novel crosslinking methods to design hydrogels. *Advanced Drug Delivery Reviews*, 54(1), pp. 13 – 36, recent Developments in Hydrogels.

Hinton, T.J., Jallerat, Q., Palchesko, R.N., Park, J.H., Grodzicki, M.S., Shue, H.J., Ramadan, M.H., Hudson, A.R. & Feinberg, A.W. (2015). Three-dimensional printing of complex biological structures by freeform reversible embedding of suspended hydrogels. *Science advances*, 1(9), p. e1500758.

Hoath, S.D. (2016). *Fundamentals of Inkjet Printing: The Science of Inkjet and Droplets*. John Wiley & Sons.

Hockaday, L., Kang, K., Colangelo, N., Cheung, P., Duan, B., Malone, E., Wu, J., Girardi, L., Bonassar, L., Lipson, H. *et al.* (2012). Rapid 3d printing of anatomically accurate and mechanically heterogeneous aortic valve hydrogel scaffolds. *Biofabrication*, 4(3), p. 035005.

Hölzl, K., Lin, S., Tytgat, L., Van Vlierberghe, S., Gu, L. & Ovsianikov, A. (2016). Bioink properties before, during and after 3d bioprinting. *Biofabrication*, 8(3), p. 032002.

Hopp, B., Smausz, T., Barna, N., Vass, C., Antal, Z., Kredics, L. & Chrisey, D. (2005a). Time-resolved study of absorbing film assisted laser induced forward transfer of trichoderma longibrachiatum conidia. *Journal of Physics D: Applied Physics*, 38(6), p. 833.

Hopp, B., Smausz, T., Kresz, N., Barna, N., Bor, Z., Kolozsvári, L., Chrisey, D.B., Szabó, A. & Nógrádi, A. (2005b). Survival and proliferative ability of various living cell types after laser-induced forward transfer. *Tissue engineering*, 11(11-12), pp. 1817–1823.

Hospodiuk, M., Dey, M., Sosnoski, D. & Ozbolat, I.T. (2017). The bioink: A comprehensive review on bioprintable materials. *Biotechnology advances*.

Hutmacher, D., Sittinger, M. & V Risbud, M. (2004). Scaffold-based tissue engineering: Rationale for computer-aided design and solid free-form fabrication systems. *Trends in Biotechnology*, 22(7), pp. 354–62.

Hutmacher, D.W., Schantz, T., Zein, I., Ng, K.W., Teoh, S.H. & Tan, K.C. (2001). Mechanical properties and cell cultural response of polycaprolactone scaffolds designed and fabricated via fused deposition modeling. *Journal of Biomedical Materials Research*, 55(2), pp. 203–216.

Jeong, B., Kim, S.W. & Bae, Y.H. (2012). Thermosensitive sol–gel reversible hydrogels. *Advanced drug delivery reviews*, 64, pp. 154–162.

Joly-Duhamel, C., Hellio, D. & Djabourov, M. (2002). All gelatin networks: Biodiversity and physical chemistry. *Langmuir*, 18(19), pp. 7208–7217.

Jones, R., Haufe, P., Sells, E., Iravani, P., Olliver, V., Palmer, C. & Bowyer, A. (2011). Reprap–the replicating rapid prototyper. *Robotica*, 29(1), pp. 177–191.

JP, M., JE, M., J, H. & WR, G. (1956). Successful homotransplantation of the human kidney between identical twins. *Journal of the American Medical Association*, 160(4), pp. 277–282.

Kajsa, M., Johan, S. & Paul, G. (2014). 3d bioprinting of cellulose structures from an ionic liquid. *3D Printing and Additive Manufacturing*, 1(3), pp. 115–121.

Kalshetti, P.P., Rajendra, V.B., Dixit, D.N. & Parekh, P.P. (2012). Hydrogels as a drug delivery system and applications: a review. *International Journal of Pharmacy and Pharmaceutical Sciences*, 4(1), pp. 1–7.

Kang, H., Lee, S., Ko, I., Kengla, C., Yoo, J. & Atala, A. (2016). A 3d bioprinting system to produce human-scale tissue constructs with structural integrity. *Nature Biotechnology*, 34(5), pp. 312–9.

Kang, K., Hockaday, L. & Butcher, J. (2013). Quantitative optimization of solid freeform deposition of aqueous hydrogels. *Biofabrication*, 5(3), p. 035001.

Karoly Jakab, Adrian Neagu, V.M.R.R.M. & Forgacs, G. (2004). Engineering biological structures of prescribed shape using self-assembling multicellular systems. *Proceedings of the National Academy of Sciences of the United States of America*, 101 (9), pp. 2864–2869.

Kelly, J. (2013). *3D Printing: Build Your Own 3D Printer and Print Your Own 3D Objects*. Pearson Education, ISBN 9780133553406.

Khademhosseini, A. & Langer, R. (2016). A decade of progress in tissue engineering. *Nature protocols*, 11(10), p. 1775.

Khalil, S., Nam, J. & Sun, W. (2005). Multi-nozzle deposition for construction of 3d biopolymer tissue scaffolds. *Rapid Prototyping Journal*, 11(1), pp. 9–17.

Khalil, S. & Sun, W. (2009). Bioprinting endothelial cells with alginate for 3d tissue constructs. *J Biomech Eng*, 131(11).

Khattak, S.F., Bhatia, S.R. & Roberts, S.C. (2005). Pluronic f127 as a cell encapsulation material: Utilization of membrane-stabilizing agents. *Tissue Engineering*, 11(5-6), pp. 974–983, pMID: 15998236.

Kim, G.H. & Son, J.G. (2009). 3d polycarprolactone (pcl) scaffold with hierarchical structure fabricated byáaápiezoelectric transducer (pzt)-assisted bioplotter. *Applied Physics A*, 94(4), pp. 781–785.

Kim, J.A., Kim, H.N., Im, S.K., Chung, S., Kang, J.Y. & Choi, N. (2015). Collagen-based brain microvasculature model in vitro using three-dimensional printed template. *Biomicrofluidics*, 9(2), p. 024115.

Kim, Y., Son, S., Choi, J., Byun, D. & Lee, S. (2008). Design and fabrication of electrostatic inkjet head using silicon micromachining technology. *Journal of Semiconductor Technology and Science*, 8(2), pp. 121–127.

Klebe, R.J. (1988). Cytoscribing: a method for micropositioning cells and the construction of two-and three-dimensional synthetic tissues. *Experimental cell research*, 179(2), pp. 362–373.

Koch, L., Kuhn, S., Sorg, H., Gruene, M., Schlie, S., Gaebel, R., Polchow, B., Reimers, K., Stoelting, S., Ma, N. *et al.* (2009). Laser printing of skin cells and human stem cells. *Tissue Engineering Part C: Methods*, 16(5), pp. 847–854.

Kolesky, D.B., Homan, K.A., Skylar-Scott, M.A. & Lewis, J.A. (2016). Three-dimensional bioprinting of thick vascularized tissues. *Proceedings of the National Academy of Sciences*, 113(12), pp. 3179–3184.

Kolesky, D.B., Truby, R.L., Gladman, A., Busbee, T.A., Homan, K.A. & Lewis, J.A. (2014). 3d bioprinting of vascularized, heterogeneous cell-laden tissue constructs. *Advanced materials*, 26(19), pp. 3124–3130.

Kong, H.J., Smith, M.K. & Mooney, D.J. (2003). Designing alginate hydrogels to maintain viability of immobilized cells. *Biomaterials*, 24(22), pp. 4023–4029.

Kundu, J., Shim, J.H., Jang, J., Kim, S.W. & Cho, D.W. (2015). An additive manufacturing-based pcl–alginate–chondrocyte bioprinted scaffold for cartilage tissue engineering. *Journal of tissue engineering and regenerative medicine*, 9(11), pp. 1286–1297.

Kyle, S., Jessop, Z.M., Al-Sabah, A. & Whitaker, I.S. (2017). "printability" of candidate biomaterials for extrusion based 3d printing: State-of-the-art. *Advanced healthcare materials*, 6(16), p. 1700264.

Lam, C.X., Hutmacher, D.W., Schantz, J.T., Woodruff, M.A. & Teoh, S.H. (2009). Evaluation of polycaprolactone scaffold degradation for 6 months in vitro and in vivo. *Journal of Biomedical Materials Research Part A: An Official Journal of The Society for Biomaterials, The Japanese Society for Biomaterials, and The Australian Society for Biomaterials and the Korean Society for Biomaterials*, 90(3), pp. 906–919.

Lam, C.X., Savalani, M.M., Teoh, S.H. & Hutmacher, D.W. (2008). Dynamics of in vitro polymer degradation of polycaprolactone-based scaffolds: accelerated versus simulated physiological conditions. *Biomedical materials*, 3(3), p. 034108.

Lam, C.X., Teoh, S.H. & Hutmacher, D.W. (2007). Comparison of the degradation of polycaprolactone and polycaprolactone–(β-tricalcium phosphate) scaffolds in alkaline medium. *Polymer international*, 56(6), pp. 718–728.

Landers, R., HÃŒbner, U., Schmelzeisen, R. & MÃŒlhaupt, R. (2002). Rapid prototyping of scaffolds derived from thermoreversible hydrogels and tailored for applications in tissue engineering. *Biomaterials*, 23(23), pp. 4437 – 4447.

Langer, R. & Vacanti, J. (1993). Tissue engineering. *Science*, 260(5110), pp. 920–926.

Langer, R.S. & Vacanti, J.P. (1999). Tissue engineering: the challenges ahead. *Scientific American*, 280(4), pp. 86–89.

Lee, H.J., Kim, Y.B., Ahn, S.H., Lee, J.S., Jang, C.H., Yoon, H., Chun, W. & Kim, G.H. (2015). A new approach for fabricating collagen/ecm-based bioinks using preosteoblasts and human adipose stem cells. *Advanced healthcare materials*, 4(9), pp. 1359–1368.

Lee, H., Ahn, S., Chun, W. & Kim, G. (2014). Enhancement of cell viability by fabrication of macroscopic 3d hydrogel scaffolds using an innovative cell-dispensing technique supplemented by preosteoblast-laden micro-beads. *Carbohydrate polymers*, 104, pp. 191–198.

Lee, K.Y. & Mooney, D.J. (2001). Hydrogels for tissue engineering. *Chemical reviews*, 101(7), pp. 1869–1880.

Lee, V., Singh, G., Trasatti, J.P., Bjornsson, C., Xu, X., Tran, T.N., Yoo, S.S., Dai, G. & Karande, P. (2013). Design and fabrication of human skin by three-dimensional bioprinting. *Tissue Engineering Part C: Methods*, 20(6), pp. 473–484.

Lee, W., Lee, V., Polio, S., Keegan, P., Lee, J.H., Fischer, K., Park, J.K. & Yoo, S.S. (2010). On-demand three-dimensional freeform fabrication of multi-layered hydrogel scaffold with fluidic channels. *Biotechnology and bioengineering*, 105(6), pp. 1178–1186.

Li, J., Chen, M., Wei, X., Hao, Y. & Wang, J. (2017). Evaluation of 3d-printed polycaprolactone scaffolds coated with freeze-dried platelet-rich plasma for bone regeneration. *Materials*, 10(7), p. 831.

Li, M., Tian, X., Schreyer, D.J. & Chen, X. (2011). Effect of needle geometry on flow rate and cell damage in the dispensing-based biofabrication process. *Biotechnology progress*, 27(6), pp. 1777–1784.

Li, M., Tian, X., Zhu, N., Schreyer, D.J. & Chen, X. (2009). Modeling process-induced cell damage in the biodispensing process. *Tissue Engineering Part C: Methods*, 16(3), pp. 533–542.

Li, W.J., Danielson, K.G., Alexander, P.G. & Tuan, R.S. (2003). Biological response of chondrocytes cultured in three-dimensional nanofibrous poly (e-caprolactone) scaffolds. *Journal of Biomedical Materials Research Part A: An Official Journal of The Society for Biomaterials, The Japanese Society for Biomaterials, and The Australian Society for Biomaterials and the Korean Society for Biomaterials*, 67(4), pp. 1105–1114.

Lin, R.Z., Chen, Y.C., Moreno-Luna, R., Khademhosseini, A. & Melero-Martin, J.M. (2013). Transdermal regulation of vascular network bioengineering using a photopolymerizable methacrylated gelatin hydrogel. *Biomaterials*, 34(28), pp. 6785–6796.

Lipton, J., Maccurdy, R., Boban, M., Chartrain, N., Iii, L.W., Gangjee, N., Nagai, A., Cohen, J., Sobhani, K., Liu, J. *et al.* (2012). Fab@ home model 3: a more robust, cost effective and accessible open hardware fabrication platform.

Lipton, J.I., Cohen, D., Heinz, M., Lobovsky, M., Parad, W., Bernstien, G., Li, T., Quartiere, J., Washington, K., Umaru, A. *et al.* (2009). Fab@ home model 2: Towards ubiquitous personal fabrication devices. In: *Solid Freeform Fabrciation Symposium.*

Liu, C., Xia, Z. & Czernuszka, J. (2007). Design and development of three-dimensional scaffolds for tissue engineering. *Chemical Engineering Research and Design*, 85(7), pp. 1051 – 1064.

Liu, W., Zhang, Y.S., Heinrich, M.A., De Ferrari, F., Jang, H.L., Bakht, S.M., Alvarez, M.M., Yang, J., Li, Y.C., Trujillo-de Santiago, G. *et al.* (2017). Rapid continuous multimaterial extrusion bioprinting. *Advanced materials*, 29(3), p. 1604630.

Lixandrão Filho, A., Cheung, P., Noritomi, P., da Silva, J., Colangelo, N., Kang, H., Lipson, H., Butcher, J., Malone, E. & Neto, P.I. (2009). Construction and adaptation of an open source rapid prototyping machine for biomedical research purposes-a multinational collaborative development. *Innovative developments in design and manufacturing. Leiria, Portugal: CRC Press, 469Á473.*

Loessner, D., Meinert, C., Kaemmerer, E., Martine, L.C., Yue, K., Levett, P.A., Klein, T.J., Melchels, F.P., Khademhosseini, A. & Hutmacher, D.W. (2016). Functionalization, preparation and use of cell-laden gelatin methacryloyl-based hydrogels as modular tissue culture platforms. *Nature protocols*, 11(4), pp. 727–746.

Maher, P., Keatch, R., Donnelly, K., Mackay, R. & Paxton, J. (2009). Construction of 3d biological matrices using rapid prototyping technology. *Rapid Prototyping Journal*, 15(3), pp. 204–210.

Mahesh, M., Wong, Y.S., Fuh, J.Y.H. & Loh, H.T. (2006). A six-sigma approach for benchmarking of rp&m processes. *The International Journal of Advanced Manufacturing Technology*, 31(3), pp. 374–387.

Malone, E. & Lipson, H. (2007). Fab@ home: the personal desktop fabricator kit. *Rapid Prototyping Journal*, 13(4), pp. 245–255.

Marlin (2018). Repository of marlin firmware. `https://github.com/MarlinFirmware/Marlin`.

Marquez, G.J., Renn, M.J. & Miller, W.D. (2001). Aerosol-based direct-write of biological materials for biomedical applications. *MRS Online Proceedings Library Archive*, 698.

Matias, E. & Rao, B. (2015). 3d printing: On its historical evolution and the implications for business. In: *2015 Portland International Conference on Management of Engineering and Technology (PICMET)*, pp. 551–558.

Matthew, J.E., Nazario, Y.L., Roberts, S.C. & Bhatia, S.R. (2002). Effect of mammalian cell culture medium on the gelation properties of pluronicÂ® f127. *Biomaterials*, 23(23), pp. 4615 – 4619.

Melchels, F.P., Domingos, M.A., Klein, T.J., Malda, J., Bartolo, P.J. & Hutmacher, D.W. (2012). Additive manufacturing of tissues and organs. *Progress in Polymer Science*, 37(8), pp. 1079–1104.

Miller, J. (2012). Baricuda extruder. `https://www.thingiverse.com/thing:26343`.

Miller, J.S., Stevens, K.R., Yang, M.T., Baker, B.M., Nguyen, D.H.T., Cohen, D.M., Toro, E., Chen, A.A., Galie, P.A., Yu, X. *et al.* (2012). Rapid casting of patterned vascular networks for perfusable engineered three-dimensional tissues. *Nature mate-*

rials, 11(9), pp. 768–774.

Mironov, V., Visconti, R.P., Kasyanov, V., Forgacs, G., Drake, C.J. & Markwald, R.R. (2009). Organ printing: tissue spheroids as building blocks. *Biomaterials*, 30(12), pp. 2164–2174.

Mitsak, A.G., Kemppainen, J.M., Harris, M.T. & Hollister, S.J. (2011). Effect of polycaprolactone scaffold permeability on bone regeneration in vivo. *Tissue Engineering Part A*, 17(13-14), pp. 1831–1839.

Müller, M., Becher, J., Schnabelrauch, M. & Zenobi-Wong, M. (2013). Printing thermoresponsive reverse molds for the creation of patterned two-component hydrogels for 3d cell culture. *Journal of visualized experiments: JoVE*, (77).

Müller, M., Becher, J., Schnabelrauch, M. & Zenobi-Wong, M. (2015). Nanostructured pluronic hydrogels as bioinks for 3d bioprinting. *Biofabrication*, 7(3), p. 035006.

Murphy, C., Kolan, K., Li, W., Semon, J., Day, D. & Leu, M. (2017). 3d bioprinting of stem cells and polymer/bioactive glass composite scaffolds for bone tissue engineering. *International Journal of Bioprinting*, 3(1), pp. 54–64.

Murphy, S.V. & Atala, A. (2014). 3d bioprinting of tissues and organs. *Nature biotechnology*, 32(8), pp. 773–785.

Naahidi, S., Jafari, M., Logan, M., Wang, Y., Yuan, Y., Bae, H., Dixon, B. & Chen, P. (2017). Biocompatibility of hydrogel-based scaffolds for tissue engineering applications. *Biotechnology Advances*.

Nahmias, Y. & Odde, D.J. (2006). Micropatterning of living cells by laser-guided direct writing: application to fabrication of hepatic–endothelial sinusoid-like structures. *Nature protocols*, 1(5), pp. 2288–2296.

Nahmias, Y., Schwartz, R.E., Verfaillie, C.M. & Odde, D.J. (2005). Laser-guided direct writing for three-dimensional tissue engineering. *Biotechnology and bioengineering*, 92(2), pp. 129–136.

Nair, K., Gandhi, M., Khalil, S., Yan, K.C., Marcolongo, M., Barbee, K. & Sun, W. (2009). Characterization of cell viability during bioprinting processes. *Biotechnology Journal*, 4(8), pp. 1168–1177.

Nakamura, M., Kobayashi, A., Takagi, F., Watanabe, A., Hiruma, Y., Ohuchi, K., Iwasaki, Y., Horie, M., Morita, I. & Takatani, S. (2005). Biocompatible inkjet printing technique for designed seeding of individual living cells. *Tissue engineering*, 11(11-12), pp. 1658–1666.

Neufurth, M., Wang, X., Schröder, H.C., Feng, Q., Diehl-Seifert, B., Ziebart, T., Steffen, R., Wang, S. & Müller, W.E. (2014). Engineering a morphogenetically active hydrogel for bioprinting of bioartificial tissue derived from human osteoblast-like saos-2 cells. *Biomaterials*, 35(31), pp. 8810–8819.

Ng, W.L., Yeong, W.Y. & Naing, M.W. (2016). Polyelectrolyte gelatin-chitosan hydrogel optimized for 3d bioprinting in skin tissue engineering. *International Journal of Bioprinting*, 2(1).

Nicodemus, G.D. & Bryant, S.J. (2008). Cell encapsulation in biodegradable hydrogels for tissue engineering applications. *Tissue Engineering Part B: Reviews*, 14(2), pp. 149–165.

Nilsiam, Y., Sanders, P. & Pearce, J. (2018). Applications of open source gmaw-based metal 3-d printing. *J. Manuf. Mater. Process*, 2, p. 18.

Ning, L. & Chen, X. (2017). A brief review of extrusion-based tissue scaffold bioprinting. *Biotechnology Journal*.

Nishiyama, Y., Nakamura, M., Henmi, C., Yamaguchi, K., Mochizuki, S., Nakagawa, H. & Takiura, K. (2009). Development of a three-dimensional bioprinter: construction of cell supporting structures using hydrogel and state-of-the-art inkjet technology. *Journal of Biomechanical Engineering*, 131(3), p. 035001.

Norotte, C., Marga, F.S., Niklason, L.E. & Forgacs, G. (2009). Scaffold-free vascular tissue engineering using bioprinting. *Biomaterials*, 30(30), pp. 5910–5917.

Odde, D.J. & Renn, M.J. (1999). Laser-guided direct writing for applications in biotechnology. *Trends in biotechnology*, 17(10), pp. 385–389.

Odde, D.J. & Renn, M.J. (2000). Laser-guided direct writing of living cells. *Biotechnology and bioengineering*, 67(3), pp. 312–318.

Olubamiji, A.D., Izadifar, Z., Si, J.L., Cooper, D.M., Eames, B.F. & Chen, D.X. (2016a). Modulating mechanical behaviour of 3d-printed cartilage-mimetic pcl scaffolds: influence of molecular weight and pore geometry. *Biofabrication*, 8(2), p. 025020.

Olubamiji, A.D., Izadifar, Z., Zhu, N., Chang, T., Chen, X. & Eames, B.F. (2016b). Using synchrotron radiation inline phase-contrast imaging computed tomography to visualize three-dimensional printed hybrid constructs for cartilage tissue engineering. *Journal of synchrotron radiation*, 23(3), pp. 802–812.

Ouyang, L., Highley, C.B., Sun, W. & Burdick, J.A. (2017). A generalizable strategy for the 3d bioprinting of hydrogels from nonviscous photo-crosslinkable inks. *Advanced Materials*, 29(8).

Ouyang, L., Yao, R., Chen, X., Na, J. & Sun, W. (2015). 3d printing of hek 293ft cell-laden hydrogel into macroporous constructs with high cell viability and normal biological functions. *Biofabrication*, 7(1), p. 015010.

Ouyang, L., Yao, R., Zhao, Y. & Sun, W. (2016). Effect of bioink properties on printability and cell viability for 3d bioplotting of embryonic stem cells. *Biofabrication*, 8(3), p. 035020.

Ovsianikov, A., Gruene, M., Pflaum, M., Koch, L., Maiorana, F., Wilhelmi, M., Haverich, A. & Chichkov, B. (2010). Laser printing of cells into 3d scaffolds. *Biofabrication*, 2(1), p. 014104.

Owens, C.M., Marga, F., Forgacs, G. & Heesch, C.M. (2013). Biofabrication and testing of a fully cellular nerve graft. *Biofabrication*, 5(4), p. 045007.

Ozbolat, I.T. & Hospodiuk, M. (2016). Current advances and future perspectives in extrusion-based bioprinting. *Biomaterials*, 76, pp. 321–343.

Ozbolat, I.T., Moncal, K.K. & Gudapati, H. (2017). Evaluation of bioprinter technologies. *Additive Manufacturing*, 13, pp. 179 – 200.

Ozbolat, I.T. & Yu, Y. (2013). Bioprinting toward organ fabrication: challenges and future trends. *IEEE Transactions on Biomedical Engineering*, 60(3), pp. 691–699.

Panouille, M. & Larreta-Garde, V. (2009). Gelation behaviour of gelatin and alginate mixtures. *Food Hydrocolloids*, 23(4), pp. 1074 – 1080, food Colloids: Creating Structure, Delivering Functionality.

Pardo, L., Wilson, W.C. & Boland, T. (2003). Characterization of patterned self-assembled monolayers and protein arrays generated by the ink-jet method. *Langmuir*, 19(5), pp. 1462–1466.

Park, S.A., Lee, H.J., Kim, K.S., Lee, S.J., Lee, J.T., Kim, S.Y., Chang, N.H. & Park, S.Y. (2018). In vivo evaluation of 3d-printed polycaprolactone scaffold implantation combined with β-tcp powder for alveolar bone augmentation in a beagle defect model. *Materials*, 11(2), p. 238.

Parzel, C.A., Pepper, M.E., Burg, T., Groff, R.E. & Burg, K.J. (2009). Edta enhances high-throughput two-dimensional bioprinting by inhibiting salt scaling and cell aggregation at the nozzle surface. *Journal of tissue engineering and regenerative medicine*, 3(4), pp. 260–268.

Pati, F., Shim, J.H., Lee, J.S. & Cho, D.W. (2013). 3d printing of cell-laden constructs for heterogeneous tissue regeneration. *Manufacturing Letters*, 1(1), pp. 49–53.

Patz, T., Doraiswamy, A., Narayan, R., He, W., Zhong, Y., Bellamkonda, R., Modi, R. & Chrisey, D. (2006). Three-dimensional direct writing of b35 neuronal cells. *Journal of Biomedical Materials Research Part B: Applied Biomaterials*, 78(1), pp. 124–130.

Paxton, N., Smolan, W., Bock, T., Melchels, F., Groll, J. & Jungst, T. (2017). Proposal to assess printability of bioinks for extrusion-based bioprinting and evaluation of rheological properties governing bioprintability. *Biofabrication*, 9(4), p. 044107.

Pearce, J.M., Blair, C.M., Laciak, K.J., Andrews, R., Nosrat, A. & Zelenika-Zovko, I. (2010). 3-d printing of open source appropriate technologies for self-directed sustainable development. *Journal of Sustainable Development*, 3(4), p. 17.

Pfister, A., Landers, R., Laib, A., Hübner, U., Schmelzeisen, R. & Mülhaupt, R. (2004). Biofunctional rapid prototyping for tissue-engineering applications: 3d bioplotting versus 3d printing. *Journal of Polymer Science Part A: Polymer Chemistry*, 42(3), pp. 624–638.

Piqué, A., Chrisey, D., Auyeung, R., Fitz-Gerald, J., Wu, H., McGill, R., Lakeou, S., Wu, P., Nguyen, V. & Duignan, M. (1999). A novel laser transfer process for direct writing of electronic and sensor materials. *Applied Physics A*, 69(1), pp. S279–S284.

Polzin, C., Spath, S. & Seitz, H. (2013). Characterization and evaluation of a pmma-based 3d printing process. *Rapid Prototyping Journal*, 19(1), pp. 37–43.

Prusa, J. (2018). Repository with the 3d printers developed by josef prusa. `https://github.com/josefprusa`.

Pusch, K., Hinton, T.J. & Feinberg, A.W. (2018). Large volume syringe pump extruder for desktop 3d printers. *HardwareX*, 3, pp. 49 – 61.

Rajaram, A., Schreyer, D. & Chen, D. (2014). Bioplotting alginate/hyaluronic acid hydrogel scaffolds with structural integrity and preserved schwann cell viability. *3D Printing and Additive Manufacturing*, 1(4), pp. 194–203.

Ramanath, H., Chua, C., Leong, K. & Shah, K. (2008). Melt flow behaviour of poly-ε-caprolactone in fused deposition modelling. *Journal of Materials Science: Materials in Medicine*, 19(7), pp. 2541–2550.

Rasband, W. (2018). Imagej, u. s. national institutes of health, bethesda, maryland, usa,. `https://imagej.nih.gov/ij/`.

Ratner, B.D. & Hoffman, A.S. (1976). Synthetic hydrogels for biomedical applications. *Hydrogels for Medical and Related Applications*.

Reid, J.A., Mollica, P.A., Johnson, G.D., Ogle, R.C., Bruno, R.D. & Sachs, P.C. (2016). Accessible bioprinting: adaptation of a low-cost 3d-printer for precise cell placement and stem cell differentiation. *Biofabrication*, 8(2), p. 025017.

Repetier-Host (2018). Repetier-host v1.6.2. `https://www.repetier.com/`.

RepRap (2018). Reprap website. `http://www.reprap.org`.

RepRapElectronics (2018). List of reprap compatible electronics. `https://reprap.org/wiki/List_of_electronics`.

RepRapOptions (2018). Reprap 3d printers. `https://reprap.org/wiki/RepRap_Options`.

Ribeiro, A., Blokzijl, M.M., Levato, R., Visser, C.W., Castilho, M., Hennink, W.E., Vermonden, T. & Malda, J. (2017). Assessing bioink shape fidelity to aid material development in 3d bioprinting. *Biofabrication*, 10(1), p. 014102.

RichRap (2012). Universal paste extruder. `https://www.thingiverse.com/thing:20733`.

Riegel J, Mayer W, H.Y.V. (2018). Freecad 0.17. `http://www.freecadweb.org`.

Roberson, D., Espalin, D. & Wicker, R. (2013). 3d printer selection: A decision-making evaluation and ranking model. *Virtual and Physical Prototyping*, 8(3), pp. 201–212.

Rocca, M., Fragasso, A., Liu, W., Heinrich, M.A. & Zhang, Y.S. (2018). Embedded multimaterial extrusion bioprinting. *SLAS TECHNOLOGY: Translating Life Sciences Innovation*, 23(2), pp. 154–163.

Roehm, K.D. & Madihally, S.V. (2018). Bioprinted chitosan-gelatin thermosensitive hydrogels using an inexpensive 3d printer. *Biofabrication*, 10(1), p. 015002.

Roth, E., Xu, T., Das, M., Gregory, C., Hickman, J. & Boland, T. (2004). Inkjet printing for high-throughput cell patterning. *Biomaterials*, 25(17), pp. 3707–3715.

Rutz, A.L., Hyland, K.E., Jakus, A.E., Burghardt, W.R. & Shah, R.N. (2015). A multimaterial bioink method for 3d printing tunable, cell-compatible hydrogels. *Advanced Materials*, 27(9), pp. 1607–1614.

Sanchez, F.A.C., Boudaoud, H., Muller, L. & Camargo, M. (2014). Towards a standard experimental protocol for open source additive manufacturing. *Virtual and Physical*

Prototyping, 9(3), pp. 151–167.

Saunders, R.E., Gough, J.E. & Derby, B. (2008). Delivery of human fibroblast cells by piezoelectric drop-on-demand inkjet printing. *Biomaterials*, 29(2), pp. 193–203.

Scaravetti, D., Dubois, P. & Duchamp, R. (2008). Qualification of rapid prototyping tools: proposition of a procedure and a test part. *The International Journal of Advanced Manufacturing Technology*, 38(7), pp. 683–690.

Schiele, N.R., Corr, D.T., Huang, Y., Raof, N.A., Xie, Y. & Chrisey, D.B. (2010). Laser-based direct-write techniques for cell printing. *Biofabrication*, 2(3), p. 032001.

Sears, N., Dhavalikar, P., Whitely, M. & Cosgriff-Hernandez, E. (2017). Fabrication of biomimetic bone grafts with multi-material 3d printing. *Biofabrication*, 9(2), p. 025020.

Seol, Y.J., Kang, H.W., Lee, S.J., Atala, A. & Yoo, J.J. (2014). Bioprinting technology and its applications. *European Journal of Cardio-Thoracic Surgery*, 46(3), pp. 342–348.

Seol, Y.J., Kang, T.Y. & Cho, D.W. (2012). Solid freeform fabrication technology applied to tissue engineering with various biomaterials. *Soft Matter*, 8, pp. 1730–1735.

Seyednejad, H., Gawlitta, D., Dhert, W.J., Van Nostrum, C.F., Vermonden, T. & Hennink, W.E. (2011). Preparation and characterization of a three-dimensional printed scaffold based on a functionalized polyester for bone tissue engineering applications. *Acta biomaterialia*, 7(5), pp. 1999–2006.

Shanjani, Y., Pan, C., Elomaa, L. & Yang, Y. (2015). A novel bioprinting method and system for forming hybrid tissue engineering constructs. *Biofabrication*, 7(4), p. 045008.

Sheshadri, P. & Shirwaiker, R.A. (2015). Characterization of material–process–structure interactions in the 3d bioplotting of polycaprolactone. *3D Printing and Additive Manufacturing*, 2(1), pp. 20–31.

Shim, J.H., Lee, J.S., Kim, J.Y. & Cho, D.W. (2012). Bioprinting of a mechanically enhanced three-dimensional dual cell-laden construct for osteochondral tissue engineering using a multi-head tissue/organ building system. *Journal of Micromechanics and Microengineering*, 22(8), p. 085014.

Shipley, J.R., Kapoor, J., Dreelin, R.A., Winkler, D.W. & Lecomte, N. (2017). An open-source sensor logger for recording vertical movement in free-living organisms. *Methods in Ecology and Evolution*, 9(3), pp. 465–471.

Singh, M., Haverinen, H.M., Dhagat, P. & Jabbour, G.E. (2010). Inkjet printing-process and its applications. *Advanced materials*, 22(6), pp. 673–685.

Skardal, A. & Atala, A. (2014). Biomaterials for integration with 3-d bioprinting. *Annals of Biomedical Engineering*, 43.

Skardal, A., Mack, D., Kapetanovic, E., Atala, A., Jackson, J.D., Yoo, J. & Soker, S. (2012). Bioprinted amniotic fluid-derived stem cells accelerate healing of large skin wounds. *Stem cells translational medicine*, 1(11), pp. 792–802.

Skardal, A., Zhang, J., McCoard, L., Xu, X., Oottamasathien, S. & Prestwich, G.D. (2010). Photocrosslinkable hyaluronan-gelatin hydrogels for two-step bioprinting. *Tissue Engineering Part A*, 16(8), pp. 2675–2685.

Slic3r (2018). Slic3r v1.2.9. `github.com/alexrj/Slic3r`.

Slic3r (2019). Slic3r official website. `http://slic3r.org`.

Smausz, T., Hopp, B., Kecskemeti, G. & Bor, Z. (2006). Study on metal microparticle content of the material transferred with absorbing film assisted laser induced forward transfer when using silver absorbing layer. *Applied surface science*, 252(13), pp. 4738–4742.

Smith, C.M., Christian, J.J., Warren, W.L. & Williams, S.K. (2007). Characterizing environmental factors that impact the viability of tissue-engineered constructs fabricated by a direct-write bioassembly tool. *Tissue engineering*, 13(2), pp. 373–383.

Smith, C.M., Stone, A.L., Parkhill, R.L., Stewart, R.L., Simpkins, M.W., Kachurin, A.M., Warren, W.L. & Williams, S.K. (2004). Three-dimensional bioassembly tool for generating viable tissue-engineered constructs. *Tissue engineering*, 10(9-10), pp. 1566–1576.

Sodupe, E. (2019). Modification of marlin firmware for bioprinting purposes developed by enrique sodupe. `https://github.com/ensod/Marlin`.

St-Pierre, J.P., Gauthier, M., Lefebvre, L.P. & Tabrizian, M. (2005). Three-dimensional growth of differentiating mc3t3-e1 pre-osteoblasts on porous titanium scaffolds. *Biomaterials*, 26(35), pp. 7319–7328.

Suntornnond, R., Tan, E.Y.S., An, J. & Chua, C.K. (2016). A mathematical model on the resolution of extrusion bioprinting for the development of new bioinks. *Materials*, 9(9), p. 756.

Tabriz, A.G., Hermida, M.A., Leslie, N.R. & Shu, W. (2015). Three-dimensional bioprinting of complex cell laden alginate hydrogel structures. *Biofabrication*, 7(4), p. 045012.

Tasoglu, S. & Demirci, U. (2013). Bioprinting for stem cell research. *Trends in biotechnology*, 31(1), pp. 10–19.

TELab (2018). Nih 3d print exchange repository. `https://3dprint.nih.gov/users/telab`.

Tibbitt, M.W. & Anseth, K.S. (2009). Hydrogels as extracellular matrix mimics for 3d cell culture. *Biotechnol. Bioeng.*, 103, pp. 655–663.

Trachtenberg, J.E., Mountziaris, P.M., Miller, J.S., Wettergreen, M., Kasper, F.K. & Mikos, A.G. (2014). Open-source three-dimensional printing of biodegradable polymer scaffolds for tissue engineering. *Journal of Biomedical Materials Research Part A*, 102(12), pp. 4326–4335.

Trachtenberg, J.E., Placone, J.K., Smith, B.T., Piard, C.M., Santoro, M., Scott, D.W., Fisher, J.P. & Mikos, A.G. (2016). Extrusion-based 3d printing of poly(propylene fumarate) in a full-factorial design. *ACS Biomaterials Science & Engineering*, 2(10), pp. 1771–1780.

Turksen, K. (2015). *Bioprinting in regenerative medicine*. Springer.

Tymrak, B., Kreiger, M. & Pearce, J.M. (2014). Mechanical properties of components fabricated with open-source 3-d printers under realistic environmental conditions. *Materials & Design*, 58, pp. 242–246.

Umezu, S., Hatta, T. & Ohmori, H. (2013). Fundamental characteristics of bioprint on calcium alginate gel. *Japanese Journal of Applied Physics*, 52(5S1), p. 05DB20.

Umezu, S., Kitajima, T., Ohmori, H. & Ito, Y. (2011). Fundamental characteristics of printed cell structures utilizing electrostatic inkjet phenomena. *Sensors and Actuators A: Physical*, 166(2), pp. 251–255.

Umezu, S. & Ohmori, H. (2014). Characteristics on micro-biofabrication by patterning with electrostatically injected droplet. *CIRP Annals-Manufacturing Technology*, 63(1), pp. 221–224.

UNOS (2018). United network for organ sharing (unos). accessed on april 2018.

Visser, J., Peters, B., Burger, T.J., Boomstra, J., Dhert, W.J., Melchels, F.P. & Malda, J. (2013). Biofabrication of multi-material anatomically shaped tissue constructs. *Biofabrication*, 5(3), p. 035007.

Wang, X., Ao, Q., Tian, X., Fan, J., Tong, H., Hou, W. & Bai, S. (2017). Gelatin-based hydrogels for organ 3d bioprinting. *Polymers*, 9(9), p. 401.

Wang, X., He, K. & Zhang, W. (2013). Optimizing the fabrication processes for manufacturing a hybrid hierarchical polyurethane–cell/hydrogel construct. *Journal of bioactive and compatible polymers*, 28(4), pp. 303–319.

Wijnen, B., Hunt, E.J., Anzalone, G.C. & Pearce, J.M. (2014). Open-source syringe pump library. *PloS one*, 9(9), p. e107216.

Wijshoff, H. (2010). The dynamics of the piezo inkjet printhead operation. *Physics reports*, 491(4), pp. 77–177.

Wilson, W.C. & Boland, T. (2003). Cell and organ printing 1: protein and cell printers. *The Anatomical Record*, 272(2), pp. 491–496.

Wittbrodt, B.T., Glover, A., Laureto, J., Anzalone, G., Oppliger, D., Irwin, J. & Pearce, J.M. (2013). Life-cycle economic analysis of distributed manufacturing with open-source 3-d printers. *Mechatronics*, 23(6), pp. 713–726.

Woodruff, M.A. & Hutmacher, D.W. (2010). The return of a forgotten polymer-polycaprolactone in the 21st century. *Progress in polymer science*, 35(10), pp. 1217–1256.

Wu, W., DeConinck, A. & Lewis, J.A. (2011). Omnidirectional printing of 3d microvascular networks. *Advanced Materials*, 23(24).

Wu, W., Hansen, C.J., Aragon, A.M., Geubelle, P.H., White, S.R. & Lewis, J.A. (2010). Direct-write assembly of biomimetic microvascular networks for efficient fluid transport. *Soft Matter*, 6, pp. 739–742.

Wust, S., Godla, M.E., MÃŒller, R. & Hofmann, S. (2014). Tunable hydrogel composite with two-step processing in combination with innovative hardware upgrade for cell-based three-dimensional bioprinting. *Acta Biomaterialia*, 10(2), pp. 630 – 640.

Xu, C., Chai, W., Huang, Y. & Markwald, R.R. (2012). Scaffold-free inkjet printing of three-dimensional zigzag cellular tubes. *Biotechnology and bioengineering*, 109(12), pp. 3152–3160.

Xu, T., Gregory, C.A., Molnar, P., Cui, X., Jalota, S., Bhaduri, S.B. & Boland, T. (2006). Viability and electrophysiology of neural cell structures generated by the inkjet printing method. *Biomaterials*, 27(19), pp. 3580–3588.

Xu, T., Jin, J., Gregory, C., Hickman, J.J. & Boland, T. (2005). Inkjet printing of viable mammalian cells. *Biomaterials*, 26(1), pp. 93–99.

Xu, T., Kincaid, H., Atala, A. & Yoo, J.J. (2008a). High-throughput production of single-cell microparticles using an inkjet printing technology. *Journal of Manufacturing Science and Engineering*, 130(2), p. 021017.

Xu, T., Petridou, S., Lee, E.H., Roth, E.A., Vyavahare, N.R., Hickman, J.J. & Boland, T. (2004). Construction of high-density bacterial colony arrays and patterns by the ink-jet method. *Biotechnology and bioengineering*, 85(1), pp. 29–33.

Xu, T., Rohozinski, J., Zhao, W., Moorefield, E.C., Atala, A. & Yoo, J.J. (2008b). Inkjet-mediated gene transfection into living cells combined with targeted delivery. *Tissue Engineering Part A*, 15(1), pp. 95–101.

Xu, T., Zhao, W., Zhu, J.M., Albanna, M.Z., Yoo, J.J. & Atala, A. (2013). Complex heterogeneous tissue constructs containing multiple cell types prepared by inkjet printing technology. *Biomaterials*, 34(1), pp. 130–139.

Yan, Y., Wang, X., Pan, Y., Liu, H., Cheng, J., Xiong, Z., Lin, F., Wu, R., Zhang, R. & Lu, Q. (2005). Fabrication of viable tissue-engineered constructs with 3d cell-assembly technique. *Biomaterials*, 26(29), pp. 5864–5871.

Yusof, A., Keegan, H., Spillane, C.D., Sheils, O.M., Martin, C.M., O'Leary, J.J., Zengerle, R. & Koltay, P. (2011). Inkjet-like printing of single-cells. *Lab on a Chip*, 11(14), pp. 2447–2454.

Zehnder, T., Sarker, B., Boccaccini, A.R. & Detsch, R. (2015). Evaluation of an alginate-gelatine crosslinked hydrogel for bioplotting. *Biofabrication*, 7(2), p. 025001.

Zein, I., Hutmacher, D.W., Tan, K.C. & Teoh, S.H. (2002). Fused deposition modeling of novel scaffold architectures for tissue engineering applications. *Biomaterials*, 23(4), pp. 1169–1185.

Zhang, Y., Yu, Y., Akkouch, A., Dababneh, A., Dolati, F. & Ozbolat, I.T. (2015). In vitro study of directly bioprinted perfusable vasculature conduits. *Biomaterials science*, 3(1), pp. 134–143.

Zhang, Y., Yu, Y., Chen, H. & Ozbolat, I.T. (2013a). Characterization of printable cellular micro-fluidic channels for tissue engineering. *Biofabrication*, 5(2), p. 025004.

Zhang, Y., Yu, Y. & Ozbolat, I.T. (2013b). Direct bioprinting of vessel-like tubular microfluidic channels. *Journal of nanotechnology in engineering and medicine*, 4(2), p. 020902.

Zhang, Y.S., Yue, K., Aleman, J., Mollazadeh-Moghaddam, K., Bakht, S.M., Yang, J., Jia, W., Dell'Erba, V., Assawes, P., Shin, S.R., Dokmeci, M.R., Oklu, R. &

Khademhosseini, A. (2017). 3d bioprinting for tissue and organ fabrication. *Annals of Biomedical Engineering*, 45(1), pp. 148–163.

Zhao, Y., Li, Y., Mao, S., Sun, W. & Yao, R. (2015). The influence of printing parameters on cell survival rate and printability in microextrusion-based 3d cell printing technology. *Biofabrication*, 7(4), p. 045002.

APPENDICES

Appendix A

Supplementary material of printheads and bioprinters components

Table A.1: *Bill of materials of the PH printhead, including quantity, cost, description and provider of each component*

Part Name	Qty.	Cost (US$)	Description	Provider	Code
Printhead carcass	1	1.71	3D printed	3D printer	-
Syringe cover	1	0.39	3D printed	3D printer	-
Heatsink clamp	1	0.06	3D printed	3D printer	-
Heatsink clamp thin	1	0.05	3D printed	3D printer	-
3D printer coupling	1	0.68	3D printed	3D printer	-
Al block	1	13.49	SMC[a]	Misumi	A6061FNM
Al plate	1	4.77	SMC	Misumi	A6061FNM
M3 brass insert	6	1.52	SMC	RS Online	278-584
Thermistor NTC 100k	3	4.68	SMC	RS Online	528-8592
M3x10 mm screw	10	4.77	SMC	RS Online	660-4636
M3x25 mm screw	4	1.92	SMC	RS Online	304-4435
Peltier module	2	14.80	SMC	Hebei I.T.	TES1-12704
Heatsink and axial fan	2	17.59	SMC	StarTech	FANP1003LD
		66.43			

[a]SMC = Standard Mechanical Component

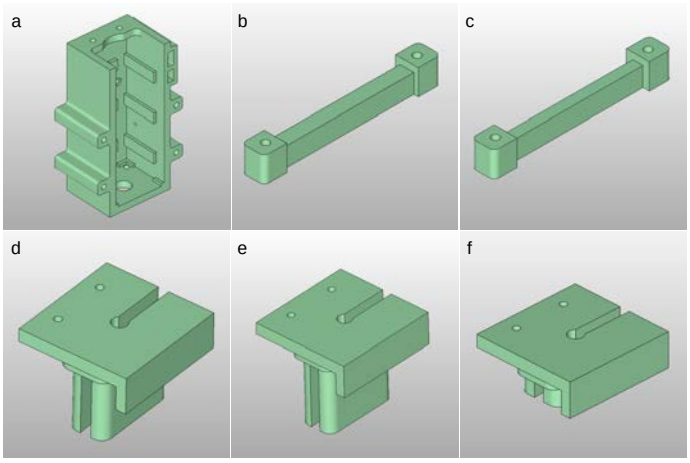

Figure A.1: *Images of the PH printhead .STL files. (a) Printhead carcass; (b) Heatsink clamp; (c) Thin heatsink clamp; (d) Cover syringe 3ml; (e) Cover syringe 5ml; (f) Cover syringe 10ml.*

Table A.2: *Bill of materials of the PHR printhead, including quantity, cost, description and provider of each component*

Part Name	Qty.	Cost (US$)	Description	Provider	Code
Printhead carcass	1	1.03	3D printed	3D printer	-
Syringe cover	1	0.20	3D printed	3D printer	-
Heatsink clamp	1	0.35	3D printed	3D printer	-
3D printer coupling	1	0.68	3D printed	3D printer	-
Al block	1	13.49	SMC[a]	Misumi	A6061FNM
Al plate	1	3.18	SMC	Misumi	A6061FNM
M3 brass insert	6	1.52	SMC	RS Online	278-584
Thermistor NTC 100k	3	4.68	SMC	RS Online	528-8592
M3x10 screw	10	4.77	SMC	RS Online	660-4636
M3x25 screw	4	1.92	SMC	RS Online	304-4435
Peltier module	2	14.80	SMC	Hebei I.T.	TES1-12704
Heatsink	2	4.10	SMC	RS Online	750-0951
Axial fan	2	13.71	SMC	RS Online	111-8315
		64.43			

[a]SMC = Standard Mechanical Component

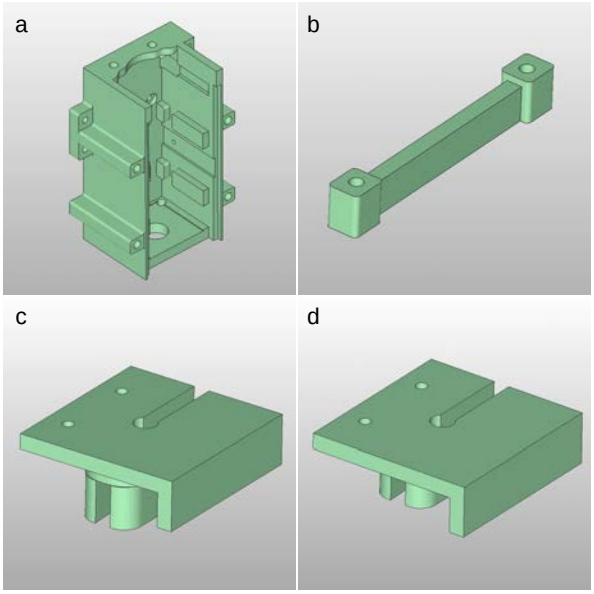

Figure A.2: *Images of the PHR printhead .STL files. (a) Printhead carcass; (b) Heatsink clamp; (d) Cover syringe 3ml; (e) Cover syringe 5ml.*

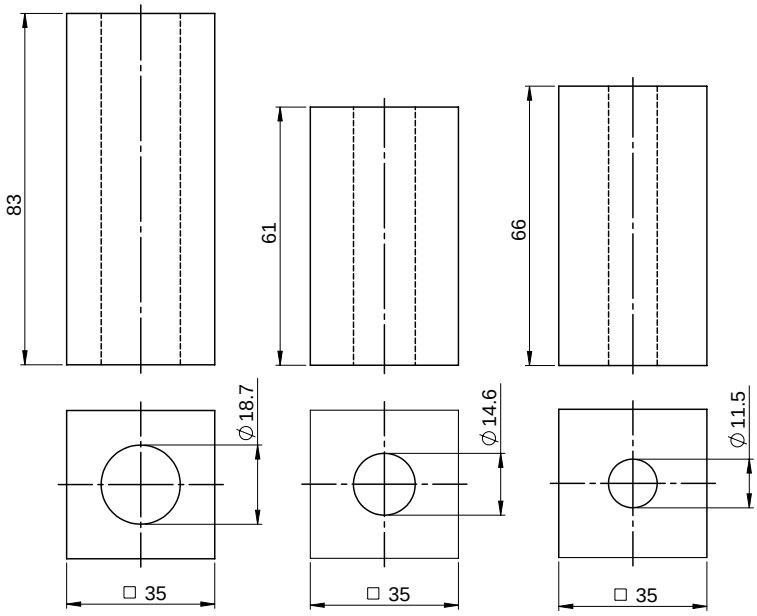

Figure A.3: *Dimensioned drawing of the PH printhead Al blocks for the 10 mL, 5 mL, and 3 mL (from left to right).*

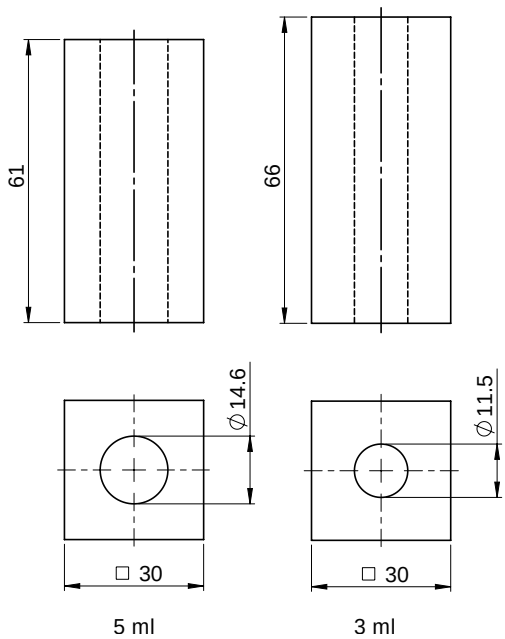

Figure A.4: *Dimensioned drawing of the PHR printhead Al blocks for the 10 mL, 5 mL, and 3 mL (from left to right).*

Table A.3: *Bill of materials of the high-temperature printhead, including quantity, cost, description, and provider of each component*

Part Name	Qty.	Cost (US$)	Description	Provider	Code
Printhead carcass	1	1.03	3D printed	3D printer	-
Front cover	1	0.20	3D printed	3D printer	-
Syringe cover	1	0.35	3D printed	3D printer	-
Al block	1	13.49	SMC[a]	3D printer	-
M3 brass insert	6	1.52	SMC	RS Online	278-584
Band heater (22v) (25x25mm)	1	7.00	SMC	LJXH	32856328124
Relay 12V-40A	1	3.00	SMC	Nagares	RLP/5-12D
Thermistor NTC 100k	1	1.56	SMC	RS Online	528-8592
M3x10 mm screw	6	2.86	SMC	RS Online	660-4636
M3x25 mm screw	4	1.92	SMC	RS Online	304-4435
		32.93			

[a]SMC = Standard Mechanical Component

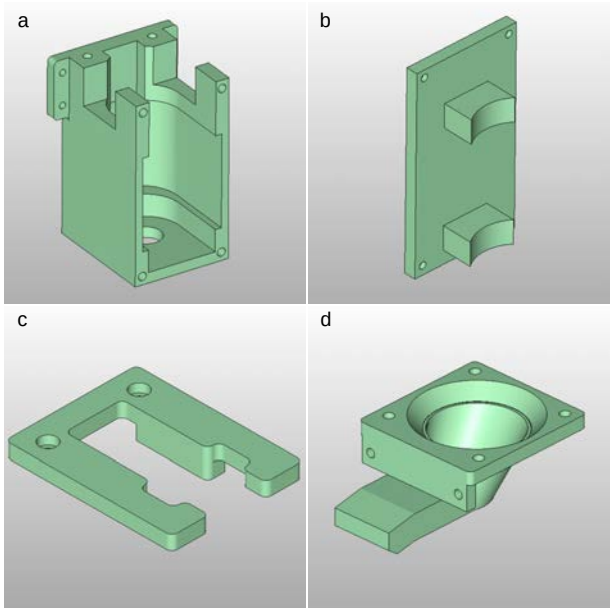

Figure A.5: *Images of the STL files of the high-temperature printhead components. (a) Printhead_carcass.STL; (b) Front_cover.STL; (c) Syringe_cover.STL; (d) Fan_support.STL.*

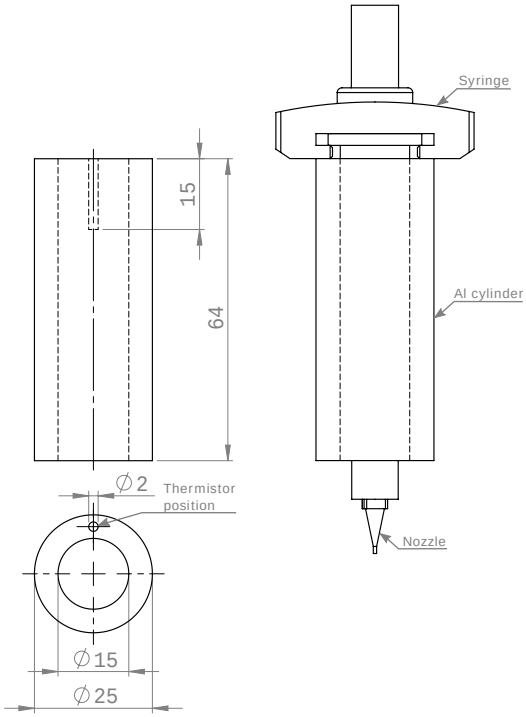

Figure A.6: *Dimensions of the Al block located inside the polycarbonate carcass of the printhead for heating the 5 mL stainless steel syringe (see scheme on the right side).*

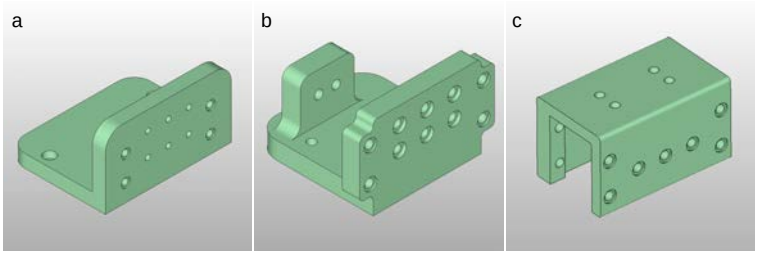

Figure A.7: *Images of the 3D printers couplings .STL files for a single printhead. (a) Coupling BCN3D+; (b) Coupling Witbox 2; (c) Coupling Sigma.*

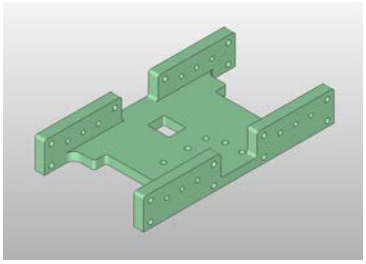

Figure A.8: *Image of Witbox 2 coupling .STL file for multiple printheads.*

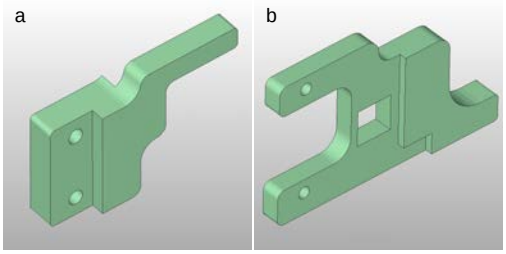

Figure A.9: *Images of Witbox 2 endstop modifications .STL files in x-axis (a) and y-axis (b).*

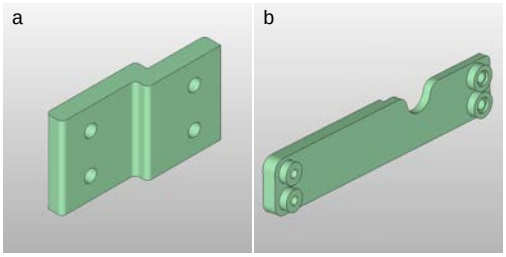

Figure A.10: *Images of Sigma endstops modifications .STL files in x-axis (a) and y-axis (b).*

Appendix B

G-code post-processing script

Perl script utilized in Slic3r software to post-process the G-code generated.

Listing B.1: *G-code post-processing Perl script*

```
#!/usr/bin/perl -i.before_postproc
# Author  : Enrique Sodupe
# Last modification: 08/01/2019
# Version : 1

use strict;
use warnings;

use constant X_homing => 179;  # X-homing for right carriage (x2_max endstop)
use constant time_open => 50;  # time valve is open before start to move [ms]
use constant time_close => 50; # time printhead is paused before valve closes [
    ms]

use constant zfeedrate => 400; #replace all z feedrates for Z axis
use constant Z_security => 4; # Option disabled
use constant Z_offset_E1 => 0; # Enable Z-offset for E1 (respect E0) (+ add)
use constant Z_offset_E2 => 0; # Enable Z-offset for E2 (respect E0)
use constant Z_offset_E3 => 0; # Enable Z-offset for E3 (respect E0)

my $t2 = 0;
my $z5 = 0;
my $z6 = 0;

while (<> ) {

#-------------------
# Clean GCode:
#-------------------

# Delete M104 S? T?; set extruder temperature
# SLIC3R: Filament settings-->Filament
# If Extruder and Bed temperatures are set to zero in SLIC3R this is not
    necessary because M104 are not included in the code
        if (/M104 S([0-9.]+) T([0-9.]+) ; set temperature/) {
                #print ";DELETED: M104 S? ; set temperature\n";
                #print ";del(M104)\n";
                print "";
                next;
        }

#Delete M104 S? T?; wait for temperature to be reached
#SLIC3R: Filament settings-->Filament
```

```
# If Extruder and Bed temperatures are set to zero in SLIC3R this is not
    necessary because M104 are not included in the code
        if (/M109 S([0-9.]+) T([0-9.]+) ; wait for temperature to be reached/) {
                #print ";DELETED:␣M109␣S37␣;␣wait␣for␣temperature␣to␣be␣reached\
                    n";
                #print ";del(M109)\n";
                print "";
                next;
        }
#Delete G21, G90 and M82: are already added in the Start GCode
        if (/G21 ; set units to millimeters/) {
                #print ";DELETED:␣G21␣;␣set␣units␣to␣millimeters\n";
                print "";
                next;
        }
        if (/G90 ; use absolute coordinates/) {
                #print ";DELETED:␣G90␣;␣use␣absolute␣coordinates\n";
                print "";
                next;
        }
        if (/M82 ; use absolute distances for extrusion/) {
                #print ";DELETED:␣M82␣;␣use␣absolute␣distances␣for␣extrusion\n";
                print "";
                next;
        }

#Delete "G92␣E0" (set extruder position to zero):
        if (/G92 E0/) {
       #print ";DELETED␣G92␣E0␣\n";
       print "";
       next;
    }
#Delete "G1␣E-2␣F2400":
        if (/^G1 E-2.00000 F2400.00000/) {
                print "";
                next;
        }
#----------------------------------
# Open-Close solenoid valves:
#----------------------------------
# Every time T0,T1,T2 or T3 appears in the GCODE $t2 stores which printhead is
    being used (T_?)
$t2 = $1 if (/^T([0-9.]+)/);
# Every time the bed moves (G1 Z) the height is recored. Utilized for the push
    button to lower the bed after Z-Homing.
$z6 = $1 if (/^G1 Z([0-9.]+) F([0-9.]+)/);

#Open-valve: "M106␣P0?␣S255". Replace the extruder first push to compensate the
    retraction.
        if (/^G1 E2.00000 F2400.00000/) {
        if ($t2<1) {
                        print "\nM106␣P$t2␣S255;␣-->␣Open␣valve\nG4␣P".time_open
                            ".";␣Wait␣[msec]\n\n";
                        next;
            }
            elsif ($t2==1) {
                        print "\nM106␣P$t2␣S255;␣-->␣Open␣valve\nG4␣P".time_open
                            ".";␣Wait␣[msec]\n\n";
                        next;
```

```
            }
            elsif ($t2==2) {
                        print "\nM106␣P$t2␣S255;␣-->␣Open␣valve\nG4␣P".time_open
                            ".";␣Wait␣[msec]\n\n";
                        next;
            }
            elsif ($t2==3) {
                        print "\nM106␣P$t2␣S255;␣-->␣Open␣valve\nG4␣P".time_open
                            ".";␣Wait␣[msec]\n\n";
                        next;
            }
        else {
            }
    }

#Close-valve: "M106␣P0?␣S0" and wait before next movement. Replace extruder
    retraction with valve closing.
        if (/G1 E([0-9.]+) F([0-9.]+)/) {
                if ($t2<1) {
                        print "\nM106␣P$t2␣S0;␣-->␣Close␣valve\nG4␣P".time_close
                            ".";␣Wait␣[msec]\n\n";
                        next;
            }
            elsif ($t2==1) {
                        print "\nM106␣P$t2␣S0;␣-->␣Close␣valve\nG4␣P".time_close
                            ".";␣Wait␣[msec]\n\n";
                        next;
            }
            elsif ($t2==2) {
                        print "\nM106␣P$t2␣S0;␣-->␣Close␣valve\nG4␣P".time_close
                            ".";␣Wait␣[msec]\n\n";
                        next;
            }
            elsif ($t2==3) {
                        print "\nM106␣P$t2␣S0;␣-->␣Close␣valve\nG4␣P".time_close
                            ".";␣Wait␣[msec]\n\n";
                        next;
            }
        else {
            }
    }
#-------------------------------------------------------
# Park printheads when not used (only for IDEX systems):
#-------------------------------------------------------
     if (/^;CHANGE PRINTHEAD/) {
                if ($t2<1) {
                        print "G1␣X0␣F5000;␣----------------------->␣Homing␣E$t2\
                            n";
                        }
                elsif ($t2==1) {
                        print "G1␣X0␣F5000;␣----------------------->␣Homing␣E$t2\
                            n";
                        }
                elsif ($t2==2) {
                        print "G1␣X".X_homing."␣F5000;␣----------->␣Homing␣E$t2\
                            n";
                        }
                elsif ($t2==3) {
```

```
                        print "G1 X".X_homing." F5000; ----------> Homing E$t2\
                            n";
                        }
                else {
                        }
        }
#-----------------------------------------------------------------------
#Move x-carriages to X-Homing when print ends (only for IDEX systems):
#-----------------------------------------------------------------------
 if (/^;END GCODE/) {
        if ($t2<1) {
                print "G1 X0 F5000; ----------------------> Homing E$t2\n";
        }
        elsif ($t2==1) {
                print "G1 X0 F5000; ----------------------> Homing E$t2\n";
        }
        elsif ($t2==2) {
                print "G1 X".X_homing." F5000; -----------> Homing E$t2\n";
        }
        elsif ($t2==3) {
                print "G1 X".X_homing." F5000; -----------> Homing E$t2\n";
        }
        else {
            }
 }
#-------------------------------------------------------------------------
# Z-Offsets between printheads (not utilized if the push-button is enabled):
#-------------------------------------------------------------------------
#Change Z axis speed and independent offset for each printhead:
if (/^G1 Z([0-9.]+) F([0-9.]+)/) {
    my ($z2) = $1;   #store the original value of Z height
    my ($f3) = $2;   #store the original Z feedrate
    my ($new_f3) = zfeedrate;   # new variable to replace the Z feedrate with a
        constant declared at the beginning

    my ($new_z2) = $z2 + Z_offset_E1;  # new Z heights for E1 considering E1 Z-
        offset
    my ($new_z3) = $z2 + Z_offset_E2;  # new Z heights for E2 considering E2 Z-
        offset
    my ($new_z4) = $z2 + Z_offset_E3;  # new Z heights for E2 considering E2 Z-
        offset

        if ($t2<1) {
                        print "G1 Z$z2 F$new_f3; --------------> E$t2 Z-travel (
                            NO offset) E$t2 \n";
                        next;
            }
            elsif ($t2==1) {
                print "G1 Z$new_z2 F$new_f3; --------------> E$t2 Z-travel (E1 
                    offset) E$t2 \n";
                next;
            }
            elsif ($t2==2) {
                print "G1 Z$new_z3 F$new_f3; --------------> E$t2 Z-travel (E2 
                    offset) E$t2 \n";
                next;
            }
            elsif ($t2==3) {
```

```
                print "G1 Z$new_z4 F$new_f3; --------------> E$t2 Z-travel (E3 offset) E$t2 \n";
                next;
            }
        else {
            }
    }
#-------------------------------------------------------------------
#Go to push button (Z-Homing) when the printhead is changed
#-------------------------------------------------------------------
        if (/^T0/) {
                print "T0 \n";
                print "G1 X75 Y38 F3000 ; ---------------> P0 go to push button \n";
                print "G28 Z ; --------------------------> Z-Homing P0 \n";
                print "G1 Z$z6 F400 ; ----------------> Lower bed Z-travel \n";
                print "\n";
                next;
        }
        if (/^T1/) {
                print "T0 \n";
                print "G1 Z20 F400 ; --------------> Lower bed for nozzle change \n";
                print "G1 X73 Y129 F3000 ; --------------> P1 go to push button \n";
                print "G28 Z ; --------------------------> Z-Homing P1 \n";
                print "G1 Z$z6 F400 ; ----------------> Lower bed Z-travel \n";
                print "\n";
                next;
        }
        if (/^T2/) {
                print "T1 \n";
                print "G1 Z20 F400 ; --------------> Lower bed for nozzle change \n";
                print "G1 X9 Y47 F3000 ; ----------> P2 go to push button \n";
                print "G28 Z ; --------------------------> Z-Homing P2 \n";
                print "G1 Z$z6 F400 ; ----------------> Lower bed Z-travel \n";
                print "\n";
                next;
        }
        if (/^T3/) {
                print "T1 \n";
                print "G1 Z20 F400 ; --------------> Lower bed for nozzle change \n";
                print "G1 X7 Y129 F3000 ; -----------> P3 go to push button \n";
                print "G28 Z ; --------------------------> Z-Homing P3 \n";
                print "G1 Z$z6 F400 ; ----------------> Lower bed Z-travel \n";
                print "\n";
                next;
        }
        else { print or die $!;}
}
```